

Kinetics and Reaction Engineering Aspects of Syngas Production by the Heterogeneously Catalysed Reverse Water Gas Shift Reaction

Von der Fakultät für Angewandte Naturwissenschaften
der Universität Bayreuth
zur Erlangung der Würde eines
Doktor-Ingenieurs (Dr.-Ing.)
genehmigte Dissertation

vorgelegte von

M.Tech. Unde Rajabhau Bajirao

aus

Undewadi (Indien)

| | |
|----------------------------|--|
| Erstgutachter: | Prof. Dr.-Ing. Andreas Jess |
| Zweitgutachter: | Prof. Dr. rer. nat. Peter Wasserscheid |
| Tag der mündlichen Prüfung | 11. June 2012 |

Lehrstuhl für Chemische Verfahrenstechnik
Universität Bayreuth

2012

Acknowledgements

First of all I would like to express my sincerely thank to Prof. Dr. Andreas Jess for giving me the opportunity to work in this group, for making my wish become realistic, for his excellent guidance and support, for the enthusiasm in supervision and tiredless correction of my dissertation. His advice and insight into things throughout my doctoral project have been invaluable.

My thanks go to Prof. Dr. Peter Wasserscheid for agreeing co-referee to my thesis, and also to Prof. Dr. Ruth Freitag and Prof. Dr. Ralf Moos for accepting to be in my examination committee.

I thank to Dr. Christoph Kern for his support in the modelling, for providing valuable suggestions, and for the correction of my dissertation and also to Dr. Wolfgang Korth for correction of my dissertation and helpful comments as well as many useful discussions.

I also thanks to Dr. Leonid Datsevich for his fruitful discussions, Mr. Jörg Gerchau for much help of experimental set-up and the operation of instruments, and for the help of solving computer problems, Mrs. Birgit Brunner for her help and support during my research work.

I thank Secretary Mrs. Rita Pannek for her administrative assistances.

I thank my colleagues from Chair of Chemical Engineering Johannes Thiessen and Lisa Schilder for a good time of sharing the office with them and for their help, Florian Heym, Amadeus Rose, Anne Piegsa, Stefan Fritz, Stephan Aschauer, Philipp Kaiser, Peter Fremerey and Susanne Fritschi for their help, support and providing pleasant and friendly research atmosphere over the years.

I thank to all my friends and my country-mates in Bayreuth for their love, supports and encouragement.

I am forever indebted to my parents, parents in law, family members and friends for their love, prayers, supports and encouragement.

Finally, I thank to my lovely wife, Sudha, for her support, understanding, encouragement and endless patience.

Parts of this work were already published:

1. A. Jess, P. Kaiser, C. Kern, R. B. Unde and C. von Olshausen, Considerations concerning the Energy Demand and Energy Mix for Global Welfare and Stable Ecosystems. *Chemie Ingenieur Technik* 83, 1777–1791 (2011).
2. R. B. Unde, C. Kern and A. Jess, High temperature CO₂ hydrogenation over Ni Catalyst. *8th European Congress of Chemical Engineering, **ProcessNet**, Berlin*, September 25–29 (2011).

Table of Contents

| | |
|--|-----------|
| List of symbols..... | v |
| 1. Introduction | 1 |
| 2. Basic theory and background of the work | 3 |
| 2.1 Heterogeneous catalysis | 3 |
| 2.1.1 Diffusion processes in heterogeneous catalysis | 3 |
| 2.1.2 Influence of internal and external mass transport on heterogeneously catalysed reactions | 5 |
| 2.1.3 Catalyst deactivation phenomena..... | 13 |
| 2.2 Utilization of CO ₂ for production of chemicals and fuels | 16 |
| 2.3 Concept of production of liquid fuels from CO ₂ via reverse water gas shift (RWGS) and Fischer Tropsch synthesis (FTS)..... | 20 |
| 2.4 Thermodynamics of CO ₂ conversion (reverse water gas shift and methanation)..... | 27 |
| 2.5 Kinetics of reverse water gas shift reaction and methanation..... | 32 |
| 3. Objective and scope of the work | 39 |
| 4. Experimental method and data analysis | 41 |
| 4.1 Experimental setup..... | 41 |
| 4.2 Experimental procedure | 43 |
| 4.3 Catalyst characterisation | 45 |
| 4.4 Evaluation of the experimental data..... | 47 |
| 4.4.1 CO ₂ hydrogenation reaction | 47 |
| 4.4.1.1 Conversion of CO ₂ and yield of CO and CH ₄ | 47 |
| 4.4.1.2 Determination of the intrinsic kinetic parameters..... | 48 |
| 4.4.1.3 Internal mass transport calculations..... | 49 |
| 4.4.1.4 Calculation of external mass transport limitations | 51 |
| 4.4.2 CO hydrogenation (methanation) reaction..... | 52 |
| 4.4.2.1 Conversion of CO and yield of CO ₂ and CH ₄ | 52 |
| 4.4.2.2 Kinetic analysis and mass transport calculations..... | 52 |
| 4.4.3 Water gas shift (WGS) reaction | 53 |
| 4.4.3.1 Conversion of CO and yield of CO ₂ and CH ₄ | 53 |
| 4.4.3.2 Kinetic analysis and mass transport calculations..... | 53 |
| 5. Results and discussion..... | 55 |

| | | |
|---------|--|-----|
| 5.1 | CO ₂ hydrogenation (RWGS)..... | 55 |
| 5.1.1 | Effect of reduction temperature on CO ₂ hydrogenation (RWGS) | 55 |
| 5.1.2 | Reproducibility of CO ₂ hydrogenation | 58 |
| 5.1.3 | Effect of residence time at varying temperature (RWGS and consecutive methanation)..... | 60 |
| 5.1.4 | Effect of residence time at constant temperature (RWGS and consecutive methanation)..... | 62 |
| 5.1.5 | Effect of catalyst particle size (RWGS and consecutive methanation)..... | 64 |
| 5.1.6 | Stability of the Ni catalyst for the RWGS reaction at high temperature..... | 65 |
| 5.1.7 | Kinetic analysis of the RWGS on the Ni catalyst | 66 |
| 5.1.8 | Kinetic analysis of the RWGS on the Al ₂ O ₃ catalyst..... | 74 |
| 5.1.9 | Comparison of catalysts activity and yield of CO and CH ₄ (CO ₂ hydrogenation) . | 77 |
| 5.2 | CO hydrogenation (methanation) reaction..... | 79 |
| 5.2.1 | Effect of reaction temperature on methanation | 79 |
| 5.2.2 | Stability of the Ni catalyst in CO methanation | 80 |
| 5.2.3 | Effect of residence time on methanation..... | 82 |
| 5.2.4 | Effect of residence time at constant temperature | 84 |
| 5.2.5 | Effect of catalyst particle size on methanation | 85 |
| 5.2.6 | Kinetic analysis and influence of internal and external mass transfer on methanation | 87 |
| 5.3 | Water gas shift (WGS) reaction | 93 |
| 5.3.1 | Influence of temperature on the WGS reaction..... | 93 |
| 5.3.2 | Influence of residence time at varying and constant temperature on the WGS reaction | 94 |
| 5.3.3 | Stability of the Ni catalyst in the WGS reaction | 96 |
| 5.3.3.1 | Low temperature stability | 96 |
| 5.3.3.2 | High temperature stability | 97 |
| 5.3.4 | Kinetic analysis and influence of internal and external mass transfer on the WGS reaction | 100 |
| 5.4 | Simulation of a reactor for a technical RWGS process..... | 107 |
| 5.4.1 | Basis equations of the reactor model | 107 |
| 5.4.2 | Results of the simulations of technical RWGS reactors | 111 |
| 5.4.3 | Pressure drop in fixed bed technical RWGS reactors | 118 |

| | |
|--|------------|
| 5.4.4 Estimation of the size of the RWGS reactor with regard to a subsequent Fischer Tropsch fixed bed reactor | 120 |
| 6. Summary and outline | 123 |
| 7. Zusammenfassung und Ausblick | 127 |
| Appendix A | 131 |
| A.1 Utilization of CO ₂ in catalytic conversion processes..... | 131 |
| Appendix B | 140 |
| B.1 Calculation of reaction order (CO hydrogenation, water gas shift reaction) | 140 |
| B.2 Diffusion coefficients of CO in the pores of the Ni catalyst..... | 143 |
| B.3 Characteristics data of catalysts | 144 |
| References | 147 |

List of symbols

Latin letters

| | | |
|--------------------|---|---|
| A_{BET} | internal surface area of particles | $\text{m}^2 \text{kg}^{-1}$ |
| $A_{m,ext}$ | specific internal surface area | $\text{m}^2 \text{kg}^{-1}$ |
| C | gas bulk concentration | mol m^3 |
| c_p | specific heat at constant pressure | $\text{J mol}^{-1} \text{K}^{-1}$ |
| d | diameter | m |
| D | diffusion coefficient | $\text{m}^2 \text{s}^{-1}$ |
| ΔG | change in Gibbs free energy | J mol^{-1} |
| Δp_b | pressure drop in a fixed bed | Pa |
| $\Delta_R H^\circ$ | enthalpy of reaction | J mol^{-1} |
| ΔS | entropy change per mole | $\text{J mol}^{-1} \text{K}^{-1}$ |
| E_A | activation energy | J mol^{-1} |
| E_{min} | minimal required energy for CO_2 separation | J mol^{-1} |
| f_b | friction factor | - |
| $k_{m,CO}$ | rate constant of CO conversion to CO_2 | $\text{m}^{3.6} \text{mol}^{-0.2} \text{kg}^{-1} \text{s}^{-1}$ |
| $k_{m,CO}$ | rate constant of CO conversion to CH_4 | $\text{m}^{1.2} \text{mol}^{0.6} \text{kg}^{-1} \text{s}^{-1}$ |
| $k_{m,CO2}$ | rate constant of CO_2 conversion to CO and CH_4 | $\text{m}^{1.5} \text{mol}^{0.5} \text{kg}^{-1} \text{s}^{-1}$ |
| K_p | equilibrium constant in terms of pressure | - |
| K_c | equilibrium constant in terms of concentration | - |
| L | reactor length | m |
| L_p | characteristic length of particle | m |
| m | mass of catalyst | kg |
| m_s | mass of shell | kg |
| M | molecular weight | kg mol^{-1} |
| η_{en} | efficiency | - |
| n | amount | mol |
| \dot{n} | molar flow rate | mol s^{-1} |
| p | pressure | Pa |

| | | |
|-------------------|--|------------------------------------|
| r_m | reaction rate per unit of mass of catalyst | $\text{mol kg}^{-1} \text{s}^{-1}$ |
| r_p | particle radius | m |
| R | ideal gas law constant (8.3142) | $\text{J mol}^{-1} \text{K}^{-1}$ |
| S | selectivity | - |
| t | time | s |
| t_s | particle shell thickness | m |
| T | temperature | $^{\circ}\text{C}$, K |
| u | interstitial fluid velocity | m s^{-1} |
| u_s | superficial velocity | m s^{-1} |
| V | volume | m^3 |
| V_p | volume of particle | m^3 |
| V_s | volume of particle shell | m^3 |
| \tilde{V} | molar gas volume | $\text{m}^3 \text{mol}^{-1}$ |
| V_{pore} | particle pore volume | $\text{m}^3 \text{kg}^{-1}$ |
| \dot{V} | volume rate | $\text{m}^3 \text{s}^{-1}$ |
| X | degree of conversion | - |
| y | gas volume fraction | - |
| Y | yield of product | - |

Greek symbols

| | | |
|-----------------|-------------------------------|----------------------------------|
| β | mass transfer coefficient | m s^{-1} |
| λ | wavelength | m |
| η | particle effectiveness factor | - |
| ε_b | porosity of reactor bed | - |
| ε_p | porosity of particle | - |
| μ | viscosity | $\text{kg m}^{-1} \text{s}^{-1}$ |
| ρ_b | bulk density | kg m^{-3} |
| ρ_p | particle density | kg m^{-3} |
| ρ_f | fluid density | kg m^{-3} |

| | | |
|----------|--|----------------------------|
| ν | kinematic viscosity (μ/ρ) | $\text{m}^2 \text{s}^{-1}$ |
| τ_m | modified residence time (m_{cat}/\dot{V}) | kg s m^{-3} |
| τ | residence time (empty tube) | s |
| τ_p | particle tortuosity | - |
| ϕ | Thiele modulus | - |

Subscripts

| | |
|---------|---------------------------|
| 0 | inlet |
| b | reactor bed |
| cat | catalyst |
| e | empty tube |
| eq | equilibrium |
| eff | effective |
| g | gas |
| i | species i |
| in | inlet of reactor |
| knu | Knudsen diffusion |
| m | related to mass |
| mol | related to molecule |
| out | outlet of reactor |
| p | particle |
| $pore$ | related to pore |
| R | reactor |
| s | related to surface |
| $total$ | related to total pressure |

Dimensionless numbers

| | |
|-----------|-----------------|
| <i>Nu</i> | Nusselt number |
| <i>Pr</i> | Prandtl number |
| <i>Re</i> | Reynolds number |
| <i>Sc</i> | Schmidt number |
| <i>Sh</i> | Sherwood number |

Abbreviations

| | |
|------|---|
| CCC | carbon capture and conversion |
| FTS | Fischer Tropsch synthesis |
| HTE | high temperature electrolysis of water |
| MFC | mass flow controller |
| NTP | normal temperature and pressure (20 °C and 1 atm) |
| RWGS | reverse water gas shift |
| toe | tonnes of oil equivalent, 1 toe = 42 GJ |
| TPR | temperature programmed reduction |
| TPS | technical photosynthesis |
| WGS | water gas shift |
| XRD | x-ray diffraction |

1. Introduction

Carbon dioxide is the most important greenhouse gas being emitted into the atmosphere from fossil fuel combustion and other anthropogenic activities. According to the National Oceanic and Atmospheric Administration (NOAA), the CO₂ concentration in the atmosphere was 392 ppm in February 2011 [1] which is very high compared to 379 ppm in 2005 and far from the natural range of the last 650,000 years [2]. The annual emissions of CO₂ have grown between 1970 and 2004 by about 80% from 21 to 39 gigatonnes [2]. The growing concentration of carbon dioxide in the atmosphere increased the impact on the environment such as global warming and forcing a climate change. The main greenhouse gases are water vapour (H₂O), carbon dioxide (CO₂), methane (CH₄), nitrous oxide (N₂O), hydrofluorocarbons (HFCs), perfluorocarbons (PFCs), and sulphur hexafluoride (SF₆), but CO₂ contributes about 77% to the world's greenhouse gas emissions (excluding water vapour) into the atmosphere in 2004 [2].

Alternative energy sources are not only important with regard to global warming but also to maintain the rising cost of crude oil. Both aspects have motivated researchers to look for solutions to reduce the greenhouse gas emission and/or its utilization. The mitigation of greenhouse gas emissions is also an interesting challenge in exploring new concepts and new opportunities for catalysis and industrial chemistry. Recently various carbon capture and storage technologies (CCS) are developed for a significant reduction of CO₂ emissions into the atmosphere [3]. These technologies are mainly suitable to capture CO₂ from large industrial sources such as fossil fuel fired power plants. But only with these efforts it is not possible to reduce and control CO₂ emissions [4], and the availability of sufficient storage capacity to capture carbon dioxide is also still an open question. However, very little attention has been paid by industry and academia in utilization of CO₂ because of its high thermodynamic stability. For the reduction of greenhouse gas emission various strategies have been suggested that includes promoting energy end-use efficiency, supporting the use of renewable energy resources as well as sustainable transportation and waste management [5].

One effective approach to avoid CO₂ accumulation into the atmosphere is the recovery of carbon dioxide from flue gases and its recycle by converting to useful chemicals [6, 7]. The

conversion of CO_2 to CO by catalytic hydrogenation has been recognized as a very promising process. In industry, synthesis gas containing H_2 and CO can be used to produce methanol as well as long chain hydrocarbons via the Fischer-Tropsch synthesis. Therefore, the reverse water gas shift (RWGS) reaction ($\text{CO}_2 + \text{H}_2 \rightarrow \text{CO} + \text{H}_2\text{O}$) is an important option for CO production.

The transformation of CO_2 and H_2 into CO and H_2O depends upon several factors such as catalyst selection, ratio of CO_2/H_2 , and reaction temperature and pressure. Therefore, the main focus of this study was to select a suitable catalyst and reaction conditions for CO_2 hydrogenation in a fixed bed reactor. The experiments were designed such that the RWGS reaction could be examined in the forward and reverse direction, i.e. the “normal” water gas shift reaction ($\text{CO} + \text{H}_2\text{O} \rightarrow \text{CO}_2 + \text{H}_2$) was also studied. The consecutive CO hydrogenation, i.e. methanation reaction ($\text{CO} + 3\text{H}_2 \rightarrow \text{CH}_4 + \text{H}_2\text{O}$) also had to be considered.

In heterogeneous catalysis, transport processes (external boundary layer diffusion, pore diffusion) may have an influence on the effective reaction rate, and were also studied in this work in detail.

2. Basic theory and background of the work

In the following, some basic aspects of heterogeneous catalysis and phenomena of mass transfer in heterogeneous catalysis (gas-solid diffusion in a fixed bed reactor), deactivation phenomena of catalysts are briefly outlined. Some CO₂ utilization processes including reverse water gas shift, and the thermodynamics of CO₂ conversion are also discussed.

2.1 Heterogeneous catalysis

The study of heterogeneous catalysis dates back to the early 1800s where *Faraday* was one of the first scientists who performed the ability of platinum to facilitate oxidation reactions [8]. After that, the field of heterogeneous catalysis has been grown continuously and attracted several Nobel prizes (for example, in 2007, *Gerhard Ertl*, a German physical chemist was awarded the Nobel Prize in chemistry for his contribution in the area of surface science). The production of low cost and high quality raw materials, production of transportation fuels, and pollution control are the major areas in which heterogeneous catalysis has shown a remarkable impact.

It is well known that the catalyst efficiency is directly proportional to its surface area. Many of the heterogeneous catalysts used in today's industry consist of one or more catalytically active components deposited on the surface of a support material having a high surface area, high porosity, and a suitable thermal and mechanical strength. Heterogeneous reactions occur in a system in which two or more phases are present (e.g. the solid catalyst and liquids or gases as reactants) and the reactions occur at the interface between these phases.

2.1.1 Diffusion processes in heterogeneous catalysis

The chemical reactions of heterogeneous catalysis occur between the adsorbed reactants and the surface of the solid catalyst particle. The diffusion of reactants to the catalyst surface (mostly to the inner surface of pores) and the diffusion of products from this surface are purely physical phenomena. In case of catalytic gas-solid reactions, the rate of reaction within a porous catalyst strongly depends upon the accessibility of reactants to the active sites dispersed throughout the porous structure of the catalyst (Fig. 2-1).

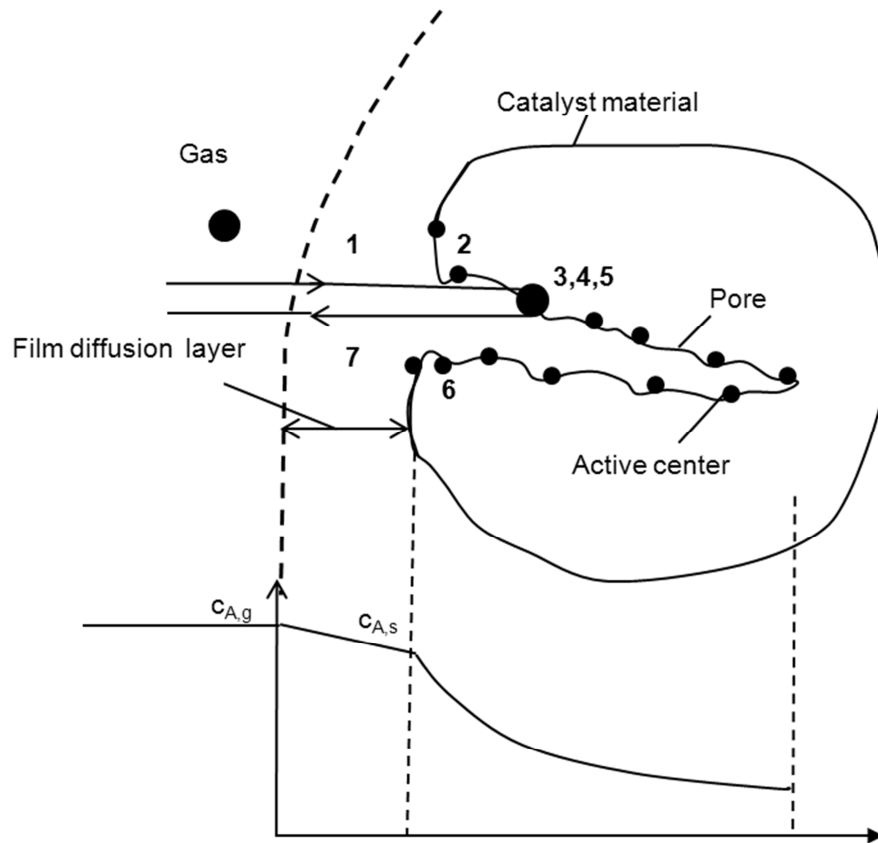


Fig. 2-1: Sequential steps involved in heterogeneous catalytic gas phase reaction.

Consider a simple gaseous reaction ($A \rightarrow B$) occurring inside a reactor containing porous catalyst particles. In order to convert the reactant A into product B, the following physical and chemical processes are important:

1. Diffusion of reactant A from the bulk gas phase through the boundary layer or stagnant gas film surrounding the catalyst particle to the external surface of the catalyst (film diffusion).
2. Diffusion of reactant A into the porous structure of the catalyst particle to the point where adsorption/reaction takes place (pore or intraparticle diffusion).
3. Adsorption of reactants on the inner surface of the catalyst.
4. Surface reaction of adsorbed reactant A to adsorbed product B at the catalyst surface.
5. Desorption of product B from the inner surface of the catalyst into the pores.
6. Diffusion of formed products through the porous network structure to the external surface of the catalyst (intraparticle diffusion).

7. Diffusion of product B from the external surface of the catalyst through the boundary layer into the bulk gas phase.

As a result of these steps, a concentration profile may exist in the catalyst pellet and outside in the film layer. The steps 3, 4, and 5 are chemical processes, which strongly depend on temperature typically with effective activation energies of 20 to 200 kJ/mol. The steps 1, 2, 6, and 7 are diffusional processes or mass transfer with relative low temperature dependence compared to the chemical processes. If these steps are very fast, then there is no resistance for mass transfer from the bulk phase to the external surface area of the particles and to the active sites inside the pore. So the concentration at the internal catalyst surface is the same as that of the bulk phase, and the mass transfer does not affect the reaction rate. But in case that mass transfer is slow relative to the chemical reactions, there may be an influence or control of the overall reaction rate by the mass transfer. The net kinetics obtained from all reaction steps (1 to 7) is thus called effective kinetics or macro-kinetics.

2.1.2 Influence of internal and external mass transport on heterogeneously catalysed reactions

In heterogeneous catalytic reactions, the consideration of internal and external mass transfer limitations is very important when experiments are performed to determine intrinsic kinetic parameters. According to Arrhenius law, the intrinsic chemical rate is nearly an exponential function of temperature and the mass transfer rate is less strongly influenced by the temperature, e.g. for gas diffusion the rate is proportional to about $T^{1.5}$. Fig. 2-2 shows an Arrhenius plot of the temperature dependence of the effective rate constant of a catalytic reaction for the three reaction rate controlling regimes.

Regime of intrinsic kinetic:

At low temperatures, the rate of the chemical reaction is slow compared to mass transport processes. Therefore only a negligible concentration gradient will be established in the exterior and interior of the catalyst particle. The reaction temperature also remains constant over the entire cross-section of the catalyst pellet and also in the boundary layer. This is called as an intrinsic region where the true intrinsic kinetics of reactions is measured. For this region, the slope of the curve $\ln k_m$ vs $1/T$ is proportional to the chemical activation

energy (E_A). The reaction rate of gas-solid reactions is often described with accuracy by a power law equation:

$$r_m = \frac{d\dot{n}_i}{dm_{cat}} = k_m C_i^n \quad (2.1)$$

The reaction rate usually depends upon the rate constant (k_m) related to the mass of catalyst (m_{cat}), concentration of reactant (C_i), and the intrinsic order of reaction (n). The temperature dependence of the reaction rate constant is given by the Arrhenius equation:

$$k_m = k_{m,0} e^{-\frac{E_A}{RT}} \quad (2.2)$$

In the Arrhenius equation, $k_{m,0}$ is the frequency factor and E_A is the intrinsic activation energy of the chemical reaction.

Regime of pore diffusion:

At intermediate temperatures, the chemical reaction rate is faster than the inner mass transport (pore diffusion). Between this regime and the regime of intrinsic kinetic, a transition regime is located where the slope of the curve changes with temperature. In the pore diffusion region, the concentration of reactants at the pore mouth is much higher than that inside the pore and drops distinctly. Here the entire catalytic surface is not accessible to the same concentration. Therefore the effective reaction rate will be less as compared to the rate without mass transfer limitations.

For this region, the effective activation energy is roughly one half of the true activation energy ($E_A/2$). In general, there is not only the change in effective activation energy but the effective order of the reaction also changes when the transition from kinetic to diffusion control occurs. For an n^{th} order reaction, the effective reaction order approaches the value of $(n + 1)/2$ in case of strong limitation by pore diffusion.

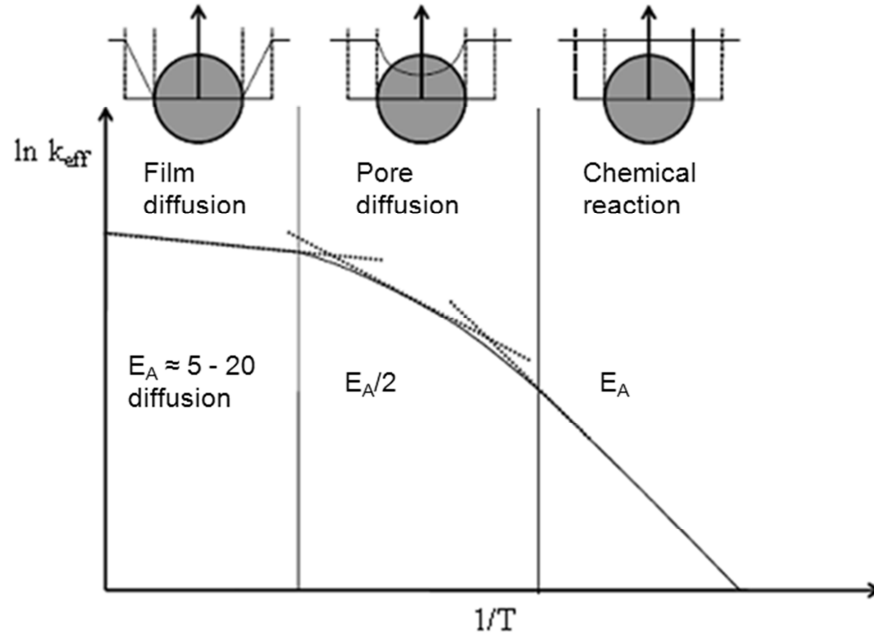


Fig. 2-2: Typical Arrhenius plot of temperature dependence of the effective rate constant of catalytic reaction; three regimes of reaction rate control for low, intermediate and high reaction temperature.

For a first order reaction the effective rate of chemical reaction is given as

$$r_{m,eff} = \eta k_m C_{i,s} \quad (2.3)$$

where $C_{i,s}$ is the concentration at the catalyst surface and η is the effectiveness factor which is a function of the Thiele modulus. The effectiveness factor η is defined as the ratio of the observed rate of reaction to the rate in the absence of any diffusional resistance, i.e.

$$\eta = \frac{\text{actual reaction rate}}{\text{intrinsic rate of chemical reaction}} = \frac{r_{m,eff}}{r_m} \quad (2.4)$$

There are several factors which influences the effectiveness factor, such as pore shape and pore structure (micro-macro), particle size distribution, and change in volume upon reaction [9]. The magnitude of the effectiveness factor ranges between 0 and 1 which indicate the relative importance of diffusion and reaction limitations [10]. The internal effectiveness factor varies for different catalyst geometries (see Fig. 2-3) and for different reaction orders (see Fig. 2-4).

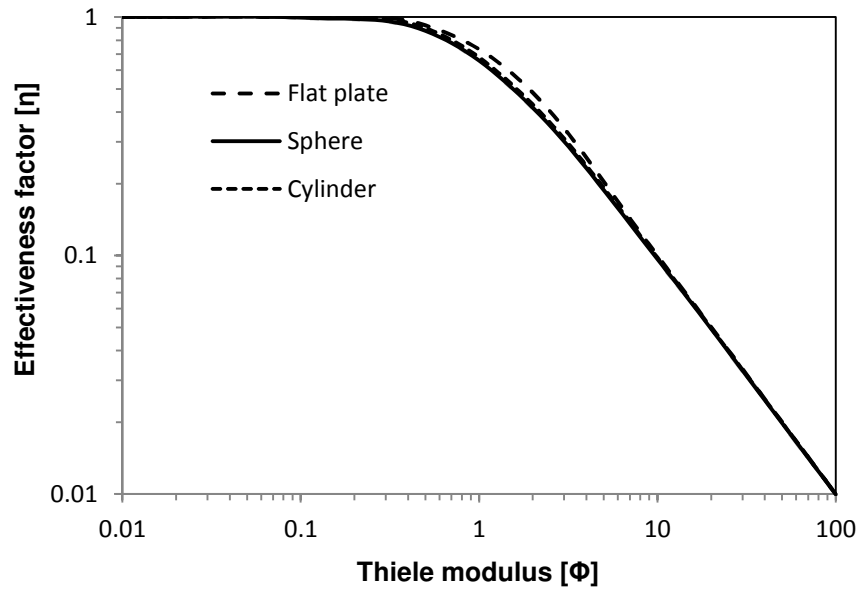


Fig. 2-3: Relationship of the effectiveness factor versus generalized Thiele modulus (Eq. (2.7)) for different shapes of catalyst.

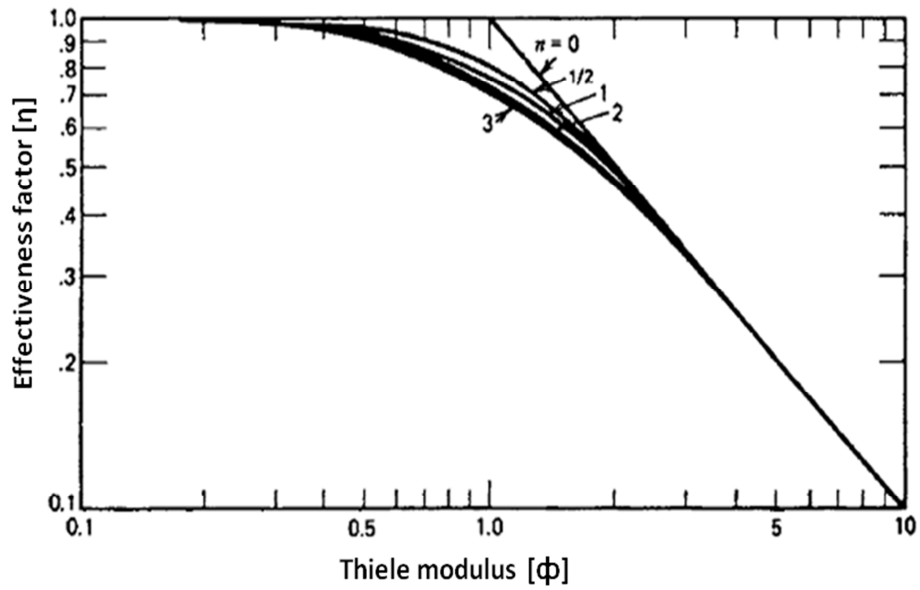


Fig. 2-4: Relationship of the effectiveness factor versus generalized Thiele modulus (Eq. (2.8)) for simple-order reactions [11].

The effectiveness factor as a function of the Thiele modulus for a flat plate and an isothermal, irreversible first-order reaction is given as:

$$\eta = \frac{\tanh \phi}{\phi} \quad (2.5)$$

For the spherical particle, an effectiveness factor is given as:

$$\eta = \frac{1}{\phi} \left[\frac{1}{\tanh(3\phi)} - \frac{1}{(3\phi)} \right] \quad (2.6)$$

The relation between Thiele modulus and effectiveness factor for a flat plate in Eq. (2.5) gives the approximation that η equals $1/\phi$ for large values of the Thiele modulus ($\phi \geq 2$). The equation of an effectiveness factor for a flat plate can be used in a good approximation for any particle geometry with characteristic length (L_p), which is given by Eq. (2.9).

The dimensionless Thiele modulus (ϕ) plays a key role in determining pore diffusion limitations. For general shape, first order and irreversible reaction, the Thiele modulus is given as [9]:

$$\phi = L_p \sqrt{\frac{k_m \rho_p}{D_{i,eff}}} \quad (2.7)$$

For a irreversible reaction and order $n \neq 1$, the Thiele modulus is given as:

$$\phi = L_p \sqrt{\left[\frac{n+1}{2} \right] \frac{k_m \rho_p C_i^{n-1}}{D_{i,eff}}} \quad (2.8)$$

where ρ_p is the density of particle, $D_{i,eff}$ is the effective diffusivity of species i , and L_p is the characteristic length for various shapes which is given as:

$$L_p = \frac{\text{volume of shape}}{\text{external area of shape}} \quad (2.9)$$

The characteristic length for cylinders is $L_p = d_p/4$, for spheres $L_p = d_p/6$ and for flat plate L_p (where d_p is the particle diameter and $2L_p$ is the plate thickness).

The point at which a pellet of optimal dimension shows the transition from chemical to diffusion control region is practically important. Small particles have a low characteristic length, which decreases the value of the Thiele modulus (see Eq. (2.7) and Eq. (2.8)) and thus increase the effectiveness factor, and lowers the pore diffusion resistance. On the other hand, a small particle size creates a high pressure drop in a fixed bed reactor. Therefore from

industrial point of view, it is very important to have particles with appropriate size that balance between the pressure drop across the catalyst bed and the effects of the diffusional resistance within the catalyst particles.

The pore structure of porous media may be extremely complex and is often not well defined. So it is common to describe the diffusion of a gas in pores in terms of an effective diffusivity. The general, inside the catalyst pellet diffusion may occur by means of three different modes, surface diffusion, molecular diffusion and Knudsen diffusion [12]. For most industrial catalysts and conditions used, only molecular and Knudsen diffusion are considered. In the regime, where the ratio of the pore radius to the mean free path of the diffusing molecule is greater than about 10, molecular diffusion dominates the overall mass transport. In the regime, where the ratio of the pore radius to the mean free path of the diffusing molecule is less than 1, Knudsen diffusion more and more dominates the transport phenomenon called (Knudsen regime). The effective diffusivity is given as

$$D_{i,eff} = \frac{\epsilon_p}{\tau_p} D_{i,pore} \quad (2.10)$$

where ϵ_p is the porosity and τ_p is the tortuosity of the porous structure. Porosity is defined as the ratio of pore volume to the total volume of the catalytic particle. In general, the porosity is typically in a range 0.25 to 0.7. The tortuosity factor is a structural factor and usually determined experimentally. It is defined as the ratio of the actual length of the diffusion path to the straight-line distance between the ends of the flow path. So, tortuosity is always greater than 1 and independent of the temperature and nature of diffusing species. Some catalyst materials with their porosity and tortuosity are shown in Table 2-1.

If the mean free path is much smaller than the pore dimension, the collision arises within other gas molecules more often than the collision with pore wall. In this case the effective diffusivity is independent of the pore diameter and only the ordinary molecular diffusivity is described in the absence of experimental data by using the well known *Stefan-Maxwell* equation of diffusion [12].

Table 2-1: Porosity and tortuosity of various catalysts.

| Material | Porosity | Tortuosity | Reference |
|--|----------|------------|-----------|
| Pt-LSM oxide | 0.3 | 6 | [13] |
| Ni-YSZ oxide | 0.3 | 3 | [14] |
| 10 % Pt on carbon | 0.4 | 1.1 | [15] |
| 1 % Pd on alumina | 0.5 | 7.5 | [16] |
| 1.5 % Ni, 4 % Mo on alumina | 0.6 | 1.3 | [17] |
| 7 % Cr ₂ O ₃ , Fe ₃ O ₄ | 0.6 | 11.1 | [18] |
| 2.9 % Al ₂ O ₃ , 1.44 % K ₂ O, Fe ₃ O ₄ | 0.52 | 12.5 | [18] |

If the pore diameter is very small compared to the mean free path of the diffusing gas molecules and the density of gas molecules is low, the gas molecules collide more frequently with the pore wall than with each other. In this Knudsen region, the Knudsen diffusivity $D_{i,knu}$ of a gas species in a pore is given by

$$D_{i,knu} = \frac{d_{pore}}{3} \sqrt{\frac{8 R T}{\pi M_i}} \quad (2.11)$$

where d_{pore} is the pore diameter, T is the temperature in Kelvin, R is the gas constant and M_i is the molecular weight of gas species i . According to Eq. (2.11), the Knudsen diffusivity $D_{i,knu}$ is proportional to $T^{1/2}$ and is independent of pressure.

If both molecular diffusion and Knudsen diffusion contribute to the pore mass transport, the combined diffusivity (transition diffusivity) can be approximated by the *Bosanquet* equation [19]:

$$\frac{1}{D_{i,pore}} = \frac{1}{D_{i,mol}} + \frac{1}{D_{i,knu}} \quad (2.12)$$

Regime of external mass transport:

At very high temperatures, external mass transport (film diffusion) may become the rate controlling step. The concentration within the catalyst pellet is then almost zero and the reactants react immediately on the outer surface of catalyst. In this region, the slope of the

curve of effective reaction rate gets small (see Fig. 2-2), and the effective activation energy is in a range of only 5 to 20 kJ/mol.

The effective reaction rate due to external mass transfer can be expressed in terms of particle mass ($\text{mol kg}^{-1} \text{ s}^{-1}$) as:

$$r_{m,eff} = \beta A_{m,ext} (C_{i,g} - C_{i,s}) \quad (2.13)$$

β (m/s) is the mass transfer coefficient, $A_{m,ext}$ (m^2/kg) is the external surface area of catalyst, and $C_{i,g}$ and $C_{i,s}$ (mol/m^3) are the concentrations in the bulk phase and at the external particle surface, respectively. When $\eta k_m \ll \beta A_{m,ext}$, the external mass transport is rapid compared to the consumption by the chemical reaction in the particle, and the concentration at the external surface is almost equal to the concentration in the bulk phase of the fluid.

For a spherical particle, the external mass transfer area is given by (with ρ_p as particle density):

$$A_{m,ext} = \frac{6}{d_p \rho_p} \quad (2.14)$$

The mass transfer coefficient (β) depends upon the particle size, particle geometry, molecular diffusion coefficient ($D_{i,mol}$), and the hydrodynamic conditions such as velocity and viscosity of the fluid. Depending upon the dimensionless Sherwood number (Sh), the value of β can be calculated as:

$$\beta = \frac{Sh D_{i,mol}}{d_p} \quad (2.15)$$

The Sherwood number represents the ratio of convective to the diffusive mass transfer. Several empirical correlations have been proposed related to the Sherwood number. One correlation for the Sherwood number for a single particle (Sh_p) using Reynolds number (Re) and Schmidt number (Sc) proposed by *Hayhurst and Parmar* [20] is given as

$$Sh_p = 2 + 0.69 \sqrt{Re} \sqrt[3]{Sc} \quad (2.16)$$

The Sherwood number for the mass transfer in a fixed bed (Sh) is

$$Sh = [1 + 1.5 (1 - \epsilon_b)] Sh_p \quad (2.17)$$

where ϵ_b is the bed porosity, which is defined as the ratio of void volume to the total volume of bed.

The Reynolds number is defined as

$$Re = \frac{u d_p}{\nu} \quad (2.18)$$

Its value depends upon the interstitial velocity (u), kinematic viscosity of gas (ν), and the particle diameter (d_p). The interstitial velocity (velocity within the bed) is higher than the superficial velocity, and can be calculated by the ratio of the superficial velocity to the bed porosity ($u = u_s/\epsilon_b$).

The Schmidt number is defined as

$$Sc = \frac{\nu}{D_{i,mol}} \quad (2.19)$$

The correlations for mass transfer are similar to those for in heat transfer where the Sherwood number is replaced by the Nusselt number (Nu) and the Schmidt number by the Prandtl number (Pr). For gases, both Sc and Pr are about 0.7.

The effective reaction rate for a first order reaction by considering internal and external mass transfer resistances is given as:

$$r_{m,eff} = \left[\frac{1}{\eta k_m} + \frac{1}{\beta A_{m,ext}} \right]^{-1} C_{i,g} \quad (2.20)$$

2.1.3 Catalyst deactivation phenomena

The deactivation of catalysts is a phenomenon in which the structure and state of the catalyst change leading to loss of active sites causing a decrease in activity and/or selectivity over time. There are many causes of catalyst deactivation, which are divided into four main categories [21, 22] (Fig. 2-5).

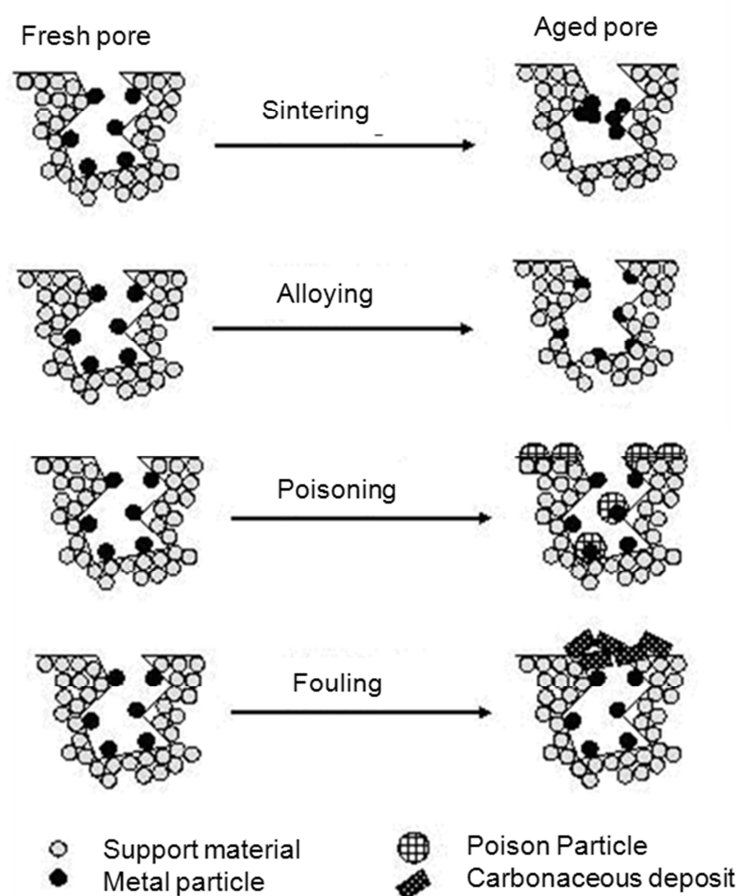


Fig. 2-5: Deactivation phenomena's of catalyst by the mechanism of sintering, alloying, poisoning, fouling and coking (modified after [23]).

Sintering:

The deactivation may be the result of the loss of the catalyst surface area due to crystallite growth of the catalytic phase or the loss of support area. Generally, sintering is irreversible and occurs at high temperature where metal atoms migrate and grow to metal crystallites thereby changing the particle size distribution. The rate of sintering increases exponentially with temperature. Sintering rate is also depending upon some other factors such as [21]:

- Type of metal (e.g. rate of sintering for Ni/Al₂O₃ is less than Pt/Al₂O₃).
- Presence of promoters or impurities (e.g. O, CaO, CeO₂, BaO reduce the rate of sintering by decreasing the atom mobility, and S, Cl, Pb, F reduce the rate of sintering by increasing the atom mobility).

(c) Atmosphere (e.g. for metals, sintering is mostly rapid in oxygen atmosphere while relatively slow in hydrogen).

(d) Metal dispersion (e.g. for Ni/SiO₂, metal dispersion is strongly affected on the rate of sintering for T > 650 °C).

(e) Support surface area and porosity (e.g. the decreasing order of stability of Pt on different supports in vacuum is Pt/Al₂O₃ > Pt/SiO₂ > Pt/C).

Poisoning:

Poisoning is defined as the loss of catalytic activity due to the chemisorption of impurities on active sites. However there is no clear difference between temporary and permanent poisoning. A strong poison at low temperatures may be less harmful at high temperature [24]. Poisoning may decrease the activity but may not affect the selectivity or sometimes even may enhance the selectivity.

Sulphur plays an important role as a poison in many catalytic processes such as hydrogenation, methanation, steam reforming, Fischer-Tropsch synthesis, and fuel cells [21]. For example, in refineries the catalytic reforming Pt catalyst strongly adsorbs sulphur that poisons the catalyst [24]. The deactivation of PdO-Al₂O₃ catalyst in lean-burn natural gas engine exhaust is due to the contamination by SO₂ and H₂O [25].

Fouling and coking:

Fouling is the physical deposition of species from the bulk fluid phase onto the catalyst surface resulting in loss of activity due to blockage of active sites and/or pores [21]. The terms carbon and coke are somewhat arbitrary and are related to their origin. Carbon is generally the product obtained by CO disproportionation while coke is obtained by decomposition or condensation of hydrocarbons (typically polymerised heavy hydrocarbons) on the catalyst surface [21]. The deactivation of catalysts by coking is very common in industrial processes [26]. Zeolites are known to have a high catalytic activity towards coke formation over the temperature range of 300 to 600 °C, which effects the diffusional properties of zeolites [22]. In the present study, the coke formation was observed in CO hydrogenation and water gas shift reaction in the temperature range of 450 to 650 °C.

Alloying:

In alloying, a combination of two or more metals takes place at high temperature (particularly under reduction conditions). Alloying may change the activity and stability of catalyst. The Cu-Zn alloy formation during the reduction of the catalyst in the temperature range of 230 to 500 °C with a mixture of H₂ and N₂ deactivates the catalyst and reduces its activity for the water gas shift [27]. Other example are formation of RhAl₂O₄ in Pt-Rh/Al₂O₃ catalysts in catalytic converters for reduction of car engine emissions, formation of Ni₂Al₂O₄ during steam reforming over Ni/Al₂O₃, and formation of KAlO₂ in FTS.

2.2 Utilization of CO₂ for production of chemicals and fuels

The energy related CO₂ emissions have increased with an average annual growth rate of 1.9% from 1990 to 2007 and the emissions are expected to rise with an annual rate of 1.3% until 2035 [8]. The global CO₂ emissions from fossil fuels combustion increase from near by zero in 1870 to 29.7 billion metric tons in 2007 and are projected to increase up to 42 billion metric tons in 2035 [8]. The analysis of world energy-related carbon dioxide emissions by the consumption of fossil fuels (Fig. 2-6) shows that coal is the largest source of carbon dioxide (12.5 billion metric tons), followed by liquid fuels (11.3 billion metric tons), and natural gas (5.9 billion metric tons).

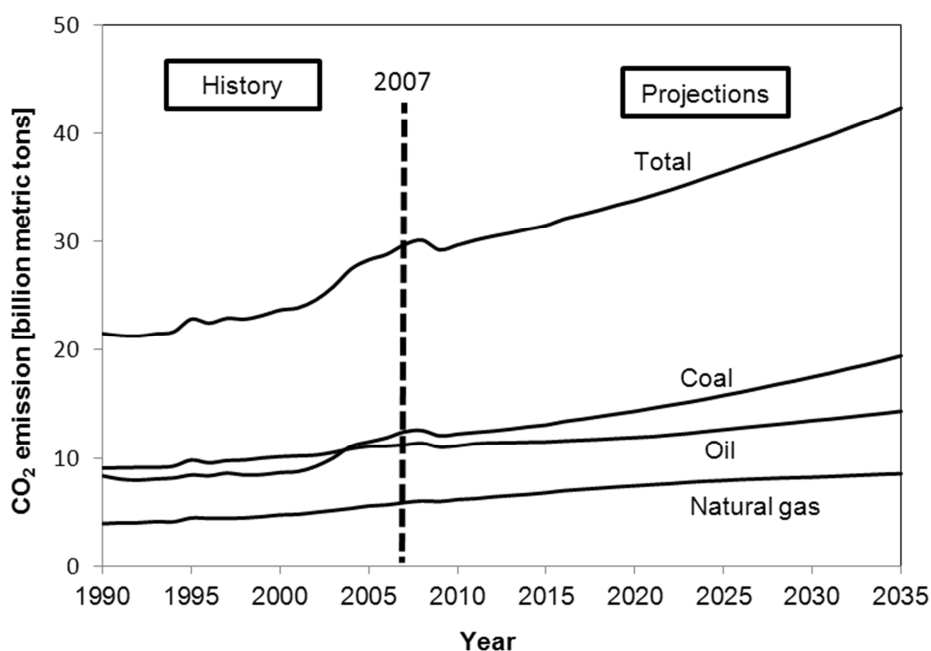


Fig. 2-6: The world energy-related carbon dioxide emissions by fuel type [8].

To avoid CO₂ emissions, various measures such as recovery, removal, and storage disposal have been proposed. Carbon capture and storage needs large amounts of energy for its capture, transportation, and sequestration. Therefore the utilization of CO₂ in chemical conversion processes may become an important option for sustainable development, mitigation of carbon emissions, and to avoid global warming. The various direct and indirect uses of CO₂ are shown in Fig. 2-7. The potential of CO₂ in the direct use is very low compared to indirect use. The indirect utilization of CO₂ has advantages such as production of value added chemicals, environment friendly processing, and non-hazards process utilization of CO₂.

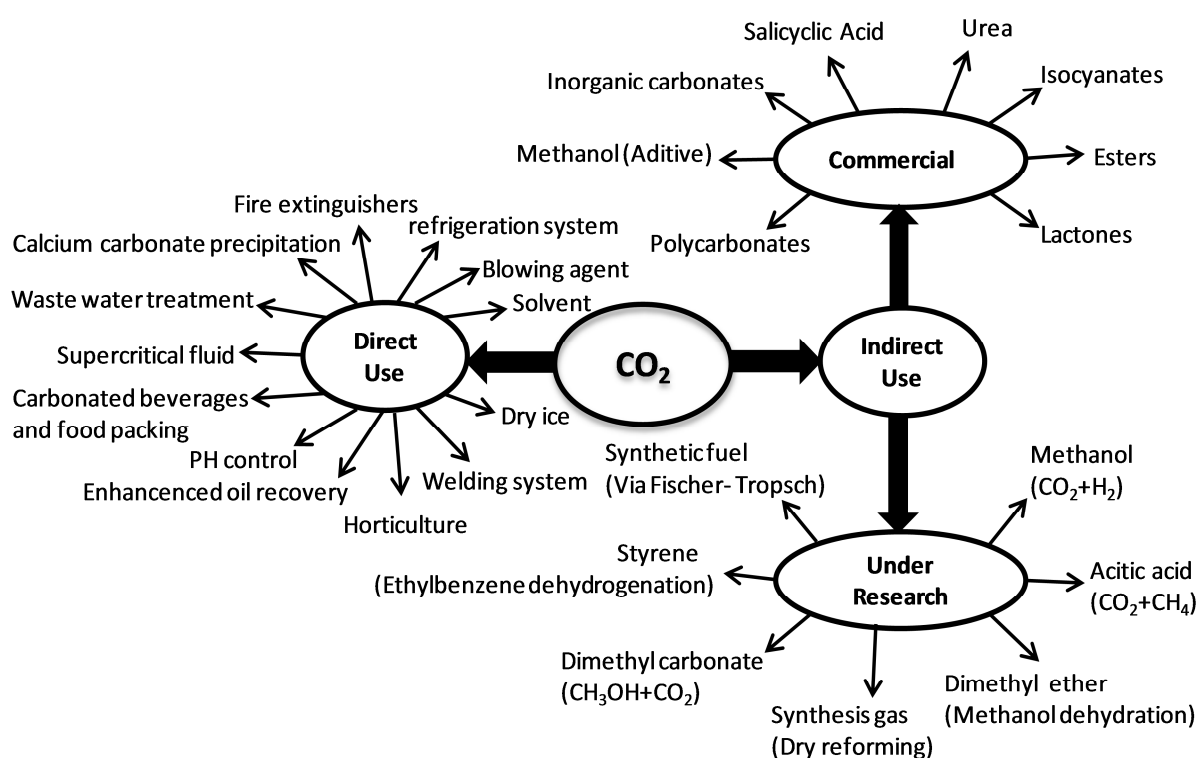


Fig. 2-7: Various direct and indirect pathways of CO₂ utilization (modified after [5]).

Until today, CO₂ is not used in its fullest potential even in the indirect way of utilization because of its high thermodynamic and kinetic stability. The use of efficient catalysts and selective reaction pathways are needed to promote the reaction rate. Undoubtedly, the chemical industry can only make little direct contribution towards the reduction of overall CO₂ emission. According to current estimates, the chemical industry could contribute to convert around 1% of global CO₂ emissions into chemical products [3]. Table 2-2 shows the utilization of CO₂ in various chemical conversion processes in 2006.

The fixation of CO₂ into these organic compounds refers to reactions that use the entire molecule. The detail description for the synthesis of these organic compounds using CO₂ is given in appendix A. All these processes use CO₂ to produce value added products in an environmentally friendly way where utilization potential assisted in terms of less energy use and lower waste production.

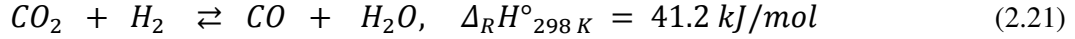
Table 2-2: Industrial process utilization of CO₂ as a raw material for synthesis of organic compounds [28].

| Industrial processes that utilize CO ₂ as raw material | World capacity per year [million tonnes] | Amount of fixed CO ₂ [million tonnes] |
|---|--|--|
| Chemical synthesis: | | |
| Salicylic acid | 0.07 | 0.025 |
| Urea | 143 | 105 |
| Cyclic carbonates | 0.080 | 0.04 |
| Poly (propylene carbonate) | 0.070 | 0.03 |
| Fuel synthesis: | | |
| Methanol | 20 | 2 |
| Synthetic natural gas | - | - |
| Other fuels | - | - |

Table 2-2 clearly indicates that the amount of CO₂ utilized today for the production of organic chemicals and fuels (methanol) is very small (around 100 million tonnes) compared to today's global CO₂ emissions of around 30 billion tonnes.

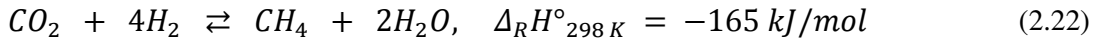
It should also be noted that only around 10% of the global crude oil consumption is used today in the chemical industry. The majorly is used as liquid fuels such as gasoline, diesel and heavy oil. Hence, an effective use of CO₂ with regard to a noticeable reduction of the global net emissions of CO₂ can only be reached, if the CO₂ (e.g. separated from flue gases or in the very far future from air) is utilized for fuels, e.g. by reverse water gas shift and subsequent Fischer Tropsch synthesis.

The reverse water gas shift reaction technology is a simple and effective way to utilize carbon dioxide in many industries [29, 30]. This reaction occurs at high temperatures where CO_2 is converted with H_2 into CO and water.

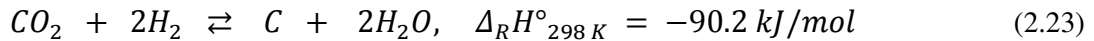


Several mostly unwanted parallel and side reactions may also take place:

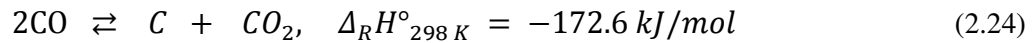
The Sabatier reaction:



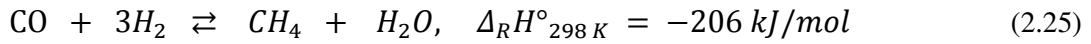
The Bosch reaction:



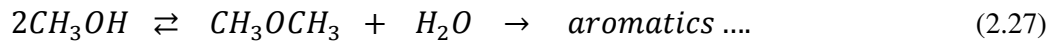
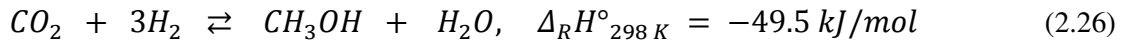
Boudouard reaction:



Methanation reaction:



The reverse water gas shift reaction has been known to chemistry since the mid 1800's but no experimental work was done to reveal its viability [31]. Since the last two decades, studies have been focused on catalytic conversion of CO_2 to industrially important chemicals such as light olefins and liquid hydrocarbons. Depending on the reaction route and catalyst used, it is divided into two groups. One is the hydrogenation of CO_2 to hydrocarbons via methanol synthesis [32, 33] which combines two reaction steps: methanol synthesis from CO_2 and subsequent conversion of methanol to gasoline by the MTG process:



Alternatively, methanol can also be used directly a liquid fuel, but the infrastructure is not yet established. The second route to convert CO_2 into liquid hydrocarbons is Fischer Tropsch synthesis [34-36], which also combines two steps: hydrogenation of carbon dioxide

by reverse water gas shift reaction (Eq. (2.21)) and, then, further hydrogenation of CO to hydrocarbons:



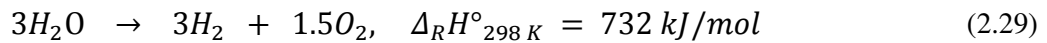
The term $(-CH_2-)$ represents a methylene group of a paraffin. This route is discussed in some details in the subsequent chapter.

2.3 Concept of production of liquid fuels from CO₂ via reverse water gas shift (RWGS) and Fischer Tropsch synthesis (FTS)

The concept for production of liquid fuels from CO₂ via RWGS and FTS was recently described and discussed [37], where some more details can be found. Here only some main aspects should be outlined.

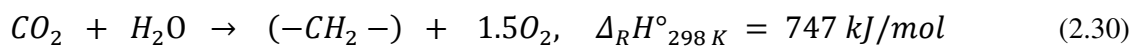
Electricity produced by solar energy (or other renewables) can be used to produce liquid fuels like diesel oil with no or little net CO₂ production by the following steps [38-42]:

- a) Separation of CO₂ from flue gases (or in the long run even from the atmosphere).
- b) H₂ production by high temperature water (steam) electrolysis and non-fossil electricity:

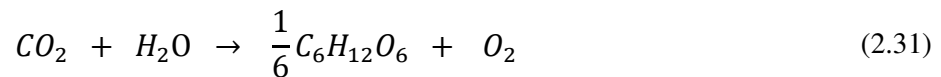


- c) CO production by reverse water gas shift (Eq. (2.21)).
- d) Fischer Tropsch synthesis of hydrocarbons (preferably of diesel oil) (Eq. (2.28)).

In summary we get:



If we compare Eq. (2.30) with natural photosynthesis



we may regard this process as a technical photosynthesis (TPS, Fig. 2-8). This route is also called carbon capture and conversion (CCC) [42]. Compared to the products of natural photosynthesis (e.g. wood), those of the technical photosynthesis have a much higher energy density related to mass (factor 3) and even more related to volume (factor 6).

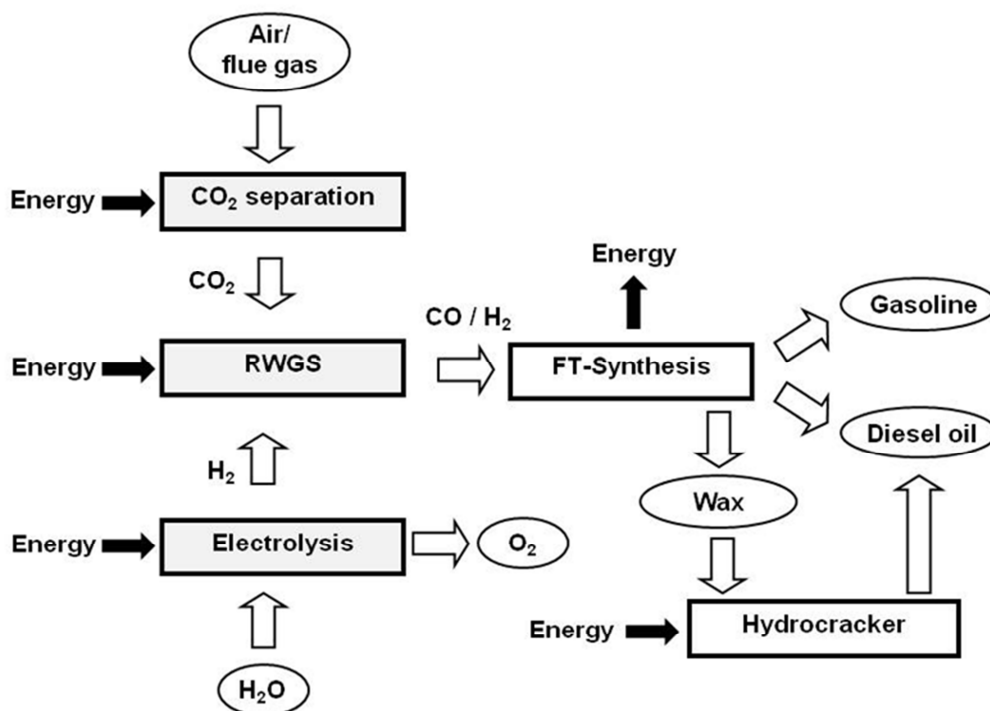


Fig. 2-8: The simplified flowsheet of a plant for production of liquid fuels from CO₂ by Fischer Tropsch synthesis and solar energy.

The technical photosynthesis may also be helpful for energy storage and transport. Liquid fuels have excellent storage, loading and transport capabilities, and appropriate large-scale storage technologies will be needed in future for the efficient use of renewable energies:

- (1) Many renewable energy sources (most notably solar and wind) are subject to natural fluctuations. These have to be compensated for by storing excess supply peaks, which increases the efficiency and economic value of renewable energy, and keeps instantaneous electrical generation and consumption in a better balance.
- (2) The economically most practical method of developing alternative energy sources is to make use of the earth's sunbelt and high-wind zones, but these regions are mostly far away from consumers. Hence, there is a need for a suitable carrier of energy in order to transport the energy from the source to suitable markets.

One could also think of using the hydrogen generated by electrolysis directly for storage and transport of solar-electrical energy. But the energy density of liquid hydrogen is only 0.2 toe/m³ (and even only 0.1 toe/m³ for compressed H₂ at 700 bar and 25 °C) compared to diesel oil with 0.8 toe/m³ (toe: tonnes of oil equivalent, 1 toe = 42 GJ). The liquefaction and

transport of H₂ is not easy: High safety requirements and a new infrastructure are needed, e.g. 20% to 30% of the energy content is consumed for liquefaction [43] and 8% for transport as compressed gas via pipelines (per 1000 km) [44].

For a preliminary basic layout of a TPS plant for the production of liquid fuels from CO₂ by solar energy and Fischer Tropsch synthesis (FTS) the following assumptions were made:

Hydrogen production

H₂ is generated by high temperature solid oxide electrolysis (HTE) at 830 °C. According to *Stoots et al.* 124 MJ electrical energy are consumed per kg H₂ (= 13.8 MJ per kg converted H₂O) [45]. If we use the energy released by the exothermic Fischer Tropsch synthesis for the production of saturated steam (22 bar, 215 °C) (see below), the energy needed to overheat the steam (215 → 830 °C) is 1.4 MJ/kg. Hence in total, 137 MJ electrical energy is needed per kg H₂ (= 15.2 MJ per kg converted H₂O).

Desalination of seawater

If freshwater is not available, seawater has to be desalinated to produce the feed of the electrolysis. 7 kJ electrical energy is sufficient per kg water, if reverse osmosis is used [46]. This requirement is only 0.04 % of the energy of the subsequent electrolysis. For comparison: 170 kJ/kg is needed, if multi-stage flash distillation is used [44], which is still only 0.9% compared to what the electrolysis consumes.

CO₂ production

CO₂ has to be separated from flue gases (or on the long run even from air). The inescapable energy requirement (in J/mol CO₂) of concentrating CO₂ from a gas mixture is given by the laws of thermodynamics, as we have at least to overcome the difference of the entropy of the mixture and of the pure compounds (see Fig. 2-9):

$$E_{min} = T \Delta S = \frac{-y_{CO_2} R T \ln(y_{CO_2}) - (1 - y_{CO_2}) R T \ln(1 - y_{CO_2})}{y_{CO_2}} \quad (2.32)$$

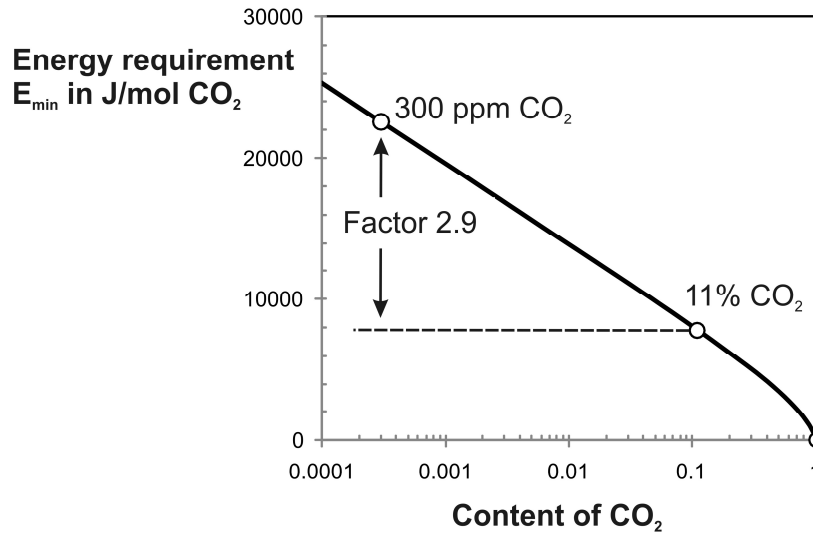


Fig. 2-9: Inescapable energy requirement of concentrating CO₂ from flue gases (11 vol.-% CO₂) and air (300 ppmv CO₂) at 25 °C (Eq. (2.32)).

For separation of CO₂ from flue gases with typically 11 vol.-% CO₂, the minimum energy requirement is 7.8 kJ/mol (177 kJ/kg) and for air 22.4 kJ/mol CO₂ (509 kJ/kg). In the ideal case, each mol of CO₂ is finally converted by FTS into one mol of CH₂-groups (hydrocarbons) with a heating value of 595 kJ/mol = 42500 kJ/kg. Hence, the energy requirement for CO₂ separation is 3.8% (air) and 1.3% (flue gases) of the energy content of the liquid fuels produced by FTS. Of course in reality, much more energy is consumed at the current status of technology. Here we use a value of 1.2 MJ/kg CO₂ as given by *Göttlicher* and *Pruschek* [47] for CO₂ separation from flue gases by chemical absorption. This value is 7 times higher than the inescapable energy requirement. For CO₂ separation from air, a value of 3.6 MJ/kg CO₂ (= 7 E_{min}) may be taken as a first estimation. In the ideal case of a technical photosynthesis, 3 mol water are converted by electrolysis per mol of CO₂ (Eq. (2.21) and (2.29)), i.e. 1.23 kg H₂O/kg CO₂. Hence, for the conversion of 1 kg of CO₂ 24.5 MJ are needed for electrolysis of water compared to 1.2 MJ for CO₂ separation from flue gases and 3.6 MJ from air.

Reverse water gas shift

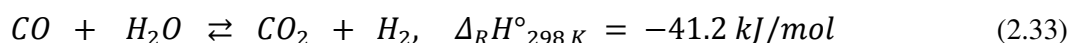
H₂ and CO₂ are converted to H₂O and CO by RWGS at a temperature of about 800 °C. At the reactor outlet, the thermodynamic equilibrium is reached as proven by respective experiments with a Ni-catalyst (see section 5.1). The reactor is heated (e.g. electrically). If

heat losses are neglected, the required energy is 41 kJ/mol CO₂ (Eq. (2.21)) or 932 kJ/kg CO₂.

Fischer Tropsch synthesis

Production of synthetic fuels via FTS has the potential to produce fuels like gasoline and diesel oil as well as petrochemicals from fossil and renewable sources. In recent years, the availability of cheap natural gas, coal, and biomass has given momentum to FT technology. The worldwide FT plant capacities will increase in future, today with natural gas favoured as feedstock. In 2015, the worldwide annual production of liquid fuels via FT will be around 30 million tonnes, mainly produced in countries like South Africa, Malaysia, and Qatar.

Beside of the main reaction of the FT synthesis (Eq. (2.28)), methanation (Eq. (2.25)) is often considered as a separate reaction. The third reaction that plays an important role (at least if iron based catalysts are used) produces unwanted CO₂ by the WGS reaction:



Two reactor types are currently favoured for FTS, the multi-tubular fixed bed and the slurry bubble column. FT reactors are usually cooled by boiling water. Saturated steam is produced and may be used after further heating as feed for the HTE. A typical FT cooling temperature is 215 °C [48]. The required thermal energy is then 2.7 MJ per kg saturated steam = 48.6 kJ/mol. Hence, 3.1 mol of steam can be generated per mol CO converted by FTS ($\Delta H^\circ_{298 K} = -152 \text{ kJ/mol CO}$), which is the amount needed for electrolysis.

Typical selectivities (in C-%) of the FTS with Fe-catalysts (30% CO conversion per pass, i.e. recycle of unconverted syngas has to be installed) are: 18% CO₂, 5% methane, 11% C₂ to C₄, 10% gasoline, 17% diesel and 39% waxes [48-50]. The waxes are further converted (mainly) to diesel oil by mild hydrocracking at 70 bar and 350 °C [51].

All light hydrocarbons (methane to C₄) and also the CO₂ formed by the water gas shift reaction in the FTS (Eq. (2.33)) may be recycled to the RWGS unit to be finally converted by steam reforming (reverse of Eq. (2.25)) or by the RWGS (Eq. (2.21)) to CO and H₂, respectively. In summary we get the following mass balance: For each mol of fresh CO₂, we have to recycle approximately 0.18 mol CO₂ and 0.18 mol carbon (as C₁ to C₄) into the RWGS reactor. Hence, about 2 times more energy is needed to run the RWGS reactor

(1.18×41 kJ/mol CO_2 and 0.16×206 kJ/mol C as C_1 to C_4 compared to 41 kJ/mol without recycle).

Based on the above listed assumptions and facts, an estimation of the energy requirements for the production of liquid fuels from CO_2 by FTS and solar energy is possible (Table 2-3). The energy required for the conversion of CO_2 to CO is calculated by including the conversion of recycled CO_2 and C_1 to C_4 hydrocarbons (counted as CH_4), both unwanted by-products of FTS, and RWGS and steam reforming (reverse of Eq. (2.25)), respectively.

Table 2-3: Estimation of energy requirements for the production of liquid fuels from CO_2 by FTS and solar energy (conversion of 1 kg CO_2 to 0.32 kg liquid fuels).

| Process/energy output | Energy [kJ] | Comment/assumption |
|--|------------------------|--|
| Separation of 1 kg CO_2 from flue gas (air) | 1200 (3600) | Value from [47], which is 7 times the thermodynamic minimum (Fig. 2-9) |
| Conversion of CO_2 to CO (RWGS) | 2144 | Only counting enthalpy of reaction |
| Desalination of 1.23 kg seawater | 9 | Reverse osmosis plant |
| HT-electrolysis of 1.23 kg water | 18700 | 13.8 MJ/kg H_2O electrical energy for electrolysis [45] and 1.4 MJ/kg to overheat saturated steam generated in the FTS ($215 \rightarrow 830$ °C) |
| FT synthesis | - | Heat of reaction is used to generate saturated steam (215 °C, 22 bar) |
| Total required energy | 21773 (24173) | |
| Production of 0.32 kg liquid fuels | 13600 | Heating value of fuel = 42500 kJ/kg |
| Process efficiency | 62% (= 13600/21773) | CO_2 from flue gases |
| | 56% (= 13600/24173) | CO_2 from air |

The process efficiencies are 62% and 56%, respectively, if the CO₂ is separated from flue gases or air. These values are comparable to those reported for the production of (non-renewable) liquid hydrocarbons based on coal (37%) and tar sands (57%) [52]. Table 2-3 shows the overall efficiency for the production of renewable liquid fuels depends critically on the method and energy requirement for the electrolysis of water and on the method used for CO₂ capture. The most important aspect is the restriction of electricity production by solar energy or other renewable sources. The overall mass balance is shown in Fig. 2-10.

CO₂ capture from flue gases in the short and medium term (and hopefully in the long term from air) and subsequent conversion to liquid fuels is an attractive alternative to CO₂ sequestration, as the latter option is problematic: The collective leak rate of the geologic reservoirs must be significantly lower than 1% over a century-to-millennium time scale. Otherwise, after 50 to 100 years of sequestration, the yearly emissions will be comparable to the emission levels that were supposed to be mitigated in the first place [53]. Secondly, a significant fraction of the existing fossil-derived power plants are too remote from the location of suitable geologic reservoirs. And thirdly, the available space is too small. For example, the US Department of Energy is doing work on sequestration with the goal of 15 Gt CO₂ storage by 2050, which is still small compared to the CO₂ emissions of 6 Gt/a [53].

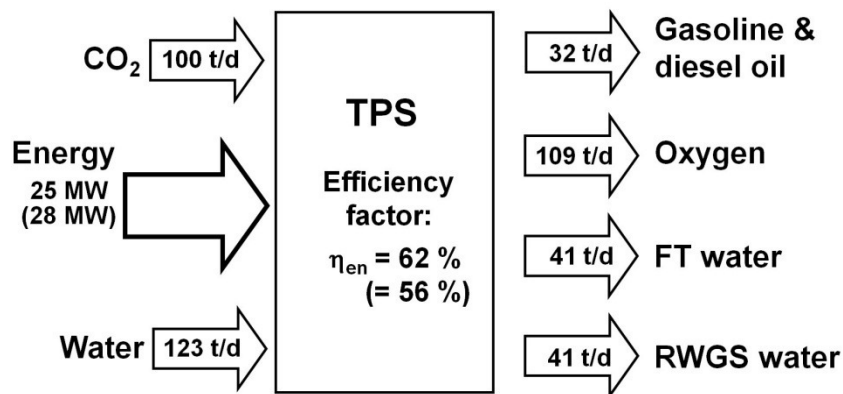


Fig. 2-10: Mass and energy balance of process for production of liquid fuels from CO₂ by FTS and solar energy (or other renewables). Values of efficiency (η_{en}) and energy input represent case of CO₂ separation from flue gases and in brackets case of CO₂ separation from air.

In a joint cooperation of the Chair of Chemical Engineering of the University Bayreuth and the *SunFire* GmbH (Bremen), the process steps of the reverse water gas shift and of the FT synthesis under the specific conditions of the process to turn carbon dioxide to liquid fuels are studied.

SunFire GmbH is aiming to commercialize a FT process for liquid fuels from CO₂ and H₂O, and is developing this technology together with scientific and industrial partners. The main focus lies on the development of industrial steam-electrolysers (together with *staxera* GmbH (Dresden) and *EIFER* (Karlsruhe)). The long term goal for the energetic efficiency including CO₂ from ambient air (in cooperation with *Climeworks* GmbH, Zürich) is > 65%.

In this work, the CO₂ hydrogenation (and not FTS) is studied at high temperatures and atmospheric pressure, where reverse water gas shift is favoured thermodynamically and produces CO as the most valuable product. A Ni catalyst manufactured by Süd-Chemie was used in this work. Thermodynamic aspects and the current knowledge of the kinetics of the CO₂ conversion and methanation are subsequently discussed.

2.4 Thermodynamics of CO₂ conversion (reverse water gas shift and methanation)

CO₂ is a highly stable molecule and therefore its chemical transformation requires significant amount of input energy (high temperature), effective reaction conditions, and very active catalysts [54]. Chemical reactions for conversion of CO₂ involve positive change in enthalpy, and thus they are endothermic. For example, CO₂ reforming of methane requires about 20% more energy input compared to steam reforming of methane [54]. Chemical reactions are driven by the difference in Gibbs free energy between the products and reactants as given by the equation below.

$$\Delta_R G^0 = \Delta H^0 - T \Delta S^0 \quad (2.34)$$

Where $\Delta_R G^0$ is the change in Gibbs free energy (at 1 bar), ΔH^0 is the change in enthalpy, T is the absolute temperature in K, and ΔS^0 is the change in entropy. The Gibbs free energy of formation for CO₂ and related compounds are shown in Fig. 2-11. From the analysis of thermodynamic data, it is clearly understood that the energy requirement for only CO₂ as a single reactant is more than the CO₂ used as a co-reactant with other compounds. In other

words, thermodynamically it becomes more feasible if CO₂ (Gibbs free energy of -394 kJ/mol) is used as a co-reactant with other reactants which has higher Gibbs free energy (less negative), such as CH₄ (-51 kJ/mol), carbon (0 kJ/mol), and H₂ (0 kJ/mol).

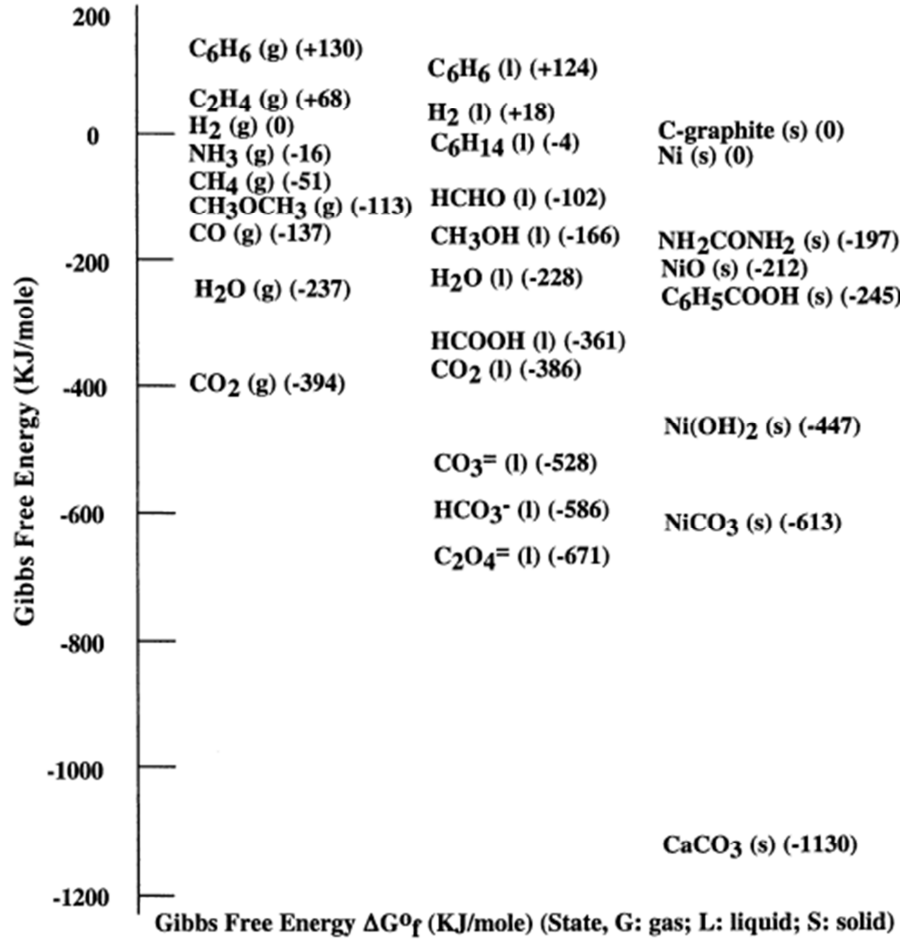


Fig. 2-11: Gibbs free energy of formation for CO₂ and related compounds [54].

As mentioned before, the reverse water gas shift reaction is an endothermic reaction which is thermodynamically favourable at high temperatures. The equilibrium constant K_p is defined in terms of the equilibrium partial pressures or concentrations of the reactants and products is given as:

$$K_p = \left(\frac{P_{CO} P_{H_2O}}{P_{CO_2} P_{H_2}} \right)_{eq} = \left(\frac{C_{CO} C_{H_2O}}{C_{CO_2} C_{H_2}} \right)_{eq} = \exp \left[-\frac{\Delta_R G^0}{R T} \right] \quad (2.35)$$

The equilibrium conversion of CO₂ may be calculated from the equilibrium constant K_p as a function of temperature. For the case where equimolar feed of CO₂ and H₂ are fed to the reactor (i.e. $y_{CO_2} = y_{H_2}$ and $y_{CO} = y_{H_2O} = 0$), the equilibrium conversion is given as:

$$X_{CO_2,eq} = \frac{\sqrt{K_p}}{1 + \sqrt{K_p}} \quad (2.36)$$

The Gibbs free energy of CO₂ hydrogenation reaction as a function of temperature is given as [55]:

$$\Delta_R G^0 = 32.197 - 0.03104 T(K) + \frac{1774.7}{T(K)}, \quad kJ/mol \quad (2.37)$$

The Gibbs free energy and equilibrium constant can be calculated by using computer program. The expression for equilibrium constant K_p as a function of temperature for RWGS reaction is given by Twigg [56] as

$$K_p = \left[\frac{1}{\exp(-0.29353 Z^3 + 0.63508 Z^2 + 4.1778 Z + 0.31688)} \right] \quad (2.38)$$

where $Z = \left[\frac{1000}{T(K)} \right] - 1$

The Gibbs free energy and equilibrium constant of CO₂ hydrogenation reaction as a function of temperature is shown in Fig. 2-12 and Fig. 2-13, respectively.

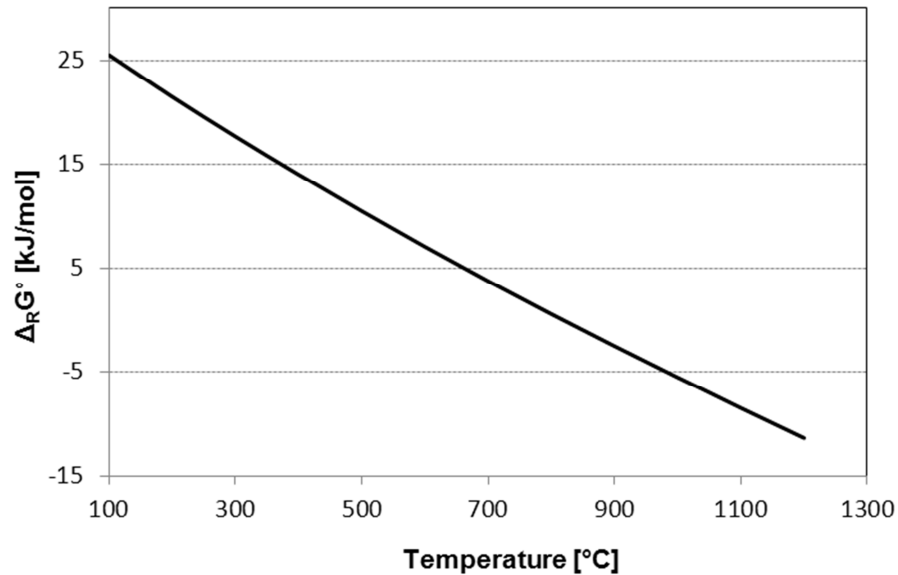


Fig. 2-12: Thermodynamic equilibrium of CO₂ hydrogenation described by the Gibbs free energy change as a function of temperature, ($y_{CO_2} = y_{H_2}$, $y_{CO} = y_{H_2O} = 0$).

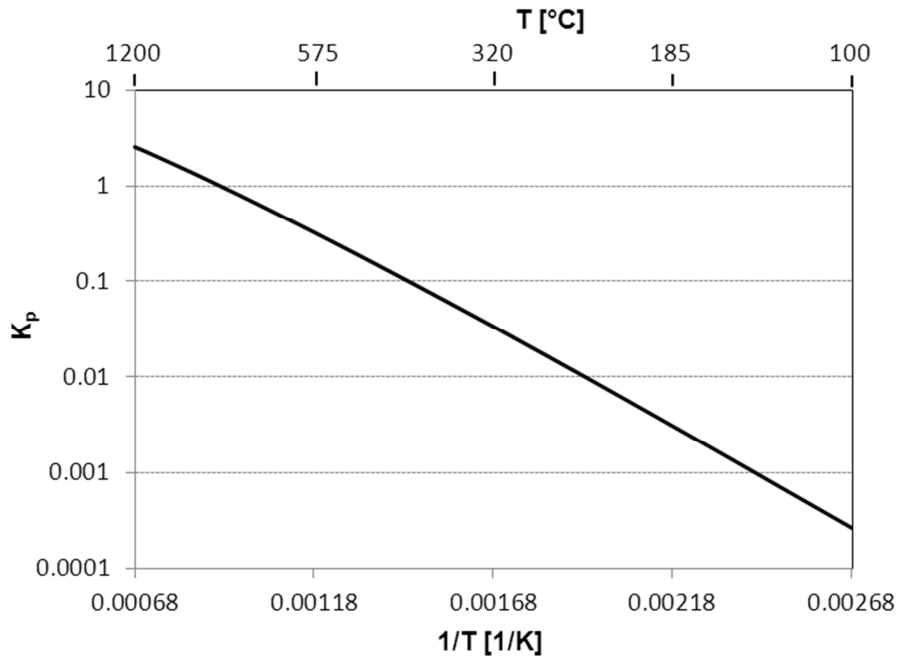


Fig. 2-13: Thermodynamic equilibrium described by the equilibrium constant of reaction as a function of temperature ($y_{\text{CO}_2} = y_{\text{H}_2}$, $y_{\text{CO}} = y_{\text{H}_2\text{O}} = 0$).

Fig. 2-12 shows that the $\Delta_R G^0$ changes from positive to negative above 800 °C. Fig. 2-13 shows the equilibrium constant of the reaction which increases with increase in temperature.

In the RWGS reaction, it is impossible to get complete conversion even at a high temperature of about 1000 °C equilibrium (Fig. 2-14 and Fig. 2-15). So, the equilibrium can be shifted to the right either by using an excess of H_2 or by using a gas recycle. The equilibrium conversion has been calculated for the RWGS reaction without methanation (Fig. 2-14) and with methanation reaction (Fig. 2-15). The RWGS reaction with methanation behaves differently than without methanation and the equilibrium CO_2 conversion decreases with increasing temperature in the low temperature range where methane formation is favoured thermodynamically. At high temperature, methanation reaction is totally suppressed thermodynamically and the normal RWGS reaction proceeds.

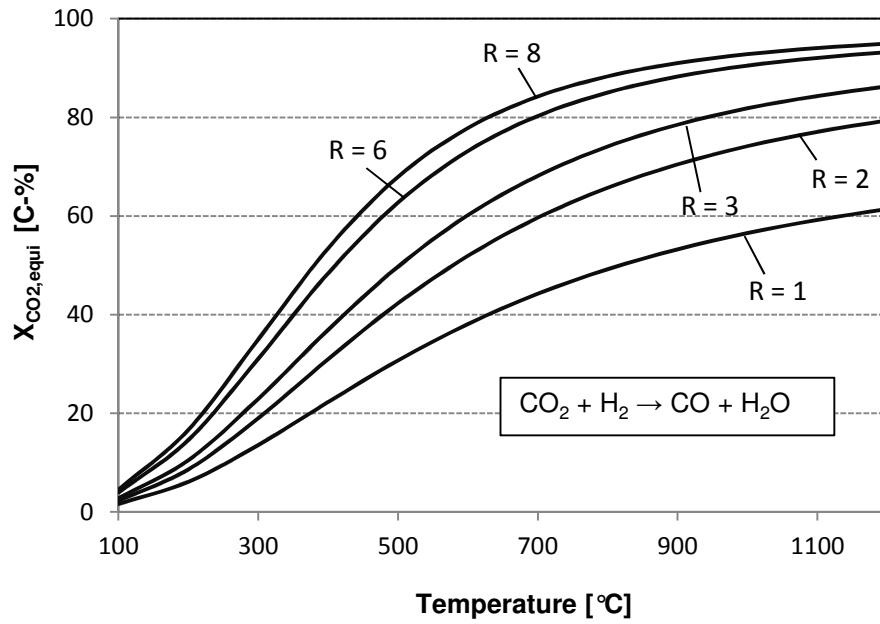


Fig. 2-14: Thermodynamic equilibrium calculation for CO₂ conversion in RWGS reaction **without methanation** ($p = 1$ atm, $R = \text{H}_2/\text{CO}_2$ ratio).

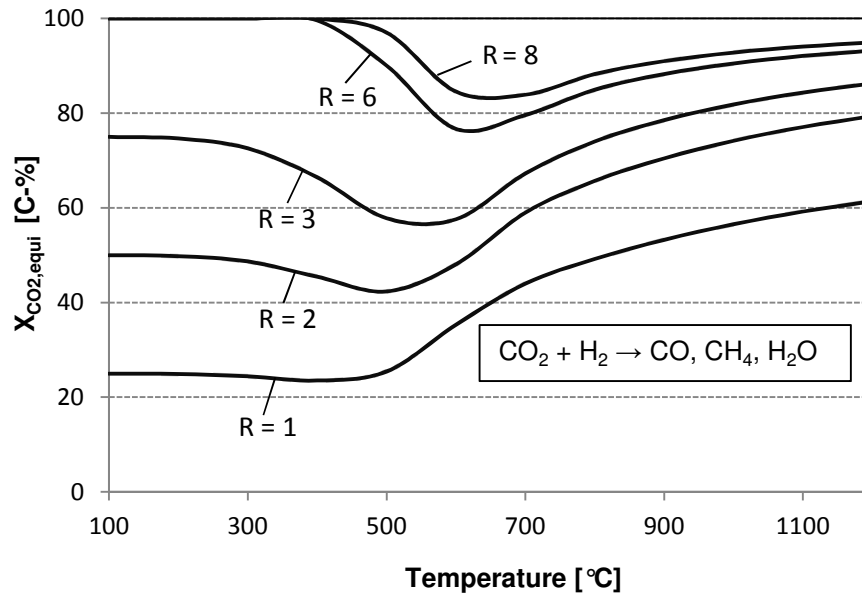


Fig. 2-15: Thermodynamic equilibrium calculation for CO₂ conversion in RWGS reaction **with methanation** ($p = 1$ atm, $R = \text{H}_2/\text{CO}_2$ ratio).

As described in section 2.3, liquid fuels can be produced from CO₂. At a high temperature, CO₂ hydrogenation can only produce CO and H₂O as a product. The outlet gas composition after removal of H₂O from syngas containing small amounts of CO₂ can be further used for

the production of fuels via Fischer Tropsch synthesis. Exemplarily, the equilibrium composition of syngas is shown in Fig. 2-16. For temperature above 750 °C, atmospheric pressure, and H_2/CO_2 inlet ratio of 2, the CO_2 hydrogenation can give the required ratio of syngas for the production of fuel. For example, at 800 °C and atmospheric pressure, the equilibrium composition at the reactor outlet is 57% CO , 28% H_2 , and 15 vol.-% CO_2 . Hence, the CO/H_2 ratio is about 2.

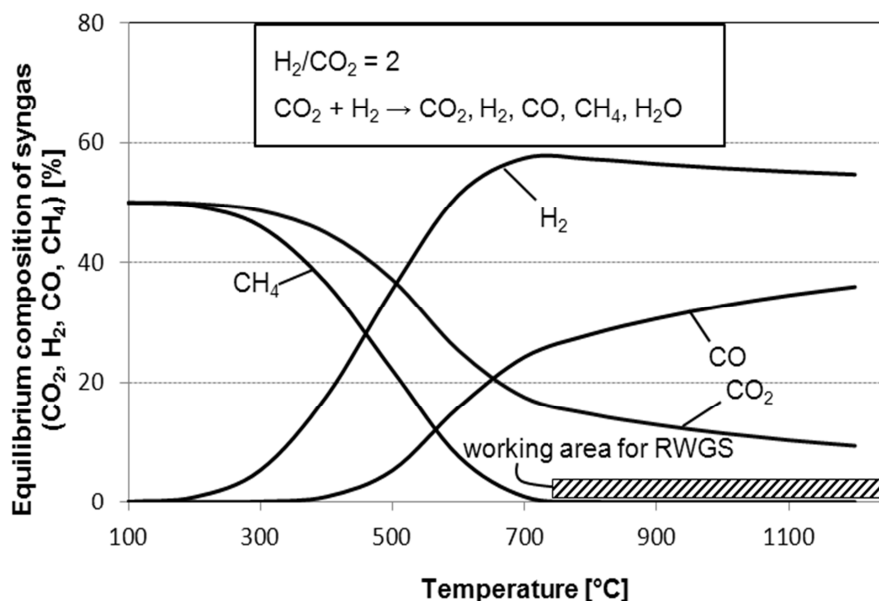


Fig. 2-16: Equilibrium composition of syngas after removal of water over temperature in CO_2 hydrogenation reaction with methanation ($p = 1$ atm, $H_2/CO_2 = 2$).

2.5 Kinetics of reverse water gas shift reaction and methanation

Two general mechanisms have been proposed for methanation of CO_2 over Ni containing catalysts [33, 57-59]. In the first mechanism of methane formation, initially CO_2 undergoes rapid dissociate adsorption with the formation of CO and atomic oxygen on the catalyst surface and, then, further steps coincide with CO hydrogenation steps, where further dissociation of CO occurs into intermediate carbon and oxygen. The intermediate carbon species is then hydrogenated in a chain mechanism to form methane. In this case, CO_2 hydrogenation principle would have to become similar as that of CO hydrogenation. The mechanism proposed for both CO_2 and CO methanation [58] are shown in Table 2-4.

Table 2-4: Mechanism for methane formation from CO₂ and CO [58].

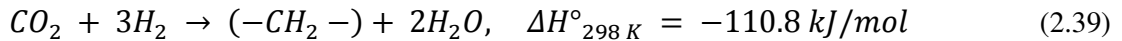
| CO ₂ Methanation Mechanism | |
|--|------|
| $\text{CO}_2 \rightleftharpoons \text{CO}^* + \text{O}^*$ | (1) |
| $\text{H}_2 \rightleftharpoons 2\text{H}^*$ | (2) |
| $\text{CO}^* \rightleftharpoons \text{CO}$ | (3) |
| $\text{CO}^* \rightleftharpoons \text{C}^* + \text{O}^*$ | (4) |
| $\text{C}^* + \text{H}^* \rightleftharpoons \text{CH}^*$ | (5) |
| $\text{CH}^* + \text{H}^* \rightleftharpoons \text{CH}_2^*$ | (6) |
| $\text{CH}_2^* + \text{H}^* \rightleftharpoons \text{CH}_3^*$ | (7) |
| $\text{CH}_3^* + \text{H}^* \rightleftharpoons \text{CH}_4^*$ | (8) |
| $\text{CH}_4^* \rightleftharpoons \text{CH}_4$ | (9) |
| $\text{O}^* + \text{H}^* \rightleftharpoons \text{OH}^*$ | (10) |
| $\text{OH}^* + \text{H}^* \rightleftharpoons \text{H}_2\text{O}^*$ | (11) |
| $\text{H}_2\text{O}^* \rightleftharpoons \text{H}_2\text{O}$ | (12) |

The second mechanism involves the pathway that does not require initial transformation of CO₂ to CO. Instead, the hydrogenation of CO₂ to methane occurs directly through the formation of intermediates (Table 2-5). This explanation was given on the basis of the difference in specific activity and selectivity with respect to methane formation in CO and CO₂ hydrogenation reaction [59]. According to [59], the steps 13 and 14 are fast and step 15 is slow, and the subsequent steps 16 to 23 are fast and irreversible.

Table 2-5: Mechanism for methane formation without CO formation [59].

| CO ₂ Methanation Mechanism | |
|--|------|
| $\text{CO}_2 \rightleftharpoons \text{CO}_2^*$ | (13) |
| $\text{H}_2 \rightleftharpoons 2\text{H}^*$ | (14) |
| $\text{CO}_2^* + \text{H}^* \rightleftharpoons \text{COOH}^*$ | (15) |
| $\text{COOH}^* + \text{H}^* \rightleftharpoons \text{COH}^* + \text{OH}^*$ | (16) |
| $\text{COH}^* + \text{H}^* \rightleftharpoons \text{CH}^* + \text{OH}^*$ | (17) |
| $\text{CH}^* + \text{H}^* \rightleftharpoons \text{CH}_2^*$ | (18) |
| $\text{CH}_2^* + \text{H}^* \rightleftharpoons \text{CH}_3^*$ | (19) |
| $\text{CH}_3^* + \text{H}^* \rightleftharpoons \text{CH}_4^*$ | (20) |
| $\text{CH}_4^* \rightleftharpoons \text{CH}_4$ | (21) |
| $\text{OH}^* + \text{H}^* \rightleftharpoons \text{H}_2\text{O}^*$ | (22) |
| $\text{H}_2\text{O}^* \rightleftharpoons \text{H}_2\text{O}$ | (23) |

The direct hydrogenation of CO₂ to hydrocarbons (Eq. (2.39)) using laser generated iron carbide catalysts has been recently investigated by *Fiato et al.* [60]. This reaction is proposed to proceed via dissociative adsorption of carbon dioxide into CO and oxygen followed by further hydrogenation of the adsorbed species on the catalyst surface via chain reaction mechanism.



The transformation of CO₂ and H₂ depends upon many factors. Several attempts have been made by several investigators to overcome the limitations of RWGS reaction. Several noble metals (e.g. Pt, Ru, Pd) and transition metals (e.g. Cu, Ni, Fe, Co) supported on different metal oxides (e.g. γ -Al₂O₃, CeO₂, SiO₂) have been explored to carry out RWGS reaction [30]. The various catalysts investigated as:

Copper catalyst:

A catalyst with 12 wt.-% Cu loaded on alumina has shown a good activity and excellent selectivity to CO in CO₂ hydrogenation [61], where 28% conversion of CO₂ with 100% CO selectivity at 350 °C and atmospheric pressure was established. The reaction was carried out with H₂/CO₂ feed ratio of 4 and at a space velocity of 100 ml/g_{cat}/min. The exclusive selectivity to CO was obtained on Cu compare to other catalyst such as Ni, Ru, Rh and Pt on alumina. These catalysts produce only CH₄ while Pd catalysts give both CH₄ and CO under the same reaction condition.

A catalyst with 5 wt.-% Cu supported on alumina (H₂/CO₂ feed ratio of 3, space velocity of 100 ml/g_{cat}/min, 220 °C, 3 MPa) produces CO and CH₃OH with the selectivity of about 87% and 7.5%, respectively [62]. Sometimes, the catalyst support may alter the selectivity of product. With the same amount of Cu on SiO₂ the selectivities are about 87% and 13% for CO and CH₃OH, respectively while on TiO₂ the values are 92.5% and 4.3% for CO and CH₃OH, respectively and 2.9% for CH₄. Similarly, when 5 wt.-% Cu/SiO₂ catalyst operated at 350 °C (pressure of 0.2 bar, gas recycle loop having a H₂/CO₂ ratio of 4), the selectivity of CO was about 97% with small amount of CH₄ (<1.5%), C₂H₄ (<0.5%) and C₂H₆ (<0.4%) [63]. The addition of a small amount of Ni to a Cu catalyst enhances the catalytic activity but also starts CH₄ formation. When the 5 wt.-% Cu/SiO₂ operated at 280 °C (6 MPa, H₂/CO₂ ratio of 3, space velocity of 50 ml/g_{cat}/min), the selectivity of CO decreases and the methanol selectivity increases to 76% and 24%, respectively [64].

Iron catalyst:

The CO₂ hydrogenation on Fe catalysts has been studied by *Lee and coworkers* [35, 65-70] and *Cubeiro et al.* [71]. At 400 °C (2 MPa, space velocity of 31.67 ml/g_{cat}/min), the Fe/Al₂O₃ catalyst gives about 49% conversion of CO₂ and 12.4% and 87.6% of selectivity towards CO and hydrocarbons, respectively [35]. The addition of potassium to Fe remarkably increases the catalyst activity and selectivity towards C₂₊-hydrocarbons. Under the same reaction condition with K/Fe molar ratio of 0.5, CO₂ hydrogenation activity increased to about 70% while selectivity changes to about 4% and 96% for CO and hydrocarbons, respectively. Further increase in molar ratio of K/Fe to 1 showed a small decrease in activity and hydrocarbon selectivity while the selectivity to CO slightly increased. The addition of alumina itself acts as a promoter when the Fe-Cu-K/Al₂O₃

catalyst was prepared by the co-precipitation method [65]. The long term stability test on Fe-K/Al₂O₃ catalyst showed a significant decrease in CO₂ conversion and selectivity to hydrocarbons [66], where the deactivation was attributed mainly due to the carbonaceous deposition on the catalyst surface. A similar behaviour was obtained with a Fe-Cu-K/Al₂O₃ catalyst, where the catalyst deactivation was caused by the growth of crystallites and the resulting decrease in dispersion of catalyst components (promoters) [67].

To improve the strength of catalysts, binders are sometimes added. At high temperatures, binders are not chemically inert. The addition of an alumina binder to a Fe-K/Al₂O₃ catalyst showed excellent activity and selectivity towards higher hydrocarbons (C₅₊) while activity and selectivity dramatically decreased with silica binder. The reason for this influence on the activity and selectivity was the change in acidity of catalyst, structure and metal-support interaction [68]. The strong metal-support interaction between Fe-K/ β -Al₂O₃ makes the catalyst more active and selective towards long chain hydrocarbons and light olefins [69]. A study on Fe/Al₂O₃ catalyst preparation methods such as impregnation, precipitation, and physical mixing and catalyst characterization was performed by *Cubeiro et al.* [71]. The effect of K promoter in both CO₂ and CO hydrogenation was also investigated.

Gold catalyst:

Gold catalysts supported on various metal oxides such as ZnO, Fe₂O₃, CeO₂, TiO₂, ZrO₂, La(OH)₃, NiO, and Co₃O₄ were used by *Sakurai et al.* [72] for CO₂ hydrogenation. All the catalysts tested for CO₂ hydrogenation were treated at 150 to 400 °C (8 MPa, H₂/CO₂ ratio of 3, space velocity of 50 ml/g_{cat}/min). Among all the catalysts, Au supported on TiO₂, Fe₂O₃, and ZnO were the most active catalysts for the reverse water gas shift reaction, where the equilibrium conversion of CO₂ was obtained at 400 °C. But even at lower temperatures between 150 and 200 °C, Au/TiO₂ gives equilibrium yield of CO. However, in the temperature range of 150 to 200 °C, Au/Fe₂O₃ and Au/ZnO catalysts produce much methanol. The activity of the catalyst and the selectivity greatly differ depending upon the reaction pressure and nature of oxide support [73], i.e. when the pressure was decreased from 5 to 0.1 MPa, the CO selectivity increased from 86% to 99% on Au/TiO₂ catalyst (250 °C).

Cobalt catalyst:

The CO₂ hydrogenation was also studied over Co Fischer Tropsch catalyst [74, 75]. The Co/SiO₂ catalyst at 210 °C (2.4 MPa, H₂/CO₂ ratio of 4, space velocity of 83.3 ml/g_{cat}/min) showed deactivation over time and also produces more than 70% of methane [74]. The comparative CO₂ hydrogenation on Fe, Co, and Ni catalyst using Al₂O₃ as structural support showed highest activity over Co/Al₂O₃ catalyst. The selectivity order for CO was Fe/Al₂O₃ > Co/Al₂O₃ > Ni/Al₂O₃ [76].

Nickel catalyst:

Currently, Ni is one of the most studied catalysts for CO₂ hydrogenation reaction because of its high activity and comparatively low cost. At low temperatures, the CO₂ hydrogenation over Ni catalyst principally produces CH₄ as a main product [58, 77-80]. A kinetic study of CO₂ hydrogenation over Ni/SiO₂ catalyst showed that the activation energy shifts from 89 to 39 kJ/mol as temperature is increased from 227 to 327 °C [58]. The preparation method is also important. The specific activity of Ni/Al₂O₃ coprecipitated catalyst decreases as the metal loading increases whereas the activity increases with metal loading for an impregnated catalyst [77]. The specific activity (related to Ni only) increases with metal loading up to 30% and then it decreases for Ni/ZrO₂ catalyst prepared by an ultrasound assisted method [78]. During the reaction, transformation of zirconium to zirconium dioxide and the crystallization of metallic Ni particles occurs [80]. At a high Ni content, nickel exists as a bulk NiO and correspondingly produces more methane [81]. The Ni catalyst prepared by coprecipitation method with a loading from 0 to 20% on CeO₂ showed that the 2 wt.-% Ni-CeO₂ exhibits excellent catalytic activity, selectivity, and stability for the reverse water gas shift reaction [81]. At 600 °C and atmospheric pressure with H₂/CO₂ ratio of 1 and a quite high space velocity of 2 l/g_{cat}/min, CO₂ conversion obtained over 2 wt.-% Ni/CeO₂ catalyst was about 35% with 100% CO selectivity. The other RWGS reaction catalyst (10 wt.-% NiO/ZnO) showed an even higher activity (CO₂ conversion of 38%, which is very near to equilibrium conversion of 40%) and a selectivity towards CO of about 98% [82].

3. Objective and scope of the work

As mentioned in the previous chapter, the consumption of fossil fuels and the release of CO₂ into the atmosphere is continuously growing. Every year billion tons of anthropogenic carbon dioxide are released into the atmosphere. The ability to separate CO₂ from flue gases and to store a several billion tons of CO₂ emitted per year is questionable as are the environmental consequences. Therefore the conversion of CO₂ to useful chemicals and fuels is an attractive option for CO₂ mitigation.

A possible avenue for sustainable development is the catalytic conversion of CO₂ to liquid fuels by Fischer Tropsch synthesis and solar or wind energy. The reverse water gas shift reaction (RWGS) is the first step, and the produced CO further converted to liquid fuels by Fischer Tropsch synthesis. The transformation of CO₂ and H₂ depends upon several factors such as catalyst selection, ratio of CO₂/H₂, and reaction temperature and pressure. Therefore, the main focus of this work was to use a suitable catalyst and to determine the optimal reaction conditions for CO₂ hydrogenation in a fixed bed reactor.

The experiments were designed such that the RWGS reaction could be examined in both the forward and reverse direction. In addition to these experiments, the consecutive reaction of CO to methane was also considered. The studies for all three reactions were performed using a commercial Ni catalyst in a lab scale fixed bed reactor.

Since transport processes (external boundary layer diffusion and pore diffusion) may have strong influence, this aspect was also considered.

The most available studies of catalytic hydrogenation of CO₂ were performed at low temperatures where methane is the main product. Therefore, in this work CO₂ hydrogenation is studied at high temperatures where the reverse water gas shift reaction is favoured thermodynamically and produces CO and H₂O as main products. For the basic investigation of catalytic activity, pure alumina and some alumina supported Cr, Zn-Cu, and Ni catalysts were used. After comparing the activity of all these catalysts, the commercial Ni catalyst supplied by Süd-Chemie (spherical pellet, $d_p = 5$ to 7 mm) was chosen for a detailed kinetic study.

The parameters that influence the reaction rate such as temperature, reactant concentration, residence time, and particle size of the catalyst were studied in a lab scale fixed bed quartz reactor. To determine the kinetic, the experiments were conducted at conditions sufficiently far away from equilibrium. Not only the RWGS reaction, but also CO hydrogenation (methanation) ($\text{CO} + 3\text{H}_2 \rightarrow \text{CH}_4 + \text{H}_2\text{O}$) and WGS reaction ($\text{CO} + \text{H}_2\text{O} \rightarrow \text{CO}_2 + \text{H}_2$) were studied in detail.

Finally, a one dimensional adiabatic and isothermal fixed bed reactor model was developed at technical conditions (high temperature) over Ni/Al₂O₃ as well as Al₂O₃ catalyst system to simulate the performance of hydrogenation of CO₂ to CO for the production of liquid fuels via Fischer Tropsch synthesis. The axial profiles of reactor performance (temperature and conversion) were simulated along the catalytic fixed bed.

4. Experimental method and data analysis

In the following, the experimental setup and the procedure used in CO₂ hydrogenation, CO hydrogenation to methane as well as water gas shift reaction, and its corresponding calculation methods are introduced.

4.1 Experimental setup

The experimental set-up with reactor apparatus constructed for this study is shown in Fig. 4-1. It mainly consists of a quartz reactor, mass flow controllers, a heating furnace and a temperature control system, a water saturator, a cooling system, and an online gas analyser.

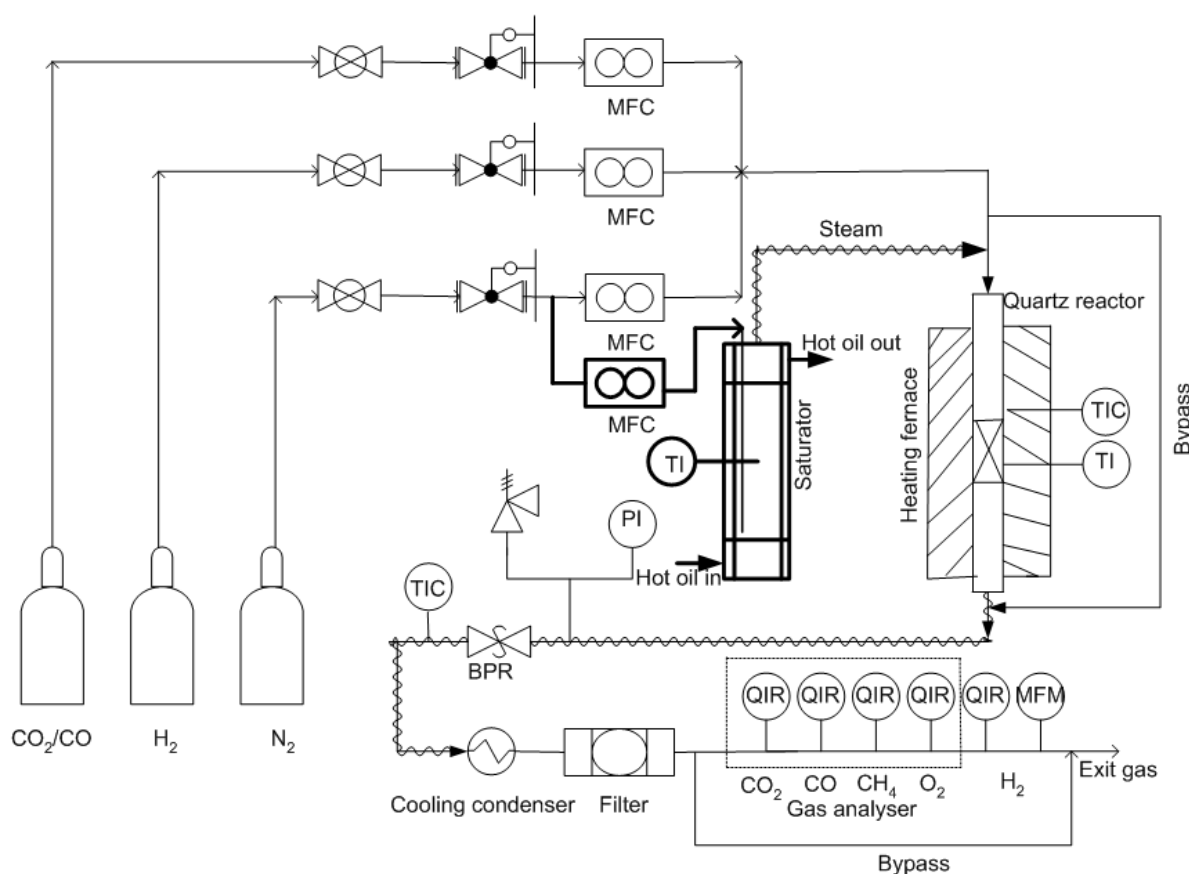


Fig. 4-1: Experimental set-up used for CO₂ hydrogenation, CO hydrogenation and water gas shift reaction.

A photograph and a schematic diagram of the bench-scale fixed bed reactor (2 cm inner diameter and 45 cm length) used for the experimental studies is shown in Fig. 4-2. In the

main system, a reactor bypass was introduced to allow the sampling of inlet feed gas conditions without catalyst interference. The gas flow lines (stainless steel tubing) from the reactor outlet to the cooled condenser were wrapped first with a conventional heating wire and then with insulating tape to prevent heat dissipation and maintain the better line temperatures. K type thermocouples were installed at a particular distance throughout the lines by weaving the probe between the heating wires and insulating tape to measure the line temperatures. A tube furnace with electric heating and temperature control system (Carbonite-210; upper temperature limit 1100 °C) was used to establish and maintain the catalyst bed temperature in the reactor. The axial temperature profile along the catalyst bed was measured with a moveable thermocouple inserted into the radial center of the catalyst bed through the top of the reactor (Fig. 4-2).

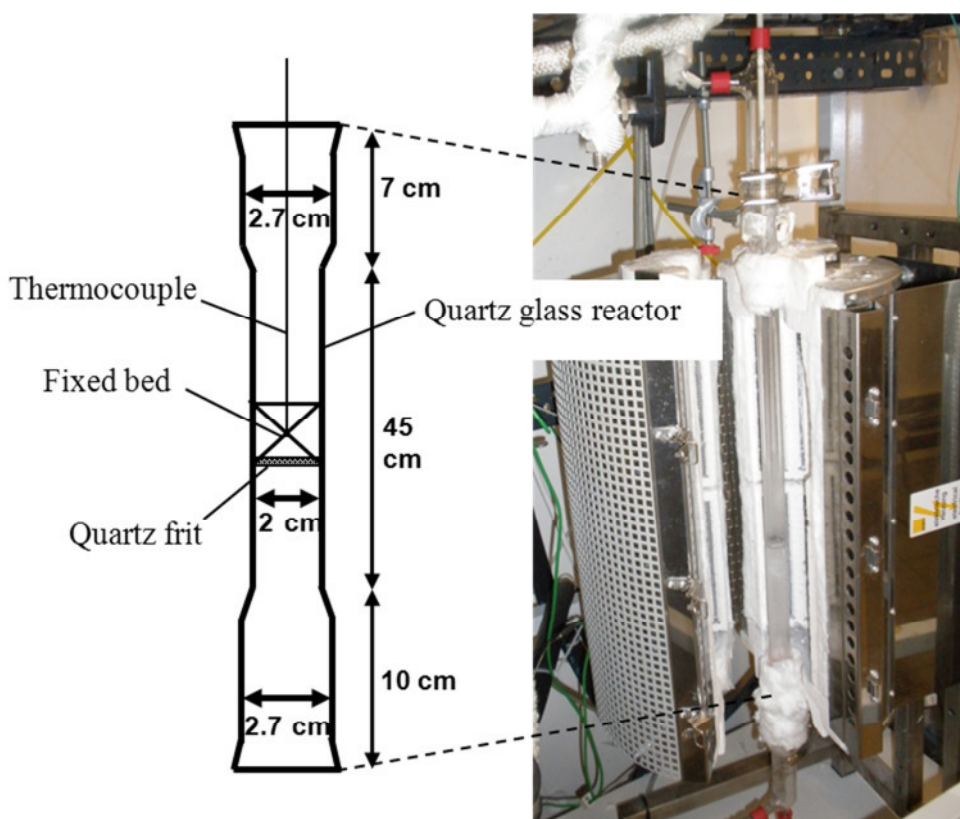


Fig. 4-2: Photograph and schematic representation of tubular fixed bed quartz reactor.

The required gases (hydrogen, carbon dioxide/carbon monoxide, and nitrogen) were delivered from commercial cylinders and the desired flow rates were adjusted by using mass flow controllers (MFC, Brooks Co.). For the collection of water produced in the reaction, a gas/liquid separator and a conventional condenser surrounded by an ice bed were used. The

analyses of the products were done using online gas analyser (Rosemount analytical Inc.). H_2 was analysed by a FID detector and the other gases (CO , CO_2 , CH_4) by IR detectors. The data acquisition system was implemented to collect the data obtained from the gas analyser.

For the water gas shift reaction experiments, a water saturator was implemented in the same experimental setup used for CO_2 and CO hydrogenation (see Fig. 4-1). The steam required was produced in the saturator and flows to the reactor by passing the carrier gas (nitrogen) through the saturator. The temperature of the water saturator was controlled by using an oil thermostat. The line temperature between saturator and reactor inlet was adjusted to $130\text{ }^\circ\text{C}$ to avoid steam condensation in the line and was controlled by using a temperature controller.

4.2 Experimental procedure

Before starting the reaction, all mass flow controllers were calibrated in the range of flow necessary for the desired feed conditions. Actual flow rates were measured with gas bubblers and compared to the MFC's readout values for each gas. Their respective values were adjusted to match the actual flow rate. The online gas analyser calibrations were performed using a constant flow rate of 30 l/h. The calibration was done with inert gas (N_2) and then with a known gas mixture of all necessary compounds (CO , CO_2 , CH_4 , and H_2). This calibration was then compared with individual gas phase species comprised of different concentrations balanced with inert nitrogen.

The experiments for the catalytic hydrogenation of CO_2 and CO were performed at atmospheric pressure in a continuous flow apparatus equipped with a tubular down-flow fixed bed quartz reactor. The reactor tube was filled with 1.2 g $\text{NiO}/\text{Al}_{12}\text{O}_{19}$ catalyst (spherical particles with 5 to 7 mm diameter) which is fixed at the centre of the reactor using a quartz frit where the maximum temperature was measured (Fig. 4-3). Then the catalyst was reduced by increasing the temperature ($10\text{ }^\circ\text{C}/\text{min}$) under a continuous flow of 10 l/h gas (50 % H_2 diluted with N_2). After reduction, the reactor was adjusted to the desired reaction temperature under the same gas flow. Once the temperature became stabilized, the reacting gas flow rates were adjusted using mass flow controllers and send through the reactor bypass system with reactor system closed off and sampled for inlet conditions. The bypass was then closed forcing the gas flow into the reaction system. The feed stream passed to the fixed bed reactor through the diffuser section (2.7 cm inner diameter and 7 cm

length) which ensure proper mixing of the feed gases. Reaction temperature was controlled using an electric heater and a temperature control system. The temperatures at the heater surface as well as in the reactor bulk (along the catalyst bed) were measured by K-type thermocouples. Due to the small bed height, no temperature gradient exists along the length of the catalyst bed used. The transfer line temperature between reactor outlet and cooling trap was maintained at 150 °C to avoid water condensation in the line.

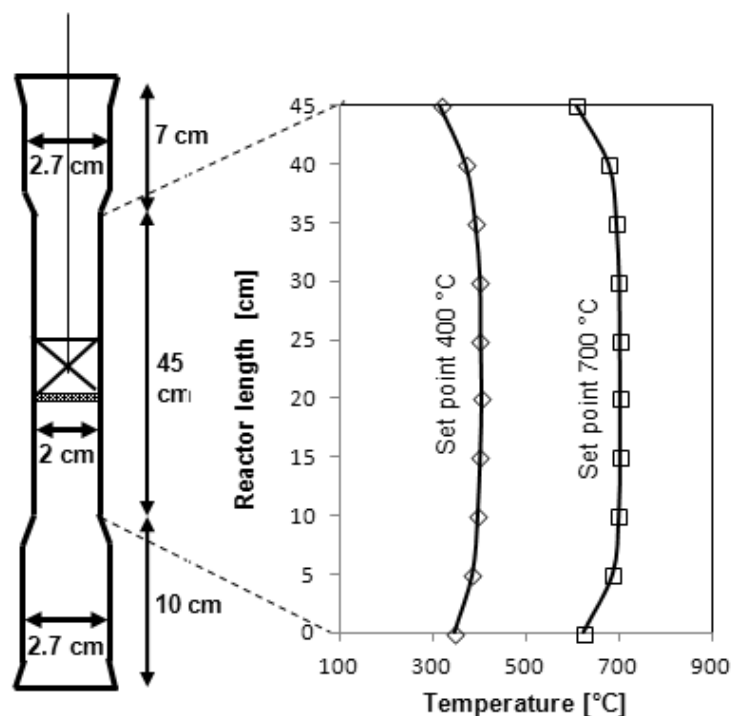


Fig. 4-3: Axial temperature profiles in the tubular empty quartz reactor.

All the exit compounds (unconverted reactant and products) were passed through the gas/liquid separator and the conventional condenser surrounded by an ice bath where water formed was collected in the condenser prior to further composition analysis. The dry gas was then sent to the online gas analyser through a cellulosic filter where fine particles of the catalyst (although never detected) would be removed. By using the gas pump, only 30 l/h of gas is passed to the analyser and the remaining amount is delivered to the exhaust using a bypass. In the online gas analysers, H_2 was analysed by a FID detector and other gases by IR detectors. Data obtained from the gas analysers were collected by the data acquisition system on a computer for every 5 seconds. The conversion of respected compounds (CO_2 , CO) and the yield of products were calculated using the data collected on computer. This data were then used to validate the kinetic models.

The experiments of the water gas shift reaction were also performed in the same tubular continuous down-flow fixed bed quartz reactor at atmospheric pressure. As mentioned above, the required gas flow rates were controlled by using MFC's while the steam flowrate was calculated and adjusted manually. For a given saturator temperature T , a constant pressure P and a flow rate of nitrogen passing through the saturator \dot{V}_{N_2} , the volume rate of steam at the outlet of the saturator (\dot{V}_{H_2O}) is calculated as

$$\dot{V}_{H_2O} = \frac{\dot{V}_{N_2}}{\left[\frac{P_{total}}{p_{H_2O}} - 1 \right]} \quad (4.1)$$

where p_{H_2O} and P_{total} is the vapour pressure of water and the total pressure of gas flowing through the saturator, respectively.

The vapour pressure of water at the outlet of saturator (in mm Hg, 760 mm Hg = 1.1013 bar) can be calculated by using the Antoine equation:

$$\log_{10} p_{H_2O} = A - \frac{B}{C + T} \quad (4.2)$$

A, B and C are constants ($A = 8.07131$, $B = 1730.63$, $C = 233.426$) and T is the saturator temperature in °C.

4.3 Catalyst characterisation

The Ni catalyst used in this work was purchased from Süd-Chemie (Germany). The catalyst of spherical size has particle diameters of 5 to 7 mm and a shell thickness of the active material (Ni) on the outer surface of about 0.5 mm (Fig. 4-4). The physical properties of the fresh Ni catalyst are given in Table 4-1. The properties of all other catalysts used in this work are given in appendix B.3.

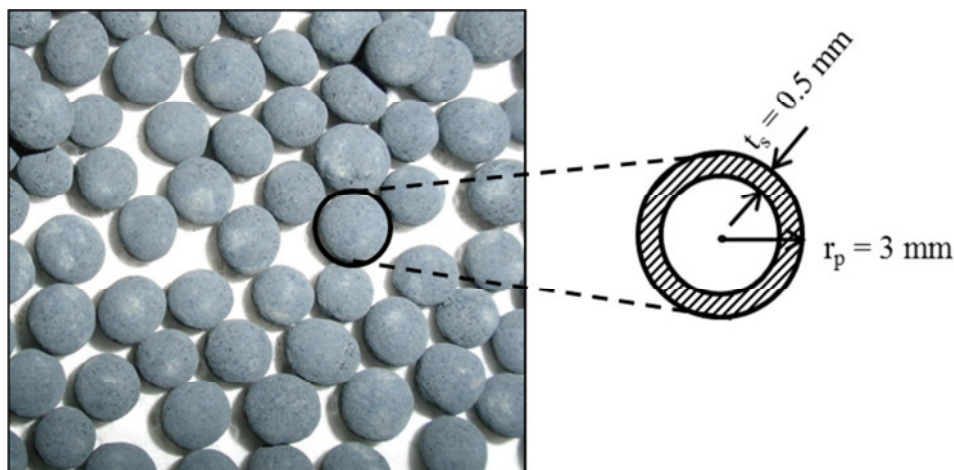


Fig. 4-4: Geometrical shape and shell balance of Ni catalyst.

Table 4-1: Characteristic data of the fresh commercial Ni catalyst.

| | |
|---------------------------------------|---|
| Catalyst name | G.90-B (commercial catalyst) |
| Manufacturer | Süd-Chemie Catalysts |
| Composition | NiO(11% Ni)/Al ₁₂ O ₁₉ CaO, Na ₂ O, K ₂ O, SiO ₂ (traces) |
| Geometry (sphere) | 5 – 7 mm (diameter) |
| Catalyst density | 1910 kg/m ³ |
| Catalyst bulk density | 1200 kg/m ³ |
| BET-surface area A _{BET} | 3 m ² /g |
| Pore volume | 0.17 cm ³ /g |
| Porosity of particle (ϵ_p) | 0.33 |
| Average pore diameter | 230 nm |

Temperature Programmed Reduction (TPR): A TPR experiment was performed by using *CHEMBET-3000* to determine the number of reducible species present in the catalyst and reveals the temperature at which the reduction of catalyst occurs. TPR analysis begins by flowing the analysis gas (10% hydrogen in argon) over the sample at ambient temperature. While the gas is flowing, the temperature of the sample increased at the rate of 10 °C/min.

Catalyst surface area: The specific surface area of catalyst was measured by nitrogen adsorption using the Brunauer Emmett Teller (BET) method.

X-ray diffraction (XRD): For the identification of crystalline phases and determination of average crystallite size, the powder X-ray diffraction were collected at room temperature on Phillips X-pert diffractometer from *Department of Materials Processing, University Bayreuth (Prof. M. Willert-Porada)* using Ni filter and Cu-K α radiation with wavelength $\lambda = 1.5418 \text{ \AA}$. The intensity of the signal was measured by step scanning over $2\theta = 15 - 65^\circ$.

4.4 Evaluation of the experimental data

4.4.1 CO₂ hydrogenation reaction

The CO₂ hydrogenation reaction studied in the temperature range of 300 to 900 °C shows some undesired product formations which may be due to consecutive reactions and/or undesired back reactions. Depending upon the catalyst used and the reaction conditions applied in this study, the reaction scheme proposed for CO₂ hydrogenation is shown in Fig. 4-5.

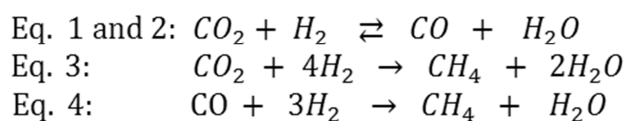
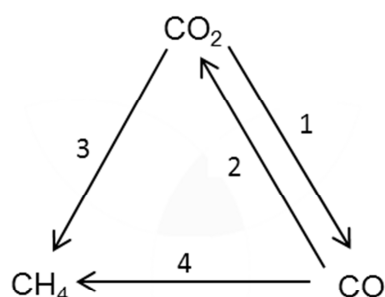


Fig. 4-5: Reaction scheme proposed for CO₂ hydrogenation on Ni catalysts.

4.4.1.1 Conversion of CO₂ and yield of CO and CH₄

The small amount of the catalyst in the reactor results in a small fixed bed height. Therefore, no temperature gradient exists along the length of fixed bed. The conversion of CO₂ and the yields of CO and CH₄ at isothermal conditions are calculated depending upon the outlet carbon percentage values obtained by the gas analysis. As the carbon monoxide and

methane are the only detectable products of CO₂ hydrogenation reaction, CO₂ conversion is calculated as:

$$CO_2 \text{ conversion } (X_{CO_2})\% = \frac{(CO)_{out} + (CH_4)_{out}}{(CO)_{out} + (CH_4)_{out} + (CO_2)_{out}} \times 100 \quad (4.3)$$

Similarly, the yield of CO and CH₄ can be calculated (no CO and CH₄ in the feed) as:

$$CO \text{ yield } (Y_{CO})\% = \frac{(CO)_{out}}{(CO)_{out} + (CH_4)_{out} + (CO_2)_{out}} \times 100 \quad (4.4)$$

$$CH_4 \text{ yield } (Y_{CH_4})\% = \frac{(CH_4)_{out}}{(CO)_{out} + (CH_4)_{out} + (CO_2)_{out}} \times 100 \quad (4.5)$$

4.4.1.2 Determination of the intrinsic kinetic parameters

The intrinsic kinetic experiments were carried out in a quartz glass fixed bed reactor with an inner diameter of 2 cm, filled with 1.2 g catalyst of 5 to 7 mm diameter. The isothermal experiments were carried out at atmospheric pressure. The inlet feed passed through the reactor (H₂/CO₂ = 6) was diluted with 23 vol.-% of nitrogen. The experiments were performed until constant conversion of CO₂ was obtained.

For the bimolecular CO₂ hydrogenation reaction (CO₂ + H₂ → CO + H₂O), the intrinsic reaction rate over solid catalyst is calculated as:

$$r_{m,CO_2} = k_{m,CO_2} C_{CO_2}^n C_{H_2}^m \quad (4.6)$$

For the reaction order $n \neq 1$, the reaction rate constant k_{m,CO_2} is given as:

$$k_{m,CO_2} = \frac{(1 - X_{CO_2})^{1-n} - 1}{(n - 1) \tau_m C_{CO_2}^{n-1} C_{H_2}^m} \quad (4.7)$$

This calculated k_{m,CO_2} in Eq. (4.7) may not be the intrinsic rate constant, which can be confirmed by calculating the effectiveness factor.

The modified residence time τ_m as a function of mass of catalyst and volume flow rate at reaction temperature and total pressure of gas is given as:

$$\tau_m = \frac{m_{cat}}{\dot{V}(T, P_{total})} \quad (4.8)$$

The activation energy E_A and frequency factor $k_{m,0}$ can be calculated from the Arrhenius equation:

$$k_{m,CO_2} = k_{m,0} e^{-\frac{E_A}{RT}} \quad (4.9)$$

4.4.1.3 Internal mass transport calculations

As mentioned in chapter 2, the pore diffusion limitations may occur, and the measured kinetics may not be the intrinsic but the effective one. The effective rate of chemical reaction is calculated with the help of the effectiveness factor η is given as:

$$r_{m,eff} = \eta r_m \quad (4.10)$$

The effectiveness factor η for n^{th} order irreversible reaction is given by:

$$\eta = \frac{r_{m,eff}}{r_m} = \frac{\tanh \phi}{\phi} \quad (4.11)$$

The Thiele modulus for the catalyst with homogeneous distribution and for n^{th} order, irreversible, bi-molecular CO_2 hydrogenation reaction is given as

$$\phi = L_p \sqrt{\left[\frac{n+1}{2}\right] \frac{k_m \rho_p C_{CO_2}^{n-1} C_{H_2}^m}{D_{CO_2,eff}}} \quad (4.12)$$

where the characteristic length L_p is the ratio of the volume of the particle to the external surface of the particle (for spherical particle $L_p = r_p/3$). For a shell catalyst the modified Thiele modulus (ϕ^I) is given as [83]

$$\phi^I = L_p \sqrt{\left[\frac{n+1}{2}\right] \frac{k_m^I \rho_p C_{CO_2}^{n-1} C_{H_2}^m}{D_{CO_2,eff}}} \quad (4.13)$$

whereas the characteristic length (L_p) for a shell catalyst is given as

$$L_p = \left\{ 1 - \left[1 - \frac{t_s}{r_p} \right]^3 \right\} \frac{r_p}{3} \quad (4.14)$$

where r_p is the radius of particle and t_s is the shell thickness of active material. The effective diffusivity of CO_2 in a porous catalyst is given as:

$$D_{CO_2,eff} = \frac{\varepsilon_p}{\tau_p} D_{CO_2,pore} = \frac{\varepsilon_p}{\tau_p} \left[\frac{1}{D_{CO_2,mol}} + \frac{1}{D_{CO_2,knu}} \right]^{-1} \quad (4.15)$$

In the present study, mass transport in the pores depends both on molecular diffusion and Knudsen diffusion. The molecular diffusion coefficients of CO₂ in the gas mixture were calculated by a computer database program while Knudsen diffusion coefficients were calculated by using Eq. (4.16) as

$$D_{CO_2,knu} = \frac{d_{pore}}{3} \sqrt{\frac{8 R T}{\pi M_{CO_2}}} \quad (4.16)$$

where d_{pore} is the pore diameter, R is the gas constant, T is the temperature, and M_{CO_2} the molecular weight of CO₂. The tortuosity factor depends upon nature of interconnecting paths which is influenced by the connectivity, shapes, and specific limiting constrictions. In this work, a typical value for τ_p of 1.6 was assumed for Ni catalyst. The calculation of the modified Thiele modulus for the shell catalyst needs the modified reaction rate constant (k_m^l), which is given for a spherical catalyst particle of radius r_p and shell thickness t_s as:

$$k_m^l = \frac{m_p}{m_s} k_m \approx \frac{V_p}{V_s} k_m \quad (4.17)$$

The factor V_p/V_s is the ratio of volume of the particle to the volume of the shell:

$$\frac{V_p}{V_s} = \left\{ 1 - \left[1 - \frac{t_s}{r_p} \right]^3 \right\}^{-1} \quad (4.18)$$

For the Ni catalyst used in this work V_p/V_s is about 2.4.

By Eq. (4.17) and Eq. (4.13), k_m^l can be calculated as

$$k_m^l = \left\{ 1 - \left[1 - \frac{t_s}{r_p} \right]^3 \right\}^{-1} k_m \quad (4.19)$$

Insertion of the characteristic length (L_p) from Eq. (4.14) and of the modified rate constant (k_m^l) from Eq. (4.19) into Eq. (4.13), yields the modified Thiele modulus for a shell catalyst having active material only in the shell:

$$\phi^I = \left\{ 1 - \left[1 - \frac{t_s}{r_p} \right]^3 \right\}^{0.5} \frac{r_p}{3} \sqrt{\left[\frac{n+1}{2} \right] \frac{k_m \rho_p C_{CO_2}^{n-1} C_{H_2}^m}{D_{CO_2,eff}}} \quad (4.20)$$

For the case of $t_s = r_p$, Eq. (4.19) leads to the same equation that is used for the calculation of the Thiele modulus for a catalyst with a homogeneous distribution of the active component (Eq. (4.12)).

4.4.1.4 Calculation of external mass transport limitations

The effective reaction rate due to external mass transfer is calculated as

$$r_{m,CO_2,eff} = \beta A_{m,ext} (C_{CO_2} - C_{CO_2,s}) \quad (4.21)$$

The external mass transfer coefficient β (m/s) depends upon the particle size and geometry, molecular diffusion coefficient of gas ($D_{CO_2,mol}$), and the hydrodynamic conditions such as velocity and viscosity of the fluid. β as a function of the dimensionless Sherwood number (Sh) for the mass transfer can be calculated as

$$\beta = \frac{Sh D_{CO_2,mol}}{d_p} \quad (4.22)$$

The external surface area $A_{m,ex}$ (m²/kg) for spherical particle is

$$A_{m,ext} = \frac{6}{d_p \rho_p} \quad (4.23)$$

where d_p and ρ_p are the particle diameter and density of particle, respectively. When gas flows through a catalyst fixed bed, the Sherwood number is given as

$$Sh = [1 + 1.5 (1 - \epsilon_b)] Sh_p \quad (4.24)$$

where ϵ_b is the bed porosity. The particle Sherwood number (Sh_p) for gas flow around the particle and for laminar flow, correlated to the Schmidt number (Sc) and the Reynolds number (Re) is given as [20]:

$$Sh_p = 2 + 0.69 \sqrt{Re} \sqrt[3]{Sc} \quad (4.25)$$

The Reynolds number (Re) depends upon the interstitial velocity u (m/s), the kinematic viscosity of gas ν (m²/s), and the particle diameter d_p (m):

$$Re = \frac{u d_p}{\nu} \quad (4.26)$$

Similarly, Schmidt number (Sc) depending upon the kinematic viscosity ν (m^2/s) and the molecular diffusion coefficient of gas $D_{CO_2, mol}$ (m^2/s) as:

$$Sc = \frac{\nu}{D_{CO_2, mol}} \quad (4.27)$$

Now the effective reaction rate due to the combined influence of internal and external mass transfer resistances is given in approximation (for an almost irreversible reaction) by

$$r_{m, eff} = \left[\frac{1}{\eta k_m C_{CO_2}^n C_{H_2}^m} + \frac{1}{\beta A_{m, ex} C_{CO_2}} \right]^{-1} \quad (4.28)$$

4.4.2 CO hydrogenation (methanation) reaction

4.4.2.1 Conversion of CO and yield of CO_2 and CH_4

Similar to CO_2 hydrogenation, the conversion of CO and the yield of CO_2 and CH_4 at given reaction condition is calculated depending upon the outlet carbon percentage values obtained over the analyser. As the methane and carbon dioxide are the main products of CO hydrogenation reactions, the CO conversion is calculated as:

$$CO \text{ conversion } (X_{CO})\% = \frac{(CO_2)_{out} + (CH_4)_{out}}{(CO)_{out} + (CH_4)_{out} + (CO_2)_{out}} \times 100 \quad (4.29)$$

and the yield of CO_2 and CH_4 in CO hydrogenation is calculated as:

$$CO_2 \text{ yield } (Y_{CO_2})\% = \frac{(CO_2)_{out}}{(CO)_{out} + (CH_4)_{out} + (CO_2)_{out}} \times 100 \quad (4.30)$$

$$CH_4 \text{ yield } (Y_{CH_4})\% = \frac{(CH_4)_{out}}{(CO)_{out} + (CH_4)_{out} + (CO_2)_{out}} \times 100 \quad (4.31)$$

4.4.2.2 Kinetic analysis and mass transport calculations

The calculations with regard to the intrinsic kinetics and internal and external mass transfer limitations for CO hydrogenation were performed by using the equations applied for CO_2 hydrogenation (see section 4.4.1).

4.4.3 Water gas shift (WGS) reaction

4.4.3.1 Conversion of CO and yield of CO₂ and CH₄

The conversion of CO and the yield of CO₂ and CH₄ in water gas shift reaction were calculated by using the same equations as for the CO hydrogenation (Eq. (4.29) to (4.31)).

4.4.3.2 Kinetic analysis and mass transport calculations

The kinetic analysis of the WGS reaction was also done by using the equations of CO₂ hydrogenation reaction (see section 4.4.1).

5. Results and discussion

As already mentioned in Chapter 4, this work is divided into four parts. In the first part (Chapter 5.1), experimental results are discussed for CO₂ hydrogenation studied by using a fixed bed reactor. This part mainly includes the reaction parameter study, the intrinsic kinetics of CO₂ hydrogenation, and the influence of pore diffusion and film diffusion on the effective reaction rate of CO₂ hydrogenation. The second part (Chapter 5.2) consists of a similar parametric study for CO hydrogenation (methanation reaction). Similar to the first and second part, the third part (Chapter 5.3) includes the parameter study of water gas shift reaction (as the reverse reaction of CO₂ hydrogenation), again the intrinsic kinetics as well as the influence of pore diffusion and film diffusion. The fourth and last part (Chapter 5.4) includes the fixed bed reactor modelling for CO₂ hydrogenation at technical conditions.

5.1 CO₂ hydrogenation (RWGS)

The studies on CO₂ hydrogenation ($\text{CO}_2 + \text{H}_2 \rightarrow \text{CO} + \text{H}_2\text{O}$) were carried out in a fixed bed quartz reactor over a wide temperature range (300 – 900 °C) and at atmospheric pressure. The commercial Ni catalyst was used. For comparison, $\gamma\text{-Al}_2\text{O}_3$ was also tested to investigate the catalytic activity of the support only.

5.1.1 Effect of reduction temperature on CO₂ hydrogenation (RWGS)

The commercial NiO/Al₁₂O₁₉ (G-90.B) catalyst was reduced at two different temperatures (500 and 800 °C) to examine the effect of the reduction temperature on the catalyst performance and the yield of products. Fig. 5-1 shows the conversion of CO₂ and the yield of CO and CH₄ obtained over the catalyst reduced at 500 and 800 °C. A strong dependence of activity and product yield on the reduction temperature was observed. On the Ni catalyst reduced at a low temperature of 500 °C for 15 h, methane was formed almost exclusively along with CO in the low reaction temperature range (below 600 °C), while on the catalyst samples reduced at high temperature of about 800 °C for 3 h, the methane formation strongly decreased in the same range of reaction temperature. The overall conversion of CO₂ obtained at any reaction temperature is high for the catalyst reduced at 500 °C compared to 800 °C. This could be due to the deactivation of the active species (particularly methane forming species) at high reduction temperatures.

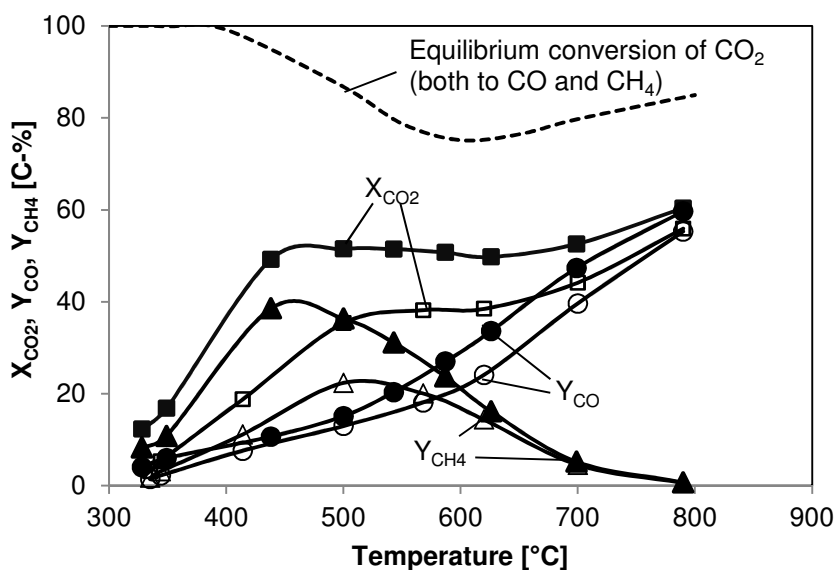


Fig. 5-1: CO₂ conversion and CO and CH₄ yield versus temperature; open symbol: catalyst reduced at 800 °C for 3 h; closed symbol: catalyst reduced at 500 °C for 15 h (p = 1 atm, m_{cat} = 1.2 g, catalyst = Ni/Al₂O₃, d_p = 6 mm, y_{H2} = 66 vol.-%, y_{CO2} = 11 vol.-%, rest N₂, gas flow rate = 138 l/h (NTP)).

Over the reduced catalyst both at 500 °C and 800 °C, methanation reaction occurs (most favoured thermodynamically at low temperature) along with the reverse water gas shift (RWGS) reaction. The yield of CO increases continuously with increase in temperature but not the conversion of CO₂. This is a clear indication of direct methane formation via CO₂ hydrogenation (Sabatier reaction) without intermediate CO formation. The overall CH₄ formation observed could be due to both CO₂ and CO hydrogenation but it is quite difficult to quantify because both reactions occur simultaneously.

Fig. 5-2 shows the XRD pattern of the Ni/Al₂O₃ catalyst (11 wt.-% Ni). The diffractogram (A) for the fresh Ni catalyst shows strong NiO lines at 2θ values of 37.3, 43.3, and 62.9 confirming the presence of free nickel oxide [84]. For both the reduced and used catalyst no free nickel oxide lines were observed. On the diffractogram (B) for the reduced catalyst, the lines were observed for nickel crystallites at 44.5 and 51.8 while for the used catalyst (C) a line was observed at 44.5. From the diffractogram (B) it is clear that the catalysts get completely reduced even at low temperature of 500 °C. On the diffractogram (C) for the used catalyst, the free NiO lines were not observed which means that no oxidation of Ni happens by the water formed during the reaction at 500 °C.

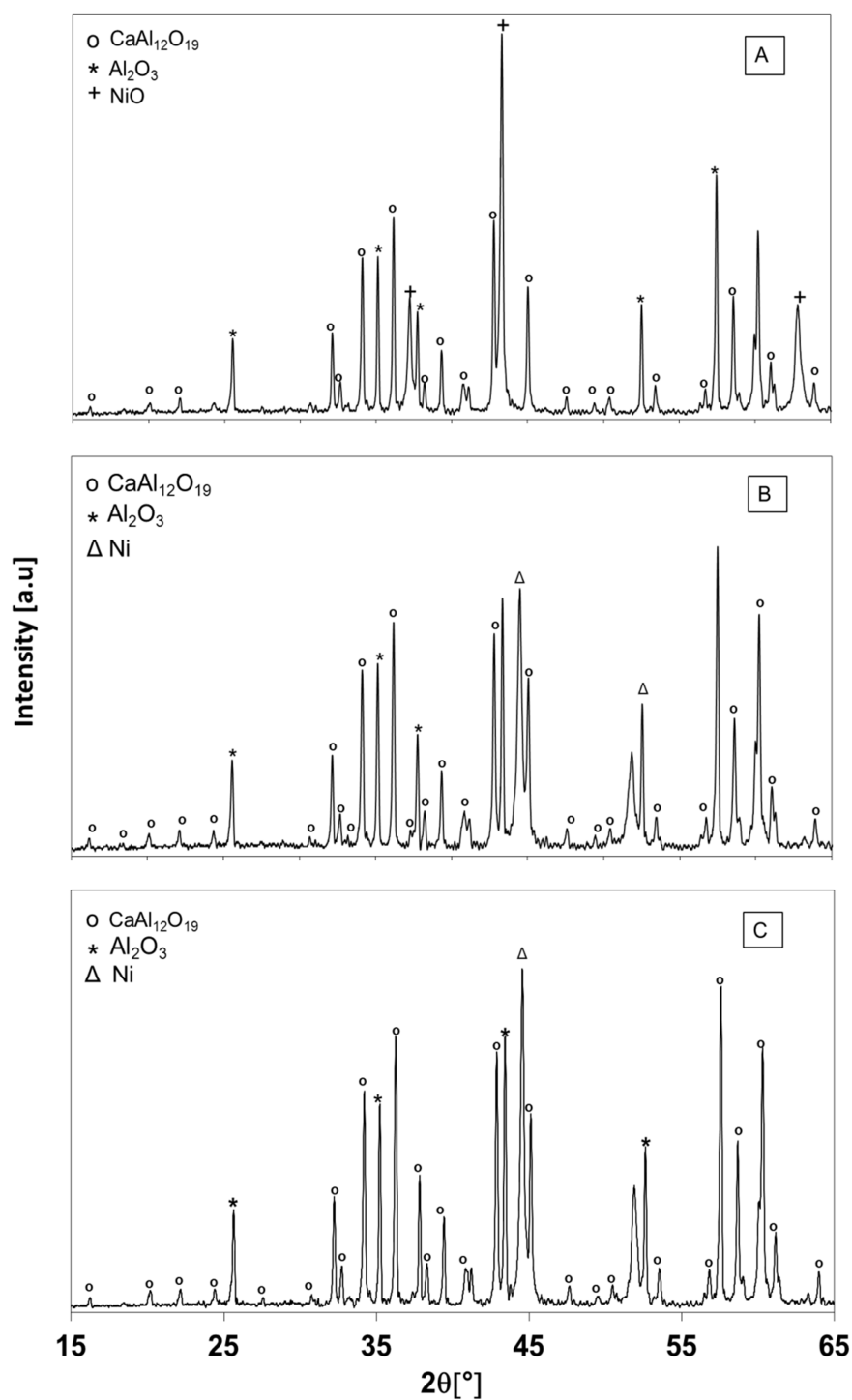


Fig. 5-2: XRD patterns for fresh $\text{NiO}/\text{Al}_{12}\text{O}_{19}$ (A), reduced catalyst at 500 °C (B), and used catalyst at 500 °C (C).

To determine the exact temperature needed for the reduction of the Ni catalyst and the number of reducible species present in the catalyst, a TPR experiment was performed by using *CHEMBET-3000*. TPR analysis begins by passing the analysis gas (10% hydrogen in

argon) over the sample at ambient temperature. While the gas is flowing, the temperature of the sample was increased to 900 °C at a rate of 10 °C/min. The reduction profile of NiO/Al₁₂O₁₉ catalyst is shown in Fig. 5-3. There was only one peak obtained at 490 °C for bulk NiO and no other peak was obtained even at high temperatures. So, a temperature of 500 °C can be regarded as sufficient for the complete reduction of the NiO/Al₁₂O₁₉ catalyst.

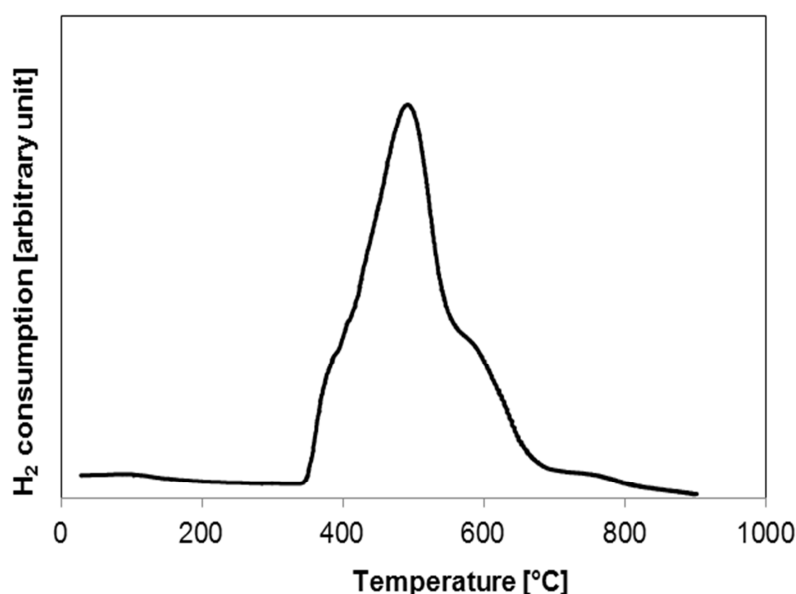


Fig. 5-3: TPR profile for NiO (11wt.-% Ni)/Al₁₂O₁₉ catalyst.

5.1.2 Reproducibility of CO₂ hydrogenation

The Ni catalyst used in the first cycle over the temperature range of 300 to 800 °C in CO₂ hydrogenation was reused for testing the reproducibility of the result. After the use of the catalyst at 800 °C in a first cycle, the catalyst was cooled to 300 °C with a small flow rate of N₂ and then a second cycle was performed by increasing the temperature. Under the same reaction condition as used in the first cycle, it was observed that the yield of both methane and CO dropped down (especially CH₄) in the low temperature range (Fig. 5-4). So it is reconfirmed that the methane formation species deactivates at high temperature. But at high temperatures of about 800 °C practically no difference in the catalyst performance was obtained. This could be due to the high temperature stability of the catalyst for CO formation.

The same procedure was repeated in a third and fourth cycle, but no more deactivation of the Ni catalyst was observed and nearly the same yields of CO and methane (within the experimental error) were obtained (Fig. 5-4).

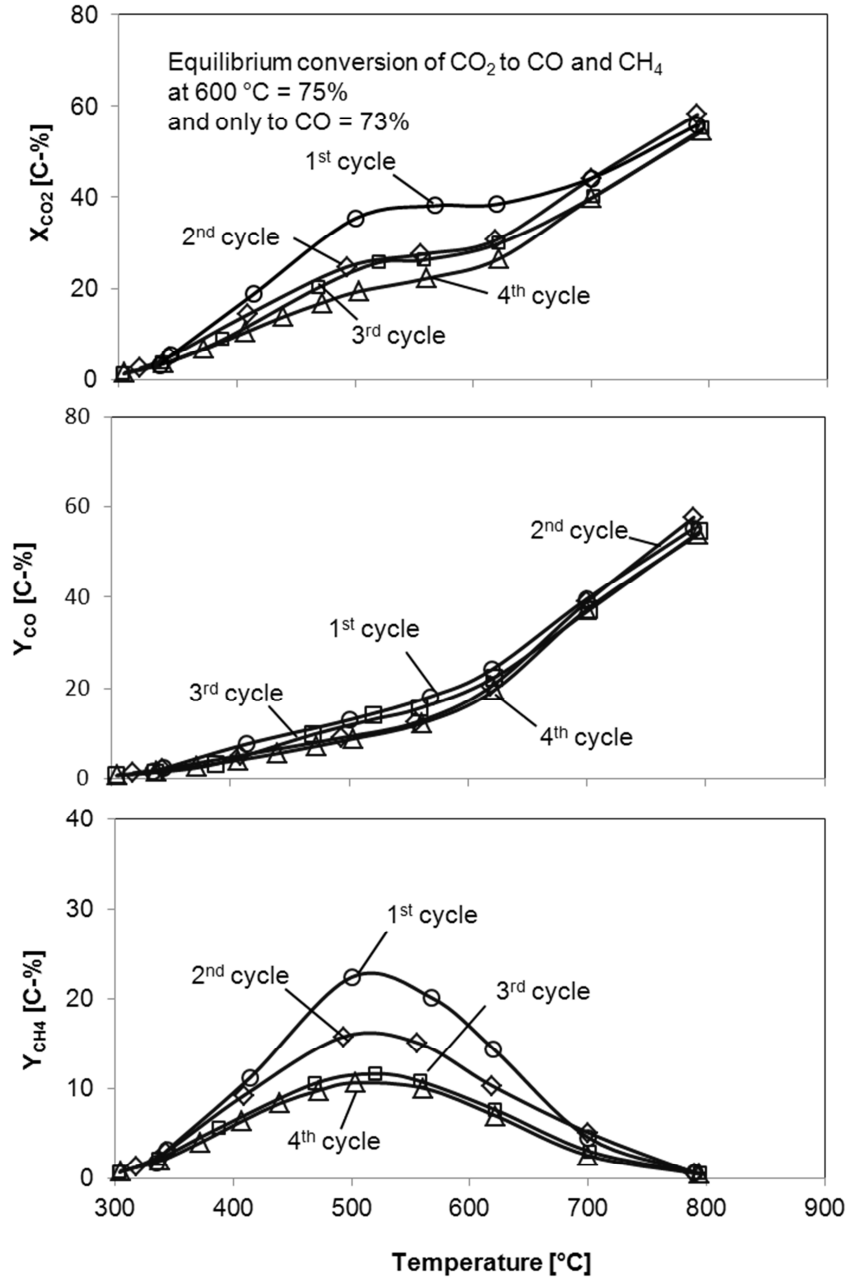


Fig. 5-4: CO_2 conversion and CO and CH_4 yield versus temperature for four repeated cycles ($p = 1\text{ atm}$, $m_{\text{cat}} = 1.2\text{ g}$, $d_p = 6\text{ mm}$, $y_{\text{H}_2} = 66\text{ vol.-%}$, $y_{\text{CO}_2} = 11\text{ vol.-%}$, rest N_2 , gas flow rate = 138 l/h (NTP)).

5.1.3 Effect of residence time at varying temperature (RWGS and consecutive methanation)

To determine the effect of the residence time on the catalyst performance in terms of conversion and yield of products over the temperature, the previously long time on stream studied catalyst was used. The study was carried out using two different gas flow rates of 48 l/h and 138 l/h at NTP, which is equivalent to residence times (empty tube, 600 °C) of 25.6 ms and 8.9 ms, respectively (Fig. 5-5).

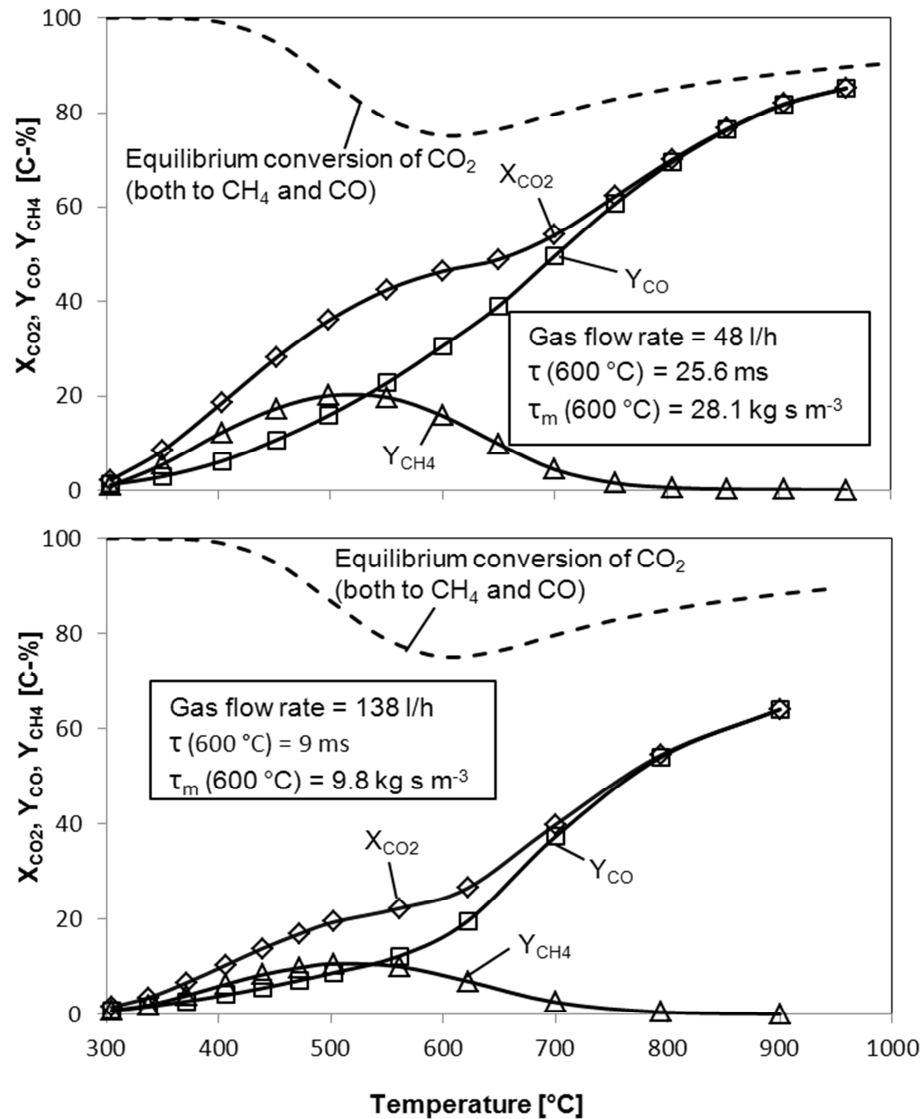


Fig. 5-5: CO₂ conversion and CO and CH₄ yield at different residence times versus temperature in CO₂ hydrogenation ($p = 1$ atm, $m_{\text{cat}} = 1.2$ g, catalyst = Ni/Al₁₂O₁₉, $d_p = 6$ mm, $y_{\text{H}_2} = 66$ vol.-%, $y_{\text{CO}_2} = 11$ vol.-%, rest N₂).

The conversion of carbon dioxide increases with decreasing the total gas flow rate (increasing residence time). The production of CO increases continuously with increasing temperature by the reverse water gas shift reaction. At a high temperature and low gas flow rate of 48 l/h, the CO₂ conversion nearly reaches the equilibrium value. In the section below (section 5.1.4) the effect of residence time on the conversion of CO₂ and the yield of CO and CH₄ at constant temperature is given in detail.

At temperatures above about 600 °C, not only Ni but also γ -Al₂O₃ as the support may contribute to the RWGS reaction [85, 86]. Therefore a test was done with 10 g cylindrical γ -Al₂O₃ pellets (1 to 3 mm).

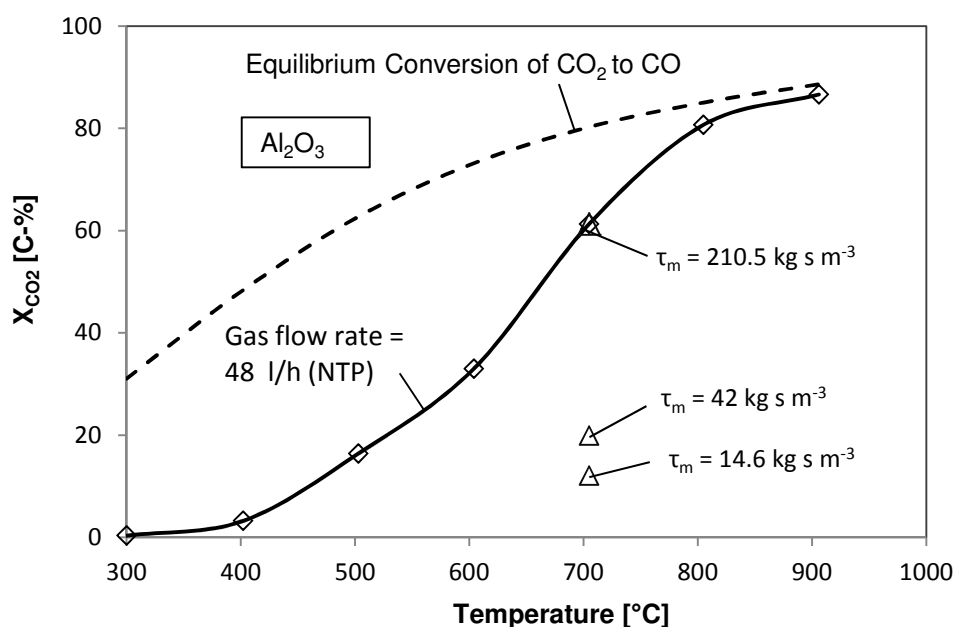


Fig. 5-6: CO₂ conversion versus temperature in CO₂ hydrogenation ($p = 1$ atm, $m_{\text{cat}} = 10$ g, catalyst = Al₂O₃, $d_p = 1 - 3$ mm, $y_{\text{H}_2} = 66$ vol.-%, $y_{\text{CO}_2} = 11$ vol.-%, rest N₂).

Fig. 5-6 shows that the conversion of CO₂ to CO over Al₂O₃ increases with increasing temperature and no CH₄ formation was observed in the studied range of temperature. At a high temperature of 900 °C, the CO₂ conversion reaches the equilibrium. In the low temperature range (300 to 700 °C), reaction is controlled kinetically while above 700 °C it is controlled thermodynamically.

5.1.4 Effect of residence time at constant temperature (RWGS and consecutive methanation)

The conversion of CO_2 increases from 13 to 29% by an increase of the modified residence time from 13 to 36 kg s m^{-3} at 405 °C and atmospheric pressure (Fig. 5-7). In the studied range of the residence time a strong increase of the yield of CH_4 was observed, corresponding to a direct conversion of CO_2 . At 405 °C, the yield of CO as a function of modified residence time demonstrates the typical behaviour of an intermediate product in consecutive reactions. Hence CO is formed but is also further converted to methane.

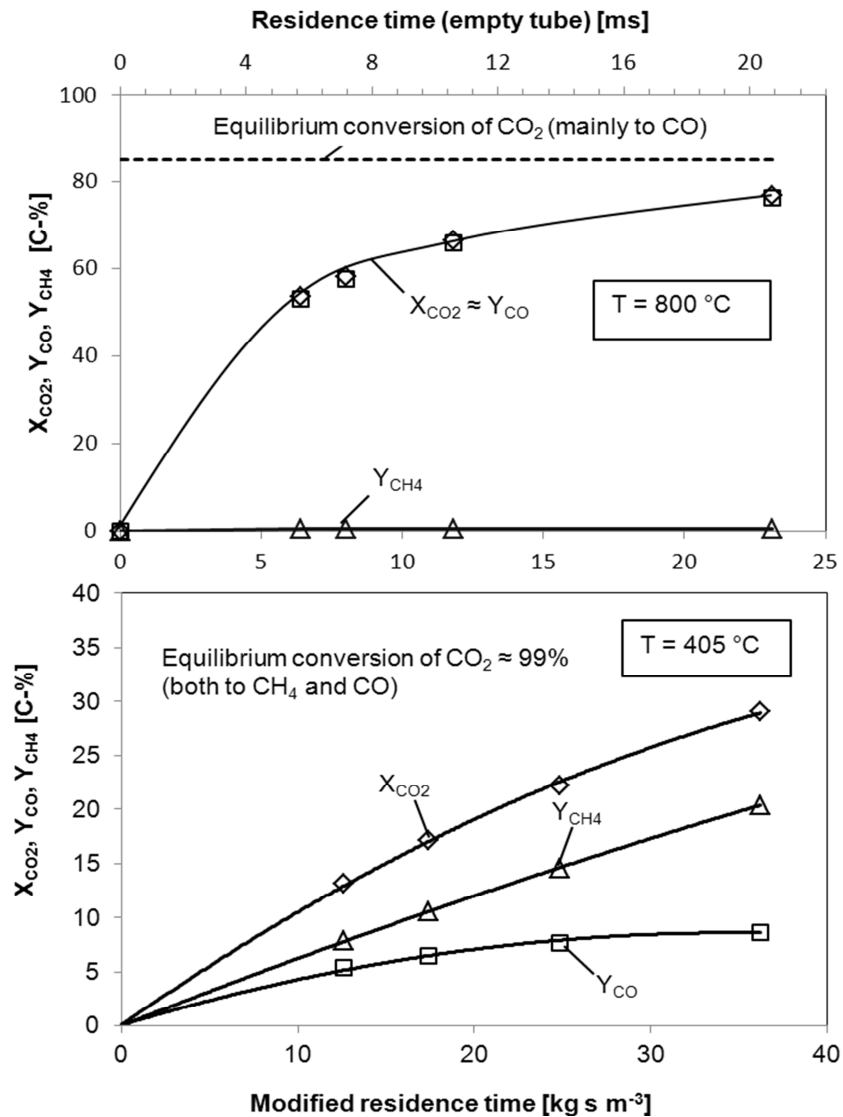


Fig. 5-7: Effect of modified residence time on CO_2 conversion and yield of CO and CH_4 in CO_2 hydrogenation ($T = 405$ and 800 °C, $p = 1$ atm, $m_{\text{cat}} = 1.2$ g, $d_p = 6$ mm, catalyst = $\text{Ni}/\text{Al}_{12}\text{O}_{19}$, $y_{\text{H}_2} = 66$ vol.-%, $y_{\text{CO}_2} = 11$ vol.-%, rest N_2).

At a high reaction temperature of about 800 °C, the reaction system differs significantly from the one at 405 °C. The conversion of CO₂ almost reaches equilibrium at the highest residence time of 23 kg s m⁻³ (21 ms). Since methane formation is negligible, the yield of CO equals the conversion of CO₂. By comparing low and high temperature data, it is clear that the formation of CO as a desired product of RWGS reaction is only possible at high reaction temperatures where methanation is suppressed thermodynamically.

Fig. 5-8 shows the selectivity to methane and CO versus the CO₂ conversion at 405 °C. The extrapolation towards zero CO₂ conversion resulted in 50% CO and 50% CH₄ selectivity, which indicates that CH₄ is (also) a primary product directly formed from CO₂ via the Sabatier reaction ($\text{CO}_2 + 4\text{H}_2 \rightarrow \text{CH}_4 + 2\text{H}_2\text{O}$).

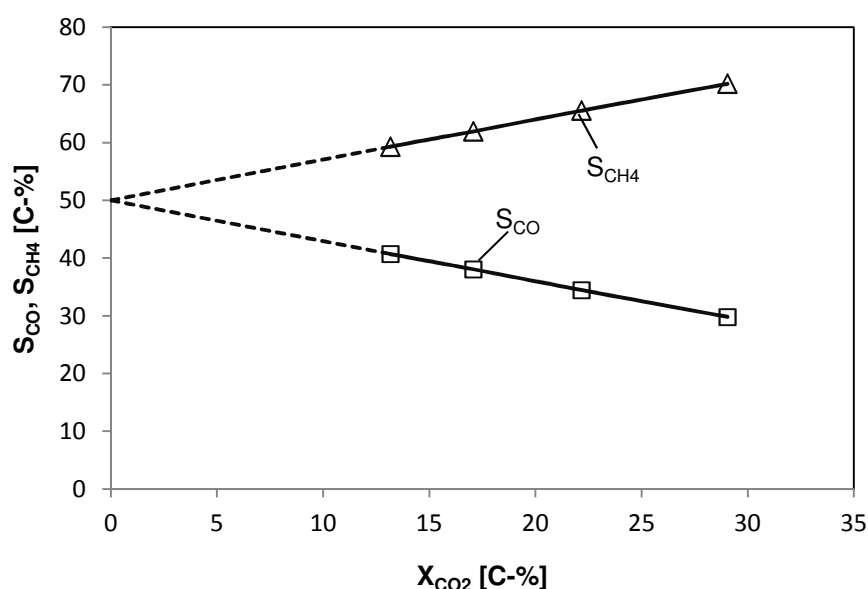


Fig. 5-8: CO₂ conversion versus selectivity of CO and CH₄ in CO₂ hydrogenation (T = 405 °C, p = 1 atm, $\tau_m = 12.6 - 36.5$ kg s m⁻³, d_p = 6 mm, m_{cat} = 1.2 g, catalyst = Ni/Al₁₂O₁₉, y_{H2} = 66 vol.-%, y_{CO2} = 11 vol.-%, rest N₂).

For the γ -Al₂O₃ as a catalyst, no CH₄ formation was obtained and only the conversion of CO₂ to CO formation was observed over the studied range of the residence time (Fig. 5-9). As the residence time increases, the conversion of CO₂ to CO rises and nearly reaches the equilibrium conversion. Note that the residence time needed for a certain conversion of CO₂ is higher for pure Al₂O₃ compared to the Ni catalyst. For example, at 700 °C, 20% CO₂ conversion is reached for Al₂O₃ at a residence time of 42 kg s m⁻³ (Fig. 5-9), whereas for the

Ni catalyst 40% CO₂ conversion is reached at about 9 kg s m⁻³ (Fig. 5-5). Hence, the activity of the Ni catalyst is about 10 times higher.

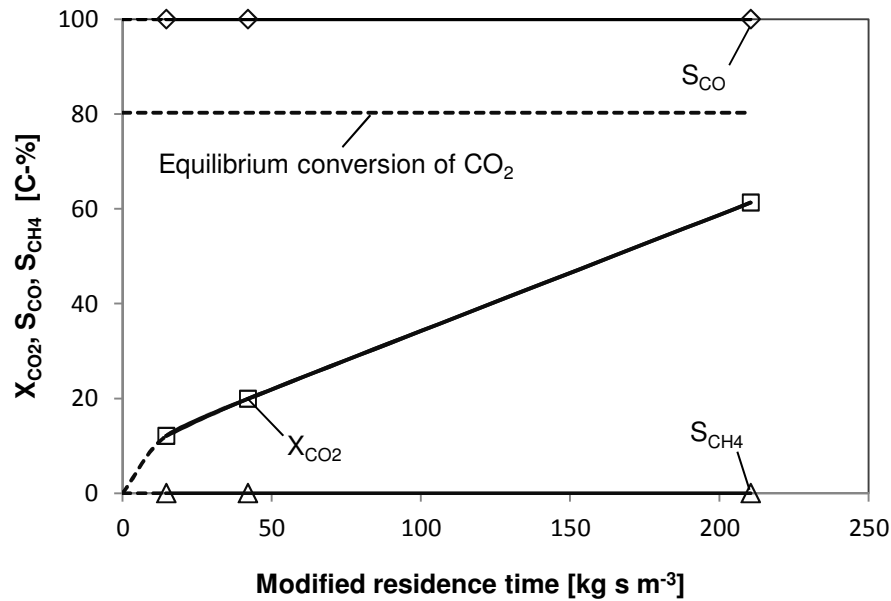


Fig. 5-9: Effect of modified residence time on CO₂ conversion and selectivity of CO and CH₄ (T = 700 °C, p = 1 atm, m_{cat} = 10 g, catalyst = Al₂O₃, d_p = 1 – 3 mm, y_{H₂} = 66 vol.-%, y_{CO₂} = 11 vol.-%, rest N₂).

According to the data obtained in this study, methane formation during CO₂ hydrogenation may be due to the direct methanation ($\text{CO}_2 + 4\text{H}_2 \rightarrow \text{CH}_4 + 2\text{H}_2\text{O}$) or to the consecutive reaction of CO hydrogenation ($\text{CO} + 3\text{H}_2 \rightarrow \text{CH}_4 + \text{H}_2\text{O}$). The consecutive reaction mechanism in CO₂ hydrogenation implies the difficulty that the optimum reaction conditions for each of the reactions are different (high temperature for RWGS and low temperature for CO hydrogenation).

5.1.5 Effect of catalyst particle size (RWGS and consecutive methanation)

To determine the effect of particle size on the catalyst performance, particles of Ni catalyst with less than 0.5 mm diameter (crushed catalyst) and 6 mm diameter were used. Fig. 5-10 shows the conversion of CO₂ and the yield of CO and CH₄ at different temperatures.

The catalyst particles with diameter of less than 0.5 mm show a higher conversion than the 6 mm particles with the active material only at the shell side which may due to two reasons. One is the fresh catalyst which is not treated at high temperature for long time has higher

activity than the used one (see Fig. 5-4). On the hand the influence of diffusion resistances may be smaller for small particles. This will be analysed in more detail in section 5.1.7.

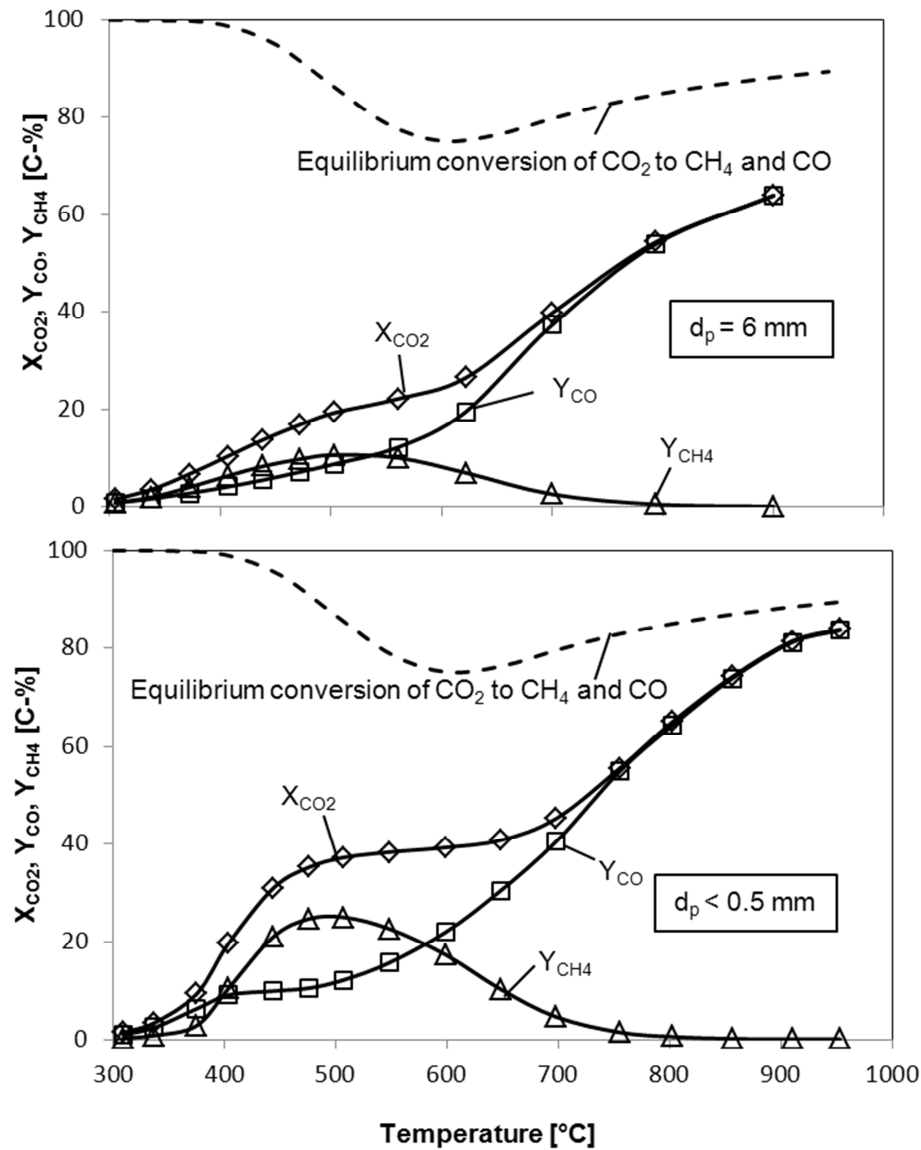


Fig. 5-10: CO_2 conversion and CO and CH_4 yield at different particle size in CO_2 hydrogenation ($p = 1 \text{ atm}$, $m_{cat} = 1.2 \text{ g}$, catalyst = $Ni/Al_{12}O_{19}$, gas flow rate = 138 l/h (NTP), $y_{H_2} = 66 \text{ vol.-%}$, $y_{CO_2} = 11 \text{ vol.-%}$, rest N_2).

5.1.6 Stability of the Ni catalyst for the RWGS reaction at high temperature

The time on stream stability of $Ni/Al_{12}O_{19}$ catalyst was tested at $900 \text{ }^\circ\text{C}$ and atmospheric pressure with the total gas flow rate of 138 l/h in the fixed bed reactor. The test was carried out for four days with intermediate cooling cycles. At the beginning of the experiment, the

catalyst bed temperature was increased from ambient temperature to 900 °C at the rate of 10 °C/min with a small flow rate of N₂ and then held constant for 30 min to get a stable temperature. Then the required gas composition (CO₂/H₂/N₂) in the reaction mixture was adjusted and fed to the reactor system.

Fig. 5-11 shows the conversion of CO₂ obtained over time on stream of the reaction mixture. At such a high temperature of 900 °C, the CO₂ is practically only converted by the reverse water gas shift reaction and CO is the main product. On the first day of time on stream, the catalyst showed some deactivation where CO₂ conversion decreased from 68% to 66% in 8 h. After that the catalyst was cooled to 300 °C and kept constant overnight. No deactivation was observed on further time on stream, but a small loss in catalyst activity during heating and cooling cycle was observed which may be due to surface modifications.

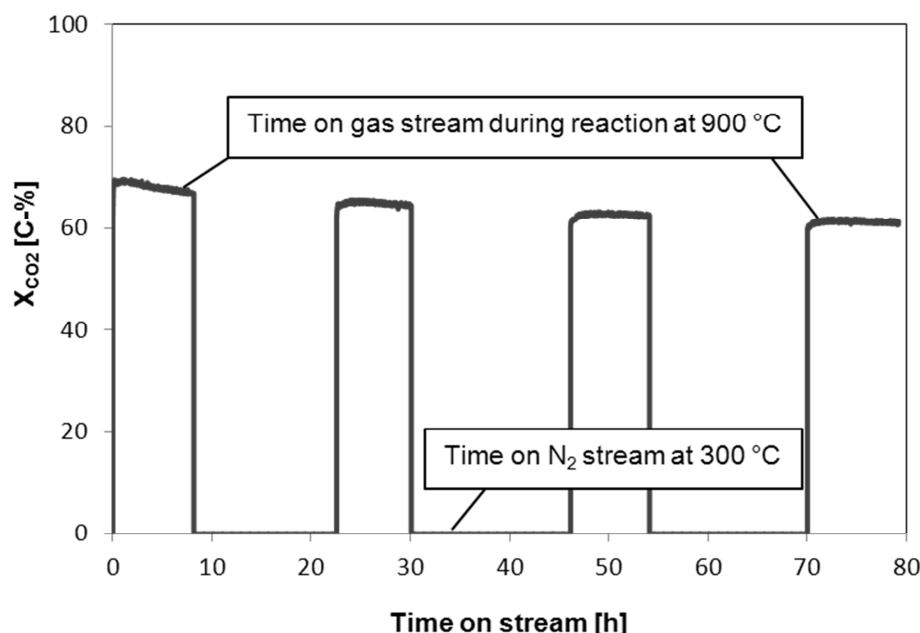


Fig. 5-11: Conversion of CO₂ versus time on stream at 900 °C in CO₂ hydrogenation (p = 1 atm, m_{cat} = 1.2 g, catalyst = Ni/Al₁₂O₁₉, d_p = 6 mm, y_{CO2} = 11 vol.-%, y_{H2} = 66 vol.-%, rest N₂, gas flow rate = 138 l/h (NTP)).

5.1.7 Kinetic analysis of the RWGS on the Ni catalyst

Intrinsic kinetics

For the kinetic analysis, the concentrations of CO₂ and H₂ were varied (Fig. 5-12 and Fig. 5-13). The temperature was kept low (340 °C) to avoid an influence of mass transport on the effective reaction rate, which then equals the intrinsic rate.

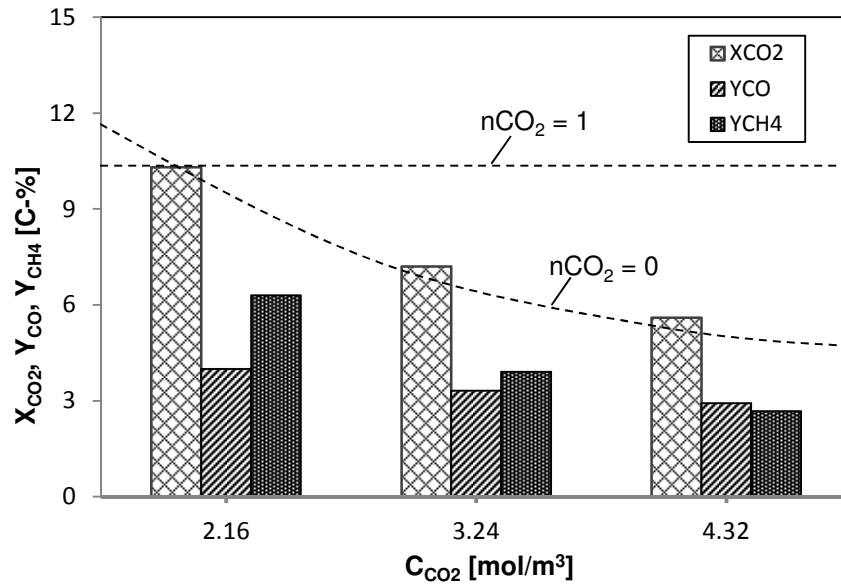


Fig. 5-12: Effect of CO_2 concentration on the CO_2 conversion and the CO and CH_4 yield in CO_2 hydrogenation ($T = 340\text{ }^\circ\text{C}$, $p = 1\text{ atm}$, $m_{cat} = 1.2\text{ g}$, catalyst = $Ni/Al_{12}O_{19}$, $d_p = 6\text{ mm}$, $y_{H_2} = 66\text{ vol.-%}$, $y_{CO_2} = 11 - 22\text{ vol.-%}$, $N_2 =$ remaining proportion, gas flow rate = 48 l/h (NTP)).

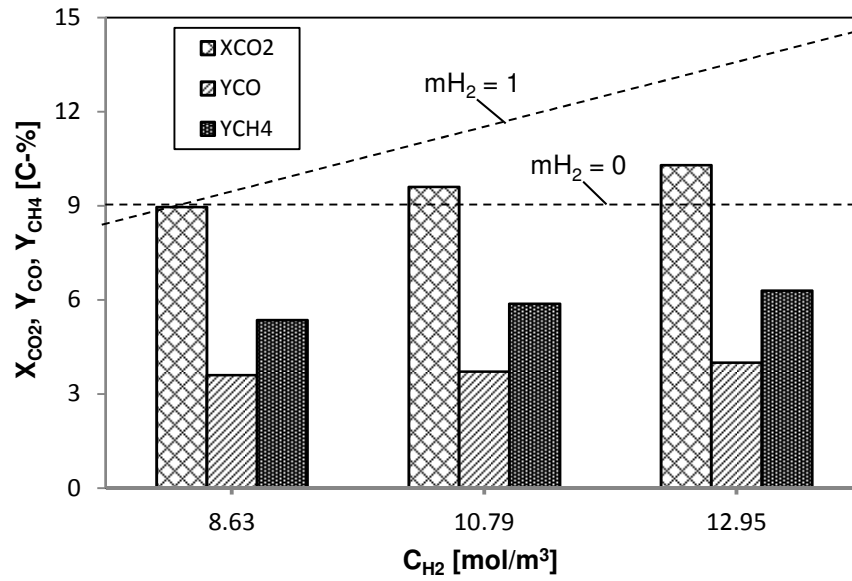


Fig. 5-13: Effect of H_2 concentration on the CO_2 conversion and the CO and CH_4 yield in CO_2 hydrogenation ($T = 340\text{ }^\circ\text{C}$, $p = 1\text{ atm}$, $m_{cat} = 1.2\text{ g}$, catalyst = $Ni/Al_{12}O_{19}$, $d_p = 6\text{ mm}$, $y_{H_2} = 44 - 66\text{ vol.-%}$, $y_{CO_2} = 11\text{ vol.-%}$, $N_2 =$ remaining proportion, gas flow rate = 48 l/h (NTP)).

The reaction order with respect to each reactant can be determined by using the following equation:

$$X_{CO_2} = 1 - \{k_{m,CO_2} \tau_m C_{H_2}^m (n-1) C_{CO_2}^{n-1} + 1\}^{\frac{1}{1-n}} \quad (5.1)$$

Fig. 5-14 shows the plot of X_{CO_2} versus C_{CO_2} . The order was calculated by the integral method i.e. the value of the reaction order was determined by the best fit to the measured data. For the experimental conditions used, the reaction order of CO_2 is 0.1.

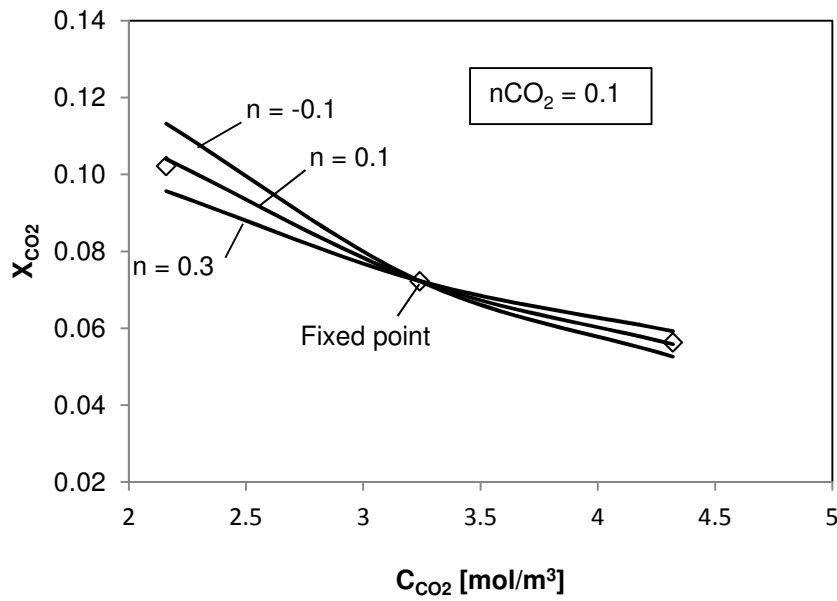


Fig. 5-14: Dependence of CO_2 conversion upon CO_2 concentration ($T = 340\text{ }^\circ\text{C}$, $p = 1\text{ atm}$, $m_{cat} = 1.2\text{ g}$, catalyst = $Ni/Al_{12}O_{19}$, $d_p = 6\text{ mm}$, $y_{CO_2} = 11 - 22\text{ vol.-%}$, $y_{H_2} = 66\text{ vol.-%}$, $N_2 = \text{remaining proportion}$, gas flow rate = 48 l/h (NTP)).

Similarly, the reaction order with respect to hydrogen was determined (Fig. 5-15), which leads to a value of 0.4. The reaction rate and the reaction rate constant of CO_2 hydrogenation was calculated by using Eq. (4.6) and Eq. (4.7), respectively.

The Arrhenius plot is shown in Fig. 5-16. Only the values of k_{m,CO_2} for $T < 410\text{ }^\circ\text{C}$ are included, because then the reaction rate is solely determined by the intrinsic kinetics. Above this temperature, the reaction rate is then also controlled by mass transport limitations.

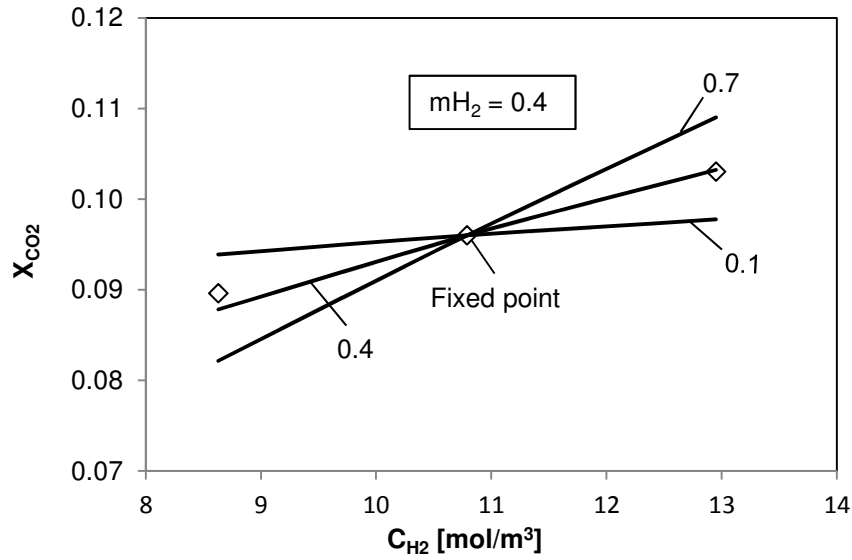


Fig. 5-15: Dependence of CO₂ conversion upon H₂ concentration (T = 340 °C, p = 1 atm, m_{cat} = 1.2 g, catalyst = Ni/Al₁₂O₁₉, d_p = 6 mm, y_{H2} = 44 – 66 vol.-%, y_{CO2} = 11 vol.-%, N₂ = remaining proportion, gas flow rate = 48 l/h (NTP)).

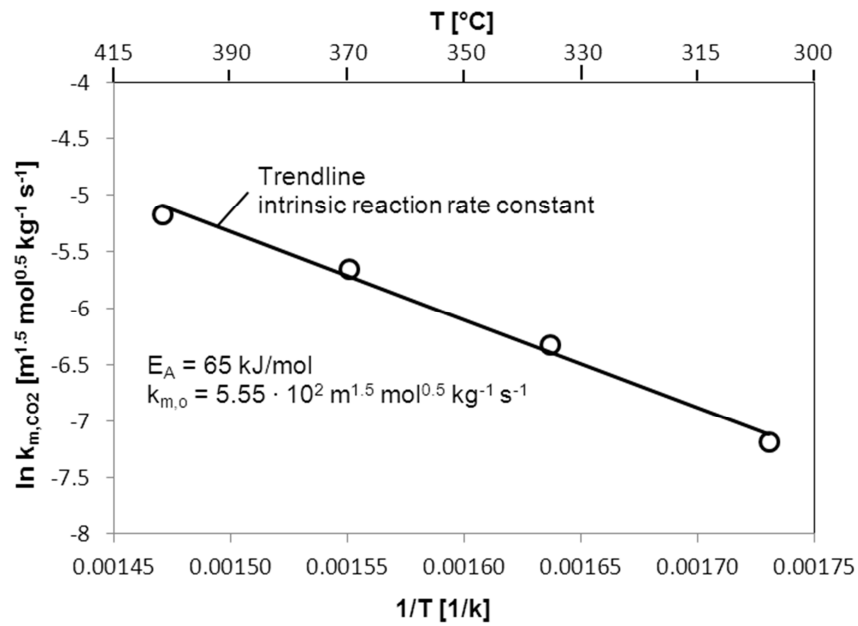


Fig. 5-16: Arrhenius plot (1/T versus ln k_{m,CO2}) for CO₂ conversion (p = 1 atm, m_{cat} = 1.2 g, catalyst = Ni/Al₁₂O₁₉, d_p = 6 mm, y_{H2} = 66 vol.-%, y_{CO2} = 11 vol.-%, rest N₂, gas flow rate = 138 l/h (NTP)).

The frequency factor and activation energy (Fig. 5-16) are $5.55 \cdot 10^2 \text{ m}^{1.5} \text{ mol}^{0.5} \text{ kg}^{-1} \text{ s}^{-1}$ and 65 kJ/mol, respectively. The value of E_A (65 kJ/mol) obtained in this study is within the range found by other authors for CO₂ hydrogenation reaction over Ni catalysts (Table 5-1).

Table 5-1: Activation energies reported for CO₂ hydrogenation on nickel catalysts.

| Catalyst | Temperature (°C) | Pressure (atm) | E _A (kJ/mol) | References |
|--|------------------|----------------|-------------------------|------------|
| 75.3-84.6% Rany Ni | 160 – 270 | 1 | 88 – 91 | [33] |
| 20% Ni/Al ₂ O ₃ | 250 – 400 | 1 | 87 | [76] |
| 3% Ni/SiO ₂ | 227 – 277 | 1 | 81 | [87] |
| 59% Ni-88 | 283 – 397 | 2 – 30 | 58 – 55 | [88] |
| 58% Ni-104 | 277 – 318 | 6 – 18 | 61 | [89] |
| 33.6% Ni (G-65) | 200 – 230 | 1 | 106 | [90] |
| 42% NiO/Al ₂ O ₃ | 210 – 315 | 1 | 80 – 92 | [91] |
| 11% Ni (G.90-B) | 305 – 410 | 1 | 65 | This work |

Influence of internal mass transport (pore diffusion)

The pore diffusion limitations were determined for both the shell and non-shell catalyst (homogeneous material). The model parameters required in the calculation of the effective reaction rate are given in Table 5-2.

The effective rate of chemical reaction is given as:

$$r_{m,CO_2,eff} = \eta r_{m,CO_2} \quad (5.2)$$

The Thiele modulus for an irreversible, isothermal, nth order reaction and for the spherical particle of 0.5 mm and 6 mm diameter (non-shell catalyst) was calculated by using Eq. (4.12) while for the shell catalyst Eq. (4.17) was used. The effectiveness factor as a function of the Thiele modulus was determined by Eq. (4.11).

The Knudsen diffusion coefficient $D_{CO_2,knu}$ was calculated by using Eq. (4.16) and the combined pore diffusion coefficient $D_{CO_2,pore}$ was calculated by using Eq. (4.15). The diffusion coefficient of CO₂ in the catalyst pore at 500 °C and 1 bar is shown in Fig. 5-17. For the average pore diameter of 230 nm, the diffusion of CO₂ in the pores of the Ni catalyst is determined by both Knudsen and molecular diffusion (transition area). The Knudsen

diffusion dominates the transport phenomenon at pore diameter of less than 100 nm while molecular diffusion dominates above the pore diameter of 10000 nm.

Table 5-2: Model parameters used for the calculation of effective reaction rate of CO₂ hydrogenation over Ni catalyst (p = 1 atm).

| Parameters | Values |
|---|--|
| Frequency factor ($k_{m,0}$) | $5.55 \cdot 10^2 \text{ m}^{1.5} \text{ mol}^{0.5} \text{ kg}^{-1} \text{ s}^{-1}$ |
| Activation energy (E_A) | 65 kJ/mol |
| Particle density (ρ_p) | 1910 kg/m ³ |
| Porosity of particle (ε_p) | 0.33 |
| Tortuosity of particle τ_p (assumption) | 1.6 |
| Molecular diffusion coefficient ($D_{\text{CO}_2,\text{mol}}$) at 773 K | $1.83 \cdot 10^{-4} \text{ m}^2/\text{s}$ |
| Knudsen diffusion coefficient ($D_{\text{CO}_2,\text{knu}}$) at 773 K | $4.68 \cdot 10^{-5} \text{ m}^2/\text{s}$ |
| Pore diffusion coefficient ($D_{\text{CO}_2,\text{pore}}$) at 773 K | $3.72 \cdot 10^{-5} \text{ m}^2/\text{s}$ |
| Kinematic viscosity of CO ₂ (ν_{CO_2}) at 773 K | $1.63 \cdot 10^{-4} \text{ m}^2/\text{s}$ |

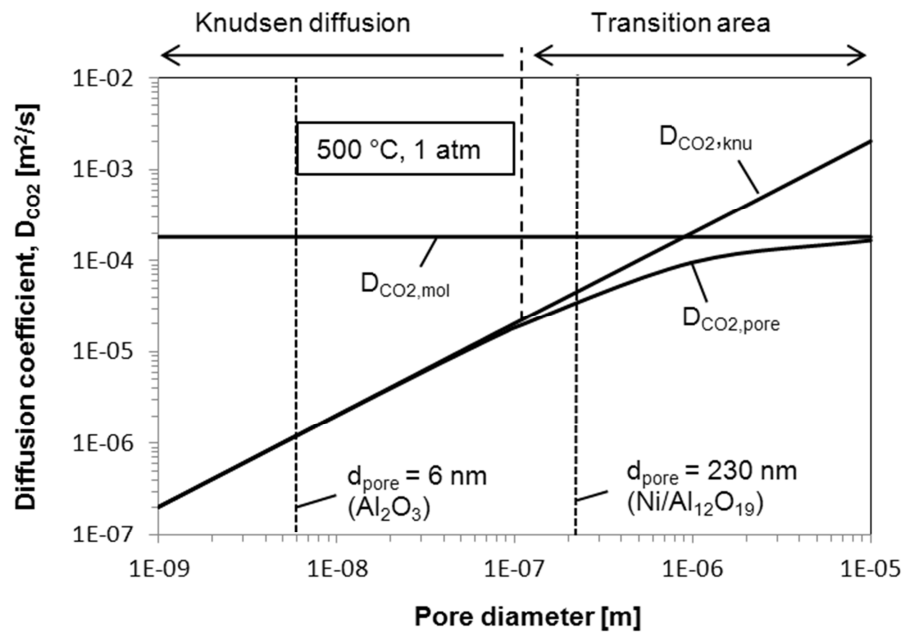


Fig. 5-17: Diffusion coefficient of CO₂ in the pores of the Ni/Al₁₂O₁₉ and Al₂O₃ catalysts determined at 500 °C and 1 bar.

The plot of the effectiveness factor versus temperature is shown in Fig. 5-18. Internal mass transfer resistance in the catalyst pores is not negligible for $T > 400$ °C even for the shell catalyst with 0.5 mm shell thickness of active material (Ni).

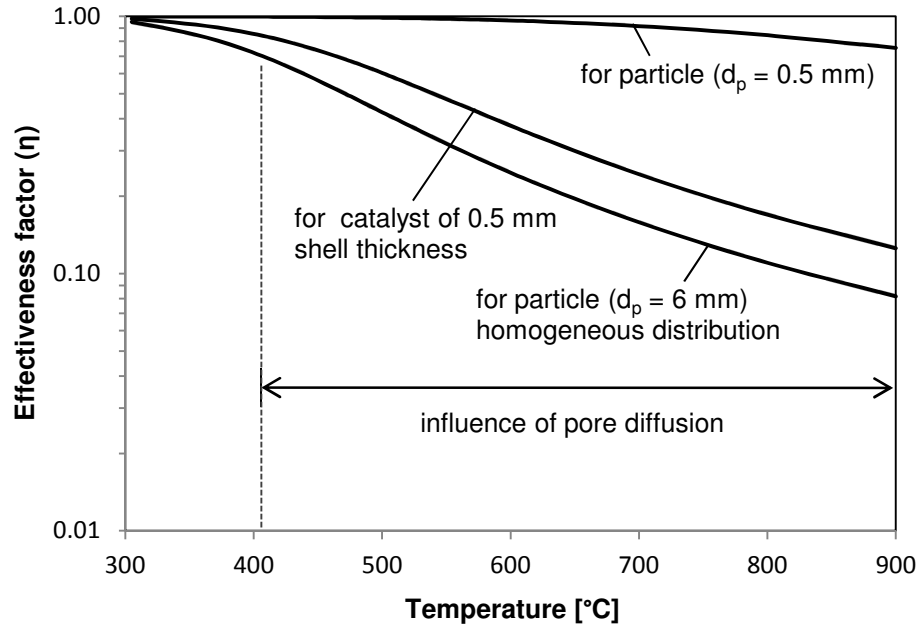


Fig. 5-18: Effectiveness factor for catalyst particle versus temperature ($p = 1$ atm, catalyst = Ni/Al₂O₃, $y_{\text{CO}_2} = 11$ vol.-%, $y_{\text{H}_2} = 66$ vol.-%, rest N₂, gas flow rate = 138 l/h (NTP)).

Influence of external mass transport (boundary layer diffusion)

To determine the influence of film diffusion, the effective reaction rate $r_{m,\text{CO}_2,\text{eff}}$ as a function of external mass transfer coefficient β and external surface area per mass of the catalyst $A_{m,\text{ext}}$ has been calculated by Eq. (4.21). All the calculations for the external mass transfer coefficient (β), external surface area of the catalyst ($A_{m,\text{ext}}$), Sherwood number (Sh), Reynolds number (Re), and Schmidt number (Sc) are given in section 4.4.1.4. The effective reaction rate due to the combined influence of internal and external mass transport is calculated as:

$$r_{m,\text{eff}} = \left[\frac{1}{\eta k_{m,\text{CO}_2} C_{\text{CO}_2}^{0.1} C_{\text{H}_2}^{0.4}} + \frac{1}{\beta A_{m,\text{ext}} (C_{\text{CO}_2} - C_{\text{CO}_2,\text{eq}})} \right]^{-1} \quad (5.3)$$

Fig. 5-19 shows a good agreement of the calculations and the measurements for the used shell catalyst. It also reveals that for the hypothetical case of a non-shell catalyst (particle

diameter of 6 mm) the effective reaction rate is lower than for the shell catalyst. For a very small particle size ($d_p = 0.5$ mm) the effective reaction rate is only influenced by pore diffusion at temperature above 700 °C while no influence of external mass transport was observed in the studied range of temperature (not shown here). Considering $\eta = 1$ in Eq. (5.3) enables to separate the kinetic limitation from internal mass transfer limitation. In Fig. 5-19, the effective reaction rate without internal mass transfer limitation differs significantly from the effective reaction rate with internal mass transport limitation for the shell catalyst as well as for the non-shell catalyst of 6 mm particle diameter. Fig. 5-19 shows that the shell catalyst operates in a mixed regime with both internal and external mass transfer. The catalyst performance is more and more controlled by external mass transfer above a temperature of about 900 °C.

Note that Eq. (5.3) is only an approximation because of two reasons:

- The reverse reaction ($\text{CO} + \text{H}_2\text{O} \rightarrow \text{CO}_2 + \text{H}_2$) is not considered in the pore diffusion term.
- For the external mass transfer, the equilibrium concentration is assumed at the external surface. In reality, this value is higher and only reached, if the chemical reaction is very fast.

Eq. (5.3) is therefore only exact if only pore diffusion or only external mass transfer plays a role. For the regime in between these two extremes, Eq. (5.3) is only a hopefully good approximation.

Furthermore, in Fig. 5-19, intrinsic rate of the chemical reaction (r_m) Eq. (4.6), the reaction rate for diffusion boundary layer ($r_{m,ext}$) Eq. (4.21), and the effective reaction rate due to internal and external mass transport ($r_{m,eff}$) Eq. (5.3) are shown. The effective reaction rates ($r_{m,eff} (calculated)$) were calculated based on the inlet concentrations while the measured values ($r_{m,eff} (measured)$) were calculated based on the conversion, inlet concentration, and mass of catalyst.

Note that for temperatures between about 500 °C and 900 °C, the equilibrium conversion is not 100% (see Fig. 2-13 for $R = 6$) and reaches a minimum value of around 75% at 600 °C. This was not considered for the calculations of $r_{m,eff}$ and was only included to calculate $r_{m,ext}$ ($= \beta A_{m,ext} (C_{\text{CO}_2} - C_{\text{CO}_2,eq})$).

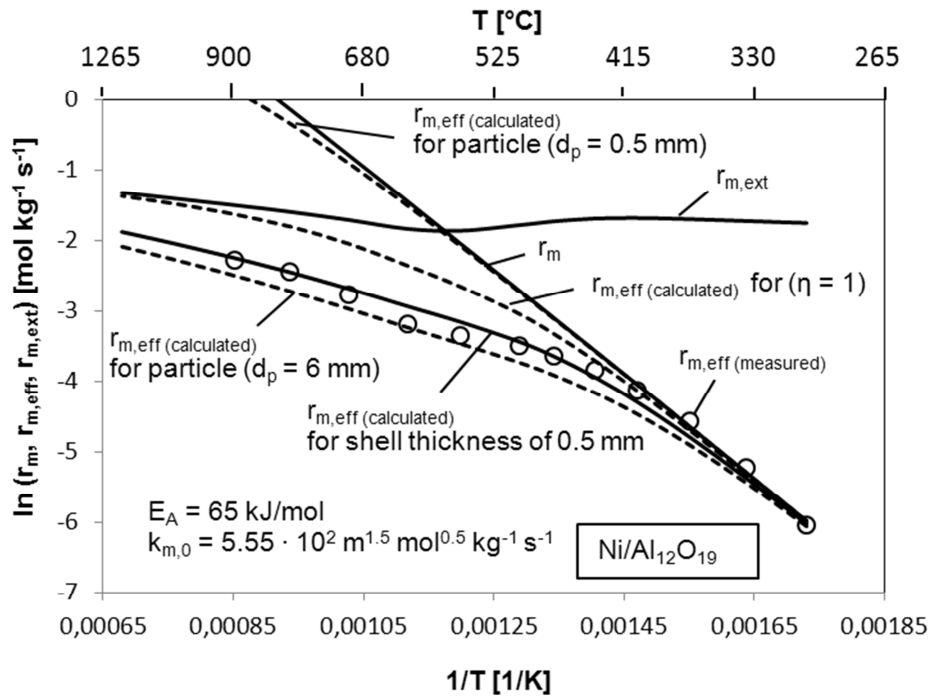


Fig. 5-19: Influence of internal and external mass transport on the effective reaction rate of CO₂ hydrogenation ($p = 1$ atm, $m_{\text{cat}} = 1.2$ g, catalyst = Ni/Al₁₂O₁₉, $d_p = 6$ mm, $y_{\text{CO}_2} = 11$ vol.-%, $y_{\text{H}_2} = 66$ vol.-%, rest N₂, gas flow rate = 138 l/h (NTP)).

5.1.8 Kinetic analysis of the RWGS on the Al₂O₃ catalyst

The reaction order with respect to CO₂ and H₂ is simplifying assumed to be first and zero order, respectively. For the determination of the intrinsic kinetics, only the values of k_{m,CO_2} for a temperature of less than 600 °C are included in the Arrhenius plot shown in Fig. 5-20. The activation energy and frequency factor are 72 kJ/mol and 40.9 mol kg⁻¹ s⁻¹, respectively.

The pore diffusion and film diffusion limitations for the Al₂O₃ catalyst (homogeneous material) were determined by using the same equation as that of Ni catalyst for a first order irreversible reaction (section 5.1.7). The model parameters required for the calculation of the effective reaction rate over Al₂O₃ catalyst are given in Table 5-3. The diffusion coefficient of CO₂ in the catalyst pores of the Al₂O₃ was determined at 500 °C and 1 bar (see Fig. 5-17). For 6 nm average pore diameter, the diffusion of CO₂ in the pores of the Al₂O₃ catalyst is only determined by Knudsen diffusion.

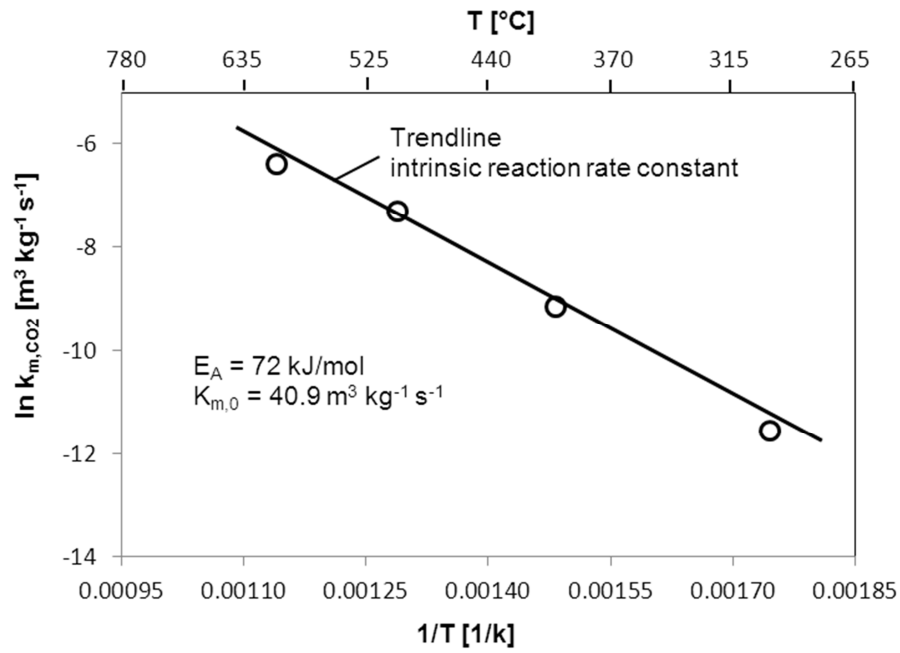


Fig. 5-20: Arrhenius plot ($1/T$ versus $\ln k_{m,CO_2}$) for CO_2 conversion by RWGS ($p = 1$ atm, $m_{cat} = 10$ g, catalyst = Al_2O_3 , $d_p = 2$ mm, $y_{H_2} = 66$ vol.-%, $y_{CO_2} = 11$ vol.-%, rest N_2 , gas flow rate = 48 l/h (NTP)).

Table 5-3: Model parameters used for the calculation of effective reaction rate of CO_2 hydrogenation over Al_2O_3 catalyst ($p = 1$ atm).

| Parameters | Values |
|---|---|
| Frequency factor ($k_{m,0}$) | $40.9 \text{ m}^3 \text{ kg}^{-1} \text{ s}^{-1}$ |
| Activation energy (E_A) | 72 kJ/mol |
| Particle density (ρ_p) | 1450 kg/m^3 |
| Porosity of particle (ε_p) | 0.4 |
| Tortuosity of particle (τ_p) | 2.8 |
| Molecular diffusion coefficient ($D_{CO_2,mol}$) at 773 K | $1.83 \cdot 10^{-4} \text{ m}^2/\text{s}$ |
| Knudsen diffusion coefficient ($D_{CO_2,knu}$) at 773 K | $1.2 \cdot 10^{-6} \text{ m}^2/\text{s}$ |
| Pore diffusion coefficient ($D_{CO_2,pore}$) at 773 K | $1.21 \cdot 10^{-6} \text{ m}^2/\text{s}$ |
| Kinematic viscosity of CO_2 (ν_{CO_2}) at 773 K | $1.63 \cdot 10^{-4} \text{ m}^2/\text{s}$ |

In the calculation of the effective reaction rate methane formation is not considered. Fig. 5-21 shows a good agreement of the calculation with the measurements of the effective reaction rate constant of CO₂ hydrogenation over the Al₂O₃ catalyst. It also reveals that for the used Al₂O₃ catalyst, the effective reaction rate is only influenced by pore diffusion and no influence of external mass transport was observed in the studied range of temperature. For a particle diameter of 2 mm (as used in the experiments), pore diffusion limitations start at a temperature above 600 °C, while for a 6 mm particle diameter (shown for comparison as this is the diameter of the Ni catalyst), pore diffusion limitations start above 400 °C.

The comparison of the effective reaction rate of CO₂ hydrogenation on the 6 mm particle diameter of the Ni and Al₂O₃ catalyst is shown in Fig. 5-22. It reveals that the effective reaction rate over Ni (shell catalyst) is about 40 times compared to the Al₂O₃ (non-shell) catalyst.

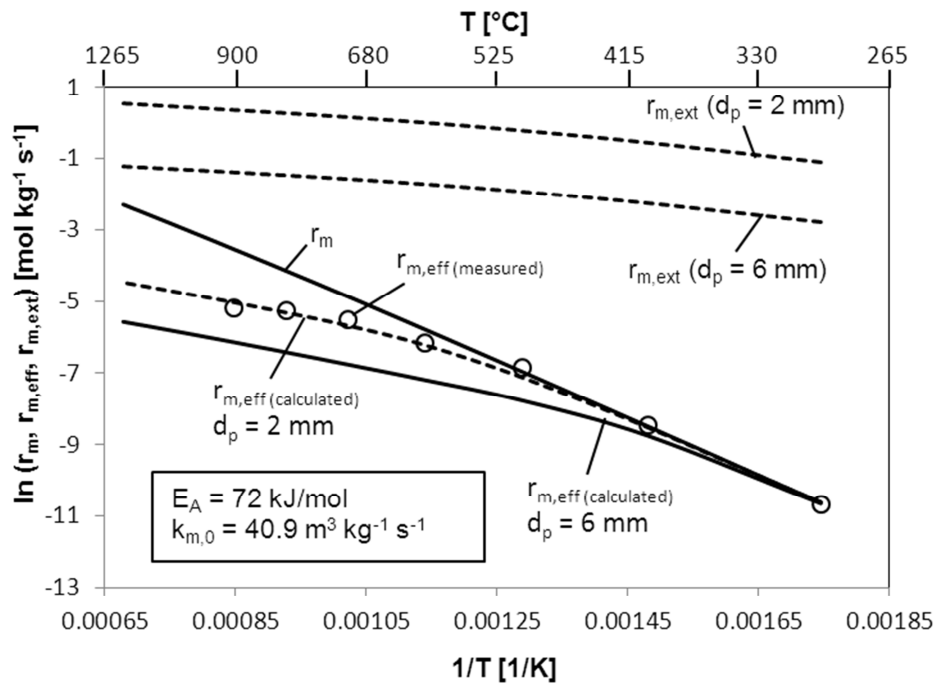


Fig. 5-21: Influence of internal and external mass transport on the effective reaction rate of CO₂ hydrogenation ($p = 1$ atm, $m_{\text{cat}} = 10$ g, catalyst = Al₂O₃, $d_p = 2$ mm, $y_{\text{CO}_2} = 11$ vol.-%, $y_{\text{H}_2} = 66$ vol.-%, rest N₂, gas flow rate = 48 l/h (NTP)).

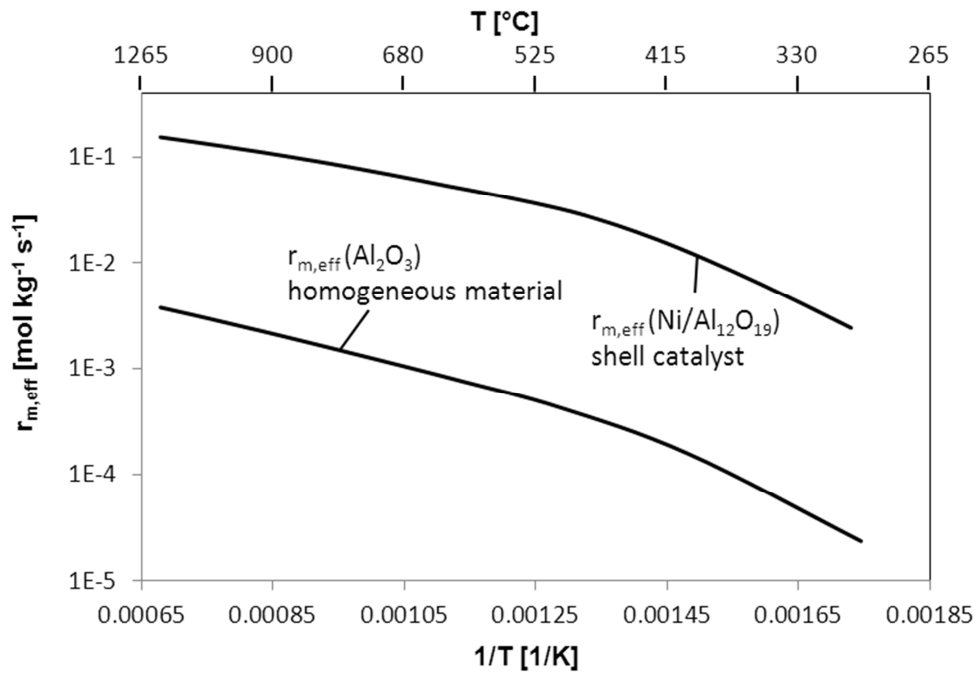


Fig. 5-22: Comparison of the effective reaction rate of CO₂ hydrogenation over Ni and Al₂O₃ catalyst ($p = 1$ atm, $d_p = 6$ mm, $y_{\text{CO}_2} = 11$ vol.-%, $y_{\text{H}_2} = 66$ vol.-%, rest N₂).

5.1.9 Comparison of catalysts activity and yield of CO and CH₄ (CO₂ hydrogenation)

The activity of various commercial catalysts for CO₂ hydrogenation was studied in the same tubular down-flow fixed bed quartz reactor. The measurements were carried out at two different temperatures of 500 and 700 °C and gas flow rates of 48 and 138 l/h (NTP) using 2 g catalyst. Table 5-4 shows the performance of the catalysts in terms of conversion of CO₂ and the yield of products (CO and CH₄). The characteristic data for the Ni catalyst are given in Table 4-1 and for all other catalysts in Appendix B.3.

Prior to the experimental study, Cr₂O₃/Al₂O₃ and ZnO/CuO/Al₂O₃ catalysts were reduced at 500 °C overnight under the gas flowrate of 10 l/h containing 50% H₂ in N₂ while Al₂O₃ and NiO/Al₁₂O₁₉ were treated at 800 °C overnight. After the reduction, the reaction gas mixture containing H₂/CO₂ ratio of 6 with 23% of N₂ was passed through the reactor and the products were analyzed using online gas analyzer.

Table 5-4: Conversion of CO₂ and yield of CO and CH₄ over various catalysts (p = 1 atm, m_{cat} = 2 g, y_{CO2} = 11 vol.-%, y_{H2} = 66 vol.-%, rest N₂).

| Catalyst | Temp, °C | Gas flow, l/h | d _p , mm | X _{CO2} , % | Y _{CO} , % | Y _{CH4} , % |
|--|----------|---------------|---------------------|----------------------|---------------------|----------------------|
| Cr ₂ O ₃ /Al ₂ O ₃ | 500 | 138 | 1 – 3 | 3.9 | 3.9 | - |
| | 700 | 138 | 1 – 3 | 13.1 | 13.1 | - |
| | 700 | 48 | 1 – 3 | 25.7 | 25.7 | - |
| ZnO/CuO/Al ₂ O ₃ | 500 | 138 | 1 – 3 | 8.1 | 8.1 | - |
| | 700 | 138 | 1 – 3 | 32.7 | 32.7 | - |
| | 700 | 48 | 1 – 3 | 51.7 | 51.7 | - |
| γ-Al ₂ O ₃ | 500 | 138 | 1 – 3 | 1.2 | 1.2 | - |
| | 700 | 138 | 1 – 3 | 12.1 | 12.1 | - |
| | 700 | 48 | 1 – 3 | 20 | 20 | - |
| NiO/Al ₁₂ O ₁₉ (G.90-B) | 500 | 138 | 5 – 7 | 44.5 | 14.5 | 30 |
| | 700 | 138 | 5 – 7 | 60.5 | 55.2 | 5.3 |
| | 700 | 48 | 5 – 7 | 74.6 | 68.4 | 6.2 |

For all catalysts, the conversion of CO₂ increases with temperature while it decreases with increasing total gas flow rate (decreasing residence time). As compared to all other catalysts, the activity of Ni/Al₁₂O₁₉ is very high but it produces CH₄ along with CO as a product (see Table 5-4). The yield of CH₄ decreases and the CO yield increases with temperature. For example, the yield of methane decreased from 30% to 5.3% and yield of CO increased from 14.6 to 55.2% when the temperature was increased from 500 °C to 700 °C at 138 l/h. All other catalysts produced only CO and H₂O. In comparison, ZnO/CuO/Al₂O₃ catalyst also showed good activity but it is less stable at temperatures above 700 °C. The highest conversion of CO₂ and thus yield of CO obtained over ZnO/CuO/Al₂O₃ catalyst was 51.7% at 700 °C and a gas flow rate of 48 l/h. The γ-Al₂O₃ used in the experiment is not inert and acts as a catalyst at high temperature. The conversion of CO₂ obtained over γ-Al₂O₃ was 20% at 700 °C and a gas flow rate of 48 l/h.

5.2 CO hydrogenation (methanation) reaction

The CO methanation ($\text{CO} + 3\text{H}_2 \rightarrow \text{CH}_4 + \text{H}_2\text{O}$) as a consecutive reaction in CO_2 hydrogenation was carried out in the same fixed bed quartz reactor in a wide temperature range (300 – 800 °C) at atmospheric pressure. In this section the reaction kinetic as well as influence of mass transport on the effective reaction rate of CO hydrogenation is described.

5.2.1 Effect of reaction temperature on methanation

The same Ni catalyst applied in CO_2 hydrogenation was continued for CO hydrogenation. Fig. 5-23 shows the conversion of CO and the yield of CH_4 and CO_2 . In CO hydrogenation, main products were CH_4 and CO_2 and no other hydrocarbons were observed. CH_4 is formed by direct CO methanation reaction ($\text{CO} + 3\text{H}_2 \rightarrow \text{CH}_4 + \text{H}_2\text{O}$) probably via dissociation of CO to intermediate carbon species [33, 58]. However, CO_2 can be produced either by CO disproportionation ($2\text{CO} \rightarrow \text{C} + \text{CO}_2$) and/or water gas shift reaction in presence of catalyst ($\text{CO} + \text{H}_2\text{O} \rightarrow \text{CO}_2 + \text{H}_2$) [92, 93].

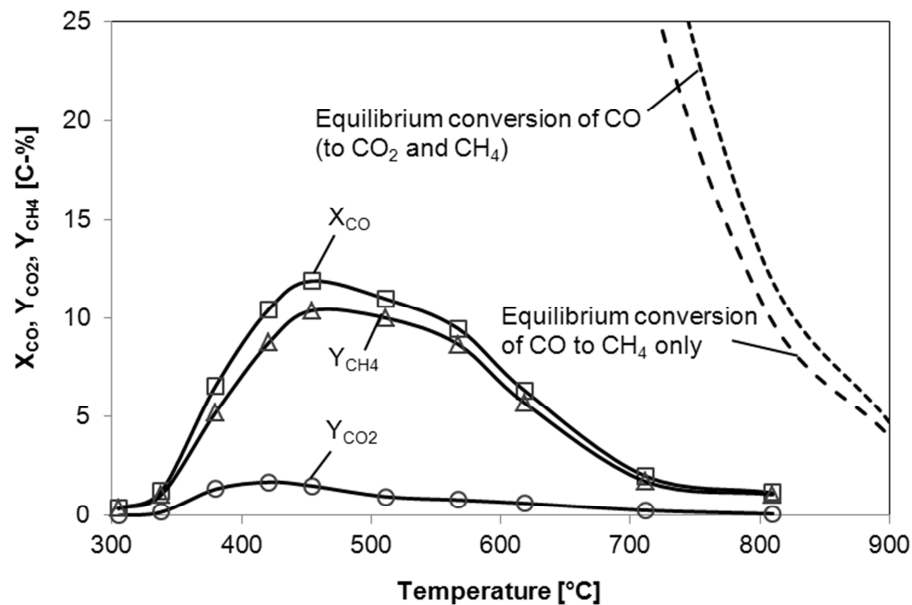


Fig. 5-23: CO conversion and the yield of CO_2 and CH_4 versus temperature in CO hydrogenation ($p = 1$ atm, $m_{\text{cat}} = 1.2$ g, catalyst = Ni/ $\text{Al}_{12}\text{O}_{19}$, $d_p = 6$ mm, $y_{\text{H}_2} = 66$ vol.-%, $y_{\text{CO}} = 11$ vol.-%, rest N_2 , gas flow rate = 138 l/h (NTP)).

The CO methanation is an exothermic reaction which is favorable at low temperatures. In the low temperature range, the conversion of CO and the yield of CH_4 and CO_2 increases

with temperature until about 450 °C are reached. No catalyst deactivation was observed. In the low temperature range, the reaction is controlled kinetically and no coke formation took place. At low temperatures (below 450 °C) a small amount of CO₂ was produced by the water gas shift reaction [93]. At a very high temperature of about 800 °C, also no catalyst deactivation was observed, but the coke formed in the temperature range of 480 to 710 °C may not completely gasified at 800 °C, and therefore the conversion of CO was low and far from equilibrium. The decrease in conversion due to the catalyst deactivation over time on stream is shown below (see section 5.2.2 (Fig. 5-26)).

The coke formation may occur via Boudouard reaction ($2\text{CO} \rightleftharpoons \text{C} + \text{CO}_2$) which is related to CO dissociation activity in CO hydrogenation [94] and/or direct carbon monoxide hydrogenation ($\text{CO} + \text{H}_2 \rightleftharpoons \text{C} + \text{H}_2\text{O}$) over the Ni catalyst [95]. Fig. 5-24 shows the equilibrium conversion of CO over the temperature by both Boudouard reaction and direct CO hydrogenation. At high temperatures both reactions are limited thermodynamically.

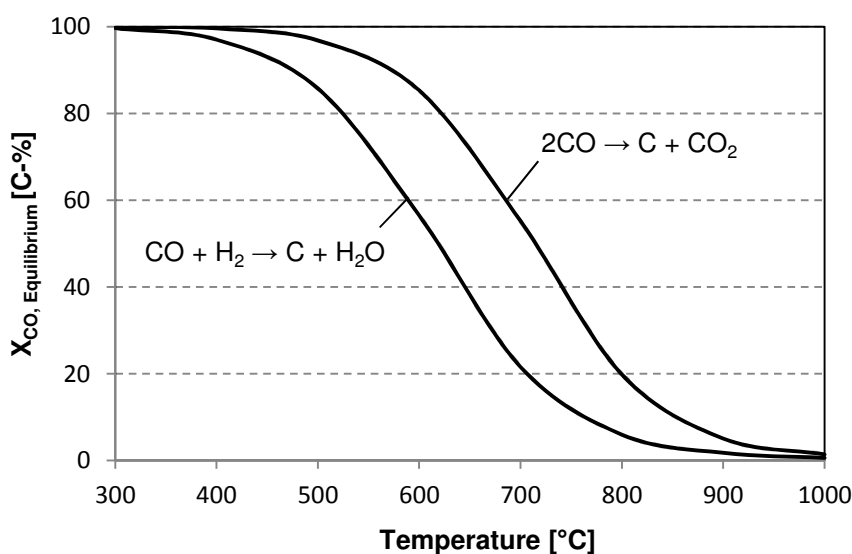


Fig. 5-24: The equilibrium conversion of CO in the Boudouard reaction (CO = 1 mole) and direct hydrogenation reaction (H₂/CO = 1) as function of temperature and at atmospheric pressure.

5.2.2 Stability of the Ni catalyst in CO methanation

Fig. 5-25 shows time on stream behaviour of the Ni catalyst for the CO conversion and the yield of CO₂ and CH₄ (450 °C, atmospheric pressure). The maximum deactivation of the

catalysts occurs generally in the initial stage of the reaction [93, 96]. In this experiment, no deactivation was observed in 2 h time on stream at 450 °C, and the steady state of reaction was reached within some minutes. When the temperature increased further (keeping all other conditions constant), the coke formation starts above 480 °C, where CO conversion decreases over time on stream in the temperature range of 480 to 710 °C (Fig. 5-26). For example, at 620 °C, the conversion of CO decreases from 7 to 6.3% in 100 min of reaction time. At the temperature of 710 and 810 °C, a small increase in conversion over time on stream was observed which may be due to the gasification of coke formed in the temperature range of 480 to 710°C.

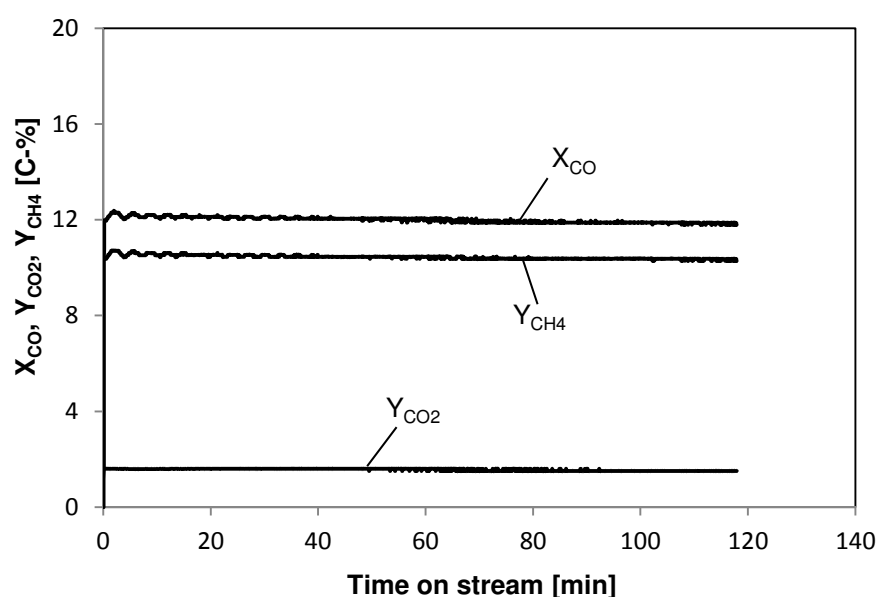


Fig. 5-25: CO conversion and the yield of CO₂ and CH₄ versus time on stream in CO hydrogenation (T = 450 °C, p = 1 atm, m_{cat} = 1.2 g, d_p = 6 mm, y_{H2} = 66 vol.-%, y_{CO} = 11 vol.-%, rest N₂, catalyst = Ni/Al₁₂O₁₉, gas flow rate = 138 l/h (NTP)).

After the completion of the experiment at 810 °C, the reactor temperature was decreased to 300 °C in the presence of small N₂ stream. Then the reactor temperature was increased again from 300 to 700 °C at the rate of 10 °C/min by adding 10% O₂ in N₂. The presence of CO and CO₂ species in the outlet gas stream during the oxidation of catalyst shows that the coke formed was not completely gasified at 810 °C.

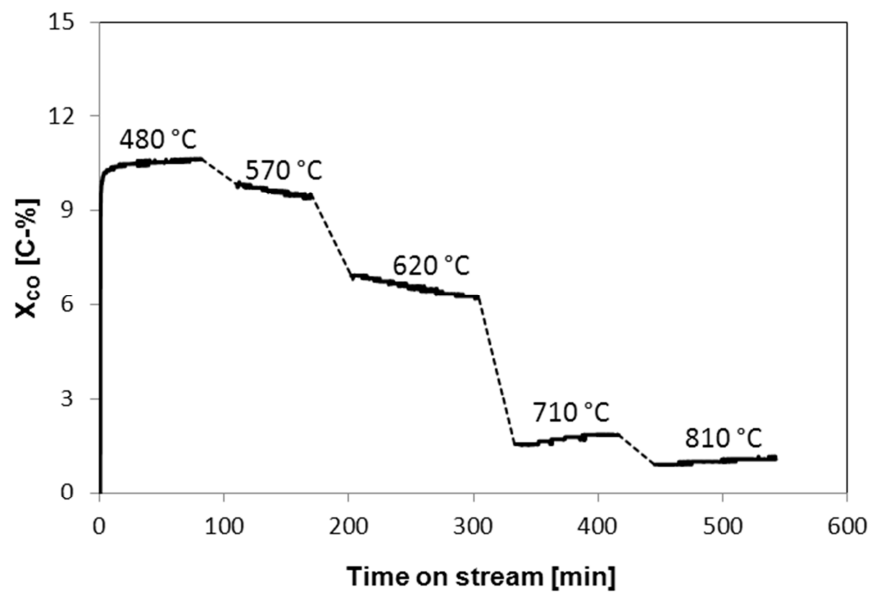


Fig. 5-26: Time on stream stability of catalyst in CO hydrogenation at different temperature ($p = 1$ atm, $m_{cat} = 1.2$ g, catalyst = Ni/Al₁₂O₁₉, $d_p = 6$ mm, $y_{H_2} = 66$ vol.-%, $y_{CO} = 11$ vol.-%, rest N₂, gas flow rate = 138 l/h (NTP)).

5.2.3 Effect of residence time on methanation

The effect of the residence time on the conversion of CO and yield of CO₂ and CH₄ over temperature (300 – 800 °C) was studied at two different gas flow rates of 48 l/h and 138 l/h. In both cases, a similar trend for CO conversion as well as yield of CO₂ and CH₄ was obtained. In the low temperature range of 300 to 450 °C, methane production increases rapidly with temperature and the reaction is controlled kinetically. Above 450 °C, catalyst deactivation due to coke formation may also decrease CO conversion and the yield of CH₄.

At a temperature of about 800 °C and a low gas flow rate of 48 l/h, the conversion of CO almost reached equilibrium. The effect of the residence time on the catalyst performance at constant temperature is given below (section 5.2.4) in detail.

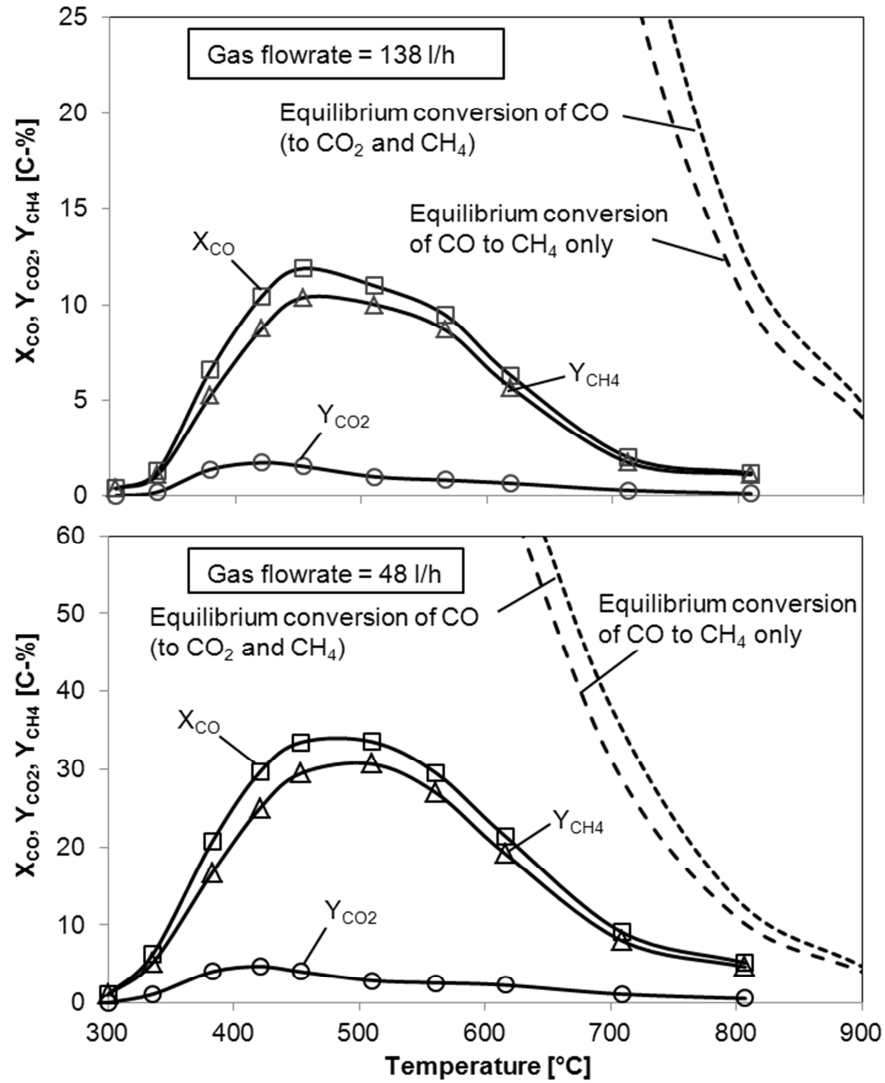


Fig. 5-27: CO conversion and CO₂ and CH₄ yield at different gas flow rate versus temperature in CO hydrogenation ($p = 1$ atm, catalyst = Ni/Al₂O₃, $d_p = 6$ mm, $m_{cat} = 1.2$ g, $y_{H_2} = 66$ vol.-%, $y_{CO} = 11$ vol.-%, rest N₂).

The effect of decrease in CO conversion with increasing temperature is not the result of the equilibrium (at least for $T < 700$ °C) and also not of a rather slow deactivation by coke formation (sees Fig. 5-26 and Fig. 5-27). Hence, the increase of the temperature obviously leads to a reversible deactivation of the catalyst for the methanation reaction. This strong shift in selectivity with temperature (less methane) was also found in case of CO₂ hydrogenation (Fig. 5-4).

It must be noted that the two experiments shown in Fig. 5-27 were done one after the other, i.e. the experiment with the lower flow rate (48 l/h) was done after the experiment with

138 l/h. In between these experiments, the catalyst was only oxidised (coke burn-off) and then reduced with H_2 (600 °C). In both experiments, the activity profile is similar. Hence, a high temperature does not lead an irreversible deactivation and only to a strong decrease of the CH_4 selectivity (for $T > 400$ °C). Whether and to what extent this selectivity shift is induced by the temperature and/or by the formation of coke is still an open question.

5.2.4 Effect of residence time at constant temperature

The influence of modified residence time on catalyst performance as well as on the yield of CO_2 and CH_4 was measured by varying the total gas flow rate at 405 °C and atmospheric pressure. As shown in Fig. 5-28, the conversion of CO and the yield of CH_4 and CO_2 increases with an increasing modified residence time.

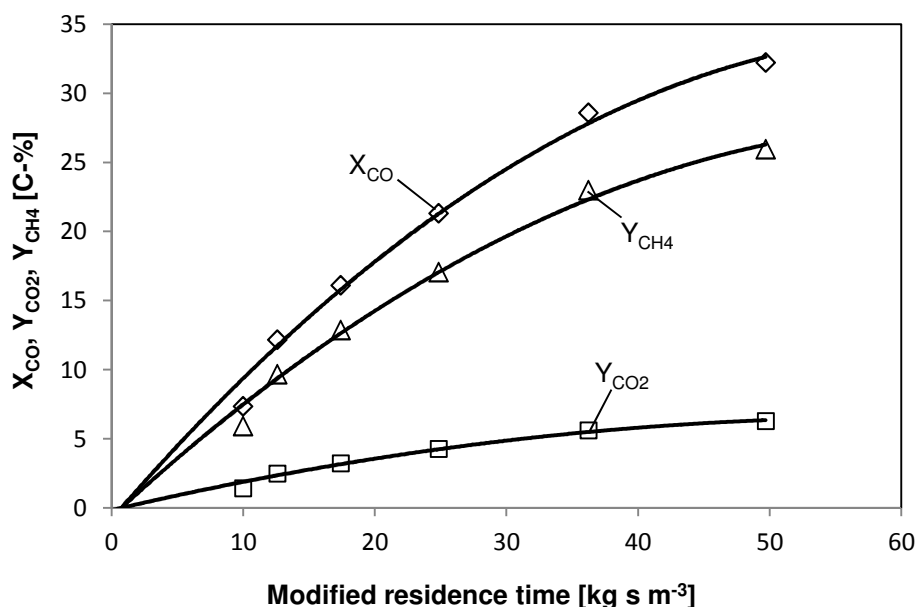


Fig. 5-28: Influence of modified residence time on CO conversion and yield of CO_2 and CH_4 in CO hydrogenation ($T = 405$ °C, $p = 1$ atm, $m_{cat} = 1.2$ g, $d_p = 6$ mm, catalyst = Ni/ $Al_{12}O_{19}$, $y_{H_2} = 66$ vol.-%, $y_{CO} = 11$ vol.-%, rest N_2).

Interestingly there was no influence of the modified residence time (and thus of the CO conversion) on the selectivity of CO_2 and CH_4 (Fig. 5-29). The extrapolation towards zero CO conversion at zero residence time resulted into no change in selectivity of CH_4 and CO_2 . Hence most probably, direct conversion of CO to CO_2 ($2CO + 2H_2 \rightarrow CO_2 + H_2O$) may take place (parallel to the CO methanation i.e. $CO + 3H_2 \rightarrow CH_4 + H_2O$). By comparing the

conversion data obtained for CO hydrogenation (Fig. 5-28) and for CO₂ hydrogenation (Fig. 5-7) at 405 °C, it is clear that the catalyst has a similar activity for CO and CO₂ hydrogenation, but less CH₄ and more CO are obtained in CO₂ hydrogenation compared to the CH₄ and CO₂ in the CO hydrogenation.

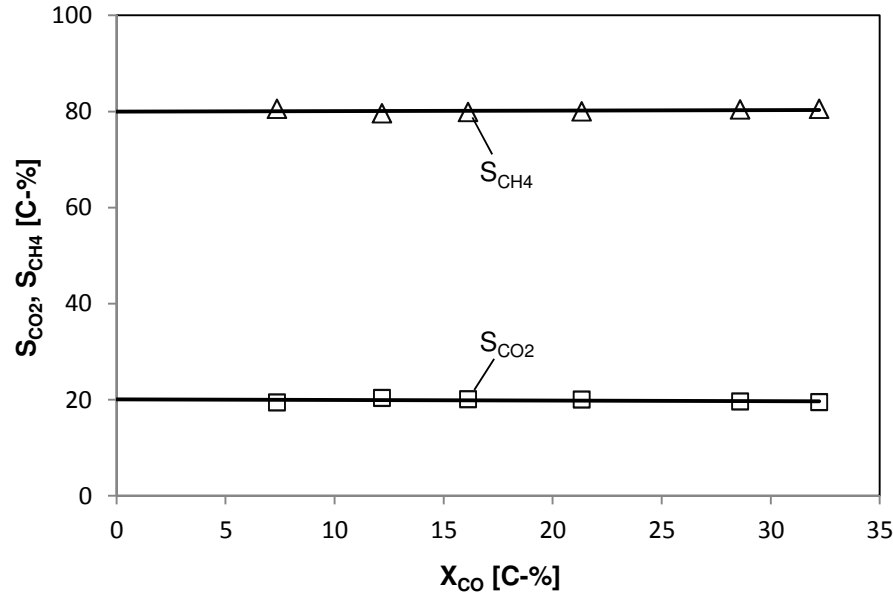


Fig. 5-29: CO conversion versus selectivity of CO₂ and CH₄ over Ni catalyst in CO hydrogenation ($T = 405$ °C, $p = 1$ atm, $\tau_m = 10 - 49.7$ kg s m⁻³, $m_{cat} = 1.2$ g, $d_p = 6$ mm, catalyst = Ni/Al₁₂O₁₉, $y_{H_2} = 66$ vol.-%, $y_{CO} = 11$ vol.-%, rest N₂).

5.2.5 Effect of catalyst particle size on methanation

The performance of the Ni catalyst for a particle diameter of less than 0.5 mm and 6 mm over the temperature is shown in Fig. 5-30. For both sizes of catalyst particles a similar trend of CO conversion and yield of CO₂ and CH₄ was obtained. The conversion of CO increases up to 450 °C and then continuously decreases due to the decrease of the methane selectivity by coke formation and/or increasing temperature.

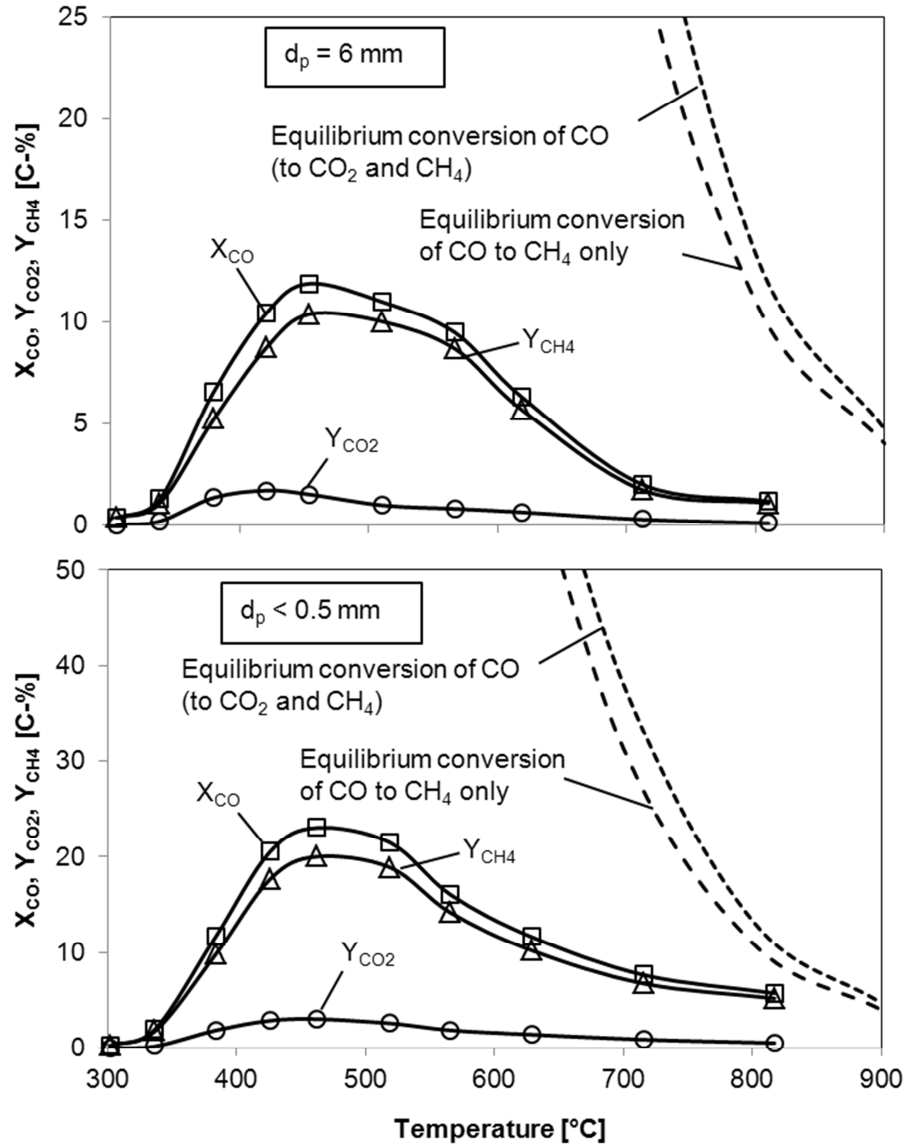


Fig. 5-30: CO conversion and CO₂ and CH₄ yield at different particle size of catalyst versus temperature in CO hydrogenation ($p = 1$ atm, $m_{cat} = 1.2$ g, catalyst = Ni/Al₁₂O₁₉, $y_{H_2} = 66$ vol.-%, $y_{CO} = 11$ vol.-%, rest N₂, gas flow rate = 138 l/h (NTP)).

The previously used catalyst particles of 6 mm diameter in CO₂ hydrogenation study were applied in this experiment. As mentioned in section 5.1.2, the long-time treatment of this catalyst at high temperature reduced its methanation activity. The 0.5 mm size catalyst particles applied in this experiment were used before only in the particle size effect study in CO₂ hydrogenation. Therefore the catalyst particles of 0.5 mm have a higher activity than the 6 mm particles. Due to this reason, in the low temperature kinetic regime a higher conversion of CO and a higher yield of CH₄ was obtained over 0.5 mm size catalyst. Hence,

the direct comparison of reaction rate over particle size with different treatment is not possible.

5.2.6 Kinetic analysis and influence of internal and external mass transfer on methanation

Intrinsic Kinetics

The influence of CO and H₂ concentrations on the methanation is shown in Fig. 5-31 and Fig. 5-32. To determine the reaction order with respect to each reactant, a similar equation that was already applied in CO₂ hydrogenation (Eq. (5.1)) was used:

$$X_{CO} = 1 - \{k_{m,CO} \tau_m C_{H_2}^q (p - 1) C_{CO}^{p-1} + 1\}^{\frac{1}{1-p}} \quad (5.4)$$

The conversion of CO was measured by varying the respective concentration of the reactants CO and H₂ at 340 °C and atmospheric pressure. Fitting this data by Eq. (5.4) shows a negative reaction order for CO ($p = -0.3$) and a positive order for H₂ ($q = 0.7$) (for detail see Appendix B.1.1). These values are in good agreement with typical values reported in the literature [97, 98].

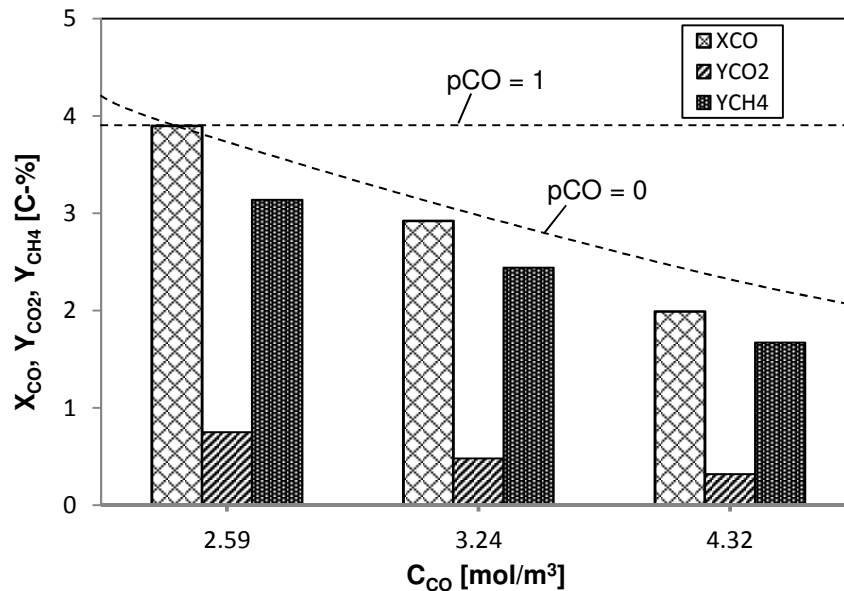


Fig. 5-31: Effect of CO concentration on the CO conversion and the CO₂ and CH₄ yield (T = 340 °C, p = 1 atm, m_{cat} = 1.2 g, d_p = 6 mm, catalyst = Ni/Al₁₂O₁₉, y_{H₂} = 66 vol.-%, y_{CO} = 13.2 – 22 vol.-%, N₂ = remaining proportion, gas flow rate = 48 l/h (NTP)).

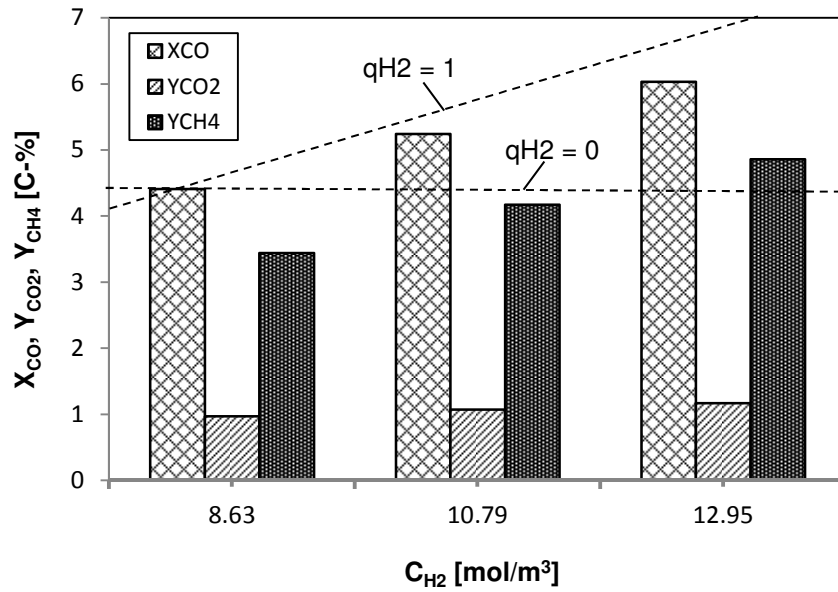


Fig. 5-32: Effect of H_2 concentration on the CO conversion and the CO_2 and CH_4 yield ($T = 340\text{ }^\circ\text{C}$, $p = 1\text{ atm}$, $m_{cat} = 1.2\text{ g}$, $d_p = 6\text{ mm}$, catalyst = $Ni/Al_{12}O_{19}$, $y_{H_2} = 66\text{ vol.-%}$, $y_{CO} = 11\text{ vol.-%}$, $y_{H_2} = 44 - 66\text{ vol.-%}$, N_2 = remaining proportion, gas flow rate = 48 l/h (NTP)).

The intrinsic rate of CO hydrogenation reaction is therefore given as

$$r_{m,CO} = k_{m,CO} \frac{C_{CO}^{0.7}}{C_{H_2}^{0.3}} \quad (5.5)$$

where $k_{m,CO}$ is the reaction rate constant for CO hydrogenation reaction which can be calculated as:

$$k_{m,CO} = \frac{(1 - X_{CO})^{1-p} - 1}{(p - 1) \tau_m C_{CO}^{p-1} C_{H_2}^q} \quad \text{where } \begin{cases} p = -0.3 \\ q = 0.7 \end{cases} \quad (5.6)$$

The Arrhenius plot is shown in Fig. 5-33. Only the values of $k_{m,CO}$ for $T < 420\text{ }^\circ\text{C}$ are included where the reaction rate is exclusively determined by the intrinsic kinetic. The activation energy E_A and frequency factor $k_{m,0}$ calculated from the Arrhenius equation (Eq. (4.9)) are 102 kJ/mol and $2.35 \cdot 10^5\text{ m}^{1.2}\text{ mol}^{0.6}\text{ kg}^{-1}\text{ s}^{-1}$, respectively. The value of E_A obtained in this study (102 kJ/mol) for CO hydrogenation (methanation) is within the range found by other authors using Ni catalysts (see Table 5-5).

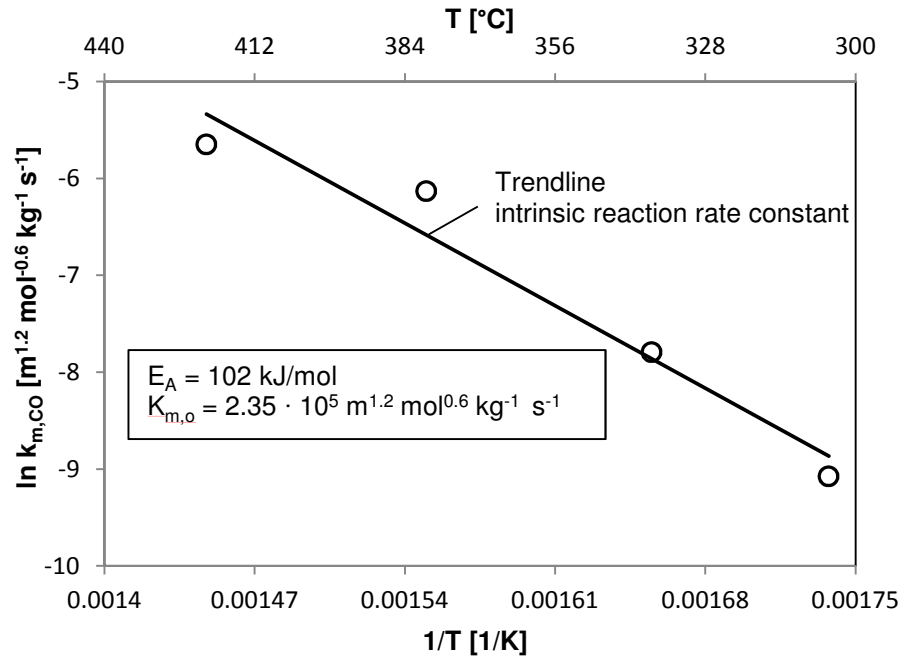


Fig. 5-33: Reaction rate constant ($1/T$ versus $\ln k_{m,CO}$) of CO hydrogenation ($p = 1$ atm, $m_{cat} = 1.2$ g, $d_p = 6$ mm, catalyst = Ni/Al₂O₃, $y_{H_2} = 66$ vol.-%, $y_{CO} = 11$ vol.-%, rest N₂, gas flow rate = 138 l/h (NTP)).

Table 5-5: Activation energies reported in literature for CO hydrogenation on Ni catalysts.

| Catalyst | Temperature (°C) | Pressure (atm) | E_A (kJ/mol) | References |
|---|------------------|----------------|----------------|------------|
| Monolithic Ni | 200 – 350 | 6.8 | 104 – 89 | [98] |
| 3% Ni/SiO ₂ | 227 – 277 | 1.38 | 96 | [99] |
| Ni/MgAl ₂ O ₄ | 205 – 290 | 1.4 | 96.7 | [100] |
| 10% Ni/SiO ₂ | 270 – 320 | 1 | 112 | [101] |
| 1.04Ni/K-Al ₂ O ₄ | 339 – 364 | 1 | 94 ± 3 | [102] |
| 11% Ni (G.90-B) | 305 – 345 | 1 | 102 | This work |

Influence of mass transfer limitation

The influence of internal mass transport on the effective reaction rate of CO hydrogenation was determined for the shell catalyst as well as non-shell catalyst (6 mm particle diameter with homogeneous distribution). For external mass transport, external surface per mass of

catalyst is important. Therefore, the external mass transport calculations are made based on the catalyst particle of 6 mm diameter. All calculations were performed by using the equations from section 4.4.1 where the analysis was presented for CO₂ hydrogenation. The effective reaction rate of CO hydrogenation due to the influence of internal and external mass transport is calculated by

$$r_{m,eff} = \left[\frac{1}{\eta k_{m,CO} C_{CO}^{-0.3} C_{H_2}^{0.7}} + \frac{1}{\beta A_{m,ext} (C_{CO} - C_{CO,eq})} \right]^{-1} \quad (5.7)$$

This equation is only a very rough approximation, i.e. the influence of the thermodynamics is only considered for the external mass transfer. The model parameters required in the calculation of the effective reaction rates of CO hydrogenation reaction are given in Table 5-6. For the details of pore diffusion calculation see Appendix B.2 (Fig. B-7).

Table 5-6: Model parameters used for the calculation of effective reaction rate of CO hydrogenation over Ni catalyst (p = 1 atm).

| Parameters | Values |
|---|--|
| Frequency factor ($k_{m,0}$) | $2.35 \cdot 10^5 \text{ m}^{1.2} \text{ mol}^{0.6} \text{ kg}^{-1} \text{ s}^{-1}$ |
| Activation energy (E_A) | 102 kJ/mol |
| Particle density (ρ_p) | 1910 kg/m ³ |
| Porosity of particle (ε_p) | 0.33 |
| Tortuosity of particle τ_p (assumption) | 1.65 |
| Molecular diffusion coefficient of CO ($D_{CO,mol}$) at 773 K | $2.32 \cdot 10^{-4} \text{ m}^2/\text{s}$ |
| Knudsen diffusion coefficient ($D_{CO,knu}$) at 773 K | $5.86 \cdot 10^{-5} \text{ m}^2/\text{s}$ |
| Pore diffusion coefficient ($D_{CO,pore}$) at 773 K | $4.68 \cdot 10^{-5} \text{ m}^2/\text{s}$ |
| Kinematic viscosity of CO (ν_{CO}) at 773 K | $1.95 \cdot 10^{-4} \text{ m}^2/\text{s}$ |

The internal mass transport effect was evaluated from the effectiveness factor η . Fig. 5-34 shows the effectiveness factor versus temperature for shell catalyst of 6 mm diameter with 0.5 mm shell thickness and for the non-shell catalyst of 0.5 mm and 6 mm diameter. The effectiveness factor decreases strongly above a temperature of 420 °C for both the shell as

well as non-shell catalyst of 6 mm diameter. It must be noted that η was estimated here only assuming an irreversible reaction (methanation).

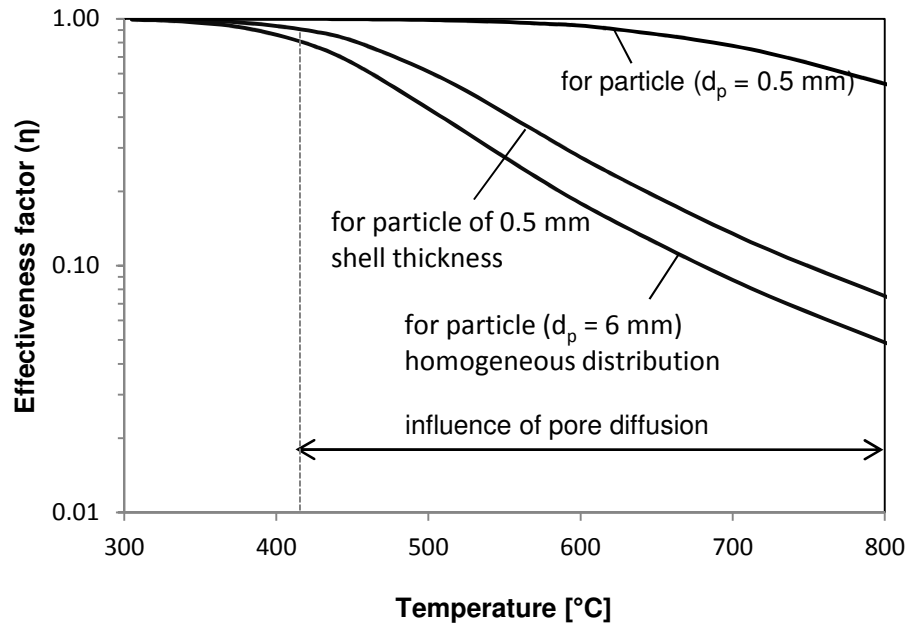


Fig. 5-34: Effectiveness factor η for the Ni/Al₁₂O₁₉ catalyst versus temperature ($p = 1$ atm, $y_{\text{CO}} = 11$ vol.-%, $y_{\text{H}_2} = 66$ vol.-%, rest N₂, gas flow rate = 138 l/h (NTP)).

Fig. 5-35 shows that the calculated values for the effective reaction rate due to the combined influence of pore and external diffusion are much higher than the measured ones in the high temperature range. The reason is that the chemical reaction rate and the influence of pore diffusion is influenced by the reverse reaction (thermodynamic limitation), and Eq. (5.7) does not consider this effect. Also note that the shift of the selectivity (less methane) with increasing temperature is not considered in Fig. 5-34.

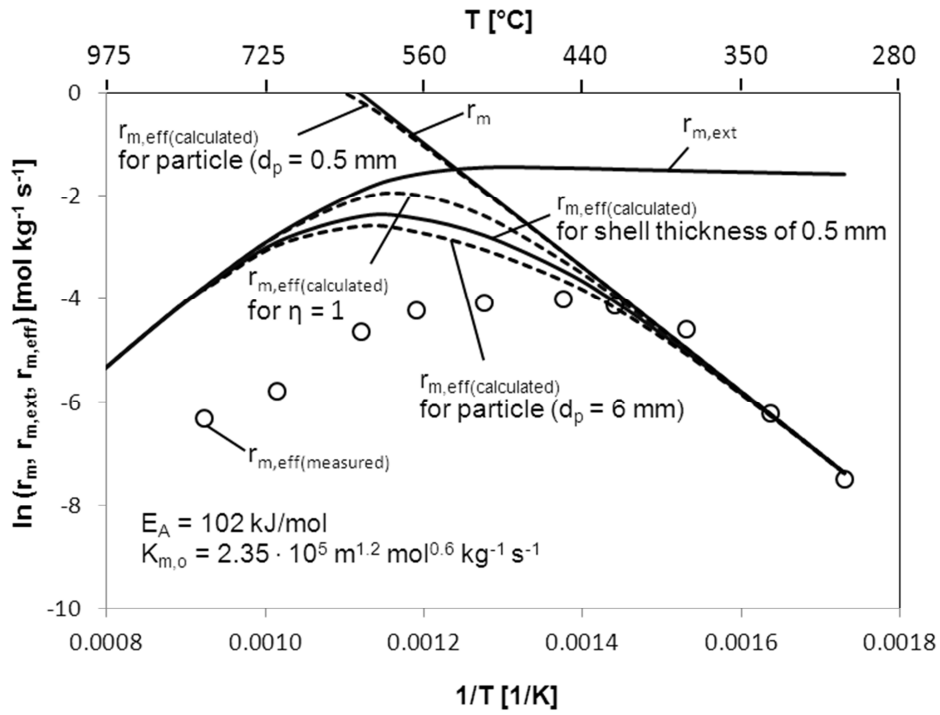


Fig. 5-35: Influence of internal and external mass transport on the effective reaction rate of CO hydrogenation ($p = 1$ atm, $m_{\text{cat}} = 1.2$ g, $d_p = 6$ mm, catalyst = Ni/Al₁₂O₁₉, $y_{\text{CO}} = 11$ vol.-%, $y_{\text{H}_2} = 66$ vol.-%, rest N₂, gas flow rate = 138 l/h (NTP)).

5.3 Water gas shift (WGS) reaction

The water gas shift reaction ($\text{CO} + \text{H}_2\text{O} \rightarrow \text{CO}_2 + \text{H}_2$) as the reverse reaction of CO_2 hydrogenation (RWGS reaction) was carried out in the fixed bed quartz reactor setup over a wide temperature range (300 – 900 °C) at atmospheric pressure. The reaction kinetics as well as the influence of mass transport on the effective reaction rate of WGS reaction is now described.

5.3.1 Influence of temperature on the WGS reaction

For the WGS reaction, 1.2 g $\text{Ni}/\text{Al}_{12}\text{O}_{19}$ catalyst of 6 mm particle diameter was reduced in the reactor for 24 h with a gas flow rate of 10 l/h containing 50 % H_2 in N_2 at 800 °C. The experiments were started by lowering the temperature to 300 °C and at atmospheric pressure. The $\text{H}_2\text{O}/\text{CO}$ ratio was maintained at 4. The experiments were carried out with two different conditions, i.e. with addition of 10% H_2 and without addition of H_2 . Hydrogen was added into the reaction mixture to avoid the oxidation of Ni to NiO by H_2O . Fig. 5-36 shows the conversion of CO and the yield of CH_4 and CO_2 at different temperature. In both cases, the conversion of CO and the yield of CO_2 showed a similar behavior. The conversion of CO and the yield of CO_2 rise with increasing temperature up to 450 °C where the catalyst showed stable activity. In the temperature range of 450 to 700 °C, deactivation of catalyst due to coke formation was observed where the conversion of CO and simultaneously the yield of CO_2 decrease over time on stream (see Fig. 5-40). The coke formation may occur via CO disproportionation (Boudouard reaction) at the Ni catalyst. Details about the equilibrium conversion of CO by the Boudouard reaction are given in section 5.2.1 (Fig. 5-24). The formation of formate-carbonate is the key intermediate in the production of hydrogen via water gas shift reaction where substantial reduction to Ni metal cluster above 400 °C favors the transformation of formate into carbonate species, providing the route for catalyst deactivation by coking [103].

The CH_4 formation was not observed over the entire temperature when no H_2 was added into reaction mixture while a small amount of CH_4 was observed in the low temperature range (300 – 600 °C) when the 10 vol.-% H_2 were added into the reaction mixture which is possibly due to the CO methanation reaction. The addition of H_2 cannot prevent the catalyst from deactivation due to coke formation, but slightly reduces the CO conversion.

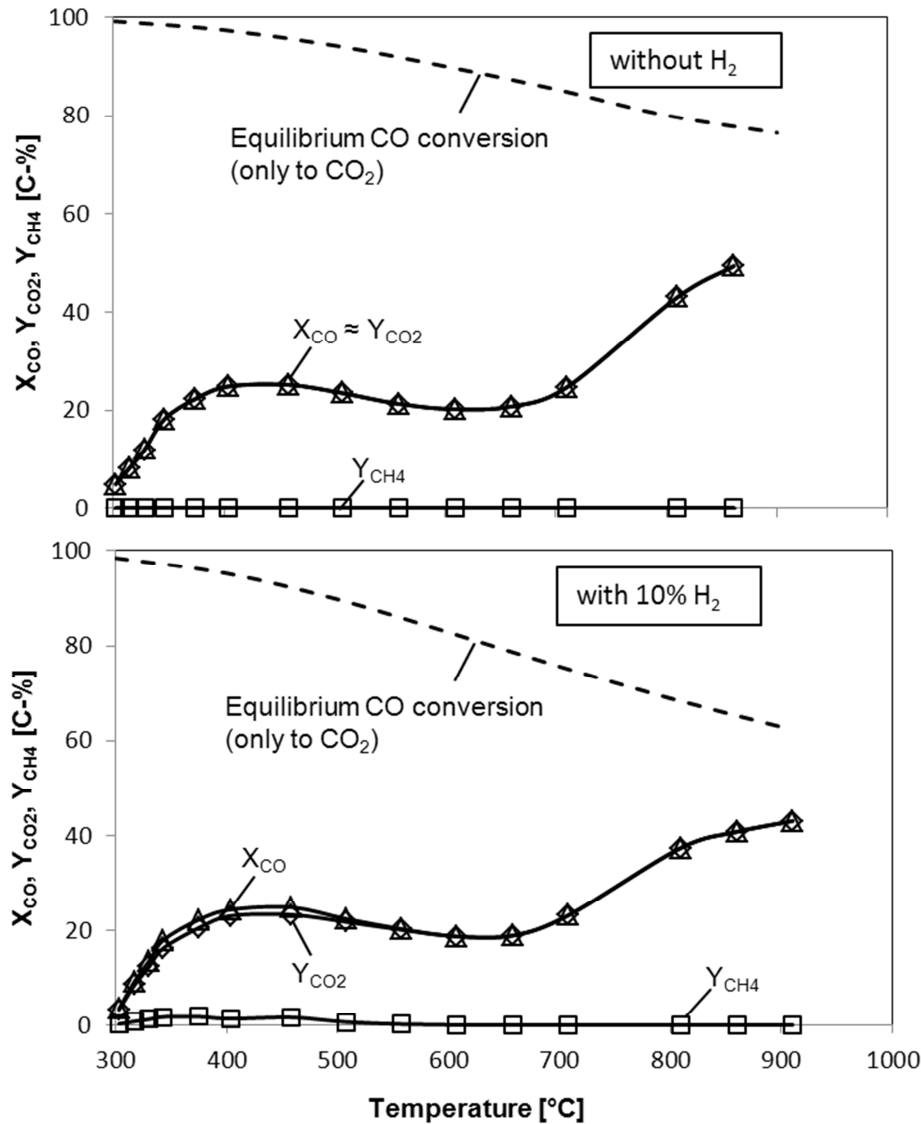


Fig. 5-36: CO conversion and the yield of CO₂ and CH₄ versus temperature in WGS reaction with and without addition of H₂ in feed gas mixture ($p = 1$ atm, $m_{cat} = 1.2$ g, $d_p = 6$ mm, catalyst = Ni/Al₁₂O₁₉, $y_{H_2O} = 44$ vol.-%, $y_{CO} = 11$ vol.-%, rest N₂, $y_{H_2} = 0$ and 10 vol.-%, gas flow rate = 48 l/h (NTP)).

5.3.2 Influence of residence time at varying and constant temperature on the WGS reaction

The conversion of CO by the water gas shift reaction over the temperature was measured using a gas flow rate of 48 l/h and 138 l/h (NTP) and a constant catalyst amount of 1.2 g for the evaluation of the effect of the residence time. A similar trend for catalyst performance was observed in both cases. The WGS reaction is an exothermic reaction and favoured at

low temperatures. But even at high temperatures, the equilibrium conversion of CO is still high (e.g. 80% at 800 °C). So the reaction was not controlled thermodynamically in the studied temperature range. As mentioned above, the deactivation of catalyst occurs in the temperature range of 450 to 700 °C and the activity of catalyst drops down in this region. Above 700 °C, the catalyst showed again an increase in activity which may be due to the gasification of coke at high temperatures. By comparing the data obtained for 48 l/h and 138 l/h (NTP), shown in Fig. 5-37, it is observed that the conversion of CO increases with decreasing the total gas flow rate (increasing residence time) at any temperature, and no CH₄ formation was observed.

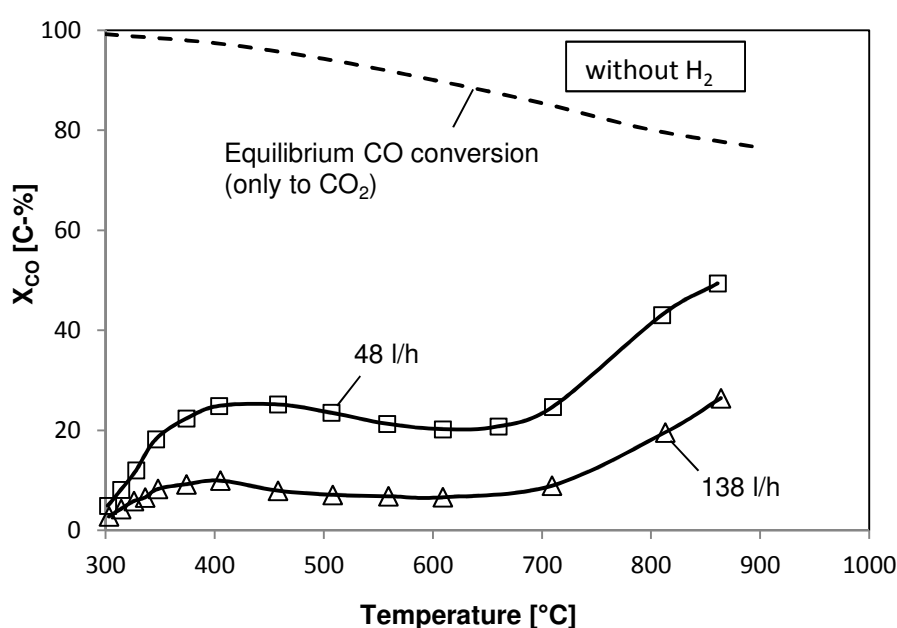


Fig. 5-37: Conversion of CO (water gas shift reaction) versus temperature at different residence times without addition of H₂ in feed gas ($p = 1$ atm, $m_{\text{cat}} = 1.2$ g, catalyst = Ni/Al₁₂O₁₉, $d_p = 6$ mm, $y_{\text{H}_2\text{O}} = 44$ vol.-%, $y_{\text{CO}} = 11$ vol.-%, rest N₂).

The influence of the modified residence time on the CO conversion and the yield of CO₂ and CH₄ was measured at 405 °C, atmospheric pressure, H₂O/CO ratio of 4, and by changing the total gas flow rate over 1.2 g Ni catalyst. Fig. 5-38 shows the conversion of CO and the yield methane and CO₂ obtained at different modified residence time. CH₄ formation was not observed in the whole range of the modified residence time studied except at a high residence time (36 kg s m⁻³), where a negligible yield of CH₄ (less than 0.1%) was obtained. So the consecutive CO methanation does not play a role for the given conditions.

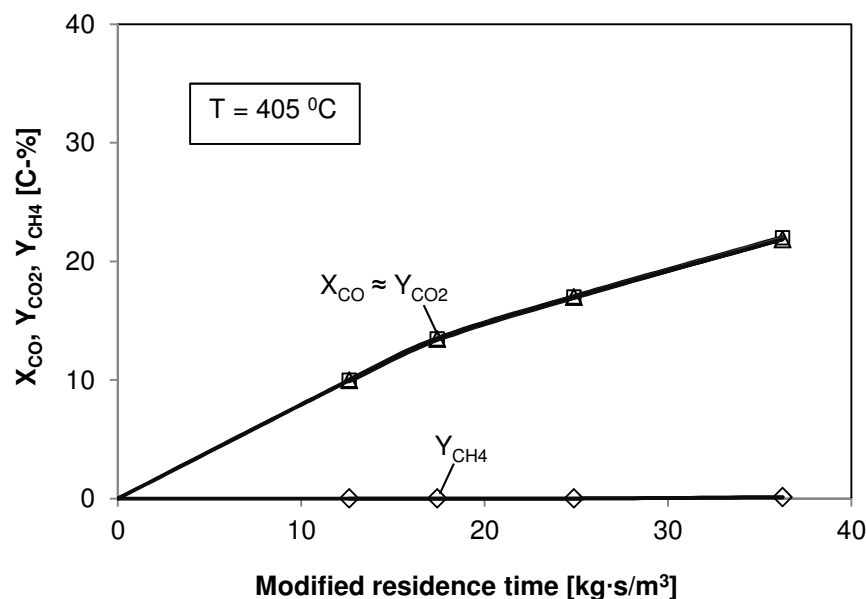


Fig. 5-38: Influence of modified residence time on CO conversion and the yield of CO_2 and CH_4 in water gas shift reaction ($T = 405\text{ }^{\circ}\text{C}$, $p = 1\text{ atm}$, $m_{\text{cat}} = 1.2\text{ g}$, $d_p = 6\text{ mm}$, catalyst = $\text{Ni}/\text{Al}_{12}\text{O}_{19}$, $y_{H_2O} = 44\text{ vol.-%}$, $y_{CO} = 11\text{ vol.-%}$, rest N_2).

5.3.3 Stability of the Ni catalyst in the WGS reaction

5.3.3.1 Low temperature stability

In the water gas shift reaction, the Ni catalyst behaves differently at different temperature. No deactivation was observed below $450\text{ }^{\circ}\text{C}$, but the catalyst shows deactivation due to coke formation in the temperature range of 450 to $700\text{ }^{\circ}\text{C}$. So, depending upon this behaviour the time on stream stability of catalyst was studied at both low and high temperatures.

The low temperature catalytic stability of the $\text{Ni}/\text{Al}_{12}\text{O}_{19}$ catalyst in the WGS reaction was tested for about 100 min at $340\text{ }^{\circ}\text{C}$ and $450\text{ }^{\circ}\text{C}$, and atmospheric pressure. Fig. 5-39 shows the conversion of CO over the time on stream. The $\text{Ni}/\text{Al}_{12}\text{O}_{19}$ catalyst showed a good stability at these low temperatures ($340\text{ }^{\circ}\text{C}$ and $450\text{ }^{\circ}\text{C}$).

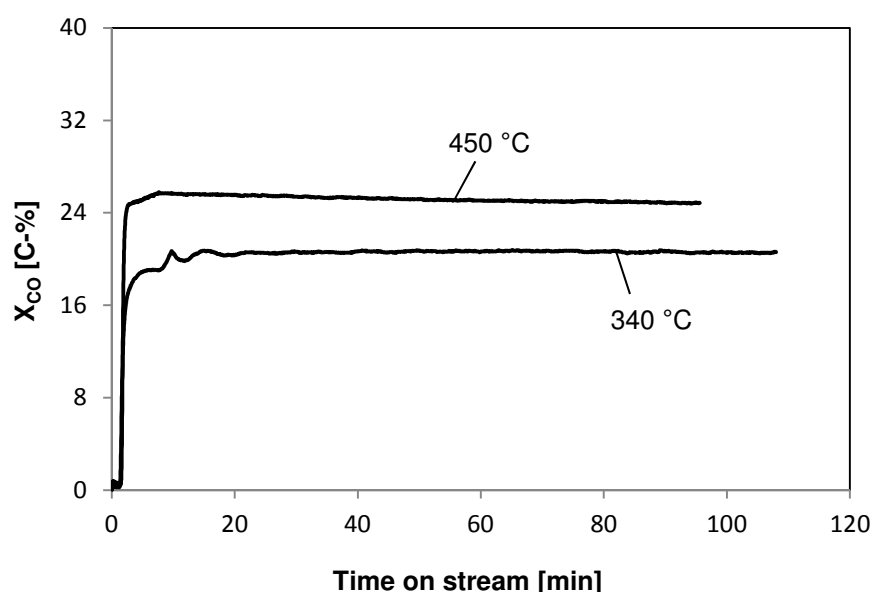


Fig. 5-39: CO conversion versus time on stream in WGS reaction at low temperature ($p = 1$ atm, $m_{\text{cat}} = 1.2$ g, catalyst = Ni/Al₁₂O₁₉, $d_p = 6$ mm, $y_{\text{CO}} = 11$ vol.-%, $y_{\text{H}_2\text{O}} = 44$ vol.-%, rest N₂, gas flow rate = 48 l/h (NTP)).

5.3.3.2 High temperature stability

The time on stream behaviour of the Ni catalyst in the high temperature range of 500 °C to 900 °C and at atmospheric pressure for water gas shift reaction is shown in Fig. 5-40. It was difficult to determine the amount of coke formed via thermogravimetric analysis because a very small amount of coke is formed and the mass loss by burning of the coke and the mass gain by catalyst oxidation takes place simultaneously.

The experimental procedure was as follows:

At first, the water gas shift reaction was performed at a certain temperature, e.g. at 500 °C (Fig. 5-40). Then the temperature was increased to 900 °C, where not only the WGS reaction takes place but also the gasification of the coke formed at the low temperature experiment (Fig. 5-41).

Fig. 5-40 indicates that at 900 °C, no coke is formed, i.e. the coke that may be formed is gasified with steam at an appropriate rate. Hence, the catalysts used for WGS reaction at lower temperatures for about 100 min regain their activity by gasification, if the temperature of 900 °C is adjusted afterwards. This is shown in Fig. 5-41.

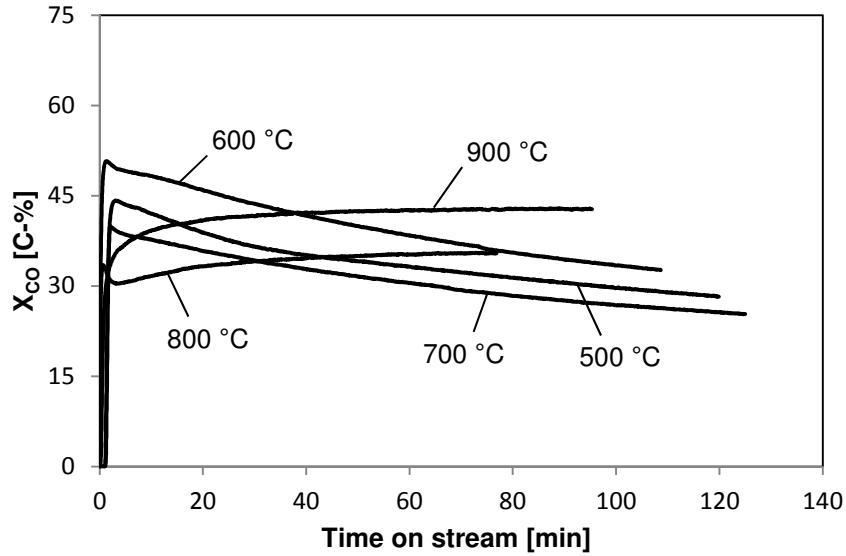


Fig. 5-40: CO conversion versus time on stream in WGS reaction at high temperatures ($p = 1$ atm, $m_{\text{cat}} = 1.2$ g, catalyst = Ni/Al₁₂O₁₉, $d_p = 6$ mm, $y_{\text{CO}} = 11$ vol.-%, $y_{\text{H}_2\text{O}} = 44$ vol.-%, rest N₂, gas flow rate = 48 l/h (NTP)).

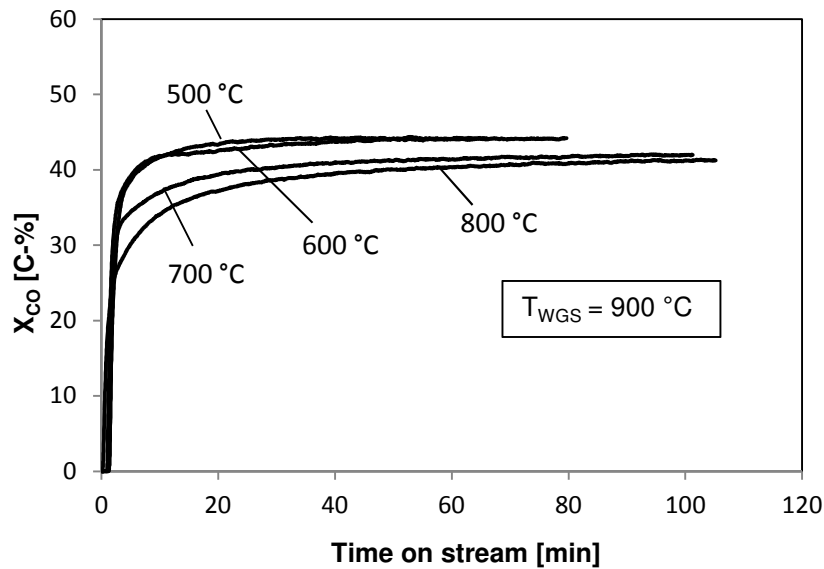


Fig. 5-41: CO conversion versus time on stream in WGS reaction at 900 °C after the lower temperature experiments ($p = 1$ atm, $m_{\text{cat}} = 1.2$ g, $d_p = 6$ mm, $y_{\text{CO}} = 11$ vol.-%, $y_{\text{H}_2\text{O}} = 44$ vol.-%, rest N₂, catalyst = Ni/Al₁₂O₁₉, gas flow rate = 48 l/h (NTP)).

In another experiment, the freshly reduced Ni catalyst (800 °C) was applied for 6 h in the reaction at 650 °C where the catalyst shows deactivation with time on stream (Fig. 5-42). Then this used catalyst was oxidised in the same reactor using 5.5 vol.-% O₂ in N₂ by increasing the temperature from 300 to 700 °C at a rate of 10 °C/min. The presence of CO

and CO_2 species in the outlet gas stream during oxidation of catalyst (coke burning) were analysed using a micro-gas analyser and the amount of coke formed was quantified from the CO_2 produced during the catalyst oxidation. The activity of the catalyst was then recovered by oxidation/reduction. The regenerated catalyst was again used for 3 h and the same procedure was repeated to confirm the coke formation.

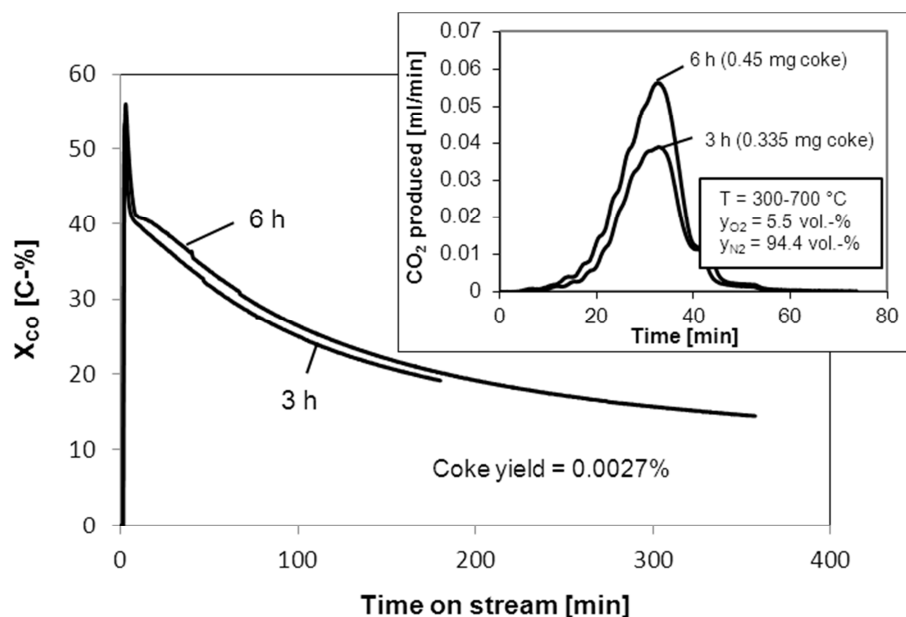


Fig. 5-42: Time on stream stability and coke formation over freshly reduced catalyst in WGS reaction ($T = 650\text{ }^{\circ}\text{C}$, $p = 1\text{ atm}$, $m_{\text{cat}} = 1.2\text{ g}$, $d_p = 6\text{ mm}$, $y_{\text{CO}} = 11\text{ vol.-%}$, $y_{\text{H}_2\text{O}} = 44\text{ vol.-%}$, rest N_2 , catalyst = $\text{Ni}/\text{Al}_{12}\text{O}_{19}$, gas flow rate = 48 l/h (NTP)).

Fig. 5-42 clearly shows that the regeneration by coke burn-off is possible. The amount of coke is rather small compared to the carbon (as CO) that has passed through the reactor. During the 6 h experiment, about 17 g of carbon (as CO) have entered the reactor but only 0.45 mg of coke was formed. Nevertheless this small amount of coke is sufficient for a strong deactivation of the catalyst, although the amount of coke (0.04 mmol C) is still small compared to the amount of Ni (2 mmol), but at least in the same order of magnitude (and not all of the Ni material is accessible by reactants).

5.3.4 Kinetic analysis and influence of internal and external mass transfer on the WGS reaction

Intrinsic kinetics

The reaction orders of the water gas shift reaction with respect to reactant and product components over the Ni/Al₁₂O₁₉ catalyst were determined by fitting the experimental data to Eq. (5.8).

$$X_{CO} = 1 - \{k_{m,CO} \tau_m C_{H_2O}^S C_{H_2}^u C_{CO_2}^v C_{CO}^{r-1} (r - 1) + 1\}^{\frac{1}{1-r}} \quad (5.8)$$

The respective experimental results are shown in the Fig. 5-43 to Fig. 5-46. The reaction orders with respect to reactant CO and H₂O are 0.8 and 0.4 while the products H₂ and CO₂ shows a -0.15 and -0.1 order dependencies on the reaction rate of WGS reaction. (see Appendix B.1.2). Both of these negative order dependencies of products were not considered in the intrinsic rate calculation.

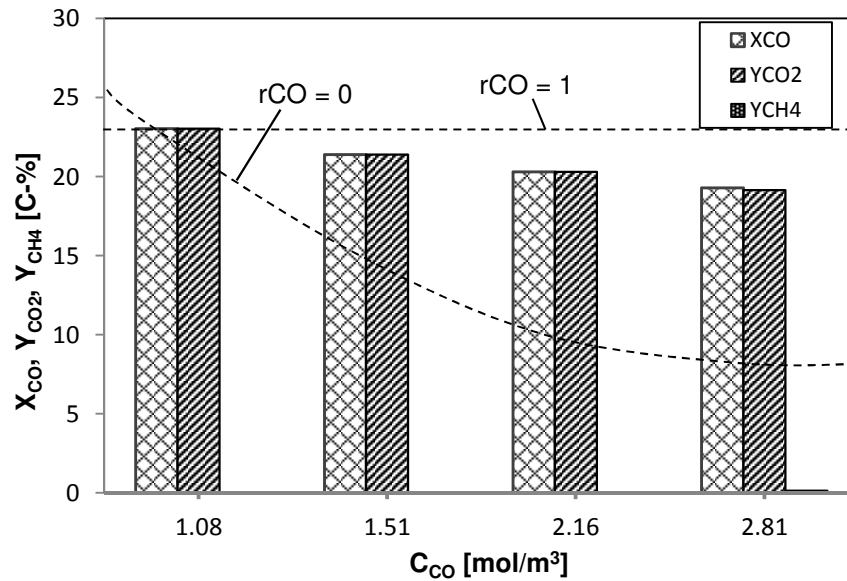


Fig. 5-43: Effect of CO concentration on the CO conversion and the CO₂ and CH₄ yield in WGS reaction (T = 340 °C, p = 1 atm, m_{cat} = 1.2 g, d_p = 6 mm, y_{H2O} = 44 vol.-%, y_{CO} = 5.5 – 14.3 vol.-%, N₂ = rest proportion, catalyst = Ni/Al₁₂O₁₉, gas flow rate = 48 l/h (NTP)).

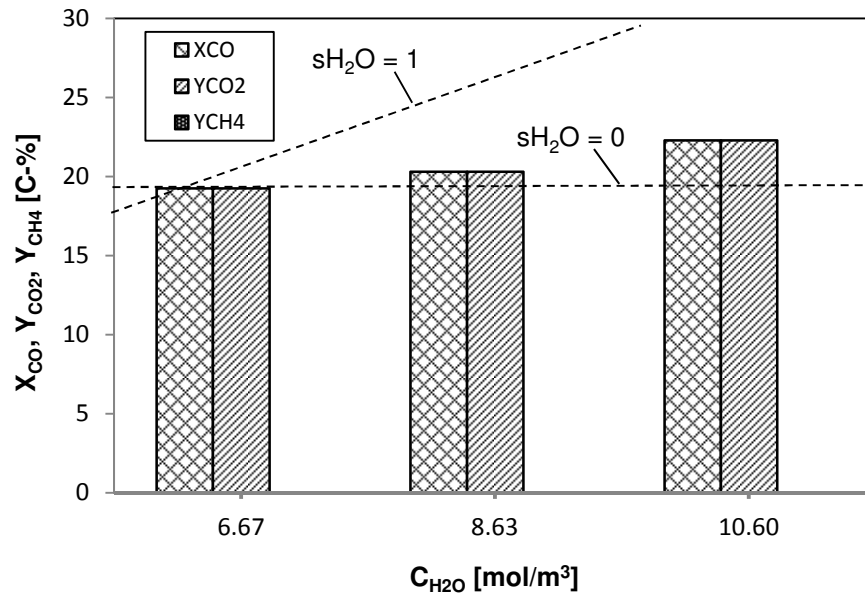


Fig. 5-44: Effect of H_2O concentration on the catalyst activity and the CO_2 and CH_4 yield in WGS reaction ($T = 340$ °C, $p = 1$ atm, $m_{cat} = 1.2$ g, $d_p = 6$ mm, $y_{CO} = 11$ vol.-%, $y_{H_2O} = 34 - 54$ vol.-%, N_2 = rest proportion, catalyst = Ni/ $Al_{12}O_{19}$, gas flow rate = 48 l/h (NTP)).

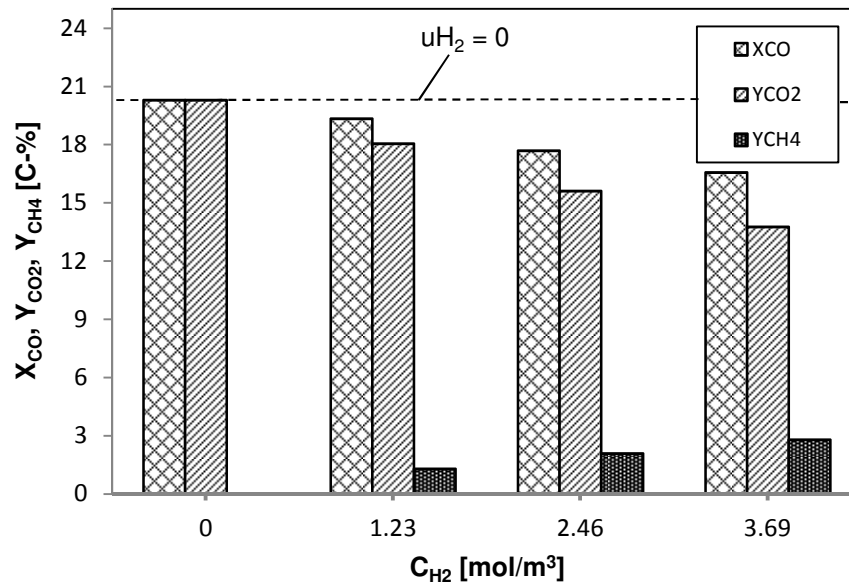


Fig. 5-45: Effect of H_2 addition into the feed gas of WGS reaction ($T = 340$ °C, $p = 1$ atm, $m_{cat} = 1.2$ g, $d_p = 6$ mm, catalyst = Ni/ $Al_{12}O_{19}$, $y_{CO} = 11$ vol.-%, $y_{H_2O} = 44$ vol.-%, $y_{H_2} = 0 - 18.75$ vol.-%, N_2 = rest proportion, gas flow rate = 48 l/h (NTP)).

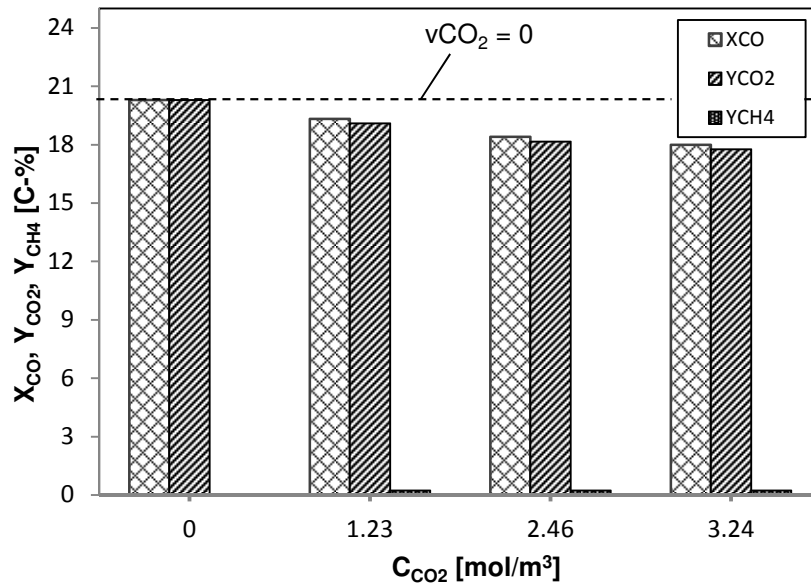


Fig. 5-46: Effect of CO_2 addition into the feed gas of WGS reaction ($T = 340\text{ }^\circ\text{C}$, $p = 1\text{ atm}$, $m_{cat} = 1.2\text{ g}$, $d_p = 6\text{ mm}$, catalyst = $Ni/Al_{12}O_{19}$, $y_{CO} = 11\text{ vol.-%}$, $y_{H_2O} = 44\text{ vol.-%}$, $y_{CO_2} = 0 - 16.67\text{ vol.-%}$, $N_2 = \text{rest proportion}$, gas flow rate = 48 l/h (NTP)).

The intrinsic reaction rate of WGS reaction has been calculated as

$$r_{m,CO} = k_{m,CO} C_{CO}^{0.8} C_{H_2O}^{0.4} = k_{m,0} e^{-\frac{E_A}{RT}} C_{CO}^{0.8} C_{H_2O}^{0.4} \quad (5.9)$$

where $k_{m,CO}$ is the reaction rate constant for WGS reaction which can be calculated as:

$$k_{m,CO} = \frac{(1 - X_{CO})^{1-0.8} - 1}{(0.8 - 1) \tau_m C_{CO}^{0.8-1} C_{H_2O}^{0.4}} \quad (5.10)$$

The temperature dependency of $k_{m,CO}$ is shown in Fig. 5-47.

To determine the intrinsic kinetic, only the values of $k_{m,CO}$ for $T < 345\text{ }^\circ\text{C}$ are included where no mass transport or thermodynamic limitations occur. The frequency factor $k_{m,0}$ and apparent activation energy of reaction E_A are $3.46 \cdot 10^5\text{ m}^{3.6}\text{ mol}^{-0.2}\text{ kg}^{-1}\text{ s}^{-1}$ and 96 kJ/mol , respectively. The activation energy data reported in literature for the water gas shift reaction over Ni containing catalyst is given in Table 5-7. The value of E_A (96 kJ/mol) obtained in this study is within the range found by other authors.

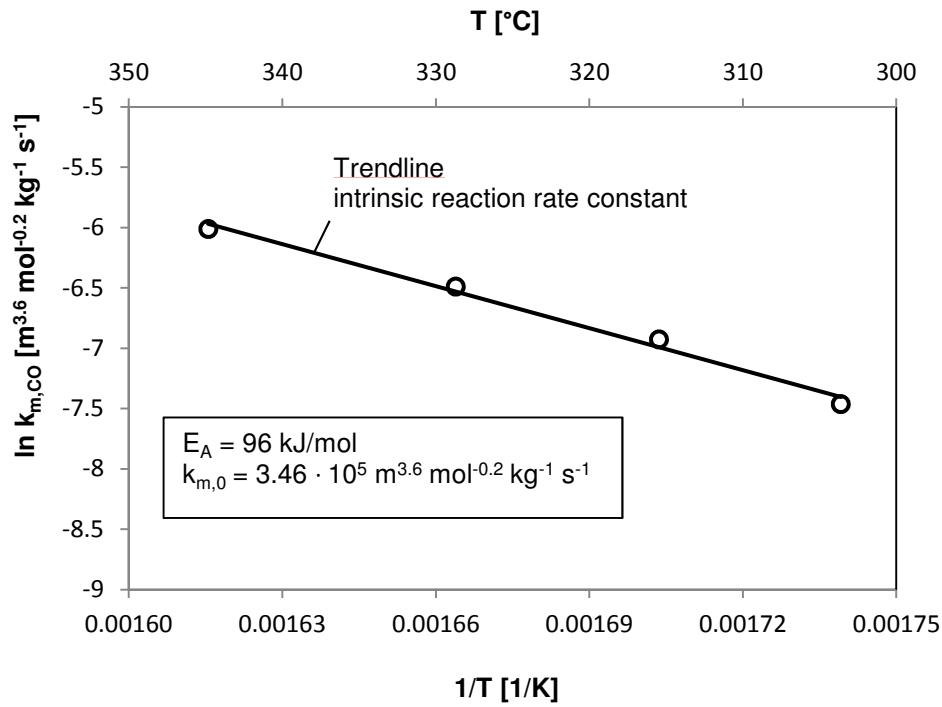


Fig. 5-47: Reaction rate constant ($1/T$ versus $\ln k_{m,\text{CO}}$) of the WGS reaction ($p = 1 \text{ atm}$, $m_{\text{cat}} = 1.2 \text{ g}$, $d_p = 6 \text{ mm}$, catalyst = $\text{Ni}/\text{Al}_{12}\text{O}_{19}$, $y_{\text{H}_2\text{O}} = 44 \text{ vol.}\%$, $y_{\text{CO}} = 11 \text{ vol.}\%$, rest N_2 , gas flow rate = 48 l/h (NTP)).

Table 5-7: Activation energies reported for water gas shift reaction on nickel catalysts.

| Catalyst | Temp ($^{\circ}\text{C}$) | Pressure (atm) | E_A (kJ/mol) | Ref. |
|--|-----------------------------|----------------|----------------|-----------|
| 5% $\text{Ni}/\text{Al}_2\text{O}_3$ monolith | 300 – 1000 | 1 | 85 | [104] |
| 5% $\text{Ni}/5\% \text{ Ce}/\text{Al}_2\text{O}_3$ monolith | 300 – 1000 | 1 | 85 | [104] |
| 5 at.% $\text{Ni}/\text{Ce}(10\% \text{ La})\text{O}_x$ | 275 – 300 | 1 | 38 | [105] |
| Black NiO | 200 – 300 | 1 | 96 ± 4 | [106] |
| Green NiO | 200 – 300 | 1 | 89 ± 4 | [106] |
| 11% Ni (G.90-B) | 305 – 345 | 1 | 96 | This work |

Influence of mass transport

To determine the influence of mass transport on the effective reaction rate of water gas shift reaction, all the calculations were made by using the equations from section 4.4.1. Similar to

CO₂ and CO hydrogenation, the influence of mass transfer in WGS reaction was calculated for both shell catalyst (thickness of 0.5 mm) and non-shell catalyst ($d_p = 6$ mm). The effective reaction rate due to the influence of both internal and external mass transport was calculated as:

$$r_{m,eff} = \left[\frac{1}{\eta k_{m,CO} C_{CO}^{0.8} C_{H_2O}^{0.4}} + \frac{1}{\beta A_{m,ext} (C_{CO} - C_{CO,eq})} \right]^{-1} \quad (5.11)$$

The model parameters required in the calculation of effective reaction rates of water gas shift reaction are given in Table 5-8. The detailed pore diffusion calculation for Ni/Al₁₂O₁₉ catalyst is given in appendix B.2 (Fig. B-8).

Table 5-8: Model parameters used for the calculation of effective reaction rate of the water gas shift reaction over Ni catalyst ($p = 1$ atm).

| Parameters | Values |
|---|---|
| Frequency factor ($k_{m,0}$) | $3.46 \cdot 10^5 \text{ m}^{3.6} \text{ mol}^{-0.2} \text{ kg}^{-1} \text{ s}^{-1}$ |
| Activation energy (E_A) | 96 kJ/mol |
| Particle density (ρ_p) | 1910 kg/m ³ |
| Porosity of particle (ε_p) | 0.33 |
| Tortuosity of particle τ_p (assumption) | 1.65 |
| Molecular diffusion coefficient of CO ($D_{CO,mol}$) at 773 K | $1.07 \cdot 10^{-4} \text{ m}^2/\text{s}$ |
| Knudsen diffusion coefficient ($D_{CO,knu}$) at 773 K | $5.86 \cdot 10^{-5} \text{ m}^2/\text{s}$ |
| Pore diffusion coefficient ($D_{CO,pore}$) at 773 K | $3.78 \cdot 10^{-5} \text{ m}^2/\text{s}$ |
| Kinematic viscosity of CO (ν_{CO}) at 773 K | $8.17 \cdot 10^{-5} \text{ m}^2/\text{s}$ |

In the water gas shift reaction, the influence of pore diffusion on the effective reaction rate was evaluated from effectiveness factor η . Fig. 5-48 shows the effectiveness factor versus temperature for the shell as well as for a hypothetical non-shell catalyst. For both catalysts the effectiveness factor decreases strongly with increasing temperature close to 345 °C. Fig. 5-49 compares the effective reaction rates (considering $\eta = 1$ and with actual η). There is a clear influence of pore diffusion for both the shell and non-shell catalyst.

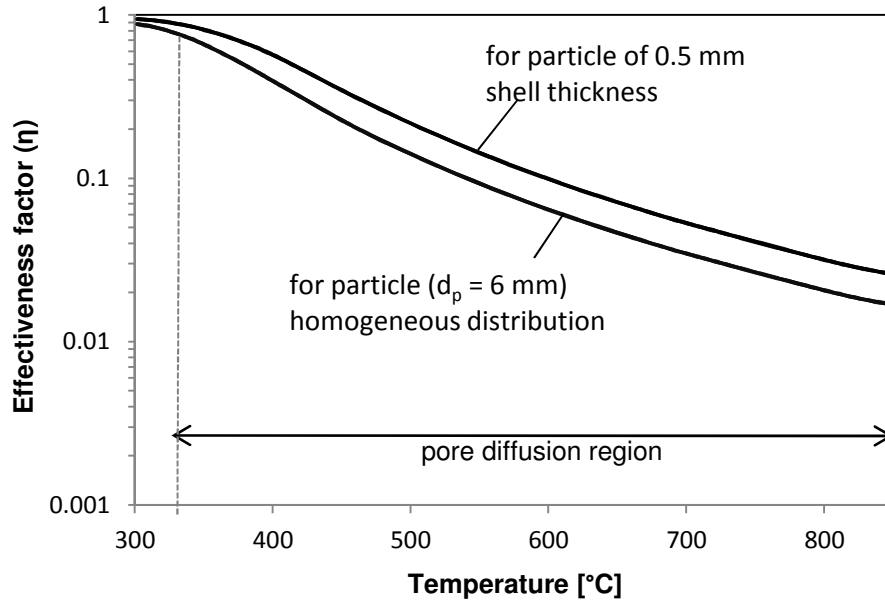


Fig. 5-48: Effectiveness factor for catalyst versus temperature ($p = 1$ atm, $m_{\text{cat}} = 1.2$ g, catalyst = Ni/Al₁₂O₁₉, $y_{\text{CO}} = 11$ vol.-%, $y_{\text{H}_2\text{O}} = 44$ vol.-%, rest N₂, gas flow rate = 48 l/h (NTP)).

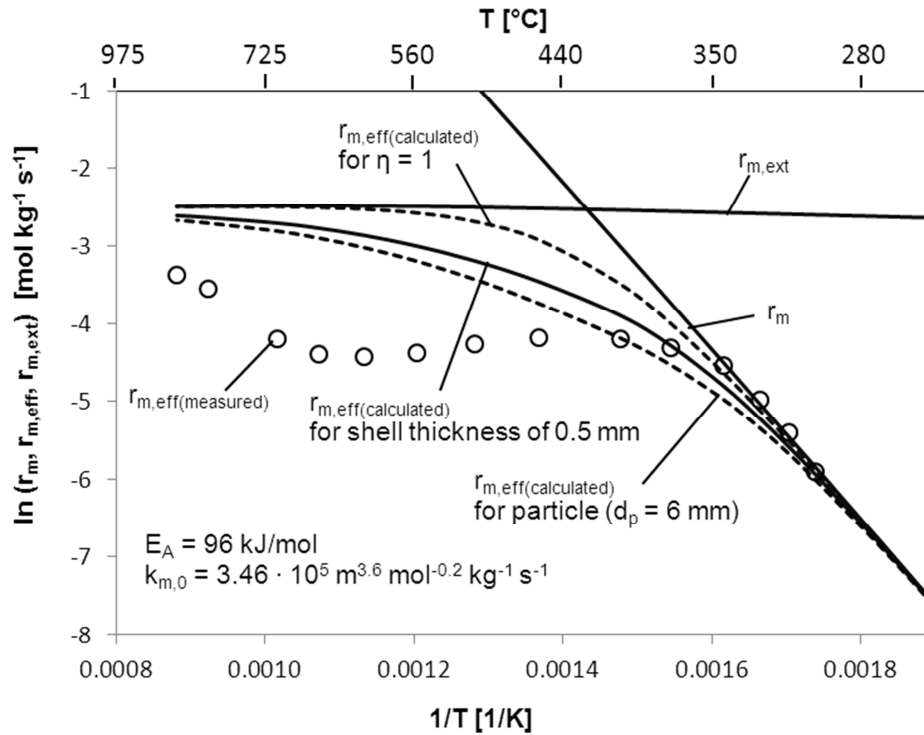


Fig. 5-49: Influence of internal and external mass transport on the effective reaction rate of WGS reaction ($p = 1$ atm, $m_{\text{cat}} = 1.2$ g, $y_{\text{CO}} = 11$ vol.-%, $y_{\text{H}_2\text{O}} = 44$ vol.-%, rest N₂, catalyst = Ni/Al₁₂O₁₉, gas flow rate = 48 l/h (NTP)).

The measured values of the effective reaction rate are decreasing above 450 °C at which catalyst deactivation due to coke formation started. Below this temperature, no coke formation takes place due to kinetic limitations while at a very high temperature (e.g. 900 °C), the coke (if formed) is converted with steam. Therefore, the calculated values of the effective reaction due to combined influence of internal and external mass transfer are much higher than the measured one in the temperature range of 450 to 700 °C. Fig. 5-49 also reveals that at high temperatures of about 900 °C, the measured values of the effective reaction rate are near to the external mass transfer regime.

5.4 Simulation of a reactor for a technical RWGS process

Based on the kinetic data of the RWGS reaction, which were determined for both the Ni- and Al₂O₃-catalyst, technical reactors were simulated. The basic equations and assumptions of the respective reactor model are described in the subsequent section 5.4.1. Two cases were considered as attractive for a technical RWGS process, isothermal and adiabatic operation in a fixed-bed tubular reactor. The latter concept would be easier to realize on a technical scale, because external or internal heating would not be required. But at least for comparison, the isothermal case was also considered. The respective modelling results are discussed in section 5.4.2.

5.4.1 Basis equations of the reactor model

For the simulation of a fixed bed RWGS reactor, a one-dimensional heterogeneous reactor model was applied, i.e. changes of concentrations and temperatures were only considered in axial but not in radial direction. The differential equations for mass and energy were solved by using the program *Berkeley Madonna*. The following assumptions were made for the adiabatic fixed bed reactor model:

- (1) No axial dispersion of mass and heat in the gas as well as in the solid phase.
- (2) No heat losses and thus no radial temperature gradient.
- (3) The enthalpy of reaction is assumed to be constant, i.e. not a function of the temperature.
- (4) The catalyst particle is assumed to be isothermal. In addition, an external heat transfer resistance is not considered (temperature of particle = temperature of gas phase).
- (5) Both pore diffusion and film diffusion concentration gradients were taken into account.
(As shown below, the external resistance is very small, above all at high gas velocities)

For a differential element of the fixed bed (Fig. 5-50) the mass and energy balances are

$$u_s \frac{dC_{CO_2}}{dz} = -\rho_b r_{m,eff} \quad (5.12)$$

$$u_s \rho_{f,mol} C_{p,g} \frac{dT}{dz} = -\Delta_R H \rho_b r_{m,eff} \quad (5.13)$$

u_s is the superficial gas velocity, ρ_b the catalyst bulk density, $r_{m,eff}$ the effective reaction rate (which may be influenced by internal and external mass transfer), $\rho_{f,mol}$ the gas density, $C_{p,g}$ the heat capacity of the gas, and $\Delta_R H$ the enthalpy of reaction.

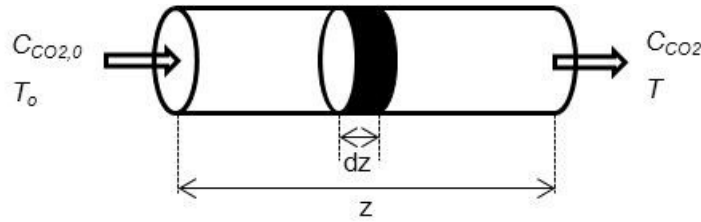


Fig. 5-50: Differential element of the fixed bed reactor and definitions.

The boundary and initial conditions are

$$T = T_0 \text{ and } C_{CO_2} = C_{CO_2,0} \quad \text{when } z = 0 \quad (5.14)$$

$$\frac{dT}{dz} = 0 \text{ and } \frac{dC_{CO_2}}{dz} = 0 \quad \text{at all } z \quad (5.15)$$

where T_0 is the inlet temperature and $C_{CO_2,0}$ the inlet gas phase concentration of CO_2 .

For the simulation of an isothermal reactor (externally heated in an industrial operation) only the mass balance (Eq. (5.12)) is considered.

The inlet composition of reaction gas mixture only consists of CO_2 and H_2 . The reaction order assumed to be first order for CO_2 and zero order for H_2 . The parameters required in the pore diffusion and external mass transport calculations are given in Table 5-9.

Table 5-9: Model parameters used to calculate the effective rate of CO_2 hydrogenation.

| Parameter | Ni/Al ₁₂ O ₁₉ | Al ₂ O ₃ |
|---|-------------------------------------|--------------------------------|
| Frequency factor ($k_{m,0}$), m ³ kg ⁻¹ s ⁻¹ | $1.7 \cdot 10^3$ | 40.9 |
| Activation energy (E_A), kJ/mol | 68.5 | 72 |
| External mass transfer coefficient (β) at 1000 °C, m/s | 2.56 | 2.56 |
| External mass transfer area ($A_{m,ext}$), m ² /kg | 0.52 | 0.69 |

For the reversible RWGS reaction, the effective reaction rate due to the influence of internal mass transport only is calculated as

$$r_{m,pore} = \eta k_{m,CO_2} \left[C_{CO_2} - \frac{C_{CO} C_{H_2O} C_{H_2}^{-1}}{K_c} \right] \quad (5.16)$$

The effectiveness factor η is a function of the Thiele modulus for a reversible reaction (Eq. (5.17)) and k_{m,CO_2} is calculated by the Arrhenius equation (Eq. (4.9)).

$$\phi_{reversible} = \frac{d_p}{6} \sqrt{\left[\frac{K_c + 1}{K_c} \right] \frac{k_{m,CO_2} \rho_p}{D_{CO_2,eff}}} \quad (5.17)$$

In case of control by external mass transport, the reaction rate is given by

$$r_{m,ext} = \beta A_{m,ext} (C_{CO_2} - C_{CO_2,eq}) \quad (5.18)$$

The values of β and $A_{m,ext}$ are calculated by the Eqs. (4.22) to (4.27). Other parameters required for the simulation are given in Table 5-10.

Table 5-10: Reactor and catalyst dimensions, and operating conditions.

| Simulation case | Notation and unit | Values |
|--|--|---|
| Reactor and catalyst: | | |
| molar specific heat at constant pressure | $C_{p,g}$ (J/(mol K)) | 30 |
| molar density of fluid (gas) | $\rho_{f,mol}$ (mol/m ³) = $p/(R T)$ | – |
| particle density of catalyst | ρ_b (kg/m ³) | 1910 (Ni/Al ₁₂ O ₁₉) |
| bulk density of catalyst | ρ_b (kg/m ³) | 1200 (Ni/Al ₁₂ O ₁₉) |
| superficial velocity | u_s (m/s) | 0.1 – 15 |
| particle diameter | d_p (m) | 0.006 |
| enthalpy of reaction | $\Delta_R H_{1273 K}$ (J/mol) | 31800 |
| Operating conditions: | | |
| inlet temperature | T (°C) | 1000 – 1200 |
| pressure | p (bar) | 1 |

The effective rate by the combined influence of internal and external mass transport is calculated as

$$r_{m,eff} = \left[\frac{1}{r_{m,pore}} + \frac{1}{r_{m,ext}} \right]^{-1} \quad (5.19)$$

Note that Eq. (5.19) is only an approximation because in the pore diffusion term the unknown surface concentration has to be considered (and not the gas phase values) and for the external mass transport, the equilibrium concentration is only established at the external surface, if the external mass transfer is the rate depending step. Hence, Eq. (5.19) is only correct, if only pore diffusion or only the external mass transport play a role. For the regime between these two extremes, Eq. (5.19) is only an approximation.

The equilibrium concentration of CO₂ ($C_{CO_2,eq}$) of the RWGS reaction can be calculated based on the following mass balances for oxygen, hydrogen and carbon:

$$O: 2C_{CO_2,in} + C_{CO,in} + C_{H_2O,in} = 2C_{CO_2,eq} + C_{CO,eq} + C_{H_2O,eq} \quad (5.20)$$

$$H: C_{H_2,in} + C_{H_2O,in} = C_{H_2,eq} + C_{H_2O,eq} \quad (5.21)$$

$$C: C_{CO_2,in} + C_{CO,in} = C_{CO_2,eq} + C_{CO,eq} \quad (5.22)$$

The equilibrium constant for the RWGS reaction ($K_p = K_c$) is defined as

$$K_p = \left(\frac{C_{CO} C_{H_2O}}{C_{CO_2} C_{H_2}} \right)_{eq} \quad (5.23)$$

Combination of the Eq. (5.20) to (5.23) leads to

$$C_{CO_2,eq} = \frac{(C_{CO_2,in} + C_{CO,in} - C_{CO_2,eq})(C_{CO_2,in} + C_{H_2O,in} - C_{CO_2,eq})}{K_p(C_{H_2,in} - C_{CO_2,in} - C_{CO_2,eq})} \quad (5.24)$$

Rewriting of Eq. (5.24) in the quadratic form $a x^2 + b x + c = 0$ yields

$$\begin{aligned} [K_p + 1] C_{CO_2,eq}^2 + [K_p C_{CO_2,in} - K_p C_{H_2,in} - C_{H_2O,in} - 2C_{CO_2,in} - \\ C_{CO,in}] C_{CO_2,eq} + [C_{CO_2,in}(C_{CO,in} + C_{H_2O,in}) + C_{CO,in} C_{H_2O,in} + C_{CO_2,in}^2] = 0 \end{aligned} \quad (5.25)$$

The equilibrium constant K_p for the RWGS reaction is given by Twigg [56] as

$$K_p = \left[\frac{1}{\exp(-0.29353 Z^3 + 0.63508 Z^2 + 4.1778 Z + 0.31688)} \right] \quad (5.26)$$

where $Z = \left[\frac{1000}{T(K)} \right] - 1$

5.4.2 Results of the simulations of technical RWGS reactors

In order to check, whether the external mass transfer has to be considered, the reactor simulation was done at first by using Eq. (5.19) for three different cases:

Case I: $k_{m,CO_2} \rightarrow \infty$

Case II: $\beta \rightarrow \infty$

Case III: regular model

The comparison of the conversion of CO_2 obtained over the reactor length at 1000 °C and 1200 °C for both the adiabatic and the isothermal reactor (Fig. 5-51) at the three different cases shows that there is almost no influence of the external mass transport on the effective reaction rate of CO_2 hydrogenation over the Ni catalyst. The effective reaction rate is only controlled by the interplay of pore diffusion and of the chemical reaction, which is the reason that case II and III lead to almost the same result (Fig. 5-51).

The CO_2 conversion obtained at inlet temperatures of 1000 °C and 1200 °C for both the adiabatic and isothermal case does not show a very big difference because of two reasons:

- (1) The difference of the equilibrium conversion at 1000 °C and 1200 °C is not very pronounced (82% and 87%, respectively, see Fig. 2-14 for $R = 3$).
- (2) The influence of pore diffusion is pronounced for both temperatures, because the calculated effectiveness factor is only about 3% and 4% at 1200 °C and 1000 °C, respectively. So the effective (apparent) activation energy is roughly half of the intrinsic value of 68.5 kJ/mol (Table 5-9). Hence, an increase of the temperature from 1000°C to 1200 °C only leads to an increase of the effective reaction rate constant by a factor of 1.6. As expected, this is also roughly the difference in reactor length needed to reach a certain conversion (see Fig. 5-51, regular model for isothermal conditions).

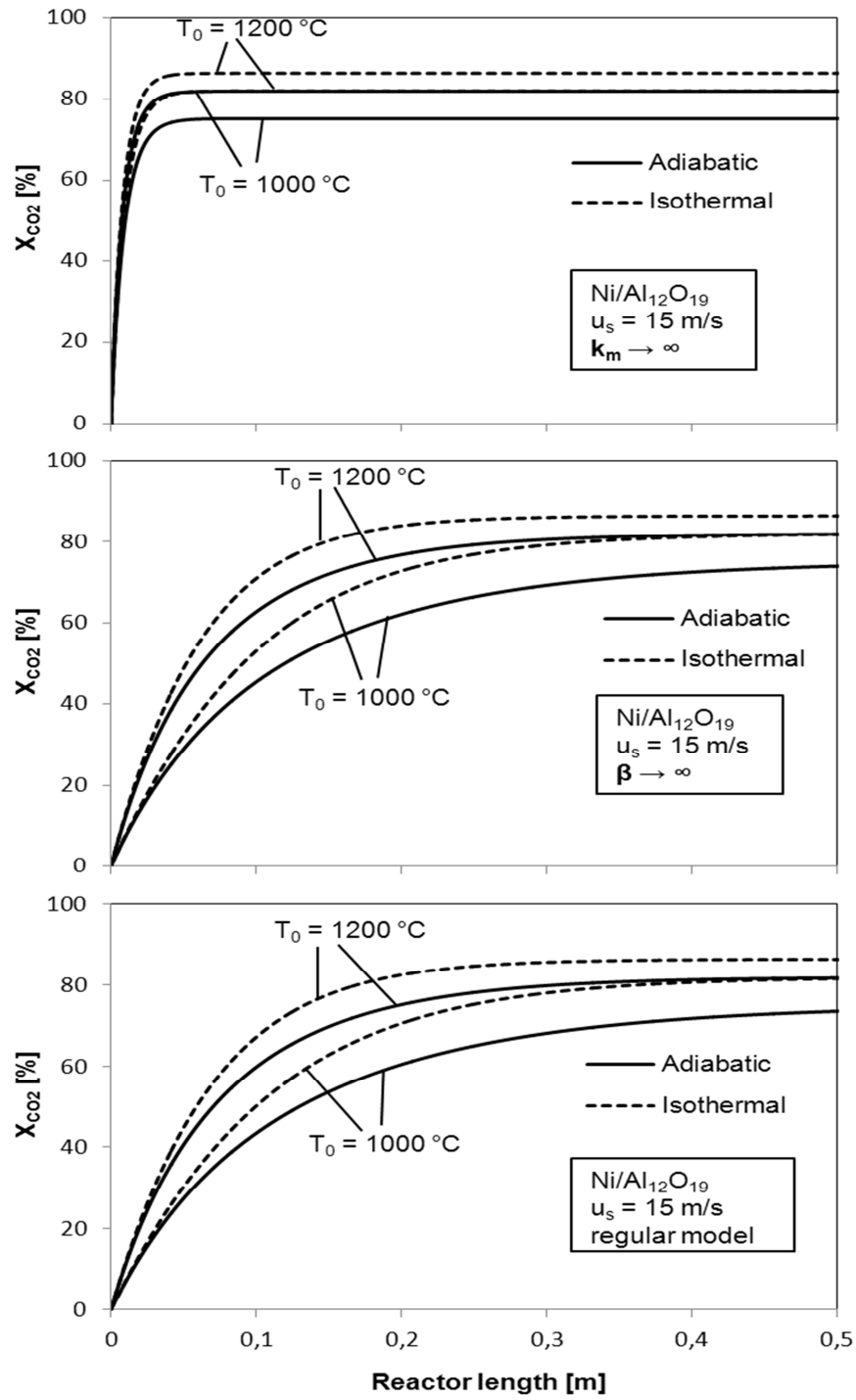


Fig. 5-51: Axial profiles of CO₂ conversion for the Ni/Al₁₂O₁₉ catalyst and three different cases (Eq. (5.19)); $k_{m,CO_2} \rightarrow \infty$, $\beta \rightarrow \infty$, and regular model ($H_2/CO_2 = 3$).

The simulated adiabatic temperature profiles at different gas superficial velocities along the axial reactor coordinate are shown in Fig. 5-52 both for Ni/Al₁₂O₁₉ and Al₂O₃ as catalyst. The reaction temperature decreases along the length due to the prevailing endothermic

RWGS reaction, i.e. the energy consumption by the reaction leads to a cooling of the gas. For an inlet gas temperature of 1200 °C and the highest superficial gas velocity of 15 m/s (at T_0), the adiabatic final temperature of 998 °C is reached at a reactor length of about 0.4 m for the Ni catalyst and at about 25 m for the Al_2O_3 catalyst. The respective residence times (related to the empty tube) are only about 30 ms for the Ni catalyst and about 2 s for the Al_2O_3 . For lower gas velocities, the required lengths (and residence times) are smaller.

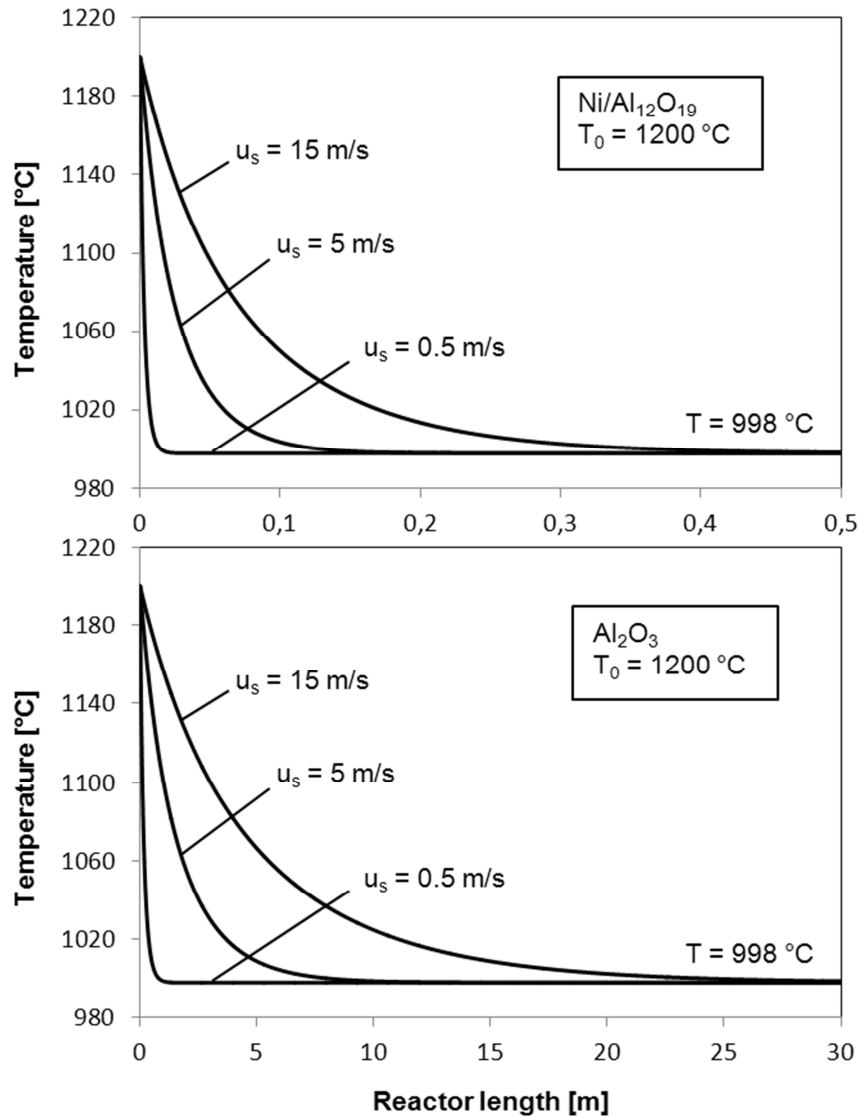


Fig. 5-52: Axial temperature profiles of an adiabatic reactor for Ni/Al₁₂O₁₉ and Al₂O₃ as catalysts ($\text{H}_2/\text{CO}_2 = 3$).

Similarly, the axial profiles of the CO₂ conversion are shown in Fig. 5-53 for the simulated adiabatic and isothermal case both for the Ni and Al₂O₃ catalyst. The conversion of CO₂ and

thus the yield of CO increases along the reactor length and reaches the maximum (equilibrium) value at the reactor outlet. As the gas superficial velocity increases, the reactor length required to reach the equilibrium also increases. As already stated, an increasing gas velocity also increases the required length of the reactor to reach (almost) the final equilibrium value. For the Ni catalyst and an inlet temperature of 1200 °C, an increase from 0.5 m/s to 15 m/s leads to an increase of the reactor length from about 0.013 m to 0.4 m for the adiabatic reactor and from 0.01 m to 0.3 m for the isothermal reactor.

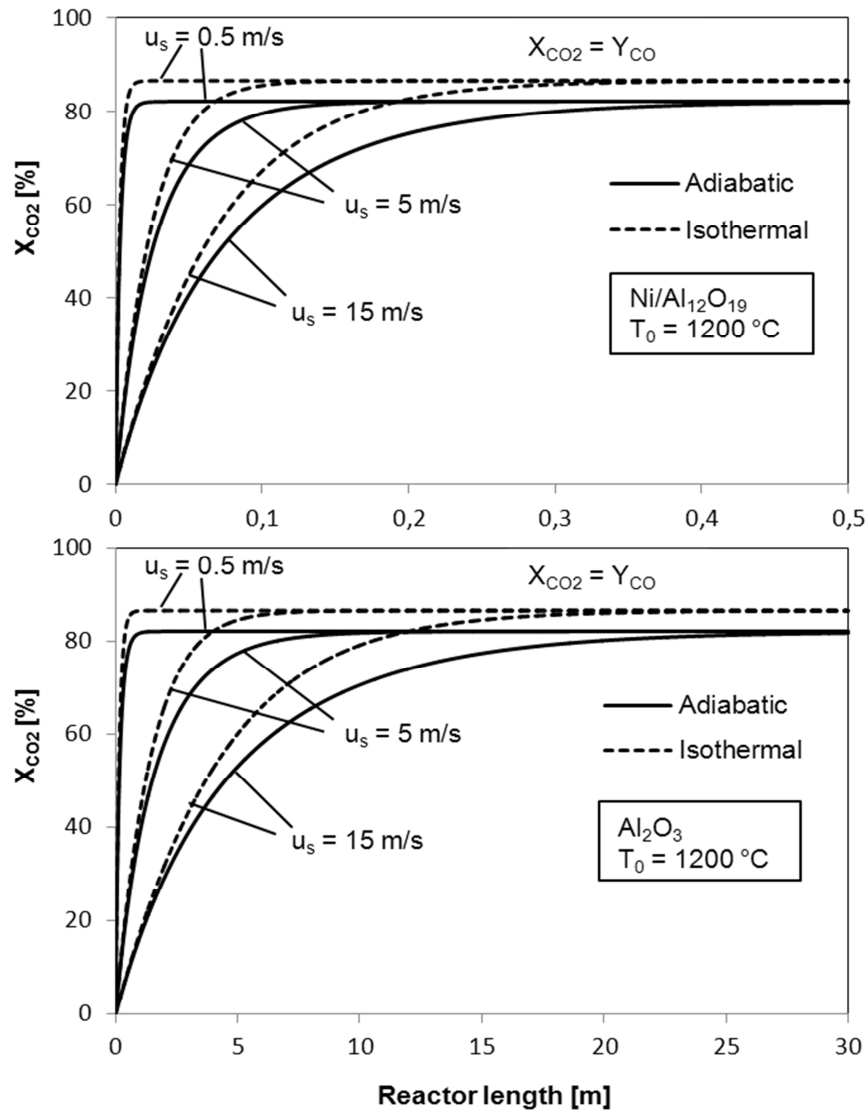


Fig. 5-53: Conversion of CO₂ over Ni/Al₁₂O₁₉ and Al₂O₃ catalysts at different gas superficial velocities versus axial reactor co-ordinate ($H_2/CO_2 = 3$).

The conversion of CO₂ to CO obtained at the reactor outlet is about 82% for the adiabatic reactor and 87% for the isothermal reactor.

Fig. 5-54 shows the conversion of CO_2 along the reactor length at different H_2/CO_2 ratios for the adiabatic and isothermal simulation (again both for the Ni and Al_2O_3 catalyst). As the ratio H_2/CO_2 increases, the conversion of CO_2 raises along the reactor length. For example, if the inlet ratio of H_2/CO_2 is increased from 1 to 6, the conversion of CO_2 at the reactor outlet increases from about 55% to 91% for the adiabatic reactor and from 62% to 93% for the isothermal reactor. But high inlet H_2/CO_2 ratios also increase the H_2/CO ratio of the produced syngas, which then may not be optimal for a subsequent Fischer Tropsch synthesis. The H_2/CO ratio of the syngas at the reactor outlet (R_{syngas}) for different H_2/CO_2 ratios of the feed to the RWGS reactor is shown in Fig. 5-55.

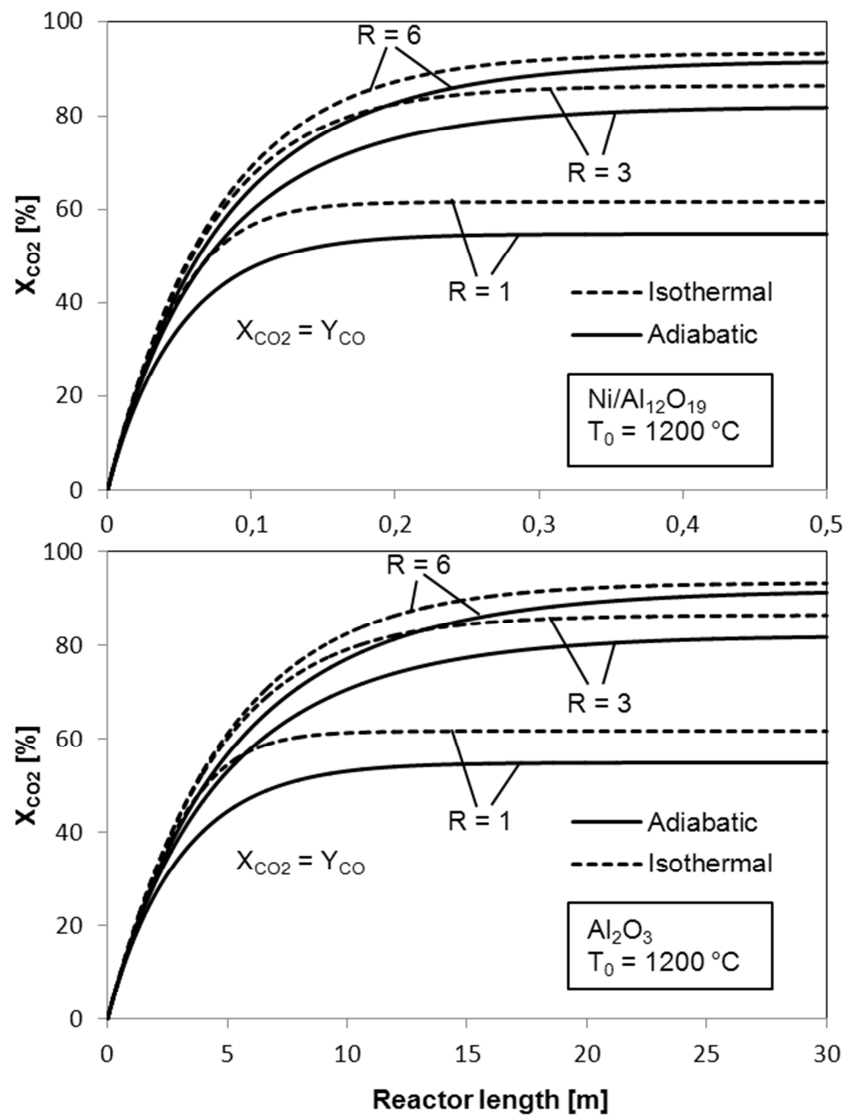


Fig. 5-54: Conversion of CO_2 over $\text{Ni}/\text{Al}_{12}\text{O}_{19}$ and Al_2O_3 catalysts at different inlet gas composition versus axial reactor co-ordinate ($u_s = 15$ m/s, $R = \text{H}_2/\text{CO}_2$).

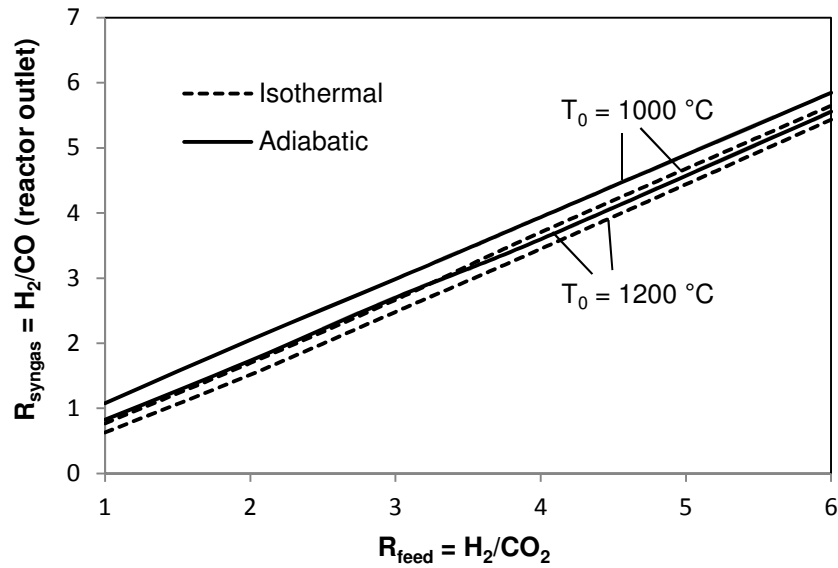


Fig. 5-55: Molar H_2/CO ratio of the syngas (R_{syngas}) at the reactor outlet for different molar H_2/CO_2 ratios of the feed (R_{feed}) to the RWGS reactor ($p = 1$ bar).

Fig. 5-55 indicates that an almost optimal H_2/CO ratio of the syngas of slightly above two (to account for the methanation, which always takes place during Fischer Tropsch) is reached for a H_2/CO_2 ratio of the feed of about three. This ratio was therefore used for further simulations.

As mentioned before, the reactor length required to get a particular conversion depends upon the gas inlet temperature, the gas superficial velocity, and the inlet gas composition. For the RWGS reaction over the $\text{Ni}/\text{Al}_{12}\text{O}_{19}$ catalyst (inlet temperature of $1200\text{ }^\circ\text{C}$, inlet H_2/CO_2 ratio of 3), the reactor length required to reach 99% of the equilibrium conversion in the adiabatic and isothermal case is shown in Fig. 5-56.

Fig. 5-57 shows the similar pattern for Al_2O_3 catalyst. As the effective rate of the RWGS reaction over Al_2O_3 is by about a factor of 40 lower compared to the Ni catalyst, the reactor length required is much higher compared to $\text{Ni}/\text{Al}_{12}\text{O}_{19}$ catalyst to get the same conversion.

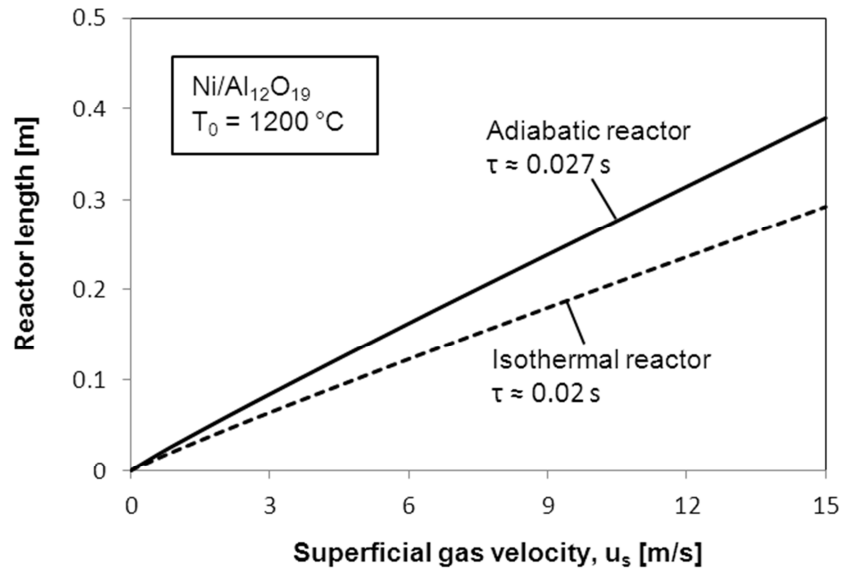


Fig. 5-56: Reactor length required for 99% of equilibrium conversion in adiabatic reactor ($X_{\text{CO}_2} = 81\%$) and isothermal reactor ($X_{\text{CO}_2} = 86\%$) versus superficial gas velocity over $\text{Ni}/\text{Al}_{12}\text{O}_{19}$ catalyst ($\text{H}_2/\text{CO}_2 = 3$, $p = 1\text{ bar}$).

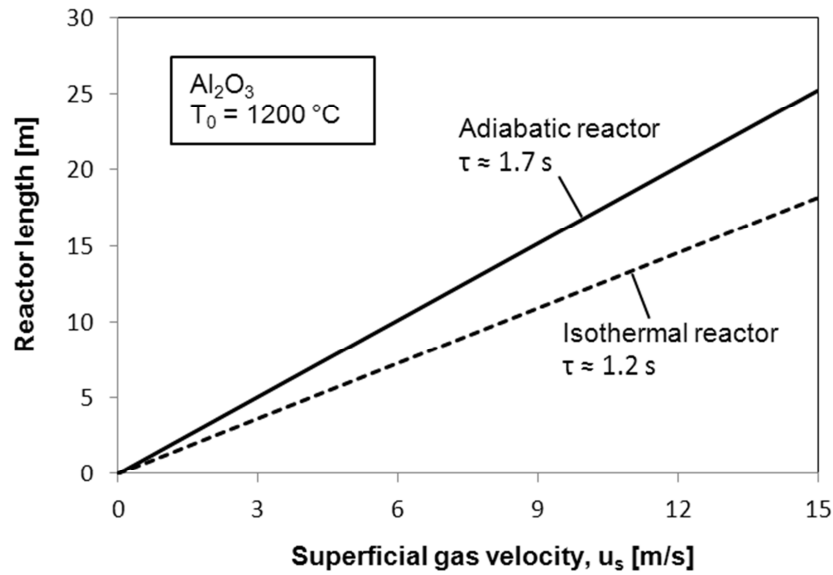


Fig. 5-57: Reactor length required for 99% of equilibrium conversion in adiabatic reactor ($X_{\text{CO}_2} = 81\%$) and isothermal reactor ($X_{\text{CO}_2} = 86\%$) versus superficial gas velocity over Al_2O_3 catalyst ($\text{H}_2/\text{CO}_2 = 3$, $p = 1\text{ bar}$).

5.4.3 Pressure drop in fixed bed technical RWGS reactors

According to *Ergun* [107], the pressure loss in a fixed (packed) bed is given by

$$\Delta p_b = \left[f_b \frac{L}{d_p} \frac{\rho_f u_s^2}{2} \right] \quad (5.27)$$

where ρ_f is the density of the fluid (kg/m^3), f_b the friction factor of a packed bed, which is given by the following equation based on the particle Reynolds number, $Re = u_s d_p / \nu$:

$$f_b = \frac{(1 - \epsilon_b)}{\epsilon_b^3} \left[3.5 + (1 - \epsilon_b) \frac{300}{Re} \right] \quad (5.28)$$

For non-spherical particles an equivalent particle diameter is used

$$d_p = \left[\frac{6 V_p}{A_{m,ext}} \right] \quad (5.29)$$

which is the diameter of a sphere with the same external surface area per unit volume as the actual particle.

For a packed bed of spheres (equal diameter, porosity $\epsilon_b = 0.4$), Eq. (5.28) simplifies to

$$f_b = 33 + \frac{1700}{Re} \quad (5.30)$$

The particle diameter and the fluid velocity have a strong influence on Δp_b . As we can see by insertion of Eq. (5.30) into Eq. (5.27), Δp_b is proportional to u_s / d_p^2 for low values of Re and to u_s^2 / d_p for high values.

The production of syngas by CO_2 hydrogenation would most probably been done at the typical pressure of the subsequent production of liquid fuels via Fischer Tropsch synthesis. Hence, a total pressure of 30 bar, a maximum pressure drop of 1 bar, and an inlet temperature of 1200 °C are assumed for the final simulation of a technical RWGS reactor. In addition, only adiabatic operation is subsequently considered, as this type of operation is much easier to realize in a technical reactor compared to isothermal operation. The fluid density and viscosity are calculated at 1100 °C (average temperature in adiabatic reactor). Values of the required parameters to calculate Δp_b are given in Table 5-11. Fig. 5-58 shows that the pressure drop per meter length strongly increases with increasing superficial gas velocity. In case of the Al_2O_3 catalyst and an adiabatic fixed bed reactor, the superficial gas

velocity should be less than 1.7 m/s to limit the pressure drop to the assumed value of 1 bar. The reactor length is then 2.8 m (to get 99% of the equilibrium conversion) (Fig. 5-57). At this velocity, $\Delta p_b/L$ is about 0.38 bar/m and so $\Delta p_b \approx 1$ bar over the total reactor length. In case of the Ni/Al₁₂O₁₉ catalyst and at same superficial gas velocity of 1.7 m/s, a reactor length of 0.05 m (Fig. 5-56) would be sufficient and Δp_b would only be about 0.02 bar.

The respective gas velocity for the Ni/Al₁₂O₁₉ catalyst, where the assumed limiting value of Δp_b of 1 bar is reached, is 6.7 m/s (reactor length of 0.18 m).

Table 5-11: Model parameters used to calculate the pressure drop of a RWGS reactor.

| Parameters (30 bar, 1100 °C) | Values |
|--|-------------------|
| Kinematic viscosity (ν), m ² /s | $6 \cdot 10^{-6}$ |
| Fluid density (ρ_f), kg/m ³ | 4.65 |
| Particle diameter (d_p), m | 0.006 |
| Particle Reynolds number (Re) at $u_s = 1$ m/s | 1000 |
| Friction factor (f_b) at $u_s = 1$ m/s | 34.7 |

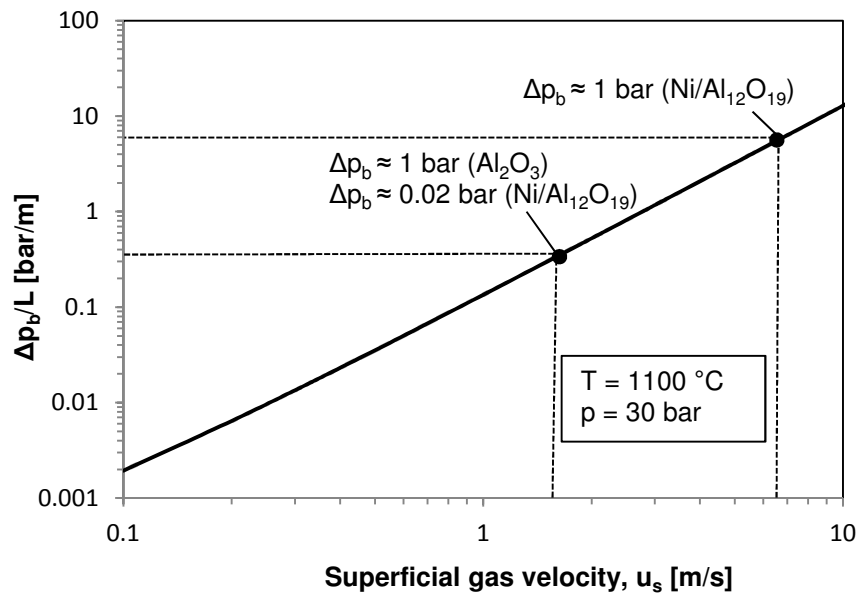


Fig. 5-58: Pressure drop in fixed bed reactor per meter length for different superficial gas velocities.

5.4.4 Estimation of the size of the RWGS reactor with regard to a subsequent Fischer Tropsch fixed bed reactor

It is interesting to estimate the size of an adiabatic RWGS reactor (both for the investigated Ni- and the Al₂O₃ catalyst) needed for a subsequent Fischer-Tropsch (FT) reactor. According to the data given by *Jess* and *Kern* [48], the parameters of a technical FT reactor are as follows:

- The FT reactor is a multitubular reactor with 8000 tubes each with a diameter of 5 cm.
- The total volume rate of fresh (dry) syngas is about 160,000 m³/h (NTP).
- The total pressure is around 30 bar.

The reactor length required to get 99% of the equilibrium conversion of CO₂ is calculated as

$$L_{99\% \text{ } x_{\text{CO}_2,eq}} = \tau_i u_s \quad (i: \text{Ni- or Al}_2\text{O}_3\text{-catalyst}) \quad (5.31)$$

And the length to reach a certain Δp_b (in this calculation $\Delta p_b = 1$ bar) as

$$L_{\Delta p_b} = \frac{2 \Delta p_b d_p}{f_b \rho_f u_s^2} \quad (5.32)$$

For the estimation of the design of the adiabatic RWGS reactor, the following assumptions were made:

- For the assumed volume rate of dry syngas of 160,000 m³/h (NTP), the volume rate through the RWGS reactor is 201,000 m³/h (NTP), because for a CO₂ conversion of 81% (reached in adiabatic operation) 20% of the syngas is water, which is separated. At a mean temperature of 1100 °C and 30 bar, this corresponds to 34,000 m³/h (= 9.4 m³/s).
- For the Ni/Al₁₂O₁₉ catalyst, the residence time required to get 99% of the equilibrium conversion of CO₂ is 0.027 s (see Fig. 5-56); the respective value for the Al₂O₃ catalyst is 1.65 s (see Fig. 5-57). (Remark: Pore diffusion is only determined by Knudsen diffusion. Hence, there is practically no influence of the total pressure on the effective reaction rate (constant) and thus also not on the required residence time.)
- For the pressure drop in the RWGS reactor a limiting value of 1 bar is assumed.

The dimensions of the fixed bed of the RWGS reactor are then estimated as follows.

- (a) Ni/Al₁₂O₁₉ catalyst: At a superficial gas velocity of 6.7 m/s, the reactor length required to get the 99% of the equilibrium conversion of CO₂ is 0.18 m and the assumed pressure

drop of 1 bar is also just reached (Fig. 5-59). As this length is rather small, a length of 0.5 m can be assumed to be appropriate (to be on the safe side with regard to bypass effect etc.), even if the pressure drop then increases to 2.5 bar. The cross-sectional area of the RWGS reactor is 1.4 m^2 (ratio of volume rate of $9.4 \text{ m}^3/\text{s}$ and gas velocity of 6.7 m/s), the reactor diameter 1.3 m, and the volume of the catalyst is 0.7 m^3 .

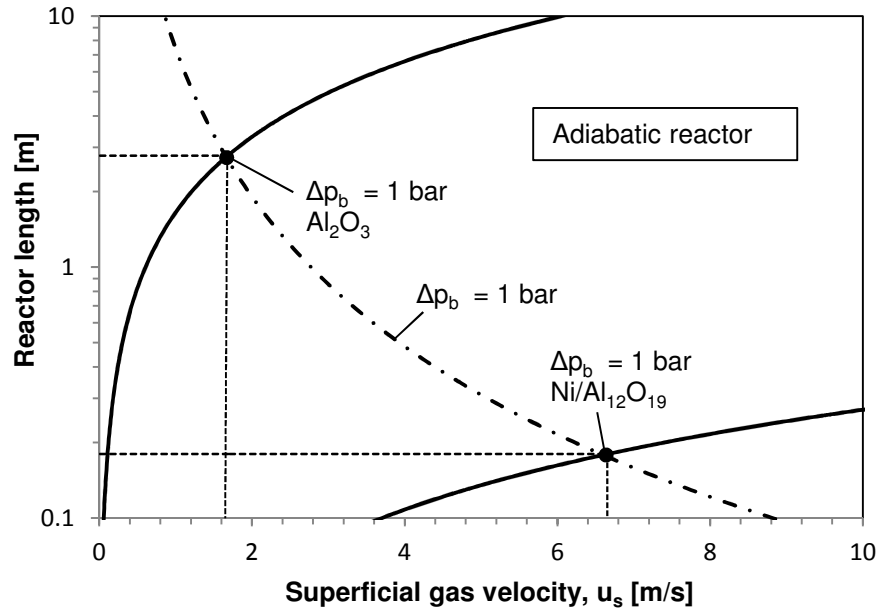


Fig. 5-59: Reactor length versus superficial gas velocity: dashed-dotted line: length, where a pressure drop of 1 bar is just reached; lines: length required to reach 99% of equilibrium conversion ($X_{\text{CO}_2} = 81\%$).

- (b) Al_2O_3 catalyst: Now a lower superficial gas velocity of 1.7 m/s has to be adjusted to reach 99% of the equilibrium conversion of CO_2 and also a pressure drop of 1 bar (Fig. 5-59). The corresponding length of the fixed bed is about 2.8 m, and the cross-sectional area 5.5 m^2 (2.6 m diameter). Increasing the reactor length by 1 m (total length of 3.8 m) to be on the safe side then corresponds to a volume of the Al_2O_3 catalyst of about 21 m^3 , which is by a factor of 30 higher compared to the Ni-catalyst.

These estimations clearly show that for both catalysts, the required volume is rather small to deliver the syngas for a huge technical FT reactor. The question, whether the Ni- or the Al-catalyst should be used is then a question of the costs of the catalyst and even more important of the long term stability of the catalyst, which should be determined by further investigations.

6. Summary and outline

Motivation and background of work: The consumption of fossil fuels is growing continuously and with that the release of CO₂ into the atmosphere by their combustion. Every year billion tons of anthropogenic CO₂ are emitted into the atmosphere, which has an impact on the environment such as global warming. The capture and storage of CO₂ is questionable. Therefore the conversion of CO₂ to useful chemicals and fuels is probably a more attractive option. Hence, there is a considerable need for research on the utilization of CO₂ in the production of liquid fuels. As a concept for sustainable development, it is possible to produce liquid fuels from CO₂ by the following steps:

- Capture and separation of CO₂ from flue gas (or in future even from air),
- production of H₂ by high temperature water electrolysis and non-fossil electricity,
- conversion of CO₂ to CO by the reverse water gas shift reaction, and finally
- conversion of CO (and H₂) to liquid fuels via Fischer Tropsch synthesis.

In this work the CO₂ hydrogenation was investigated mainly at high temperatures over a Ni/Al₁₂O₁₉ catalyst, i.e. at conditions where the reverse water gas shift reaction is favoured thermodynamically and CO and H₂O are the main products.

Outline of the experimental study: The experimental studies on CO₂ hydrogenation, CO hydrogenation, and the water gas shift reaction over the Ni catalyst were carried in a lab scale fixed bed reactor.

The reactions were carried out in the wide temperature range at atmospheric pressure. The influence of reaction parameters such as reaction temperature, concentration of reactants, residence time, and catalyst particle size was studied. The kinetics were determined for all three reactions (i.e. CO₂ hydrogenation, CO hydrogenation, and water gas shift reaction), i.e. the intrinsic and the effective kinetics (influence of internal and external diffusion) were determined. Beside of the Ni catalyst, other catalysts such as Al₂O₃ were tested.

Results of the experiments: The results of the experiments can be summarised as follows.

Hydrogenation of CO₂: To get a basic idea about the activity of the catalysts for CO₂ hydrogenation, various commercial catalysts were tested (see Table 5-4). Among all the

studied catalysts, Ni/Al₁₂O₁₉ exhibits the highest activity. Therefore, the detailed kinetic study of CO₂ hydrogenation was performed using this catalyst.

In CO₂ hydrogenation, the conversion of CO₂ and the yield of CO increases with increase in temperature (300 to 950 °C) while the yield of methane increases up to 500 °C and then continuously decreases due to thermodynamic limitations. At high temperatures, the equilibrium conversion was nearly achieved. For example, at 950 °C and atmospheric pressure about 94% of the equilibrium conversion was reached at the residence time of only 18.3 ms (empty tube) with a catalyst particle size of less than 0.5 mm size, where the external mass transfer controlled regime does not have an influence. The long time on stream behaviour of the Ni catalyst at 900 °C and atmospheric pressure shows a very good stability. The intrinsic kinetic parameters (activation energy and frequency factor) calculated by the Arrhenius equation are 65 kJ/mol and $5.55 \cdot 10^2 \text{ m}^{1.5} \text{ mol}^{0.5} \text{ kg}^{-1} \text{ s}^{-1}$, respectively. The reaction rate of CO₂ hydrogenation can be described by the following equation:

$$r_{m,CO_2} = k_{m,CO_2} C_{CO_2}^{0.1} C_{H_2}^{0.4} \quad (6-1)$$

The influence of mass transfer resistances on the effective reaction rate of CO₂ hydrogenation was calculated for the spherical Ni catalyst. The comparison of the experimental results with the calculated ones shows a good agreement for the combined influence of the pore diffusion and external diffusion on the effective reaction rate for the used shell catalyst. The catalyst performance is more and more controlled by external mass transfer above a temperature of about 900 °C, at least for the low gas velocities of the experiments.

Hydrogenation (methanation) of CO: The hydrogenation of CO is an exothermic reaction and thermodynamically favored at low temperatures. The conversion of CO increases with increasing temperature up to 450 °C and then decreases. In the temperature range of 480 to 710 °C the catalyst deactivates due to coke formation.

The reaction orders obtained at 340 °C and atmospheric pressure in CO hydrogenation were -0.3 and 0.7 for CO and H₂, respectively. The activation energy and frequency factor are 102 kJ/mol and $2.35 \cdot 10^5 \text{ m}^{1.2} \text{ mol}^{0.6} \text{ kg}^{-1} \text{ s}^{-1}$, respectively.

The mass transfer calculations for the shell catalyst show an influence of pore diffusion above a temperature of about 420 °C. Due to the catalyst deactivation, the calculated values

for the effective reaction rate by the combined influence of pore and external diffusion are much higher than the measured ones in the high temperature range.

Water gas shift reaction (WGS): The water gas shift reaction was also studied as the reverse reaction of CO₂ hydrogenation. The reaction is exothermic and therefore thermodynamically most favoured at low temperatures. H₂ and CO₂ are the main products of the WGS reaction.

The conversion of CO and the yield of CO₂ rise with temperature up to 450 °C, and no CH₄ formation as well as catalyst deactivation was observed. In the temperature range of 500 to 700 °C, the Ni catalyst shows deactivation due to coke formation.

Both reactant concentrations (CO, H₂O) show a positive impact on the WGS reaction while the addition of product components (CO₂, H₂) to the reaction mixture shows a negative impact. The reaction orders obtained for CO, H₂O, CO₂, and H₂ are 0.8, 0.4, -0.1, and -0.15, respectively. Almost no CH₄ formation was observed.

The activation energy E_A and frequency factor $k_{m,0}$ over the Ni catalyst for the WGS reaction are 96 kJ/mol and $3.46 \cdot 10^5 \text{ m}^{3.6} \text{ mol}^{-0.2} \text{ kg}^{-1} \text{ s}^{-1}$, respectively. Mass transfer calculations for the shell catalyst show an influence of pore diffusion above 350 °C. Due to catalyst deactivation in a temperature range from 500 to 700 °C, the measured values of the effective reaction rate decreases. For temperatures of more than 900 °C, the effective reaction rate is also influenced by external mass transfer.

Finally, a one dimensional adiabatic and isothermal fixed bed reactor model was used to simulate a technical reactor for the production of syngas via CO₂ hydrogenation over Ni/Al₁₂O₁₉ catalyst as well as for Al₂O₃ as catalyst. The axial profiles of temperature and conversion were calculated.

The effective rate of the RWGS reaction over Ni/Al₁₂O₁₉ catalyst is by about a factor of 40 higher compared to the Al₂O₃ catalyst, and thus the reactor length required is much lower compared to the Al₂O₃catalyst to get the same conversion.

Outline

The long term stability of the Ni and the Al₂O₃catalyst should be tested in more detail and - if possible - for a period of several weeks. Thereby a temperature of even more than 1000 °C should be realized by an appropriate reactor and heating system.

7. Zusammenfassung und Ausblick

Motivation und Hintergrund der Arbeit: Aufgrund der weltweit wachsenden Industrialisierung und dem damit verbundenen steigenden Wohlstand wird der Verbrauch fossiler Energieträger (Erdgas, Erdöl und Kohle) vermutlich weiterhin wachsen. Dies bedeutet auch, dass der CO₂-Ausstoß in die Atmosphäre zunehmen wird, was voraussichtlich zu einer weiteren Verstärkung des natürlichen Treibhauseffektes führt.

Um einen weiteren Anstieg der CO₂-Konzentration in der Atmosphäre zu verhindern bzw. zu begrenzen, wird eine CO₂-Abtrennung aus Kraftwerksrauchgasen und eine anschließende Sequestrierung erwogen (CCS-Technologie, *Carbon Capture and Storage*). Diesem Konzept steht aber ein Mangel an hierfür notwendigen Lagerstätten entgegen. Außerdem ist noch nicht eine sichere unterirdische Lagerung des CO₂ über einen sehr langen Zeitraum gewährleistet. Hinzu kommt eine möglicherweise mangelnde Akzeptanz in der Bevölkerung.

Eine Alternative zur CCS-Technologie ist die chemische Nutzung von (abgetrenntem) CO₂. CO₂ kann als Synthesebaustein in der chemischen Industrie genutzt werden oder als Einsatzmaterial zur Kraftstoffproduktion dienen. Der letztgenannte Ansatz ist im Hinblick auf die Klimaproblematik sicherlich der sinnvollere, da im Vergleich zu den Produkten der industriellen organischen Chemie deutlich mehr Kraftstoffe (wie Benzin und Dieselöl) verbraucht werden. Derzeit besteht allerdings noch ein erheblicher Forschungsbedarf, um CO₂ als Synthesebaustein bzw. für die technische Herstellung von Kraftstoffen einzusetzen.

Ein Konzept zur nachhaltigen Produktion von Kohlenwasserstoffen auf CO₂-Basis besteht aus folgenden Reaktionsschritten:

- Abtrennung und Reinigung des CO₂ aus Abgasen (oder zukünftig aus der Luft),
- Wasserstoffproduktion mittels Hochtemperaturwasserelektrolyse auf der Basis von Strom aus nicht fossilen Energiequellen (Wind- oder Sonnenenergie),
- Reverse Wasser-Gas-Shift (RWGS) Reaktion zur Umwandlung von CO₂ mit Wasserstoff in CO und schließlich
- die Fischer-Tropsch Synthese zur Produktion von Kohlenwasserstoffen aus dem vorher erzeugten Synthesegas (CO/H₂).

In der vorliegenden Arbeit wurde der dritte Schritt, die RWGS-Reaktion, untersucht. Dabei wurde vor allem ein aluminiumoxidgeträgerter Nickelkatalysator ($\text{Ni}/\text{Al}_{12}\text{O}_{19}$) verwendet. Da die RWGS-Reaktion endotherm verläuft, wurde die Reaktion bei hohen Temperaturen durchgeführt, um CO (und H_2O) als Hauptprodukte zu erhalten.

Übersicht zu den experimentellen Untersuchungen: Die experimentellen Untersuchungen aller Teilschritte (Methanisierung, Wasser-Gas-Shift bzw. RWGS) wurden in einem Festbettreaktor unter Verwendung des oben genannten Nickelkatalysators bei Normaldruck durchgeführt. Neben der Temperatur wurden auch die Konzentrationen der Reaktanten, die Verweilzeit und die Katalysatorpartikelgröße variiert. Für jede Reaktion erfolgte eine Bestimmung sowohl der intrinsischen als auch der effektiven Reaktionskinetik. Neben dem Nickelkatalysator wurden auch andere Katalysatoren wie z.B. Al_2O_3 getestet.

Die **experimentellen Ergebnisse** lassen sich folgendermaßen zusammenfassen.

CO₂-Hydrierung: Zunächst wurden verschiedene kommerzielle Katalysatoren untersucht (siehe Tab. 5-4), um ein grundsätzliches Verständnis für die Aktivität der Katalysatoren für die CO₂-Hydrierung zu erhalten. Hierbei zeigte der $\text{Ni}/\text{Al}_{12}\text{O}_{19}$ -Katalysator die höchste Aktivität. Daher wurden die weitergehenden kinetischen Untersuchungen zur CO₂-Hydrierung mit diesem Katalysator durchgeführt.

Erwartungsgemäß erhöhen sich der CO₂-Umsatz und die CO-Ausbeute mit steigender Temperatur (300 – 950 °C). Bis zu einer Temperatur von 500 °C steigt zunächst auch die Methanausbeute an, um dann aufgrund der thermodynamischen Limitierung wieder abzufallen. Bei hohen Temperaturen wurden Umsätze erzielt, die sehr nahe am Gleichgewicht liegen. So konnte beispielsweise bei 950 °C ein Umsatz von 94 % des Gleichgewichtsumsatzes erhalten werden (leerrohrbezogene Verweilzeit: 18 ms). Die Partikelgröße wurde mit weniger als 0,5 mm so gewählt, dass der äußere Stofftransport keinen Einfluss hat. Der Nickelkatalysator zeigte bei 900 °C zudem eine sehr gute Langzeitstabilität. Die Berechnung der intrinsischen kinetischen Parameter ergab eine Aktivierungsenergie von 65 kJ/mol und einen Häufigkeitsfaktor von $5,55 \cdot 10^2 \text{ m}^{1,5} \text{ mol}^{0,5} \text{ kg}^{-1} \text{ s}^{-1}$. Die Reaktionsrate der CO₂-Hydrierung kann durch folgenden Ansatz beschrieben werden:

$$r_{m,\text{CO}_2} = k_{m,\text{CO}_2} C_{\text{CO}_2}^{0,1} C_{\text{H}_2}^{0,4} \quad (7-1)$$

Die Berechnung des Stofftransporteinflusses auf die effektive Reaktionsrate der CO₂-Hydrierung zeigt, dass die experimentellen und berechneten Ergebnisse gut übereinstimmen. Bei dem verwendeten Schalenkatalysator (Durchmesser 3 mm, Schichtdicke 0,5 mm) beeinflusst sowohl die Porendiffusion als auch der externe Stofftransport die effektive Reaktionsrate. Bei den experimentell eingestellten geringen Gasgeschwindigkeiten wird die Katalysatorleistung oberhalb von 900 °C zunehmend durch den externen Massentransfer bestimmt.

CO-Hydrierung (Methanisierung): Die Methanisierung ist exotherm und somit bei niedrigen Temperaturen thermodynamisch begünstigt. Daher steigt der CO-Umsatz mit wachsender Temperatur an, um ab ca. 450 °C schließlich zu fallen. Zwischen 480 und 710 °C deaktiviert der Katalysator aufgrund der hier einsetzenden Koksbildung.

Die Reaktionsordnungen wurden bei 340 °C und Atmosphärendruck bestimmt. Für CO ergibt sich ein Wert von -0,3 und für Wasserstoff von 0,7. Die Aktivierungsenergie beträgt 102 kJ/mol und der Häufigkeitsfaktor hat einen Wert von $2,35 \cdot 10^5 \text{ m}^{1,2} \text{ mol}^{0,6} \text{ kg}^{-1} \text{ s}^{-1}$.

Die Berechnungen zum Stofftransport lassen für den Schalenkatalysator einen Einfluss der Porendiffusion oberhalb von 420 °C erwarten. Die berechneten Werte der effektiven Reaktionsrate weichen allerdings bei hohen Temperaturen von den experimentellen Werten ab. Dies ist auf die dann auftretende Deaktivierung des Katalysators zurückzuführen.

Wasser-Gas-Shift Reaktion (WGS): Die WGS-Reaktion wurde ebenfalls untersucht, da es sich hier um die Rückreaktion der CO₂-Hydrierung (RWGS) handelt. Die Hauptprodukte der WGS-Reaktion sind daher Wasserstoff und Kohlendioxid. Diese Reaktion ist exotherm und wird folglich **bei** niedrigen Temperaturen thermodynamisch begünstigt.

Bis zu einer Temperatur von 450 °C erhöhen sich sowohl der CO-Umsatz als auch die CO₂-Ausbeute. Gleichzeitig konnte in dem untersuchten Temperaturfenster weder eine Methanbildung noch eine Deaktivierung des Katalysators beobachtet werden. Im Temperaturbereich von 500 bis 700 °C zeigt der Nickelkatalysator eine Deaktivierung, die durch eine Verkokung des Katalysators hervorgerufen wird.

Die Zugabe beider Reaktanten (CO, H₂O) übt einen positiven Einfluss auf die WGS-Reaktion aus, während (wie zu erwarten) die Beimischung der Produkte (CO₂, H₂) einen negativen Einfluss auf die Reaktionsrate aufweist. Die Bestimmung der Reaktionsordnung für die einzelnen Komponenten ergab: 0,8 (CO), 0,4 (H₂O), -0,1 (CO₂) und -0,15 (H₂). Die Bildung von Methan fand im untersuchten Parameterbereich nur untergeordnet statt.

Die Aktivierungsenergie der WGS-Reaktion (Ni-Katalysator) beträgt 96 kJ/mol. Der Wert des Häufigkeitsfaktors liegt bei $3,46 \cdot 10^5 \text{ m}^{3,6} \text{ mol}^{-0,2} \text{ kg}^{-1} \text{ s}^{-1}$. Stofftransportberechnungen für den Schalenkatalysator zeigen oberhalb von 350 °C einen Einfluss der Porendiffusion. Bedingt durch eine Katalysatordeaktivierung nimmt die effektive Reaktionsrate im Temperaturbereich zwischen 500 und 700 °C ab. Oberhalb von 900 °C wird die effektive Reaktionsgeschwindigkeit mehr und mehr durch den externen Massentransfer bestimmt.

Zur Modellierung eines technischen Reaktors zur Herstellung von Synthesegas durch die CO₂-Hydrierung wurde für beide Katalysatoren (Ni/Al₁₂O₁₉; Al₂O₃) das Modell eines ein-dimensionalen Festbettreaktors verwendet, d.h. die axialen Temperatur- und Umsatz-Profile wurden berechnet. Dabei wurde der adiabate und auch der isotherme Fall berücksichtigt.

Die effektive Reaktionsrate der RWGS-Reaktion am Ni/Al₁₂O₁₉-Katalysator ist im Vergleich zum Al₂O₃-Katalysator um den Faktor 40 höher. Für einen gegebenen Umsatz kann die Reaktorlänge für den Ni-Katalysator entsprechend wesentlich kürzer gewählt werden.

Ausblick

Ausgehend von den in dieser Arbeit erhaltenen Ergebnissen sollten in weiterführenden Untersuchungen sowohl für den Ni-Katalysator als auch für den Al₂O₃-Katalysator ihre Langzeitstabilitäten untersucht werden. Hierzu sind Versuchszeiten von einigen Wochen anzustreben, um aussagekräftige Daten zu generieren. Weiterhin sollten Temperaturen von mehr als 1000 °C eingestellt werden, da dann der erreichbare CO₂-Umsatz bei der RWGS allein schon aus thermodynamischen Gründen noch höher ist (> 90%). Hierzu muss die bestehende Versuchsanlage mit einem Reaktor, der diesen Temperaturen standhält, sowie einem entsprechenden Heizsystem ausgestattet werden.

Appendix A

A.1 Utilization of CO₂ in catalytic conversion processes

The detailed description for the synthesis of value added products using CO₂ is given in this section.

A.1.1 Salicylic acid formation

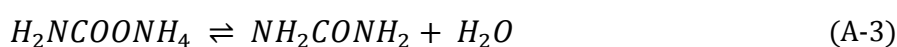
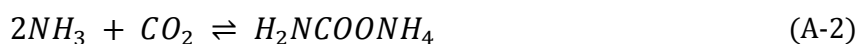
The direct synthesis of salicylic acid via the coupling of CO₂ with phenol is a “green process”, useful for the chemical fixation of CO₂. Salicylic acid is widely used in the industry as a raw material and intermediate for the production of pharmaceutical and fine chemicals.



Salicylic acid can be obtained by carboxylation of phenol with a carbon dioxide in presence of Lewis acid catalysts. AlBr₃ as a catalyst showed the best activity and selectivity towards salicylic acid among the various Lewis acids examined [108]. At 80 °C and 8 MPa, the yield of salicylic acid reached to 60% with the selectivity of 100% in 1 h. Several types of base metal oxides such as alumina, zirconia, ceria, and alkali metal and alkaline earth metal salts have been used for the synthesis of salicylic acid [109, 110]. Potassium carbonate as a catalyst under optimum condition yields 68% of salicylic acid with 99% selectivity. The systematic investigation for the direct reaction of supercritical CO₂ and phenol over the catalysts like ZrO₂, TiO₂, and KF/NaY+Mn²⁺, ZrO₂ was investigated [1].

A.1.2 Synthesis of urea and urea derivatives

The process of urea synthesis from carbon dioxide and ammonia was developed in 1922, and is called the Bosch-Meiser urea process. This non-catalytic process still exists and operates at relatively high pressure and high temperature.



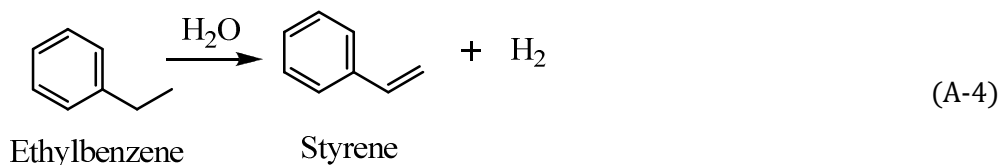
The production of urea involves formation of ammonium carbamate ($\text{NH}_2\text{COONH}_4$) using ammonia and CO_2 . Ammonium carbamate subsequently gets dehydrated into urea and water by the application of heat. The first reaction is fast, exothermic, and basically goes to completion, while the second one is relatively slow, endothermic, and does not go to completion [111]. Both of these reactions are reversible and therefore ammonia and carbon dioxide exit the reactor along with ammonium carbamate and urea. Thus, the conversion based on CO_2 is usually in the order 50 to 80% [111]. The components of this mixture in the product stream are then separated by stripping off gaseous ammonia followed by carbon dioxide.

The worldwide urea production in 2008 was 146 million metric tons which corresponds to 107 million metric tons of CO_2 consumption per annum [112]. Hence in the chemical industry, only this process has a certain potential of CO_2 reduction. Urea is mainly used for fertilizers but urea derivatives are used in the various other areas such as agrochemicals, pharmaceuticals, antioxidants in gasoline, and corrosion inhibitors [113]. Commercially urea derivatives are synthesised by using toxic phosgene as well as carbon monoxide. In a new approach, urea derivatives are produced by using amines and CO_2 as a carbonyl agent via catalytic and non-catalytic processes. The carbonylation of amines using CO_2 is simple, safe, and a clean process which avoids the use of poisonous compounds like phosgene and CO [114, 115]. The reaction of CO_2 with primary aliphatic amines also leads to urea derivative [114]. The process using the ionic liquid [Bmim]Cl with CsOH as catalyst yields about 98% of an urea derivative [115].

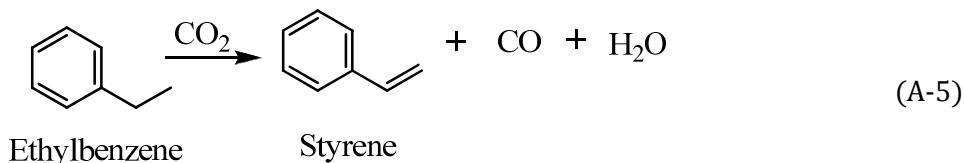
A.1.3 Styrene synthesis

Commercially styrene is produced by ethylbenzene dehydrogenation using potassium promoted iron oxide as a catalyst with a large excess of superheated steam at 600 to 650 °C. The steam plays an important role in ethylbenzene dehydrogenation as it shifts the equilibrium towards higher conversions, decreases the amount of coke formation and supply the heat for the reaction. A new route uses carbon dioxide for the dehydrogenation:

Conventional route:



New CO₂-based route:



The catalytic conversion of ethylbenzene using CO₂ have been discussed recently by *Park et al.* [116]. The direct utilization of CO₂ as an oxidant in the dehydrogenation of ethylbenzene to styrene offers several advantages. The main advantages shown in different studies [117-119] are the acceleration of the reaction rate, the drop in temperature, the enhancement of the conversion of ethylbenzene and of the selectivity. Moreover, the energy consumption for the ethylbenzene dehydrogenation using carbon dioxide is much lower than the currently operating process using steam [116].

The dehydrogenation of ethylbenzene to styrene in the presence of CO₂ was also studied over MnO₂-ZrO₂ [117], SnO₂-ZrO₂ mixed oxide nano-composite [118], cromia based catalyst [119], Co, Mo and CoMo catalysts supported on natural and aluminium-pillared clays [120], and a CeO₂-ZrO₂ mixed oxide supported SBA-15 catalyst [121]. In these catalytic systems, acidic and basic sites cooperatively activate CO₂ as well as ethylbenzene, which lead to a higher conversion of ethylbenzene. An attempt to use CO₂ as a diluent and oxidant over an activated carbon-supported iron catalyst have made by *Sugino et al.* [122]. The addition of 20 to 30 mol% lithium nitrates to the iron catalyst resulted in a significant increase in the catalytic activity.

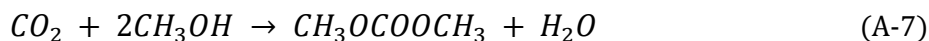
A.1.4 Dimethyl carbonate (DMC) synthesis

The conventional DMC synthesis use toxic phosgene. The use of carbon dioxide in the synthesis of DMC presents an environmentally friendly and attractive approach since it replaces phosgene and chlorine [123, 124].

Conventional route:



New CO₂-based route:

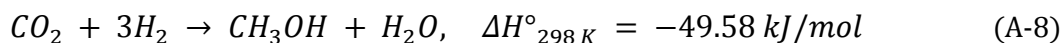


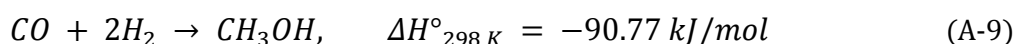
DMC has been synthesized using CO₂ and methanol over solid oxide catalysts like ZrO₂ [125, 126]. The dissociative adsorption of CO₂ occurs faster than the adsorption of methanol on ZrO₂ and species formed from methanol are bound more strongly. DMC also has been synthesized using base catalysts like K₂CO₃, Na₂CO₃, Cs₂CO₃ and CH₃I as a promoter [127]. The use of an ionic liquid along with CH₃I as a promoter over KOH catalyst shows an increase in the yield of DMC [128]. The utilization of CO₂ for synthesis of DMC is very beneficial because DMC itself is a unique molecule and can be used in new environmentally friendly reactions to replace some of the environmentally harmful processes like transesterification of DMC with phenol that produces methyl phenyl carbonate [129].

A.1.5 Methanol synthesis

Methanol is used as an important chemical feedstock for the synthesis of many compounds such as acetic acid, formaldehyde, methyl *tert*-butyl ether (MTBE), methyl methacrylate (MMA) and chloromethane. The first industrial plant for methanol production using synthesis gas was constructed by the BASF in 1923. This process was operating under high pressure of about 20 MPa and at 300 °C using a zinc oxide/chromium oxide catalyst [5].

Due to the environmental impact, methanol synthesis through the carbon dioxide hydrogenation has attracted worldwide research interest. The potential use of CO₂ to replace CO in the methanol synthesis is also an effective way of CO₂ utilization [130]. The methanol synthesis from CO₂ has two possible mechanisms. One is the direct conversion of carbon dioxide to methanol (Eq. (A-8)) and the second one is the conversion of CO₂ to CO and H₂O via the RWGS reaction with subsequent conversion of CO and H₂ to methanol (Eq. (A-9)). Commercially methanol has been produced from coal and natural gas containing small amount of CO₂ along with CO and H₂ as a feedstock [131].





The methanol formation is an exothermic reaction, so thermodynamically favored at low temperatures and high pressures. During the reaction hydrogen can be consumed by CO₂ in reverse water gas shift reaction and reduce the methanol formation. A recent study show that a mixture of a proper proportion of CO₂ and CO for methanol synthesis is not only increases the methanol yield but also decrease the apparent activation energy of the reaction [132]. The presence of CO₂ could maintain the active copper sites in the oxidation state or prevent an over-reduction of the ZnO component of Cu/Zn catalysts during methanol synthesis [132]. Table A-1 shows the data reported for conversion of CO₂ and the selectivity to methanol using CO₂ over Cu/Zn/ZrO₂ containing catalyst.

Table A-1: Methanol synthesis by CO₂ hydrogenation using Cu/Zn/ZrO₂ containing catalyst.

| Catalyst | Preparation method | T, °C | X _{CO2} , % | S _{MeOH} , % | Ref. |
|---------------------------|----------------------------|-------|----------------------|-----------------------|-------|
| Cu/Zn/ZrO ₂ | coprecipitation | 250 | 19.4 | 29.3 | [133] |
| Cu/Zn/ZrO ₂ | coprecipitation | 220 | 21 | 68 | [134] |
| Cu/Zn/ZrO ₂ | coprecipitation | 200 | 5.9 | 47.5 | [135] |
| Cu/Zn/ZrO ₂ | urea nitrate combustion | 240 | 17 | 56.2 | [136] |
| Cu/Zn/ZrO ₂ | glycine nitrate combustion | 220 | 12 | 71.1 | [137] |
| Cu/Zn/Al/ZrO ₂ | coprecipitation | 240 | 18.7 | 47.2 | [138] |
| Cu/Zn/Ga/ZrO ₂ | coprecipitation | 250 | - | 75 | [139] |

The presence of ZrO₂ enhances Cu dispersion which leads to an improved catalytic activity and stability towards methanol formation [133, 136]. The addition of an optimum amount of metal oxides like Ga₂O₃, Al₂O₃, ZrO₂, and Cr₂O₃ as a modifiers increases the methanol synthesis activity and the stability of Cu/ZnO-based ternary catalysts [135, 138-140].

A novel approach was employed using low temperature of about 170 °C and 5 MPa pressure in a semi-bath autoclave reactor with 2-butanol as a solvent [141]. CO₂ conversion and

selectivity towards methanol obtained over a Cu catalyst was about 26% and 73%, respectively.

Although much attention has been given to the methanol synthesis from CO/H₂, CO₂/H₂ and CO/CO₂/H₂ using fixed bed technology, some important subjects of investigation are still under discussion: (1) whether the active site is Cu⁰ or Cuⁿ⁺, (2) whether the carbon source for methanol synthesis is CO₂ or CO, (3) whether there is special interaction between the Cu metal and oxide support, and (4) whether the water formed during methanol synthesis has any influence on the catalytic activity.

A.1.6 Formic acid synthesis

The synthesis of formic acid is another alternative to convert carbon dioxide into valuable products. Formic acid is widely used as a pickling agent, as a reducing agent, as an antibacterial agent, a mordant in the dyeing industry, disinfectant and preservative agent in sanitary stations, and as a neutralizer in the tanning industry [142]. It has been also used as a raw material in the chemical industry for the production of formate ester, which is important feedstock for the synthesis of various organic derivatives like aldehydes, ketones, amides, and carboxylic acids [142]. Formic acid has been produced directly by the hydration of carbon monoxide, and by the hydrolysis of methyl formate. The synthesis of formic acid by direct CO₂ hydrogenation was first reported by *Farlow and Adkins* in 1935 using Raney nickel as a catalyst under 20 to 40 MPa and 80 to 150 °C in presence of amines [143]. At a temperature of 250 °C, the sheet brass used in fabricating liners for steel reaction vessel acts as an active catalyst for the hydrogenation reaction:



Most of the catalytic studies of formic acid synthesis are based the metal complexes of the second and third row transition metals, where the metal like ruthenium, palladium, and rhodium has been used with the combination of halides or hydrides as anionic ligands and phosphines as neutral ligands [142].

The catalytic hydrogenation of CO₂ to formic acid over transition metal catalyzed complexes RuH₂(PPh₃)₄ and Pd(Ph₂PCH₂CH₂PPh₂)₂, has been reported [144]. Similarly, formic acid has been produced by carbonylation of CO and H₂O using a metal complex, i.e.

$[\text{Ru}^{\text{II}}(\text{EDTA-H})\text{CO}]^-$ in the WGS reaction [145]. The highly active metal complex $\text{RuCl}(\text{O}_2\text{CMe})(\text{PMe}_3)_4$ as a catalyst with acidic alcohols was used to enhance the rate of the hydrogenation reaction. The organic bases with intermediate basicity were added to the reaction mixture to extract the formic acid [146]. Although much attention has been paid to synthesize formic acid using a homogeneous catalyst, the problem of separation of formic acid from the catalyst and the base still remains.

The hydrogenation of CO_2 to formic acid over alumina supported ruthenium hydroxide as a heterogeneous catalyst was carried out using triethylamine and ethanol as a solvent at 80°C and 13.5 MPa [142]. Also the Ruthenium(II) complex catalyzed hydrogenation of CO_2 to formic acid was theoretically investigated using *cis*- $\text{RuH}_2(\text{PH}_3)_4$ as a model catalyst [147, 148]. The hydrogenation over this catalyst took place through the insertion of CO_2 into the Ru-H bond followed by the H-OCOH reductive elimination, where CO_2 insertion was the rate determining step.

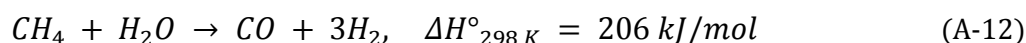
A.1.7 CO_2 reforming of methane

The reforming of CO_2 with methane has also attracted a continuous research interest. This process was carried out not only for the utilization of two undesirable greenhouse gases (CO_2 , CH_4) but also for the production of fuels by Fischer Tropsch and methanol synthesis. The dry reforming of methane with CO_2 is not yet feasible, and gives incomplete conversion of CO_2 due to thermodynamic constraints [149].

Dry reforming:



Steam reforming:



The dry reforming of CO_2 with methane was first studied by *Fischer and Tropsch* in 1928. After that many researchers investigated this reaction using various catalysts for the production of syngas. Syngas can be produced with CO/H_2 ratio of about a unity depending upon the reaction conditions. This is an endothermic reaction, generally carried out in the temperature range of 300 to 830°C and at atmospheric pressure [150]. The group VIII metals (e.g. Ni, Co, Pt, Pd, Ir, Ru, Rh etc.) are more or less catalytically active for the carbon

dioxide methane reforming reaction. Commercially Ni catalysts have also been used for the $\text{CO}_2\text{-CH}_4$ reforming because of its inherent availability and lower cost as compare to a noble metal catalyst. The main drawback of this reaction is the coke formation via methane decomposition (Eq. (A-13)) and/or CO disproportionation (Boudouard reaction, Eq. (A-14)), which leads to the catalyst deactivation and plugging of the reformer tubes [151].



Thermodynamic equilibrium for the carbon formation in the dry reforming of CO_2 is shown in Fig. A-1. The coke deposition can be avoided or minimized by using noble metal based catalysts such as Rh, Ru, Pd, Pt, and Ir [152, 153]. But this is limited by the high costs. Therefore, many efforts have been concentrated on the development of Ni based catalysts which are resistive to carbon formation. A recent study on Ni/ $\gamma\text{-Al}_2\text{O}_3$ catalyst with the addition of potassium, MnO, and CeO_2 as a promoters shows a high catalytic activity and stability for the dry reforming of methane with CO_2 [151]. The partial coverage of the nickel surface with promoters increase the CO_2 adsorption, and results in the formation of surface carbonate species responsible for the removal of carbon from the catalyst surface.

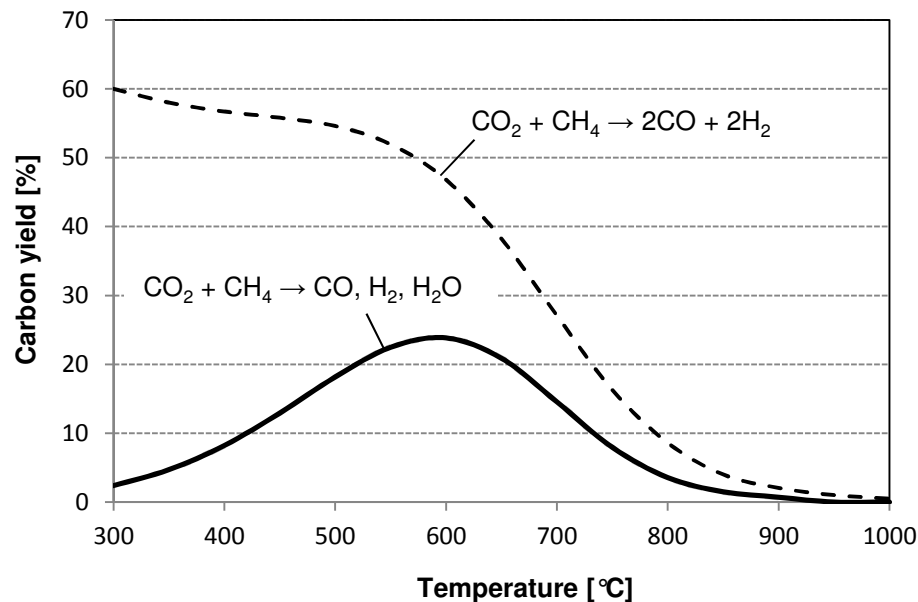


Fig. A-1: Thermodynamic calculation of carbon formation under the reforming conditions ($\text{CO}_2/\text{CH}_4 = 1$, $p = 1$ bar) with and without RWGS reaction.

Promoters like CeO_2 , ZrO_2 improve the catalytic activity and stability of $\text{Ni/MgAl}_2\text{O}_4$ catalysts within certain composition ranges [154]. The influence of the catalyst preparation and Ni loading on different supports such as MCM-41 [95], alumina [155], and alkaline earth metals [156] showed good catalytic activity and stability. The dry reforming over a solid solution of NiO/MgO catalyst using a CO_2/CH_4 ratio of unity provided about 98% and 91% conversion of CO_2 and CH_4 , respectively, at 790 °C and atmospheric pressure [156]. The rate of coke formation ($\text{Ni} > \text{Pd} \gg \text{Rh}, \text{Ir}, \text{Ru}, \text{Re}, \text{Pt}, \text{WC}, \text{Mo}_2\text{C} \approx 0$) and the activity over different catalyst in dry reforming was recognized as $\text{Ru} > \text{Rh} \approx \text{Mo}_2\text{C} > \text{Ir} > \text{WC} > \text{Pd} > \text{Pt}$ [157]. Thus, it seems to be possible to use active, carbon resistive, and cheap transition metal catalysts in the dry reforming of methane with CO_2 to produce syngas. In our lab scale experiment, the reforming of CO_2 with CH_4 using small amount of inlet hydrogen over commercial $\text{Ni/Al}_{12}\text{O}_{19}$ catalyst avoids initial deactivation of catalyst and gives very good activity and stability at 900 °C (Fig. A-2).

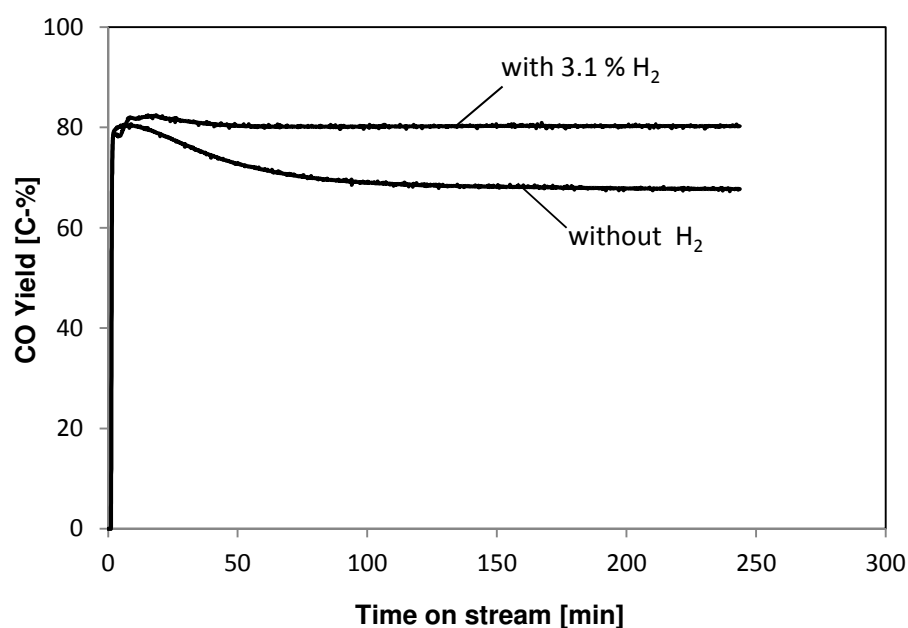


Fig. A-2: The yield of CO versus time on stream in dry reforming of CO_2 and CH_4 ($T = 900$ °C, $p = 1$ atm, $d_p = 6$ mm, $m_{\text{cat}} = 1.2$ g, catalyst = $\text{Ni/Al}_{12}\text{O}_{19}$, $y_{\text{H}_2} = 3.1$ vol.-%, $y_{\text{CO}_2} = 18.55$ vol.-%, $y_{\text{CH}_4} = 19.9$ vol.-%, rest N_2 , gas flow rate = 50 l/h (NTP)).

Appendix B

B.1 Calculation of reaction order (CO hydrogenation, water gas shift reaction)

The reaction order with respect to individual reactants in CO hydrogenation and water gas shift reaction were calculated by the integral method i.e. the value of the reaction order was determined by the best fit to the measured data (conversion versus concentration).

B.1.1 Order of CO hydrogenation (methanation) reaction

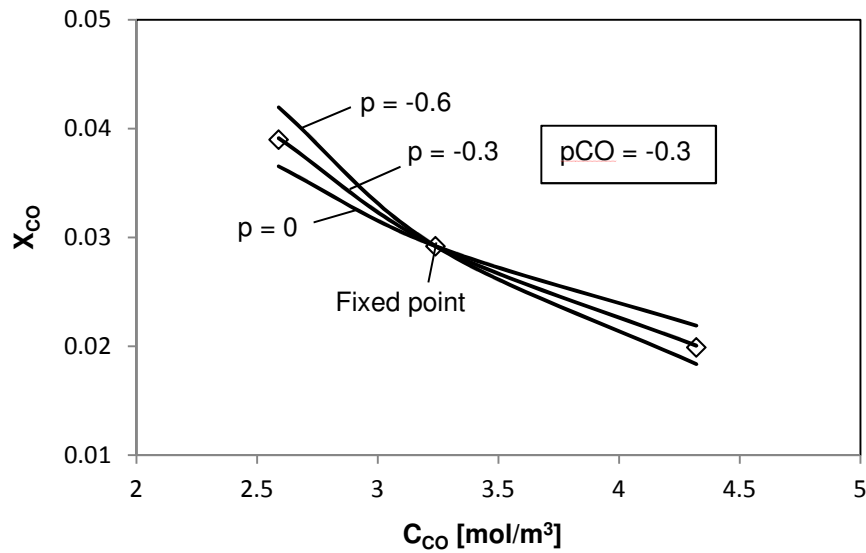


Fig. B-1: Determination of the reaction order with respect to CO in CO hydrogenation by means of the integral method (T = 340 °C, p = 1 atm, m_{cat} = 1.2 g, d_p = 6 mm, catalyst = Ni/Al₁₂O₁₉, y_{H₂} = 66 vol.-%, y_{CO} = 13.2 – 22 vol.-%, N₂ = rest proportion, gas flow rate = 48 l/h (NTP)).

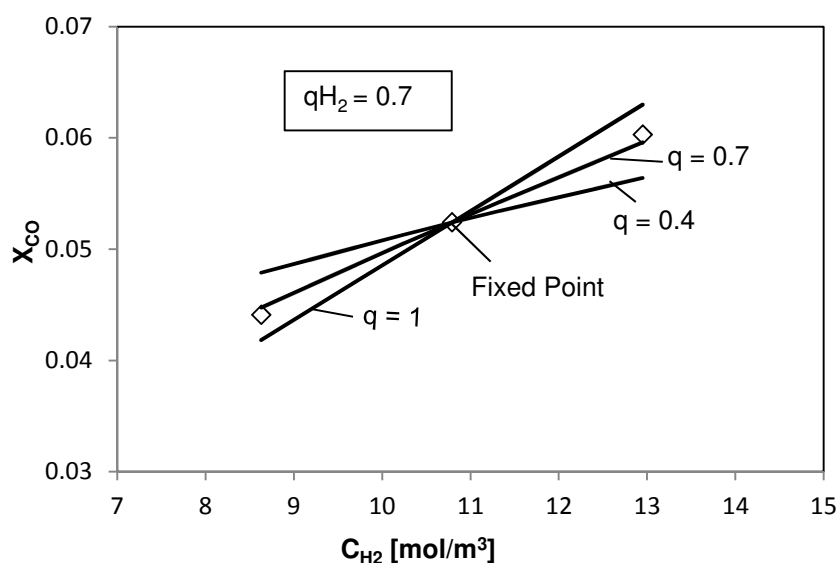


Fig. B-2: Determination of the reaction order with respect to H_2 in CO hydrogenation by means of the integral method ($T = 340\text{ }^\circ\text{C}$, $p = 1\text{ atm}$, $m_{\text{cat}} = 1.2\text{ g}$, $d_p = 6\text{ mm}$, catalyst = Ni/Al_2O_3 , $y_{CO} = 11\text{ vol.-%}$, $y_{H_2} = 44 - 66\text{ vol.-%}$, $N_2 = \text{rest proportion}$, gas flow rate = 48 l/h (NTP)).

B.1.2 Order of water gas shift reaction

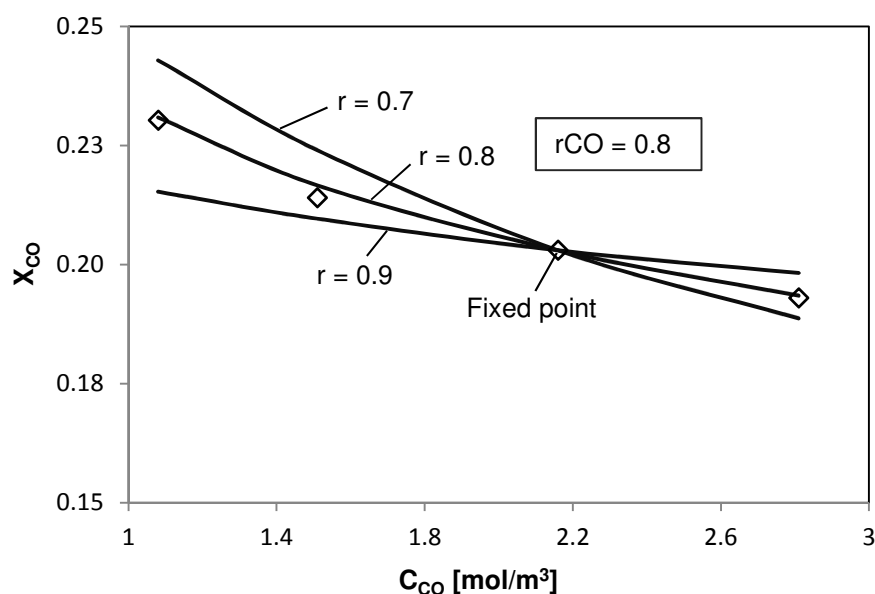


Fig. B-3: Determination of the reaction order with respect to CO in WGS reaction by means of the integral method ($T = 340\text{ }^\circ\text{C}$, $p = 1\text{ atm}$, $m_{\text{cat}} = 1.2\text{ g}$, catalyst = Ni/Al_2O_3 , $d_p = 6\text{ mm}$, $y_{H_2O} = 44\text{ vol.-%}$, $y_{CO} = 5.5 - 14.28\text{ vol.-%}$, $N_2 = \text{rest proportion}$, gas flow rate = 48 l/h (NTP)).

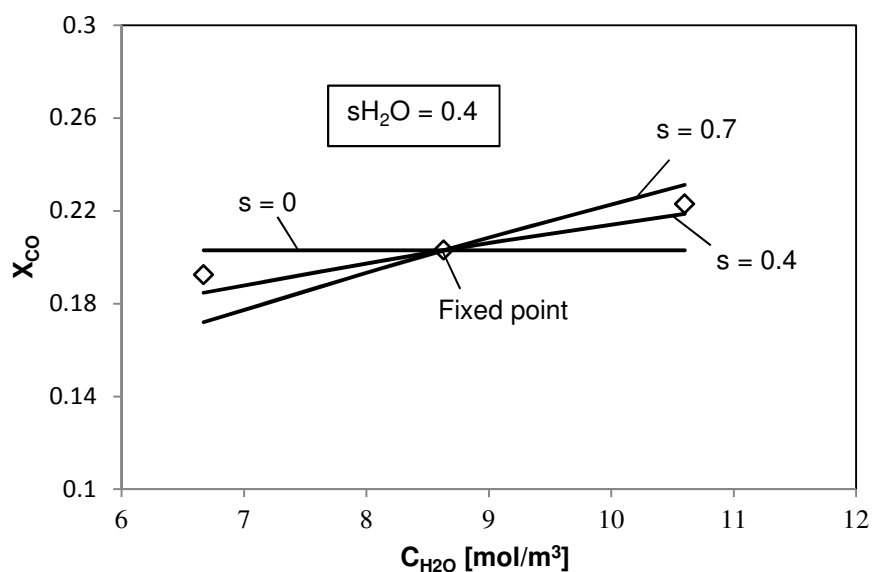


Fig. B-4: Determination of the reaction order with respect to H_2O in WGS reaction by means of the integral method ($T = 340\text{ }^\circ\text{C}$, $p = 1\text{ atm}$, $m_{\text{cat}} = 1.2\text{ g}$, $d_p = 6\text{ mm}$, catalyst = $\text{Ni}/\text{Al}_2\text{O}_3$, $y_{\text{CO}} = 11\text{ vol.-%}$, $y_{\text{H}_2\text{O}} = 34 - 54\text{ vol.-%}$, $\text{N}_2 = \text{rest proportion}$, gas flow rate = 48 l/h (NTP))).

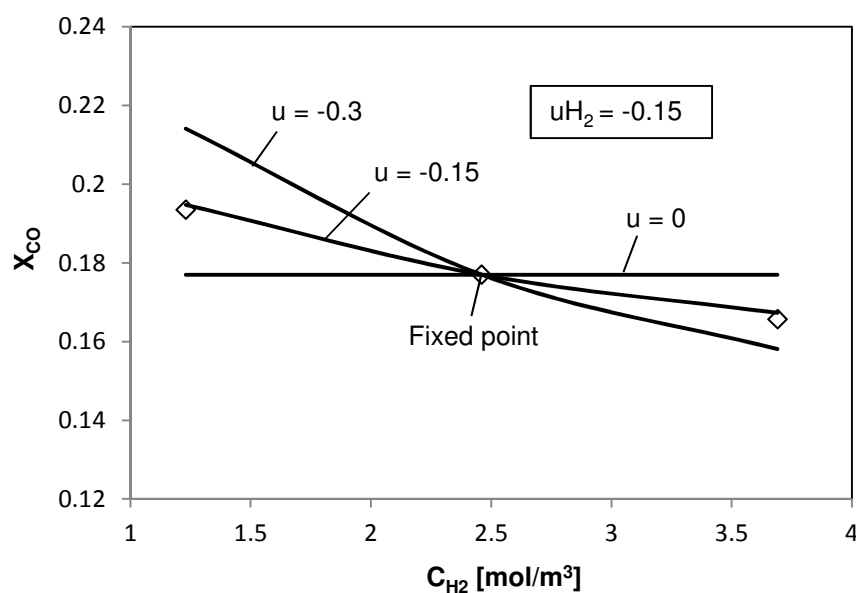


Fig. B-5: Determination of the reaction order with respect to H_2 in WGS reaction by means of the integral method ($T = 340\text{ }^\circ\text{C}$, $p = 1\text{ atm}$, $m_{\text{cat}} = 1.2\text{ g}$, catalyst = $\text{Ni}/\text{Al}_2\text{O}_3$, $d_p = 6\text{ mm}$, $y_{\text{H}_2\text{O}} = 44\text{ vol.-%}$, $y_{\text{CO}} = 11\text{ vol.-%}$, $y_{\text{H}_2} = 6.25 - 18.75\text{ vol.-%}$, $\text{N}_2 = \text{rest proportion}$, gas flowrate = 48 l/h (NTP))).

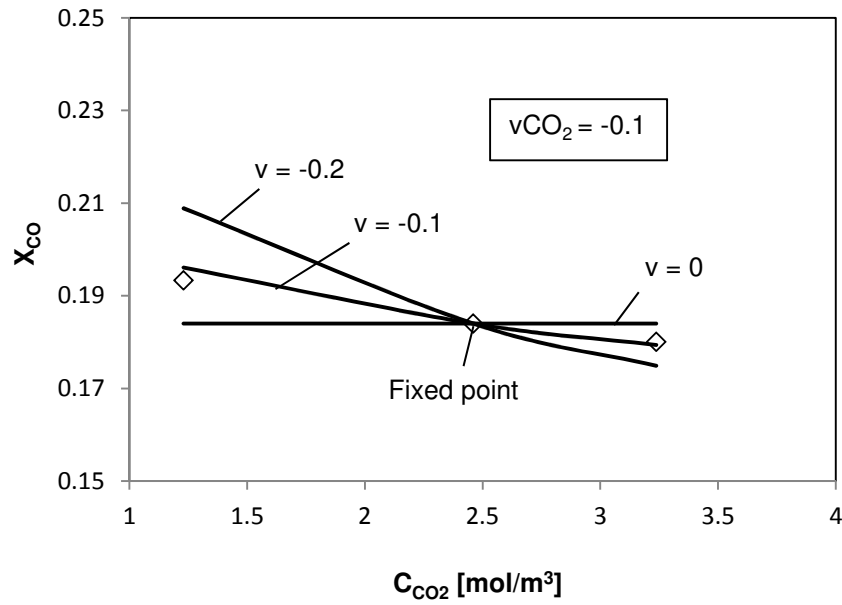


Fig. B-6: Determination of the reaction order with respect to CO_2 in WGS reaction by means of the integral method ($T = 340\text{ }^\circ\text{C}$, $p = 1\text{ atm}$, $m_{\text{cat}} = 1.2\text{ g}$, $d_p = 6\text{ mm}$, catalyst = $\text{Ni}/\text{Al}_{12}\text{O}_{19}$, $y_{\text{H}_2\text{O}} = 44\text{ vol.-%}$, $y_{\text{CO}} = 11\text{ vol.-%}$, $y_{\text{CO}_2} = 6.25 - 16.7\text{ vol.-%}$, rest N_2 , gas flow rate = 48 l/h (NTP)).

B.2 Diffusion coefficients of CO in the pores of the Ni catalyst

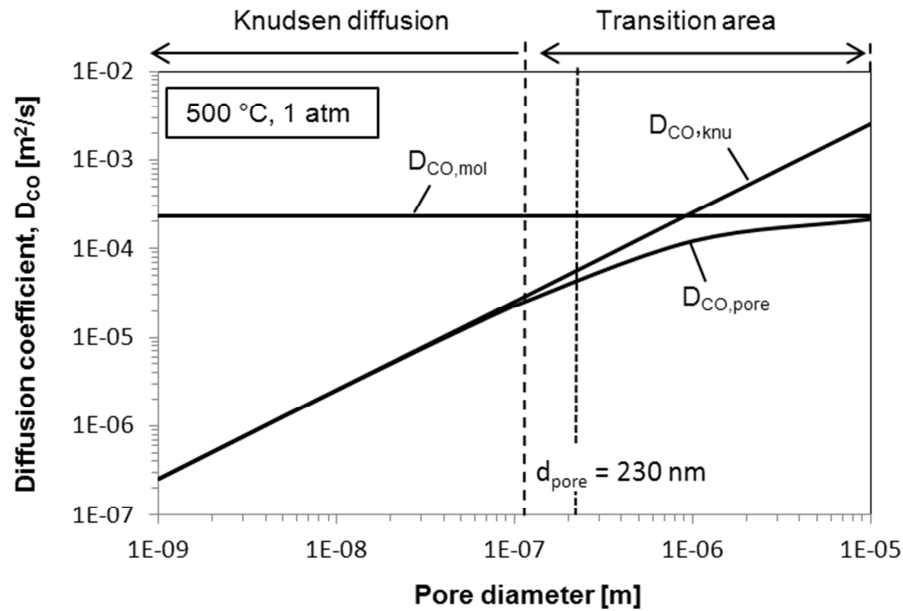


Fig. B-7: Diffusion coefficient of CO in the pores of the Ni catalyst determined at $500\text{ }^\circ\text{C}$ and 1 bar (CO hydrogenation).

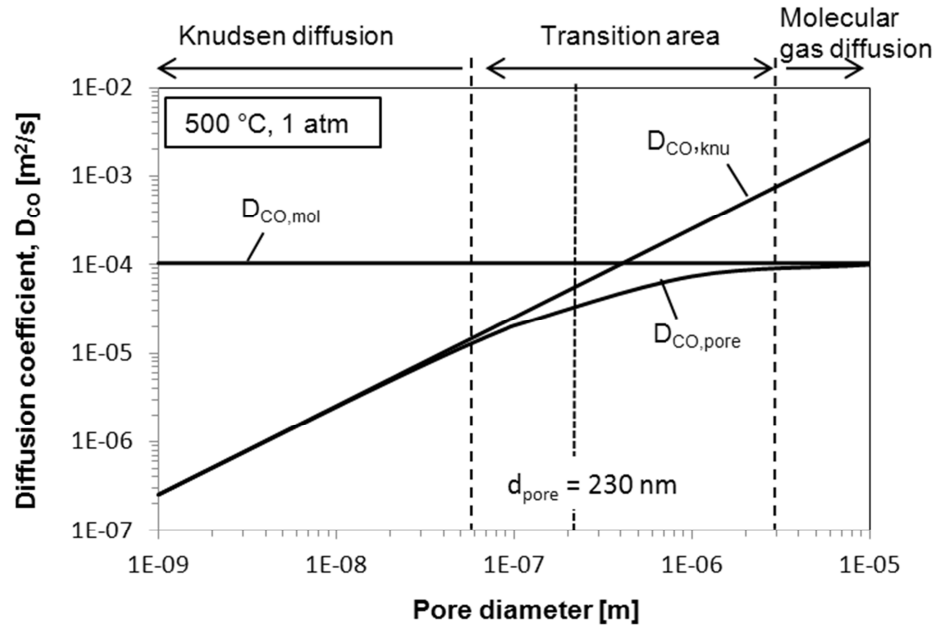


Fig. B-8: Diffusion coefficient of CO in the pores of the Ni catalyst determined at 500 °C and 1 bar (WGS reaction).

B.3 Characteristics data of catalysts

Table B-1: Characteristic data of γ -Al₂O₃ catalyst [158].

| | |
|--|--|
| Catalyst name | Al ₂ O ₃ (commercial catalyst) |
| Manufacturer | Süd-Chemie Catalysts |
| Composition | Al ₂ O ₃ : > 99% |
| Geometry (cylinder) | 4.5 × 4.5 mm |
| Catalyst density | 1450 kg/m ³ |
| Catalyst bulk density | 800 kg/m ³ |
| BET-surface area (A _{BET}) | 190 m ² /g |
| Pore volume | 0.3 cm ³ /g |
| Porosity of particle (ε _p) | 0.4 |
| Average pore diameter | 6 nm |
| Tortuosity (measured by NMR) | 2.8 |

Table B-2: Characteristic data of $\text{Cr}_2\text{O}_3/\text{Al}_2\text{O}_3$ catalyst [159].

| | |
|---------------------------------------|--|
| Catalyst name | Cr-HP-96-19 (commercial catalyst) |
| Manufacturer | BASF |
| Composition | Al_2O_3 : > 50 – 80 wt.-%, Cr_2O_3 : 15 – 30 wt.-% |
| Geometry (cylinder) | 4.5×4.5 mm |
| Catalyst density | 1900 kg/m^3 |
| Catalyst bulk density | 950 kg/m^3 |
| BET-surface area (A_{BET}) | $75 \text{ m}^2/\text{g}$ |
| Porosity of particle (ϵ_p) | 0.6 |
| Pore volume | $0.26 \text{ cm}^3/\text{g}$ |
| Average pore diameter | 9 nm |

Table B-3: Characteristic data of $\text{ZnO}/\text{CuO}/\text{Al}_2\text{O}_3$ catalyst.

| | |
|---------------------------------------|---|
| Catalyst name | STUM 19175 (commercial catalyst) |
| Manufacturer | Bayer |
| Composition | CuO : 62 wt.-%, ZnO : 34 wt.-%, rest: Al_2O_3 , Na_2O |
| Geometry (cylinder) | 4.5×4.5 mm |
| Catalyst density | 2300 kg/m^3 |
| Catalyst bulk density | 1300 kg/m^3 |
| BET-surface area (A_{BET}) | $44 \text{ m}^2/\text{g}$ |
| Porosity of particle (ϵ_p) | 0.43 |
| Pore volume | $0.19 \text{ cm}^3/\text{g}$ |
| Average pore diameter | 16 nm |

References

- [1] Z. Li and K. Su, The direct reaction between CO₂ and phenol catalyzed by bifunctional catalyst ZrO₂. *J. Mol. Catal. A: Chem.* 277 (2007), 180-184.
- [2] S. Solomon, D. Qin, M. Manning, Z. Chen, M. Marquis, K.B. Averyt, M. Tignor and H.L.M. (Editors), IPCC Fourth Assessment Report, Summary for Policymakers, Climate Change 2007: The Physical Science Basics (WGI). 2007.
- [3] Utilisation and Storage of CO₂, Position Paper, DECHEMA. 2009.
- [4] T. Sakakura, J.-C. Choi and H. Yasuda, Transformation of Carbon Dioxide. *Chem. Rev.* 107 (2007), 2365-2387.
- [5] R. Raudaskoski, E. Turpeinen, R. Lenkkeri, E. Pongrácz and R.L. Keiski, Catalytic activation of CO₂: Use of secondary CO₂ for the production of synthesis gas and for methanol synthesis over copper-based zirconia-containing catalysts. *Catal. Today* 144 (2009), 318-323.
- [6] S. Chunshan, Global challenges and strategies for control, conversion and utilization of CO₂ for sustainable development involving energy, catalysis, adsorption and chemical processing. *Catal. Today* 115 (2006), 2-32.
- [7] M. Aresta and I. Tommasi, Carbon dioxide utilisation in the chemical industry. *Energy Convers. Manage.* 38, Supplement (1997), S373-S378.
- [8] S.M. George, Introduction: Heterogeneous Catalysis. *Chem. Rev.* 95 (1995), 475-476.
- [9] L.F. Albright (Editor), Albright's Chemical Engineering Handbook. CRC Press, Taylor & Francis Group, 2009.
- [10] H.S. Fogler (Editor), Elements of Chemical Reaction Engineering. Prentice-Hall, Inc., Upper Saddle River, New Jersey, 1999.
- [11] K.B. Bischoff, Effectiveness factors for general reaction rate forms. *AIChE J.* 11 (1965), 351-355.
- [12] I.-S. Park, D.D. Do and A.E. Rodrigues, Measurement of the Effective Diffusivity in Porous Media by the Diffusion Cell Method. *Catal. Rev.* 38 (1996), 189-247.
- [13] S.H. Chan and Z.T. Xia, Polarization effects in electrolyte/electrode-supported solid oxide fuel cells. *J. Appl. Electrochem.* 32 (2002), 339-347.
- [14] S. Sunde, Simulations of Composite Electrodes in Fuel Cells. *J. Electroceram.* 5 (2000), 153-182.
- [15] A. Suzuki, T. Hattori, R. Miura, H. Tsuboi, N. Hatakeyama, H. Takaba, M.C. Williams and A. Miyamoto, Porosity and Pt content in the catalyst layer of PEMFC: effects on diffusion and polarization characteristics. *Int. J. Electrochem. Sci.* 5 (2010), 1948-1961.
- [16] C.N. Satterfield, A.A. Pelosof and T.K. Sherwood, Mass transfer limitations in a trickle-bed reactor. *AIChE J.* 15 (1969), 226-234.

-
- [17] C.H. Tsai, F.E. Massoth, S.Y. Lee and J.D. Seader, Effects of solvent and solute configuration on restrictive diffusion in hydrotreating catalysts. *Ind. Eng. Chem. Res.* 30 (1991), 22-28.
- [18] J. Hoogschagen, Diffusion in Porous Catalysts and Adsorbents. *Ind. Eng. Chem.* 47 (1955), 906-912.
- [19] J.M. Zalc, S.C. Reyes and E. Iglesia, The effects of diffusion mechanism and void structure on transport rates and tortuosity factors in complex porous structures. *Chem. Eng. Sci.* 59 (2004), 2947-2960.
- [20] A.N. Hayhurst and M.S. Parmar, Measurement of the mass transfer coefficient and sherwood number for carbon spheres burning in a bubbling fluidized bed. *Combust. Flame* 130 (2002), 361-375.
- [21] C.H. Bartholomew, Mechanisms of catalyst deactivation. *Appl. Catal., A* 212 (2001), 17-60.
- [22] S. Bhatia, J. Beltramini and D.D. Do, Deactivation of Zeolite Catalysts. *Catal. Rev.* 31 (1989), 431-480.
- [23] W. Disdale, An Experimental and Computational Investigation of the Time-Dependency of Automotive Catalyst Deactivation. Ph.D. Thesis, Coventry University, 2007.
- [24] J.A. Moulijn, A.E. van Diepen and F. Kapteijn, Catalyst deactivation: is it predictable?: What to do? *Appl. Catal., A* 212 (2001), 3-16.
- [25] D.L. Mowery, M.S. Graboski, T.R. Ohno and R.L. McCormick, Deactivation of PdO-Al₂O₃ oxidation catalyst in lean-burn natural gas engine exhaust: aged catalyst characterization and studies of poisoning by H₂O and SO₂. *Appl. Catal., B* 21 (1999), 157-169.
- [26] P. Albers, J. Pietsch and S.F. Parker, Poisoning and deactivation of palladium catalysts. *J. Mol. Catal. A: Chem.* 173 (2001), 275-286.
- [27] C.E. Quincoces, N.E. Amadeo, M.G. González, C.H. Bartholomew and G.A. Fuentes, Effects of reduction and regeneration conditions on the activity of CuO-ZnO catalysts. *Stud. Surf. Sci. Catal.* 111 (1997), 535-541.
- [28] Y. Li, B. Markley, A.R. Mohan, V. Rodriguez-Santiago, D. Thompson and D.V. Niekerk, Utilization of carbon dioxide from coal-fired power plant for the production of value-added products. *Design Engineering of Energy and Geo-Environmental Systems (EGEE 580)*, April 27, 2006.
- [29] R. Sahki, O. Benlounes, O. Chérifi, R. Thouvenot, M. Bettahar and S. Hocine, Effect of pressure on the mechanisms of the CO₂/H₂ reaction on a CO-precipitated CuO/ZnO/Al₂O₃ catalyst. *Reac. Kinet. Mech. Cat.* 103 (2011), 391-403.
- [30] G. Pekridis, K. Kalimeri, N. Kaklidis, E. Vakouftsi, E.F. Iliopoulou, C. Athanasiou and G.E. Marnellos, Study of the reverse water gas shift (RWGS) reaction over Pt in a solid oxide fuel cell (SOFC) operating under open and closed-circuit conditions. *Catal. Today* 127 (2007), 337-346.

-
- [31] R. Zubrin, B. Frankie and T. Kito, Mars In-Situ Resource Utilization Based on the Reverse Water Gas Shift: Experiments and Mission Applications. AIAA 97-2767, 1997.
- [32] Y. Souma, H. Ando, M. Fujiwara and R. Kieffer, Catalytic hydrogenation of carbon dioxide to hydrocarbons. *Energy Convers. Manage.* 36 (1995), 593-596.
- [33] G. Lee, M. Moon, J. Park, S. Park and S. Hong, Raney Ni catalysts derived from different alloy precursors Part II. CO and CO₂ methanation activity. *Korean J. Chem. Eng.* 22 (2005), 541-546.
- [34] Kas, J. par, M. Graziani, A.M. Rahman, A. Trovarelli, E.J.S. Vichi and E.C. da Silva, Carbon dioxide hydrogenation over iron containing catalysts. *Appl. Catal., A* 117 (1994), 125-137.
- [35] P.H. Choi, K.-W. Jun, S.-J. Lee, M.-J. Choi and K.-W. Lee, Hydrogenation of carbon dioxide over alumina supported Fe-K catalysts. *Catal. Lett.* 40 (1996), 115-118.
- [36] R. Dziembaj, W. Makowski and H. Papp, Carbon dioxide hydrogenation on Fe-Mn oxide catalyst doped with Rh and La. *J. Mol. Catal. A: Chem.* 75 (1992), 81-99.
- [37] A. Jess, P. Kaiser, C. Kern, R.B. Unde and C. von Olshausen, Considerations concerning the Energy Demand and Energy Mix for Global Welfare and Stable Ecosystems. *Chem. Ing. Tech.* 83 (2011), 1777-1791.
- [38] A. Behr, A. Vorholt and L. Johnen, Aus der Natur für die Chemie. *Nachr. Chem.* 57 (2009), 757-761.
- [39] G. Centi and S. Perathoner, Opportunities and prospects in the chemical recycling of carbon dioxide to fuels. *Catal. Today* 148 (2009), 191-205.
- [40] M. Saito, M. Takeuchi, T. Fujitani, J. Toyir, S. Luo, J. Wu, H. Mabuse, K. Ushikoshi, K. Mori and T. Watanabe, Advances in joint research between NIRE and RITE for developing a novel technology for methanol synthesis from CO₂ and H₂. *Appl. Organomet. Chem.* 14 (2000), 763-772.
- [41] B. Wolf, H. Scheer and Ö. aus Sonne, *Die Brennstoffformel der Erde*. Ponte Press, Bochum, Germany, 2005.
- [42] Z. Jiang, T. Xiao, V.L. Kuznetsov and P.P. Edwards, Turning carbon dioxide into fuel. *Phil. Trans. R. Soc. A* 368 (2010), 3343-3364.
- [43] M. Hirscher (Editor), *Handbook of Hydrogen Storage*. Wiley-VCH, Weinheim, 2010.
- [44] U. Bossel, Wasserstoff löst keine Energieprobleme. *Technikfolgenabschätzung - Theorie und Praxis* 15 (2006), 27-33.
- [45] C. Stoots, J. O'Brian, J. Herring and J. Hartvigsen, Recent progress at the Idaho national laboratory in high temperature electrolysis for H₂ and syngas production. 2008 ASME Int. Mechanical Engineering Congress & Exposition, Boston, November 2008.
- [46] C. Fritzmann, J. Löwenberg, T. Wintgens and T. Melin, State-of-the-art of reverse osmosis desalination. *Desalination* 216 (2007), 1-76.

-
- [47] G. Göttlicher and R. Pruschek, Comparison of CO₂ removal systems for fossil-fuelled power plant processes. *Energy Convers. Manage.* 38, Supplement (1997), S173-S178.
- [48] A. Jess and C. Kern, Modeling of Multi-Tubular Reactors for Fischer-Tropsch Synthesis. *Chem. Ing. Tech.* 32 (2009), 1164-1175.
- [49] T. Kuntze, K. Hedden and A. Jess, Kinetics of the Fischer-Tropsch-Synthesis using a Nitrogen-Rich Synthesis Gas. *Oil Gas-Eur. Mag.* 21 (1995), 19-24.
- [50] P. Kaiser, Ph.D. Thesis, University Bayreuth, (in preparation).
- [51] J.H. Gregor, Fischer-Tropsch products as liquid fuels or chemicals. *Catal. Lett.* 7 (1990), 317-331.
- [52] G. Schaub and T. Turek, *Energy flows, material cycles and global development.* Springer, Heidelberg, 2011.
- [53] N.S. Lewis, Powering the planet. *MRS Bulletin* 32 (2007), 808-820.
- [54] C. Song, CO₂ Conversion and Utilization: An Overview. *Prepr. - Am. Chem. Soc., Div. Pet. Chem.* 809 (2002), 2-30.
- [55] C.A. Callaghan, Kinetics and Catalysis of the Water-Gas-Shift Reaction: A Microkinetic and Graph Theoretic Approach. Ph.D. Thesis, Worcester Polytechnic Institute, 2006.
- [56] M.V. Twigg (Editor), *Catalyst Handbook*, second edition. Wolfe Publishing Ltd., London, 1989.
- [57] D.E. Peebles, D.W. Goodman and J.M. White, Methanation of carbon dioxide on nickel(100) and the effects of surface modifiers. *J. Phys. Chem.* 87 (1983), 4378-4387.
- [58] G.D. Weatherbee and C.H. Bartholomew, Hydrogenation of CO₂ on group VIII metals : II. Kinetics and mechanism of CO₂ hydrogenation on nickel. *J. Catal.* 77 (1982), 460-472.
- [59] Z.A. Ibraeva, N.V. Nekrasov, B.S. Gudkov, V.I. Yakerson, Z.T. Beisembaeva, E.Z. Golosman and S.L. Kiperman, Kinetics of methanation of carbon dioxide on a nickel catalyst. *Theor. Exp. Chem.* 26 (1991), 584-588.
- [60] R.A. Fiato, E. Iglesia, G.W. Rice and S.L. Soled, Iron catalyzed CO₂ hydrogenation to liquid hydrocarbons. *Stud. Surf. Sci. Catal.* 114 (1998), 339-344.
- [61] F. Nozaki, T. Sodesawa, S. Satoh and K. Kimura, Hydrogenation of carbon dioxide into light hydrocarbons at atmospheric pressure over Rh/Nb₂O₅ or Cu/SiO₂-Rh/Nb₂O₅ catalyst. *J. Catal.* 104 (1987), 339-346.
- [62] K.K. Bando, K. Sayama, H. Kusama, K. Okabe and H. Arakawa, In-situ FT-IR study on CO₂ hydrogenation over Cu catalysts supported on SiO₂, Al₂O₃, and TiO₂. *Appl. Catal., A* 165 (1997), 391-409.
- [63] Y. Kitayama, Y. Watanabe, K. Muramatsu and T. Kodama, Catalytic reduction of carbon dioxide on Ni-Cu alloys. *Energy* 22 (1997), 177-182.

-
- [64] J.-L. Dubois, K. Sayama and H. Arakawa, CO₂ Hydrogenation over Carbide Catalysts. *Chem. Lett.* (1992), 5-8.
- [65] S.-R. Yan, K.-W. Jun, J.-S. Hong, M.-J. Choi and K.-W. Lee, Promotion effect of Fe-Cu catalyst for the hydrogenation of CO₂ and application to slurry reactor. *Appl. Catal., A* 194-195 (2000), 63-70.
- [66] J.S. Hwang, K.-W. Jun and K.-W. Lee, Deactivation and regeneration of Fe-K/alumina catalyst in CO₂ hydrogenation. *Appl. Catal., A* 208 (2001), 217-222.
- [67] J.-S. Hong, J.S. Hwang, K.-W. Jun, J.C. Sur and K.-W. Lee, Deactivation study on a coprecipitated Fe-Cu-K-Al catalyst in CO₂ hydrogenation. *Appl. Catal., A* 218 (2001), 53-59.
- [68] S.-C. Lee, J.-H. Jang, B.-Y. Lee, M.-C. Kang, M. Kang and S.-J. Choung, The effect of binders on structure and chemical properties of Fe-K/[gamma]-Al₂O₃ catalysts for CO₂ hydrogenation. *Appl. Catal., A* 253 (2003), 293-304.
- [69] K.-W. Jun, S.-J. Lee, H. Kim, M.-J. Choi and K.-W. Lee, Support effects of the promoted and unpromoted iron catalysts in CO₂ hydrogenation. *Stud. Surf. Sci. Catal.* 114 (1998), 345-350.
- [70] M.-J. Choi, J.-S. Kim, H.-K. Kim, S.-B. Lee, Y. Kang and K.-W. Lee, Hydrogenation of CO₂ over Fe-K based catalysts in a fixed bed reactors at elevated pressure. *Korean J. Chem. Eng.* 18 (2001), 646-651.
- [71] M.L. Cubeiro, H. Morales, M.R. Goldwasser, M.J. Pérez-Zurita, F. González-Jiménez and C. Urbina de N, Hydrogenation of carbon oxides over Fe/Al₂O₃ catalysts. *Appl. Catal., A* 189 (1999), 87-97.
- [72] H. Sakurai, S. Tsubota and M. Haruta, Hydrogenation of CO₂ over gold supported on metal oxides. *Appl. Catal., A* 102 (1993), 125-136.
- [73] H. Sakurai, A. Ueda, T. Kobayashi and M. Haruta, Low-temperature water-gas shift reaction over gold deposited on TiO₂. *Chem. Commun.* (1997), 271-272.
- [74] Y. Zhang, G. Jacobs, D.E. Sparks, M.E. Dry and B.H. Davis, CO and CO₂ hydrogenation study on supported cobalt Fischer-Tropsch synthesis catalysts. *Catal. Today* 71 (2002), 411-418.
- [75] T. Riedel, M. Claeys, H. Schulz, G. Schaub, S.-S. Nam, K.-W. Jun, M.-J. Choi, G. Kishan and K.-W. Lee, Comparative study of Fischer-Tropsch synthesis with H₂/CO and H₂/CO₂ syngas using Fe- and Co-based catalysts. *Appl. Catal., A* 186 (1999), 201-213.
- [76] T. Osaki, N. Narita, T. Horiuchi, T. Sugiyama, H. Masuda and K. Suzuki, Kinetics of reverse water gas shift (RWGS) reaction on metal disulfide catalysts. *J. Mol. Catal. A: Chem.* 125 (1997), 63-71.
- [77] A. Erhan Aksoylu and Z. IlsenÖnsan, Hydrogenation of carbon oxides using coprecipitated and impregnated Ni/Al₂O₃ catalysts. *Appl. Catal., A* 164 (1997), 1-11.
- [78] N. Perkas, G. Amirian, Z. Zhong, J. Teo, Y. Gofer and A. Gedanken, Methanation of Carbon Dioxide on Ni Catalysts on Mesoporous ZrO₂ Doped with Rare Earth Oxides. *Catal. Lett.* 130 (2009), 455-462.

-
- [79] F.-W. Chang, M.-S. Kuo, M.-T. Tsay and M.-C. Hsieh, Hydrogenation of CO₂ over nickel catalysts on rice husk ash-alumina prepared by incipient wetness impregnation. *Appl. Catal., A* 247 (2003), 309-320.
- [80] C. Schild, A. Wokaun, R.A. Koeppel and A. Baiker, CO₂ Hydrogenation over Nickel/Zirconia Catalysts from Amorphous Precursors: On the Mechanism of Methane Formation. *J. Phys. Chem.* 95 (1991), 6341-6346.
- [81] L. Wang, S. Zhang and Y. Liu, Reverse water gas shift reaction over Co-precipitated Ni-CeO₂ catalysts. *J. Rare Earths* 26 (2008), 66-70.
- [82] T. Suzuki, H.I. Iwanami, T. Yoshizawa, H. Yamazaki and Y. Yoshida, Selective hydrogenation of CO₂ to CO in the presence of excess CO on a MoO₃/ZnO catalyst-A preliminary attempt to yield an equimolecular mixture of H₂ and CO. *Int. J. Hydrogen Energy* 20 (1995), 823-830.
- [83] A. Jess, Thermische und Katalytische Spaltung von Kohlenwasserstoffen in wasserstoff- und wasserdampfreicher Atmosphäre: Eine Modelluntersuchung zur Erzeugung von Reduktionsgas aus Koksofenrohgas. Habilitationsschrift, Universität Karlsruhe, 1996.
- [84] J.-H. Lee, E.-G. Lee, O.-S. Joo and K.-D. Jung, Stabilization of Ni/Al₂O₃ catalyst by Cu addition for CO₂ reforming of methane. *Appl. Catal., A* 269 (2004), 1-6.
- [85] O.-S. Joo and K.-D. Jung, Stability of ZnAl₂O₄ catalyst for reverse-water-gas-shift reaction (RWGS). *Bull. Korean Chem. Soc.* 24 (2003), 86-90.
- [86] L.D. Rogatis, Design of Nanostructured Catalysts for H₂ Production and CO₂ Hydrogenation. Ph.D. Thesis, Università degli Studi di Trieste, 2007.
- [87] G.D. Weatherbee and C.H. Bartholomew, Hydrogenation of CO₂ on group VIII metals : IV. Specific activities and selectivities of silica-supported Co, Fe, and Ru. *J. Catal.* 87 (1984), 352-362.
- [88] J.N. Dew, R.R. White and C.M. Sliepcevich, Hydrogenation of Carbon Dioxide on Nickel-Kieselguhr Catalyst. *Ind. Eng. Chem.* 47 (1955), 140-146.
- [89] J.H. Chiang and J.R. Hopper, Kinetics of the hydrogenation of carbon dioxide over supported nickel. *Ind. Eng. Chem. Prod. Res. Dev.* 22 (1983), 225-228.
- [90] T. Van Herwijnen, H. Van Doesburg and W.A. De Jong, Kinetics of the methanation of CO and CO₂ on a nickel catalyst. *J. Catal.* 28 (1973), 391-402.
- [91] R. Maatman and S. Hiemstra, A kinetic study of the methanation of CO₂ over nickel-alumina. *J. Catal.* 62 (1980), 349-356.
- [92] M. Araki and V. Poncet, Methanation of carbon monoxide on nickel and nickel-copper alloys. *J. Catal.* 44 (1976), 439-448.
- [93] C. Mirodatos, H. Praliaud and M. Primet, Deactivation of nickel-based catalysts during CO methanation and disproportionation. *J. Catal.* 107 (1987), 275-287.
- [94] A. Erdohelyi and F. Solymosi, Effects of the support on the adsorption and dissociation of CO and on the reactivity of surface carbon on Rh catalysts. *J. Catal.* 84 (1983), 446-460.

-
- [95] D. Liu, R. Lau, A. Borgna and Y. Yang, Carbon dioxide reforming of methane to synthesis gas over Ni-MCM-41 catalysts. *Appl. Catal., A* 358 (2009), 110-118.
- [96] A.D. Moeller and C.H. Bartholomew, Deactivation by carbon of nickel, nickel-ruthenium, and nickel-molybdenum methanation catalysts. *Ind. Eng. Chem. Prod. Res. Dev.* 21 (1982), 390-397.
- [97] M.A. Vannice, The catalytic synthesis of hydrocarbons from H₂/CO mixtures over the group VIII metals : IV. The kinetic behavior of CO hydrogenation over Ni catalysts. *J. Catal.* 44 (1976), 152-162.
- [98] E.L. Sughrue and C.H. Bartholomew, Kinetics of carbon monoxide methanation on nickel monolithic catalysts. *Appl. Catal.* 2 (1982), 239-256.
- [99] G.D. Weatherbee and C.H. Bartholomew, Hydrogenation of CO₂ on group VIII metals : I. Specific activity of Ni/SiO₂. *J. Catal.* 68 (1981), 67-76.
- [100] J. Sehested, S. Dahl, J. Jacobsen and J.R. Rostrup-Nielsen, Methanation of CO over Nickel: Mechanism and Kinetics at High H₂/CO Ratios. *J. Phys. Chem. B* 109 (2004), 2432-2438.
- [101] P. Shi and C.-J. Liu, Characterization of Silica Supported Nickel Catalyst for Methanation with Improved Activity by Room Temperature Plasma Treatment. *Catal. Lett.* 133 (2009), 112-118.
- [102] I. Rodriguez-Ramos, A. Guerrero-Ruiz, J.L.G. Fierro, P.R. de la Piscina and N. Homs, CO hydrogenation over potassium promoted iron, cobalt, and nickel Catalysts Prepared from Cyanide Complexes. *Z. Anorg. Allg. Chem.* 582 (1990), 197-210.
- [103] L. Barrio, A. Kubacka, G. Zhou, M. Estrella, A. Martínez-Arias, J.C. Hanson, M. Fernández-García and J.A. Rodriguez, Unusual Physical and Chemical Properties of Ni in Ce_{1-x}Ni_xO_{2-y} Oxides: Structural Characterization and Catalytic Activity for the Water Gas Shift Reaction. *J. Phys. Chem. C* 114 (2010), 12689-12697.
- [104] C. Wheeler, A. Jhalani, E.J. Klein, S. Tummala and L.D. Schmidt, The water-gas-shift reaction at short contact times. *J. Catal.* 223 (2004), 191-199.
- [105] Y. Li, Q. Fu and M. Flytzani-Stephanopoulos, Low-temperature water-gas shift reaction over Cu- and Ni-loaded cerium oxide catalysts. *Appl. Catal., B* 27 (2000), 179-191.
- [106] B.W. Krupay and R.A. Ross, The Kinetics of the Water-Gas Shift Reaction on Nickel(II) Oxide Catalysts in the Neel Temperature Region. *Can. J. Chem.* 52 (1974), 3063-3069.
- [107] S. Ergun, Fluid flow through packed columns. *Chem. Eng. Prog.* 48 (1952), 89-94.
- [108] T. Iijima and T. Yamaguchi, Efficient regioselective carboxylation of phenol to salicylic acid with supercritical CO₂ in the presence of aluminium bromide. *J. Mol. Catal. A: Chem.* 295 (2008), 52-56.
- [109] Y. Suzuki, T. Hattori, T. Okuzawa and S. Miyano, Lewis Acid-Mediated Carboxylation of Fused Aromatic Compounds with Carbon Dioxide. *Chem. Lett.* 31 (2002), 102-103.

-
- [110] T. Iijima and T. Yamaguchi, K_2CO_3 -catalyzed direct synthesis of salicylic acid from phenol and supercritical CO_2 . *Appl. Catal., A* 345 (2008), 12-17.
- [111] Production of Urea and Urea Ammonium Nitrate. European Fertilizer Manufacturers' Association, Brussels, 2000.
- [112] P. Zakkour and G. Cook, CCS Roadmap for Industry: High Purity CO_2 Sources: Sectoral Assessment-Final Draft Report. Carbon Counts Company (UK) Ltd., 2010.
- [113] F. Bigi, R. Maggi and G. Sartori, Selected syntheses of ureas through phosgene substitutes. *Green Chem.* 2 (2000), 140-148.
- [114] C. Wu, H. Cheng, R. Liu, Q. Wang, Y. Hao, Y. Yu and F. Zhao, Synthesis of urea derivatives from amines and CO_2 in the absence of catalyst and solvent. *Green Chem.* 12 (2010), 1811-1816.
- [115] F. Shi, Y. Deng, T. SiMa, J. Peng, Y. Gu and B. Qiao, Alternatives to phosgene and carbon monoxide: synthesis of symmetric urea derivatives with carbon monoxide in ionic liquids. *Angew. Chem. Int. Ed.* 42 (2003), 3257-3260.
- [116] S.E. Park, J.S. Yoo, J.S. Chang, K.Y. Lee and M.S. Park, Heterogeneous catalytic activation of carbon dioxide as an oxidant. *Am. Chem. Soc., Div. Fuel Chem., Prepr.* 46 (2001), 115-118.
- [117] D.R. Burri, K.M. Choi, D.-S. Han, J.-B. Koo and S.-E. Park, CO_2 utilization as an oxidant in the dehydrogenation of ethylbenzene to styrene over MnO_2 - ZrO_2 catalysts. *Catal. Today* 115 (2006), 242-247.
- [118] D.R. Burri, K.-M. Choi, D.-S. Han, Sujandi, N. Jiang, A. Burri and S.-E. Park, Oxidative dehydrogenation of ethylbenzene to styrene with CO_2 over SnO_2 - ZrO_2 mixed oxide nanocomposite catalysts. *Catal. Today* 131 (2008), 173-178.
- [119] X. Ye, W. Hua, Y. Yue, W. Dai, C. Miao, Z. Xie and Z. Gao, Ethylbenzene dehydrogenation to styrene in the presence of carbon dioxide over chromia-based catalysts. *New J. Chem.* 28 (2004), 373-378.
- [120] A. Moronta, M.E. Troconis, E. González, C. Morán, J. Sánchez, A. González and J. Quiñónez, Dehydrogenation of ethylbenzene to styrene catalyzed by Co, Mo and CoMo catalysts supported on natural and aluminum-pillared clays: Effect of the metal reduction. *Appl. Catal., A* 310 (2006), 199-204.
- [121] D.R. Burri, K.-M. Choi, J.-H. Lee, D.-S. Han and S.-E. Park, Influence of SBA-15 support on CeO_2 - ZrO_2 catalyst for the dehydrogenation of ethylbenzene to styrene with CO_2 . *Catal. Commun.* 8 (2007), 43-48.
- [122] M.-O. Sugino, H. Shimada, T. Turuda, H. Miura, N. Ikenaga and T. Suzuki, Oxidative dehydrogenation of ethylbenzene with carbon dioxide. *Appl. Catal., A* 121 (1995), 125-137.
- [123] K.T. Jung and A.T. Bell, An in Situ Infrared Study of Dimethyl Carbonate Synthesis from Carbon Dioxide and Methanol over Zirconia. *J. Catal.* 204 (2001), 339-347.
- [124] M. Aresta and E. Quaranta, Carbon dioxide: a substitute for phosgene. *Chem. Tech.* 27 (1997), 32-40.

-
- [125] K. Tomishige, T. Sakaihor, Y. Ikeda and K. Fujimoto, A novel method of direct synthesis of dimethyl carbonate from methanol and carbon dioxide catalyzed by zirconia. *Catal. Lett.* 58 (1999), 225-229.
- [126] K. Tomishige, Y. Ikeda, T. Sakaihor and K. Fujimoto, Catalytic properties and structure of zirconia catalysts for direct synthesis of dimethyl carbonate from methanol and carbon dioxide. *J. Catal.* 192 (2000), 355-362.
- [127] S. Fang and K. Fujimoto, Direct synthesis of dimethyl carbonate from carbon dioxide and methanol catalyzed by base. *Appl. Catal., A* 142 (1996), L1-L3.
- [128] H. Wang, B. lu, Q.H. Cai, F. Wu and Y.K. Shan, Synthesis of Dimethyl Carbonate from Methanol and Carbon Dioxide Catalyzed by Potassium Hydroxide under Mild Conditions. *Chin. Chem. Lett.* 16 (2005), 1267-1270.
- [129] Y. Ono, Dimethyl carbonate for environmentally benign reactions. *Catal. Today* 35 (1997), 15-25.
- [130] C. Yang, Z. Ma, N. Zhao, W. Wei, T. Hu and Y. Sun, Methanol synthesis from CO₂-rich syngas over a ZrO₂ doped CuZnO catalyst. *Catal. Today* 115 (2006), 222-227.
- [131] J. Wu, M. Saito, M. Takeuchi and T. Watanabe, The stability of Cu/ZnO-based catalysts in methanol synthesis from a CO₂-rich feed and from a CO-rich feed. *Appl. Catal., A* 218 (2001), 235-240.
- [132] J.S. Lee, K.H. Lee, S.Y. Lee and Y.G. Kim, A Comparative Study of Methanol Synthesis from CO₂/H₂ and CO/H₂ over a Cu/ZnO/Al₂O₃ Catalyst. *J. Catal.* 144 (1993), 414-424.
- [133] R. Raudaskoski, M. Niemelä and R. Keiski, The effect of ageing time on co-precipitated Cu/ZnO/ZrO₂ catalysts used in methanol synthesis from CO₂ and H₂. *Top. Catal.* 45 (2007), 57-60.
- [134] J. Sloczynski, R. Grabowski, A. Kozłowska, P. Olszewski, J. Stoch, J. Skrzypek and M. Lachowska, Catalytic activity of the M/(3ZnO·ZrO₂) system (M = Cu, Ag, Au) in the hydrogenation of CO₂ to methanol. *Appl. Catal., A* 278 (2004), 11-23.
- [135] Y. Nitta, O. Suwata, Y. Ikeda, Y. Okamoto and T. Imanaka, Copper-zirconia catalysts for methanol synthesis from carbon dioxide: Effect of ZnO addition to Cu-ZrO₂ catalysts. *Catal. Lett.* 26 (1994), 345-354.
- [136] X. Guo, D. Mao, S. Wang, G. Wu and G. Lu, Combustion synthesis of CuO-ZnO-ZrO₂ catalysts for the hydrogenation of carbon dioxide to methanol. *Catal. Commun.* 10 (2009), 1661-1664.
- [137] X. Guo, D. Mao, G. Lu, S. Wang and G. Wu, Glycine-nitrate combustion synthesis of CuO-ZnO-ZrO₂ catalysts for methanol synthesis from CO₂ hydrogenation. *J. Catal.* 271 (2010), 178-185.
- [138] X. An, J. Li, Y. Zuo, Q. Zhang, D. Wang and J. Wang, A Cu/Zn/Al/Zr Fibrous Catalyst that is an Improved CO₂ Hydrogenation to Methanol Catalyst. *Catal. Lett.* 118 (2007), 264-269.
- [139] J. Sloczynski, R. Grabowski, P. Olszewski, A. Kozłowska, J. Stoch, M. Lachowska and J. Skrzypek, Effect of metal oxide additives on the activity and stability of

- Cu/ZnO/ZrO₂ catalysts in the synthesis of methanol from CO₂ and H₂. *Appl. Catal., A* 310 (2006), 127-137.
- [140] M. Saito, M. Takeuchi, T. Watanabe, J. Toyir, S. Luo and J. Wu, Methanol synthesis from CO₂ and H₂ over a Cu/ZnO-based multicomponent catalyst. *Energy Convers. Manage.* 38 (1997), S403-S408.
- [141] Y. Liu, Y. Zhang, T. Wang and N. Tsubaki, Efficient Conversion of Carbon Dioxide to Methanol Using Copper Catalyst by a New Low-temperature Hydrogenation Process. *Chem. Lett.* 36 (2007), 1182-1183.
- [142] C. Hao, S. Wang, M. Li, L. Kang and X. Ma, Hydrogenation of CO₂ to formic acid on supported ruthenium catalysts. *Catal. Today* 160 (2011), 184-190.
- [143] M.W. Farlow and H. Adkins, The Hydrogenation of Carbon Dioxide and a Correction of the Reported Synthesis of Urethans. *J. Am. Chem. Soc.* 57 (1935), 2222-2223.
- [144] Y. Inoue, H. Izumida, Y. Sasaki and H. Hashimoto, Chemical fixation of carbon dioxide to formic acid by transition-metal complexes under mild conditions. *Chem. Lett.* 8 (1976), 863-864.
- [145] M.M.T. Khan, S.B. Halligudi, N.N. Rao and S. Shukla, Formic acid and formaldehyde as spin-off products in RU-EDTA-CO complex catalyzed liquid phase water-gas shift (WGS) reaction. *J. Mol. Catal.* 51 (1989), 161-170.
- [146] P. Munshi, A.D. Main, J.C. Linehan, C.-C. Tai and P.G. Jessop, Hydrogenation of Carbon Dioxide Catalyzed by Ruthenium Trimethylphosphine Complexes: The Accelerating Effect of Certain Alcohols and Amines. *J. Am. Chem. Soc.* 124 (2002), 7963-7971.
- [147] Y. Musashi and S. Sakaki, Theoretical Study of Ruthenium-Catalyzed Hydrogenation of Carbon Dioxide into Formic Acid. Reaction Mechanism Involving a New Type of σ -Bond Metathesis. *J. Am. Chem. Soc.* 122 (2000), 3867-3877.
- [148] Y. Ohnishi, T. Matsunaga, Y. Nakao, H. Sato and S. Sakaki, Ruthenium(II)-Catalyzed Hydrogenation of Carbon Dioxide to Formic Acid. Theoretical Study of Real Catalyst, Ligand Effects, and Solvation Effects. *J. Am. Chem. Soc.* 127 (2005), 4021-4032.
- [149] K. Aasberg-Petersen, J.H. Bak Hansen, T.S. Christensen, I. Dybkjaer, P.S. Christensen, C. Stub-Nielsen, S.E.L. Winter-Madsen and J.R. Rostrup-Nielsen, Technologies for large-scale gas conversion. *Appl. Catal., A* 221 (2001), 379-387.
- [150] S. Therdthianwong, N. Summaprasit, N. Junpanichravee and A. Therdthianwong, Synthesis Gas Production from CH₄ Reforming with CO₂ over Pd/Al₂O₃ Promoted with CeO₂. *AJEE* 3 (2002), 1-25.
- [151] N.A. Pechimuthu, K.K. Pant, S.C. Dhingra and R. Bhalla, Characterization and Activity of K, CeO₂, and Mn Promoted Ni/Al₂O₃ Catalysts for Carbon Dioxide Reforming of Methane. *Ind. Eng. Chem. Res.* 45 (2006), 7435-7443.
- [152] A. Erdohelyi, J. Cserenyi and F. Solymosi, Activation of CH₄ and Its Reaction with CO₂ over Supported Rh Catalysts. *J. Catal.* 141 (1993), 287-299.

- [153] J.R. Rostrupnielsen and J.H.B. Hansen, CO₂-Reforming of Methane over Transition Metals. *J. Catal.* 144 (1993), 38-49.
- [154] S. Corthals, J. Van Nederkassel, J. Geboers, H. De Winne, J. Van Noyen, B. Moens, B. Sels and P. Jacobs, Influence of composition of MgAl₂O₄ supported NiCeO₂ZrO₂ catalysts on coke formation and catalyst stability for dry reforming of methane. *Catal. Today* 138 (2008), 28-32.
- [155] J.-H. Kim, D.J. Suh, T.-J. Park and K.-L. Kim, Effect of metal particle size on coking during CO₂ reforming of CH₄ over Ni-alumina aerogel catalysts. *Appl. Catal., A* 197 (2000), 191-200.
- [156] E. Ruckenstein and Y.H. Hu, Carbon dioxide reforming of methane over nickel/alkaline earth metal oxide catalysts. *Appl. Catal., A* 133 (1995), 149-161.
- [157] J.B. Claridge, A.P.E. York, A.J. Brungs, C. Marquez-Alvarez, J. Sloan, S.C. Tsang and M.L.H. Green, New Catalysts for the Conversion of Methane to Synthesis Gas: Molybdenum and Tungsten Carbide. *J. Catal.* 180 (1998), 85-100.
- [158] D. Tang, Investigations on Diffusion and Dispersion in Reacting Gas/Solid-Systems - Combined Use of Reaction Engineering Methods and NMR-Techniques. Ph.D. Thesis, University Bayreuth, 2004.
- [159] N. Müller, Direkte Bestimmung von Koksdepositen auf Festbettkatalysatoren durch elektrische Sensoren. Ph.D. Thesis, University Bayreuth, 2010.

Curriculum Vitae

Personal Details

| | |
|-------------------|------------------------------|
| Name, First name: | Unde Rajabhau Bajirao |
| Birthday, place: | 20/11/1981, Undewadi (India) |
| Nationality: | Indian |

Education

| | |
|-----------------------|--|
| July 1998 – June 2000 | Padmabhushan Vasant Dada Patil Arts, Comm. and Science College, Patoda, India <i>(Higher Secondary School)</i> |
| July 2000 – July 2004 | Department of Chemical Engineering, Dr. D. Y. Patil College of Engineering and Technology, Kolhapur, India <i>(Degree granted: Bachelor of Engineering)</i> |
| Oct. 2004 – June 2007 | Department of Chemical Engineering, Institute of Technology and Management, Gwalior, India <i>(Degree granted: Master of Technology)</i> |

Profession

| | |
|----------------------|--|
| Oct. 2006- Apr. 2008 | Project Assistant at National Chemical laboratory, Pune, India |
| Aug 2008 – Till date | Scientific staff at Department of Chemical Engineering, University Bayreuth, Germany |